3D epigenome dynamics in normal and stalled development

by

Bo Hu

Department of Human Genetics
Faculty of Medicine and Health Sciences
McGill University, Montréal

April 2022

A thesis submitted to McGill University
in partial fulfillment of the requirements
of the degree of

Doctor of Philosophy

Abstract

Counted among the most complex machineries known to man, the cells that make up all living organisms lie at the foundation of life itself. Beyond traditional means of grossly assessing cellular morphology and composition, recent advances in sequencing-based assays have fuelled tremendous progress in understanding biological processes across varying scales. In particular, the importance of regulatory mechanisms that does not involve variation in actual genetic sequences – "epigenetics" – has become increasingly evident given their critical function in fine-tuning DNA compaction and folding. The dynamic epigenomic landscape thus not only underlies the diversity between cell types with specialized functions, but also distinguishes healthy and pathological states. Through the assembly of a 3D epigenome atlas of mouse germline development, we found that repressive domains and enhanced insulation maintains transcriptional integrity in the face of global DNA de-methylation and pervasion of enhancer-like signatures during epigenetic reprogramming in primordial germ cells. Subsequently in spermatogonia, these insulatory restraints and then removed en masse as global euchromatization and peripheral detachment of chromatin takes place in the preparation for meiotic entry. On the other hand, we leveraged a compendium of 3D epigenomic profiles in brain tumours to reveal that a specific histone mutation, H3K27M, specifically leads to the formation of repressive loop structures via a reader of H3K27me3, cPRC1. Following the validation of H3K27M-associated cPRC1 loops' impact in primary patient tumours, we further pinpointed this process as a therapeutic vulnerability – with the application of a cPRC1 inhibitor demonstrating the capacity to alleviate the oncogenic differentiation blockade. This thesis details how the systematic application of integrative multi-omics can dissect molecular determinants of health and disease as well as provide actionable insights towards the future development of targeted therapeutic strategies.

Résumé

Comptant parmi les machineries les plus complexes connues de l'homme, les cellules qui composent tous les organismes vivants sont à la base de la vie elle-même. Au-delà des moyens traditionnels d'évaluation grossière de la morphologie et de la composition cellulaires, les récentes avancées dans les analyses basées sur le séquençage ont alimenté des progrès considérables dans la compréhension des processus biologiques à différentes échelles. En particulier, l'importance des mécanismes de régulation qui n'impliquent pas de variation dans les séquences génétiques proprement dites - "épigénétique" - est devenue de plus en plus évidente, étant donné leur fonction critique dans le réglage fin de la compaction et du repliement de l'ADN. Le paysage épigénomique dynamique est donc non seulement à la base de la diversité des types de cellules aux fonctions spécialisées, mais il distingue également les états sains et pathologiques. Grâce à l'assemblage d'un atlas épigénome 3D du développement de la lignée germinale de la souris, nous avons constaté que les domaines répressifs et l'isolation renforcée maintiennent l'intégrité transcriptionnelle face à la déméthylation globale de l'ADN et à l'omniprésence de signatures de type enhancer pendant la reprogrammation épigénétique dans les cellules germinales primordiales. Par la suite, dans les spermatogonies, ces contraintes isolantes sont supprimées en masse lorsque l'euchromatisation globale et le détachement périphérique de la chromatine ont lieu pour préparer l'entrée méiotique. D'autre part, nous avons exploité un ensemble de profils épigénomiques 3D dans les tumeurs cérébrales pour révéler qu'une mutation spécifique de l'histone, H3K27M, conduit spécifiquement à la formation de structures en boucle répressive via un lecteur de H3K27me3, cPRC1. Après la validation de l'impact des boucles cPRC1 associées à H3K27M dans les tumeurs primaires des patients, nous avons identifié ce processus comme une vulnérabilité thérapeutique - l'application d'un inhibiteur de cPRC1 démontrant la capacité à atténuer le blocage de la différenciation oncogénique. Cette thèse montre comment l'application systématique de la multi-omique intégrative peut disséquer les déterminants moléculaires de la santé et de la maladie, et fournir des informations utiles pour le développement futur de stratégies thérapeutiques ciblées.

Contents

List of abbreviations

1D . . . . . One-dimensional
3D . . . . . Three-dimensional
AM . . . . . Allosteric modulator
APC . . . . . Adenomatous polyposis coli
ARID1A . . . . . AT-Rich Interaction Domain 1A
ATAC-seq . . . . . Assay for transposase-accessible chromatin with sequencing
BAP1 . . . . . BRCA1 Associated Protein 1
BRCA1 . . . . . Breast cancer type 1 susceptibility protein
BRD4 . . . . . Bromodomain-containing protein 4
CAGE-seq . . . . . Cap analysis gene expression sequencing
Cas9 . . . . . CRISPR-associated protein 9
CBX2 . . . . . Chromobox protein homolog 2
CBX4 . . . . . Chromobox protein homolog 4
CBX6 . . . . . Chromobox protein homolog 6
CBX7 . . . . . Chromobox protein homolog 7
CBX8 . . . . . Chromobox protein homolog 8
CFTR . . . . . Cystic fibrosis transmembrane conductance regulator
CGI . . . . . CpG island
ChIP-seq . . . . . Chromatin immunoprecipitation followed by sequencing
cPRC1 . . . . . Canonical PRC1
CRISPR . . . . . Clustered regularly interspaced short palindromic repeats
CTCF . . . . . CCCTC-binding factor
CUT&RUN . . . . . Cleavage Under Targets and Release Using Nuclease
DAPI . . . . . 4′,6-diamidino-2-phenylindole
DAZL . . . . . Deleted In Azoospermia Like

DDX4 . . . . . DEAD-Box Helicase 4

DMC1 . . . . . DNA Meiotic Recombinase 1

DMRT1 . . . . . Doublesex And Mab-3 Related Transcription Factor 1

DNA . . . . . Deoxyribonucleic acid

DNAme . . . . . DNA methylation

DNMT3A . . . . . DNA Methyltransferase 3 Alpha

DNMT3B . . . . . DNA Methyltransferase 3 Beta

DNMT3C . . . . . DNA Methyltransferase 3 C

DNMT3L . . . . . DNA Methyltransferase 3 Like

EED . . . . . Embryonic Ectoderm Development

EHMT1 . . . . . Euchromatic Histone Lysine Methyltransferase 1

EHMT2 . . . . . Euchromatic Histone Lysine Methyltransferase 2

ENCODE . . . . . Encyclopedia of DNA Elements

EpiLC . . . . . Epiblast-like cell

EPN . . . . . Ependymoma

eRNA . . . . . Enhancer RNA

ERV1 . . . . . Endogenous retrovirus-1

ERVK . . . . . Endogenous retrovirus-K

ESC . . . . . Embryonic stem cells

EVX2 . . . . . Even-Skipped Homeobox 2

EZH2 . . . . . Enhancer of zeste homolog 2

EZHIP . . . . . Enhancer of Zeste Homologs Inhibitory Protein

FISH . . . . . Fluorescence in situ hybridization

GAM . . . . . Generalized additive model

GAM . . . . . Genome architecture mapping

GATA4 . . . . . GATA Binding Protein 4

Gb . . . . . Gigabasepairs

GBM . . . . . Glioblastoma

GFAP . . . . . Glial Fibrillary Acidic Protein

GSC . . . . . Germline stem cell

GSCLC . . . . . Germline stem cell-like cell

GSEA . . . . . Gene set enrichment analysis

GWAS . . . . . Genome-wide association study

H2AK119ub . . . . . Histone H2A lysine 119 ubiquitinylation

H3K27ac . . . . . Histone H3 lysine 27 acetylation

H3K27M . . . . . Histone H3 lysine (27)-to-methionine

H3K27me . . . . . Histone H3 lysine 27 methylation

H3K27me3 . . . . . Histone H3 lysine 27 tri-methylation

H3K36M . . . . . Histone H3 lysine (36)-to-methionine

H3K36me . . . . . Histone H3 lysine 36 methylation

H3K36me2 . . . . . Histone H3 lysine 36 di-methylation

H3K36me3 . . . . . Histone H3 lysine 36 tri-methylation

H3K4me . . . . . Histone H3 lysine 4 methylation

H3K4me1 . . . . . Histone H3 lysine 4 mono-methylation

H3K4me3 . . . . . Histone H3 lysine 4 tri-methylation

H3K9me . . . . . Histone H3 lysine 9 methylation

H3K9me2 . . . . . Histone H3 lysine 9 di-methylation

H3K9me3 . . . . . Histone H3 lysine 9 tri-methylation

HDBSCAN . . . . . Hierarchical Density-Based Spatial Clustering of Applications with Noise

HGG . . . . . High-grade glioma

Hi-C . . . . . High-throughput chromosome conformation capture

hiPSC . . . . . Human induced pluripotent stem cell

HNSCC . . . . . Head and neck squamous cell carcinoma

HOX . . . . . Homeobox

HP1 . . . . . Heterochromatin protein 1

IF . . . . . Immunofluorescence

iPSC . . . . . Induced pluripotent stem cell

K9MTase . . . . . Histone H3 lysine 9 methyltransferase

Kb . . . . . Kilobasepairs

KLF4 . . . . . Kruppel Like Factor 4

KO . . . . . Knockout

LAD . . . . . Lamina associated domain

LINE1 . . . . . Long interspersed nuclear element 1

lncRNA . . . . . Long noncoding RNA

LOCK . . . . . Large organized chromatin lysine domains

MACS . . . . . Model-based Analysis of ChIP-seq

MAEL . . . . . Maelstrom Spermatogenic Transposon Silencer

Mb . . . . . Megabasepairs

mCG . . . . . Methyl Cpg

MCORE . . . . . Multiscale correlation evaluation

mESC . . . . . Mouse embryonic stem cell

mPGCLC . . . . . Mouse primordial germ cell-like cell

mRNA . . . . . Messenger RNA

MS . . . . . Mass spectrometry

ncPRC1 . . . . . Non-canonical PRC1

ncRNA . . . . . Noncoding RNA

NET-CAGE . . . . . Native elongating transcript–cap analysis of gene expression

NGS . . . . . Next generation sequencing

NIBPL . . . . . Nipped-B-Like Protein

NMR . . . . . Nuclear magnetic resonance

NPC . . . . . Neural progenitor cell

NSD1 . . . . . Nuclear Receptor Binding SET Domain Protein 1

NSD2 . . . . . Nuclear Receptor Binding SET Domain Protein 2

OCT4 . . . . . Octamer-Binding Protein 4

OPC . . . . . Oligodendrocyte progenitor cell

PAD . . . . . Polycomb-associating domains

PCA . . . . . Principal component analysis

PCH . . . . . Pericentromeric heterochromatin

PDX . . . . . Patient-Derived Xenograft

PFA . . . . . Posterior fossa group A

PGC . . . . . Primordial germ cell
PGCLC . . . . . Primordial germ cell-like cell
PHC1 . . . . . Polyhomeotic Homolog 1
PHC2 . . . . . Polyhomeotic Homolog 2
PHC3 . . . . . Polyhomeotic Homolog 3
pHGG . . . . . Pediatric high grade glioma
piRNA . . . . . Piwi-interacting RNA
PMD . . . . . Partially methylated domain
PRC1 . . . . . Polycomb Repressive Complex 1
PRC2 . . . . . Polycomb Repressive Complex 2
PSC . . . . . Pluripotent stem cell
PTM . . . . . Post-translational modification
RGC . . . . . Radial glial cell
RING1B . . . . . Really Interesting New Gene 1B
RNA . . . . . Ribonucleic acid
RNA-seq . . . . . RNA sequencing
RNAPII . . . . . RNA polymerase II
RRHO . . . . . Rank-rank hypergeometric overlap
rRNA . . . . . Ribosomal RNA
SA1 . . . . . Stromal antigen 1
SA2 . . . . . Stromal antigen 2
SA3 . . . . . Stromal antigen 3
SCC1 . . . . . Sister Chromatid Cohesion 1
SCML2 . . . . . Sex Comb On Midleg Like 2
scRNA-seq . . . . . Single cell RNA-seq
SET . . . . . Suppressor Of Variegation 3-9, Enhancer-of-zeste and Trithorax
SETD2 . . . . . SET domain containing 2
SETDB1 . . . . . SET Domain Bifurcated Histone Lysine Methyltransferase 1
SMC1 . . . . . Structural maintenance of chromosomes protein 1
SOHLH2 . . . . . Spermatogenesis And Oogenesis Specific Basic Helix-Loop-Helix 2

SOX10 . . . . . SRY-box transcription factor 10

SOX2 . . . . . SRY-box transcription factor 2

SPRITE . . . . . Split-pool recognition of interactions by tag extension

SRY . . . . . Sex-determining region Y

SSC . . . . . Spermatogonia stem cell

STAG1 . . . . . Stromal antigen 1

STAG2 . . . . . Stromal antigen 2

STAG3 . . . . . Stromal antigen 3

STAT3 . . . . . Signal Transducer And Activator Of Transcription 3

SUV39H1 . . . . . Suppressor Of Variegation 3-9 Homolog 1

SUV39H2 . . . . . Suppressor Of Variegation 3-9 Homolog 2

SUZ12 . . . . . Suppressor Of Zeste 12 Homolog

SYCP1 . . . . . Synaptonemal Complex Protein 1

TAD . . . . . Topologically-associating domain

TE . . . . . Transposable element

TET1 . . . . . Ten-eleven translocation methylcytosine dioxygenase 1

TET2 . . . . . Ten-eleven translocation methylcytosine dioxygenase 2

TET3 . . . . . Ten-eleven translocation methylcytosine dioxygenase 3

UHC . . . . . Unsupervised hierarchical clustering

UMAP . . . . . Uniform Manifold Approximation and Projection

vPRC1 . . . . . Variant PRC1

WAPL . . . . . Wings apart-like protein homolog

WGBS . . . . . Whole genome bisulfite sequencing

YY1 . . . . . Yin Yang 1

ZGA . . . . . Zygotic genome activation

List of figures

Acknowledgments

I would like to first and foremost express my sincere gratitude to Professors Jacek Majewski and Mitinori Saitou for graciously providing me with precious opportunities to work on a variety of exciting projects and ample chance to grow both inside and outside the lab under very favorable circumstances. Starting out with no bioinformatics experience, I would not have been immersed in the domain of computational biology nearly as quickly without Dr. Majewski's tireless guidance and sustained confidence in me. Dr. Saitou's stimulating discussions and infectious enthusiasm were critical bringing me, an outsider to developmental biology, quickly up to speed and soon begin contributing productively. I would also like to thank members of my supervisory committee, Professors Guillaume Bourque and Celia Greenwood, for their consistent and constructive feedback throughout the course of my studies, without which my projects would not have progressed as smoothly. Furthermore, I would like to thank Professors Fumihiko Matsuda and Ryo Yamada for their benevolent academic assistance and generous personal hospitality, making my time in Kyoto a wonderful experience that I will be sure to cherish and recall fondly.

These projects would not have been possible without the tremendous labour of fantastic collaborators with whom I've had the privilege and pleasure of working together. In particular, I'm deeply appreciative of Masahiro Nagano and Brian Krug for their partnership in spearheading these studies from the experimental side and fundamentally enabling my computational efforts; the time they charitably expended to brainstorm together with me and deliberate over the experimental design as well as data interpretation were vital in my swift acquisition of domain knowledge and allowing us to effectively tackle challenging problems. I'm also grateful to other members of the Majewski and Saitou groups as well as our internal and external collaborators who've contributed critical pieces of data and provided decisive advice that led to significant improvements of the manuscripts. Furthermore, I would like to acknowledge that the work described in this thesis is in part supported by financial support from the Canadian Institutes of Health Research, le Fonds de recherche du Québec – Santé, and the Japan Student Services Organization.

Last but not least, I'm thankful towards for family for their unwavering support.

Contribution to original knowledge

2 Nucleome programming for the foundation of totipotency in mammalian germline development

- Identified most variable histone modifications along male murine germline development and clarified regulatory impacts
- Established insulation enhancement as a novel protective mechanism during epigenetic reprogramming
- Uncovered continual maturation and euchromatization of 3D genome organization throughout germ cell development
- Pinpointed functionally important spermatogonial-specific nuclear architectural features that are conserved across species

3 H3K27me3 spreading organizes canonical PRC1 chromatin architecture to regulate developmental transcriptional program

- Detailed the effect of H3K27me3 on long-range interactions across diverse contexts with epigenetic dysregulation
- Revealed association of variable polycomb domain coverage with cPRC1 concentration as a biomarker of specific brain tumor subtypes
- Associated the degree of distal polycomb aggregation with developmental progression via transcriptional regulation
- Unveiled H3K27me3 readers as therapeutic vulnerability to modulate differentiation capacity

Format of the thesis

This thesis is presented in the manuscript-based format for a doctoral thesis according to the guidelines of the Department of Human Genetics at McGill University and is organized into five chapters. Chapter 1 introduces the regulatory importance of 3D epigenomic properties to proper cellular function, provides relevant background on the epigenome remodelling events that takes place during germline development and in K27M GBMs, and outlines the overarching goals of this thesis. Chapter 2 describes an effort to chart nucleome dynamics during male gametogenesis and highlights novel 3D epigenomic features of key stages, under the second round of reviews at the EMBO Journal. Chapter 3 is a manuscript in preparation for submission to Nature, which outlines the impact of polycomb domain re-organization on 3D genome organization and developmental progression. Chapters 4 and 5 present an overall discussion as well as general conclusions and future directions.

Contribution of authors

2 Nucleome programming for the foundation of totipotency in mammalian germline development

I conceived the project and designed the experiments together with Masahiro Nagano, Shihori Yokobayashi, and Mitinori Saitou. I performed the vast majority of the data analysis and supervised the remainder. I created all figures, with help from Masahiro Nagano for select schematics and images.

Masahiro Nagano assisted with overall data analysis. Yusuke Imoto, Killian Meehan, and Yasuaki Hiraoka assisted with polymer simulations. Masahiro Nagano performed all cell culture and induction with assistance from Hiroshi Ohta, Yukiko Ishikura and Yoshiaki Nosaka. Masahiro Nagano performed immunofluorescence and its analysis with assistance from Hiroshi Ohta, Naofumi Kawahira and Ken Mizuta. Masahiro Nagano and Fumiya Umemura performed western blot and its analysis with assistance from Yoshiaki Nosaka, Sakura Shimizu, and Yoji Kojima. Masahiro Nagano performed FISH with assistance from Ikuhiro Okamoto. Masahiro Nagano performed histone extraction and Mariel Coradin performed mass spectrometry under the supervision of Benjamin A Garcia. Masahiro Nagano and Akitoshi Yamamura performed ChIP-seq with assistance from Shihori Yokobayashi and Takuya Yamamoto. Masahiro Nagano performed ATAC-seq with assistance from Shihori Yokobayashi, Hiroki Ikeda, and Takuya Yamamoto. Masahiro Nagano performed in situ Hi-C with assistance from Shihori Yokobayashi, Roman Stocsits, Gordana Wutz, Kikue Tachibana, Jan-Michel Peters, and Leonid A Mirny. Masahiro Nagano performed NET-CAGE with assistance from Tomoko Kasahara under the supervision of Yasuhiro Murakawa. Shihori Yokobayashi, Jacek Majewski, and Mitinori Saitou supervised the project.

3 H3K27me3 spreading organizes canonical PRC1 chromatin architecture to regulate developmental transcriptional program

I conceived the project and designed the experiments together with Brian Krug, Jacek Majewski, and Nada Jabado. I performed the vast majority of the data analysis and supervised the remainder. I created all figures, with help from Brian Krug for select schematics and images.

Haifen Chen, Xiao Chen, Michael Johnston, and Marco Gallo assisted the analysis of ChIP-seq and Hi-C datasets. Nisha Kabir and Claudia Kleinman assisted the analysis of single-cell RNA-seq datasets. Brian Krug, Kristjan Gretarsson, Shriya Deshmukh, Elias Jabbour, Maud Hulswit, Ashot Harutyunyan, John Lee, and Michael D Taylor contributed to generating genomics datasets. Brian Krug, Kristjan Gretarsson and Shriya Deshmukh performed functional experiments and generated cell lines models. Damien Faury assisted the generation of single-cell RNA-seq datasets, Caterina Russo assisted performing of xenograft experiments and collection. Chao Lu, Jacek Majewski, and Nada Jabado supervised the project.

Epigenetics imparts a fundamental regulatory system beyond the sequence information of our genetic code and emphasizes that "Mendel's gene is more than just a DNA moiety."

Thomas Jenuwein & C. David Allis

Chapter 1

Introduction

Peering into genome regulation through a 3D epigenomics lens

Deoxyribonucleic acid (DNA), the code for life itself, lies at the foundation of biology through its role as the source of information flow: with the contents of DNA copied via transcription into ribonucleic acid (RNA), which is in turn translated into proteins that ultimately function as critical cogs in the elaborate cellular machineries powering every living organism (Fig. 1.1).[1] This classic view centered around sequences encoding proteins ("genes") has since been formalized as the "central dogma of molecular biology" and has dominated mainstream genetics since the establishment of DNA as the essence of heritability (or "transforming material") in the 1940s,[2] with most efforts focused on understanding how genetic sequence variations contribute to phenotypic differences ranging from subtle traits to complex disorders.[3] In particular, the elegant simplicity of considering genes as discrete units, where variant forms simply lead to a reduction

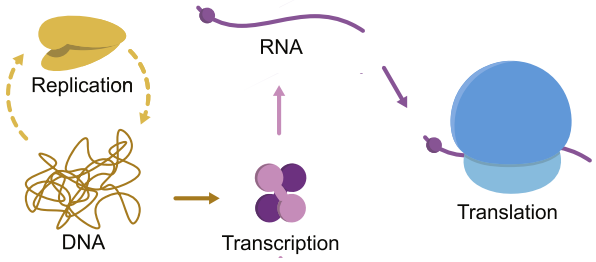

Figure 1.1: Central dogma of molecular biology. Reproduced from Costello & Badran [1]

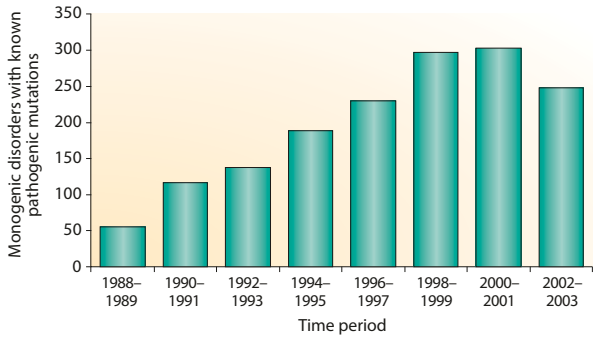

Figure 1.2: Mapping disease genes. Number of pathogenic mutations causing monogenic disorders recorded by OMIM at various times. Reproduced from Antonarakis & Beckmann [4]

in functional protein quantity, have allowed the application of the long-standing concepts such as Mendelian inheritance and pedigree analysis to achieve great successes; using these approaches to pinpoint genes whose loss alone suffices for pathogenesis, hundreds of disease-causing genes were already resolved by the early 2000s (Fig. 1.2).[4] Among one of the most well-known examples, the unambiguous association between mutations in the *CFTR* (cystic fibrosis transmembrane conductance regulator) gene with cystic fibrosis, and the accompanying direct disease mechanism, facilitated concentrated efforts that enabled breakthrough treatments substantially improving the lives of patients suffering from this debilitating affliction.[5]

Alongside the initial assembly of all sequences that constitute human DNA (the "human genome"), genome-wide association studies (GWAS) bursted to the forefront of genetics following the turn of the millennium through demonstrating the capacity to comprehensively and statistically assess the association between traits and variant across the entire genome. From these investigations it then became apparent that more complex models are required to unravel genome regulation. In particular, as protein-coding sequences only constitute less than 2% of the human genome, the vast majority of implicated sequence variants fall outside of protein-coding regions ("intergenic"), further complicating direct interpretation of their downstream impacts. Although traditionally considered "junk DNA", it's become apparent that indispensable regulatory elements are embedded within such intergenic regions and can fine-tune the activity of nearby target genes through a variety of mechanisms; these elements range from "enhancers" and "silencers" involved in modulating the transcription of DNA into RNA (also known as "gene expression"), to "insulators" demarcating boundaries that segregate the genome into discrete domains subject to co-regulation. While signatures of evolutionary conservation were historically used to gauge functional importance of DNA sequences, detailed genomic element annotations have more recently been empowered by extensive functional profiling initiatives across multiple cellular contexts covering the gamut of health and disease (Fig. 1.3).[6]

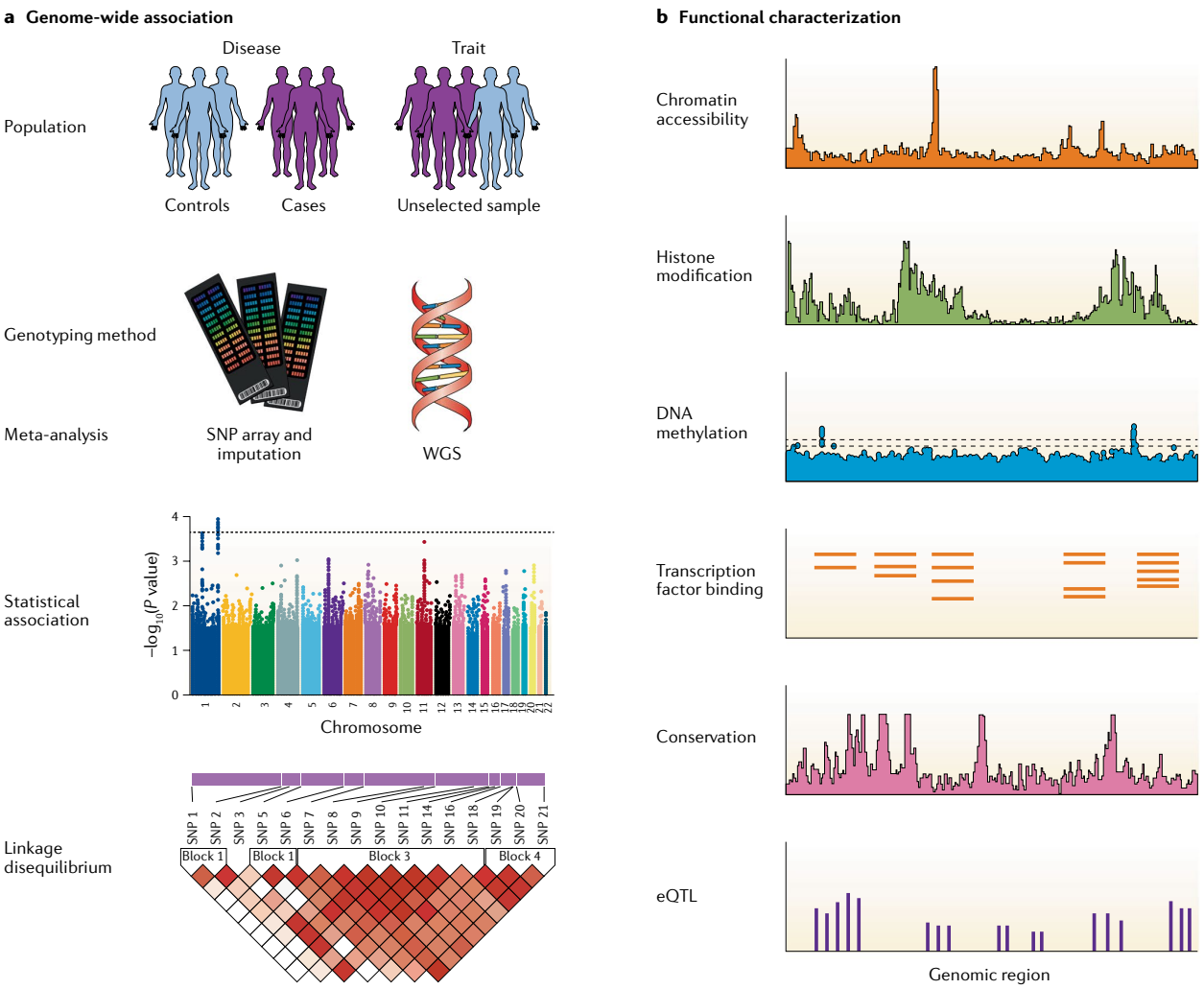

Figure 1.3: Interpreting GWAS hits. a. Set-up of typical GWAS studies; b. Means to interpret non-coding variants. Reproduced from Tam *et al.* [6]

Functional genome profiling often entails investigation into "*epi*genetic" modifications that comprise an information layer "on top" of DNA sequences, directing gene expression programs without genetic alterations – akin to diacritics modulating the tone and meaning of letters.[7] Epigenetic modifications broadly impart their influence by governing the packaging of DNA, as molecules that total meters in length are encased into micrometer-wide cell nuclei (Fig. 1.4).[8] DNA, adenines and cytosines in particular, can be chemically modified through the addition of "methyl" chemical moieties in a process called "methylation", chemically distinguishing modified nucleobases from unmodified ones and providing substrates for methyl-binding domain-containing proteins while sterically hindering the access of other regulators.[9] Stepping up the organizational hierarchy, DNA strands are then wrapped around histone proteins to form fiber-like structures called "chromatin". These histones can also take on post-translational modification at

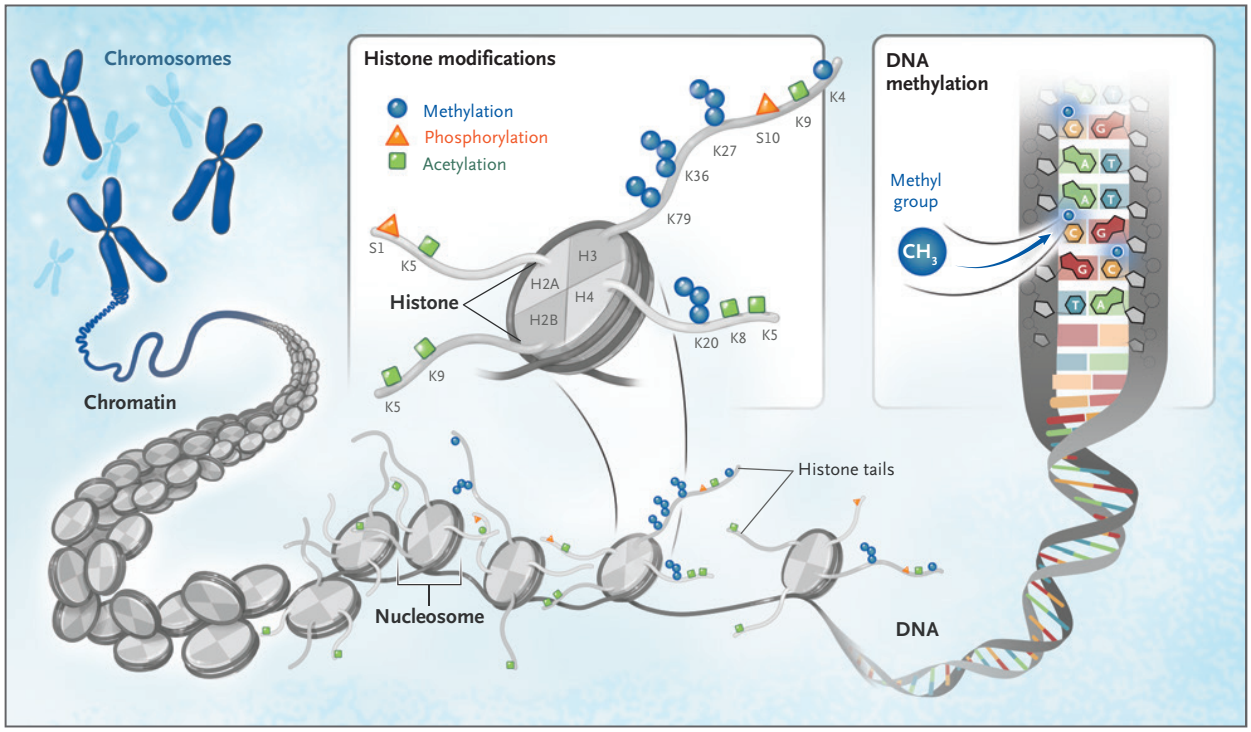

Figure 1.4: Epigenetic mechanisms. Reproduced from Bates [8]

specific residues, usually concentrated on the tail sections that protrude outwards, and acquire contrasting biochemical properties.[10] It's been found that particular combination of histone modifications can be viewed as markers of distinct genome functions, with some marking active regions ("euchromatin") and others silent ("heterochromatin"), corresponding to the degree of DNA compaction. Whereas euchromatic regions of loose DNA packaging are said to be more "accessible" to the binding of DNA-recognizing proteins such as those regulating transcription ("transcription factors"), closed heterochromatin can physically occlude the access of such factors (Fig. 1.5).[11]. It is therefore thought that the incredible diversity of cell types within multi-cellular organisms, despite them all stemming from a

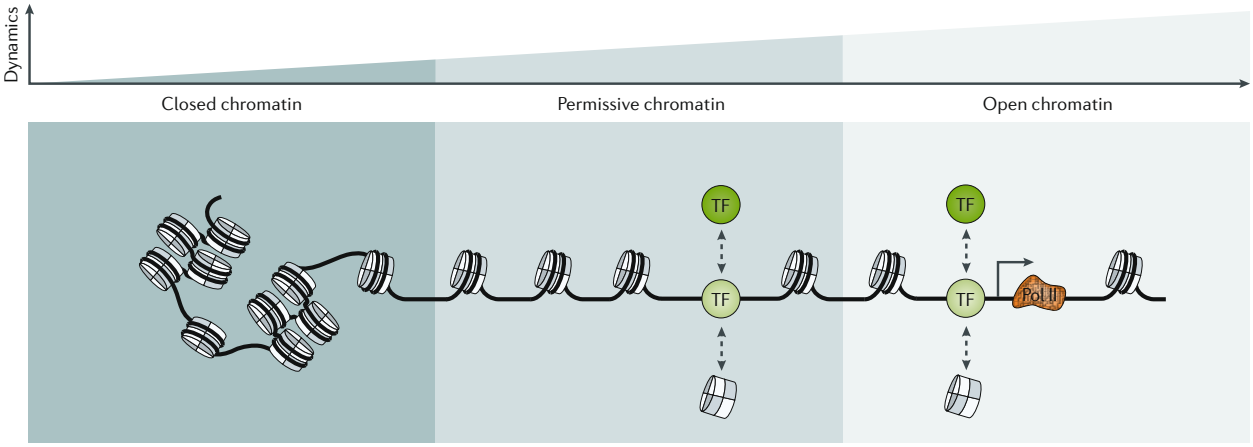

Figure 1.5: Gene regulation through chromatin accessibility. Reproduced from Klemm *et al.* [11]

single zygote and sharing the very same genetic blueprint, necessarily involves epigenetic mechanisms.[12] Indeed, the very concept of an "epigenetic landscape" stems from the works of Conrad Waddington in the mid 20th century, analogizing development and cell fate decisions as traversal between discrete cellular states.[13] With the advent of functional genome profiling, the contemporary model of the Waddington landscape is thus one where cell type-specific gene regulatory programs, precisely facilitating the expression of genes while keeping others silent, derives from the fine-tuning of epigenetic processes. And it is through the inherent characteristics of various epigenetic modifications as well as their writers and readers that complex interaction networks arise: involving crosstalks, cascades, and feedback loops that presents a daunting yet bounteous opportunity to scrupulously disentangle these interconnections that make up the "epigenome".

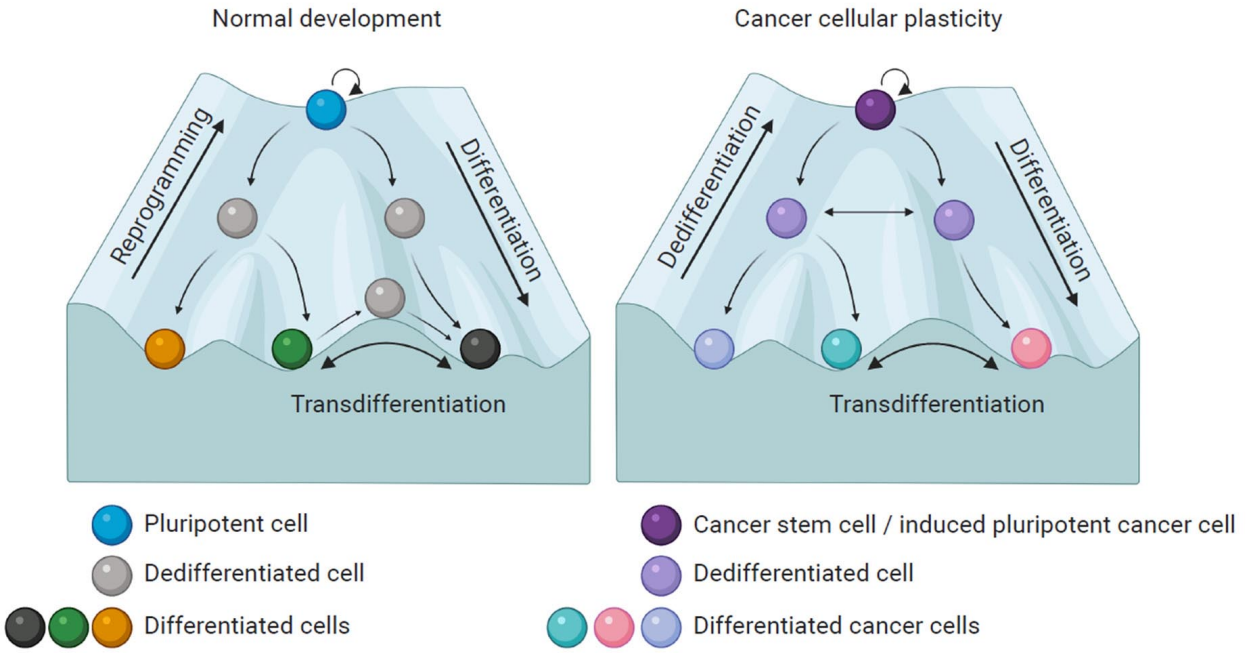

Figure 1.6: Waddington's epigenetic landscape depicting normal development and carcinogenesis. Reproduced from Granados *et al.* [14]

Beyond differentiation in development, the epigenome's malleability has also been noted as a useful model for disease: while malignant cells may co-opt epigenetic plasticity for transformation and escape physiological surveillance, this property can be likewise exploited clinically to alter and sensitize cells for otherwise untenable therapeutic strategies (Fig. 1.6).[14] Therefore, the initial step towards uncovering such epigenomic vulnerabilities will necessitate first and foremost the acquisition of comprehensive molecular portraits across both physiological and pathological settings. As an example, tissue-specific

regulatory elements identified via epigenetic profiles were reported to not only fall near genes belonging to tissue-specific expression programs, but the very same regions have also exhibited strong enrichment for variants previously implicated with phenotypes known to affect the associated tissue (e.g., GWAS hits for psychiatric traits in regions specifically accessible in neurons alone).[15] On the other hand, it's also been shown in assorted cancers that epigenetic information such as DNA methylation can prove invaluable in uncovering distinct molecular subtypes – substantially accelerating the development of targeted strategies by enabling finer patient stratification.[16]

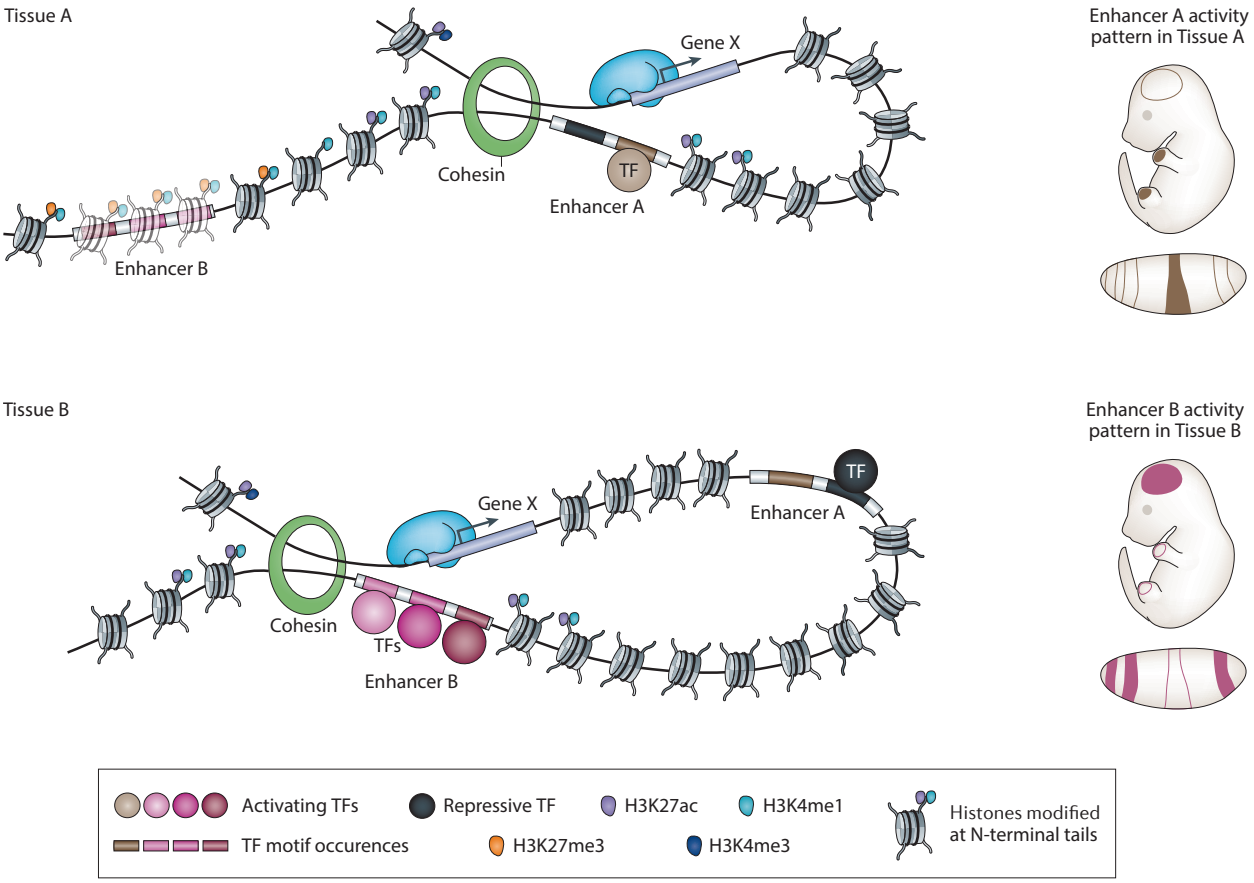

Figure 1.7: Tissue-specific cis-regulation of enhancers. Reproduced from Shlyueva *et al.* [17]

The expansive repertoire through which epigenetic mechanisms affect cellular processes range from controlling the binding of vital transcription factors that may modulate the expression of nearby genes to facilitating distal interaction between chromatin segments, and the specific identity of these processes have been linked with a combination of several telltale epigenetic markers (Fig. 1.7).[17] For instance, active elements are typically surrounded by specific modified forms of histone H3 – acetylated at 27th lysine residue (H3K27ac) and/or methylated at lysine 4 of H3 (H3K4me); it has also been observed that whereas

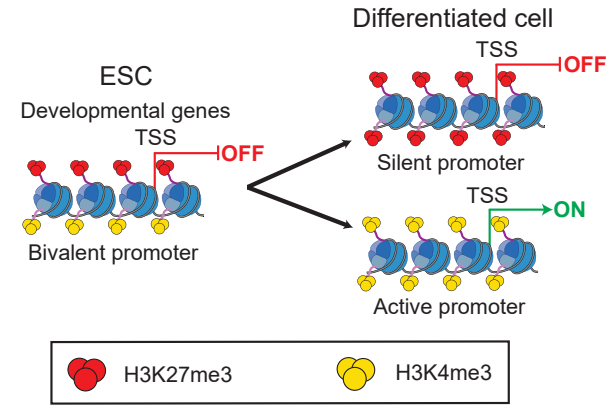

Figure 1.8: Bivalent chromatin dynamics. Reproduced from Blanco *et al.* [18]

tri-methylation of H3K4 (H3K4me3) is enriched at "promoter" elements upstream of expressed genes' transcription start sites, mono-methylated H3K4 (H3K4me1) instead marks "enhancer" elements that loop around to engage active promoters and boost transcription despite their potentially large separation on the linear genome spanning tens to hundreds of kilobases (kb). While the exact mechanisms remain under debate, it is thought that enhancers facilitate enhanced transcription of nearby genes ("in *cis*") through increasing concentration of transcription factors that are conducive to higher expression in the immediate vicinity of promoters.[19] In contrast, H3K27me3 is generally associated with repressed cis-regulatory elements (enhancers and promoters) through the inducing heterochromatinization. Yet H3K27me3 is not always distributed in a mutually exclusive manner with H3K4me, with their co-occurrence often designating regulatory elements of developmental genes, corresponding to a "poised"/"bivalent" state that may only resolve to fully active and repressed depending on subsequent cues such as developmental signals (Fig. 1.8).[18] At grander scales, other modifications can also broadly pattern heterochromatic (e.g., H3K9me) and euchromatic (e.g., H3K36me) domains that are up to hundreds of kbs or even megabases (mb) in widths. Therefore, deconvolving highly combinatorial chromatin states in a genome-wide manner generally demands the simultaneous survey of a varied set of modifications. (Fig. 1.9).[10] In addition to the

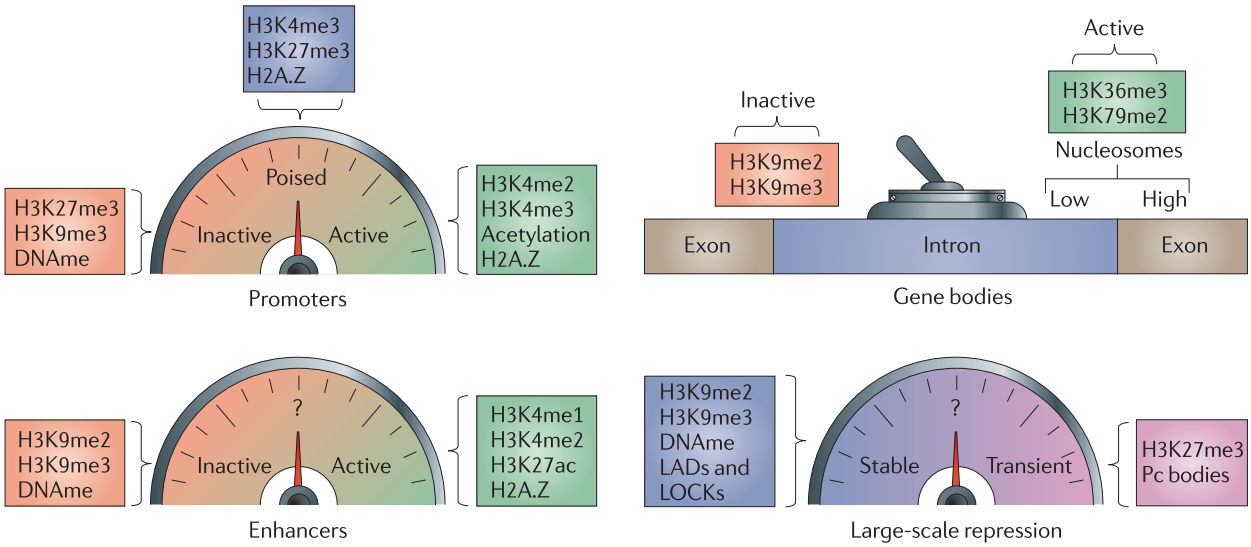

Figure 1.9: Epigenetic hallmarks of different genomic regions. Reproduced from Zhou *et al.* [10]

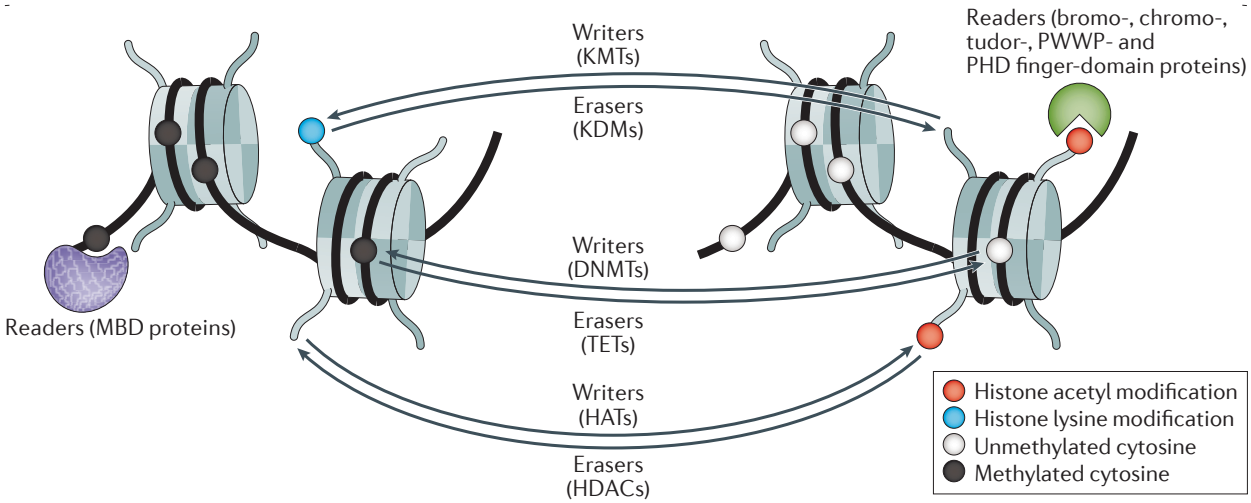

Figure 1.10: Functions of epigenetic modifiers. Reproduced from Jones *et al.* [20]

modifications themselves, further complications arise from the plethora of chromatin modifiers that read, write, and erase epigenetic modifications, as the same complex can often be endowed with multiple functions through its various subunits (Fig. 1.10).[20] For example, Polycomb Repressive Complex 2 (PRC2), a H3K27 methyltransferase (i.e., writer), recognizes H3K27me3 through the Embryonic Ectoderm Development (EED) subunit for allosteric activation, while the Enhancer of zeste homolog 2 (EZH2) subunit possessing methyltransferase catalytic activity simultaneously recognizes unmethylated H3K36 through a separate domain – partially explaining the observed general exclusion of H3K27me3 from H3K36me2/3-decorated chromatin.[21] Taken together, the collection of epigenetic markers must be considered in conjunction with the accompanying set of modifiers to decipher how proper epigenome dynamics foster normal physiological functioning as well as how epigenomic perturbations engender dysfunction.

But a conventional view of the epigenome as an 1D scaffold cannot account for how chromatin fiber is further arranged in 3D space to ultimately fit within the tiny nuclei of cells that are magnitudes smaller in width than the length of chromatin fiber simply stretched in full; and rather than behaving as an ideal chain in the context of polymer physics, it's been shown that chromatin adopts non-random 3D conformations in reality, subject to regulation at multiple scales.[22] At the highest level, the architecture of chromatin within the nucleus ("nucleome") is dictated by landmarks such the nucleolus and nuclear lamina that serve as scaffolds around which particular genomic regions attach and take on specific roles including transcriptional factories and repressive hubs (Fig. 1.11).[23] Chromatin itself, with myriad epigenetic modifications, likewise influences genome folding patterns through passive forces

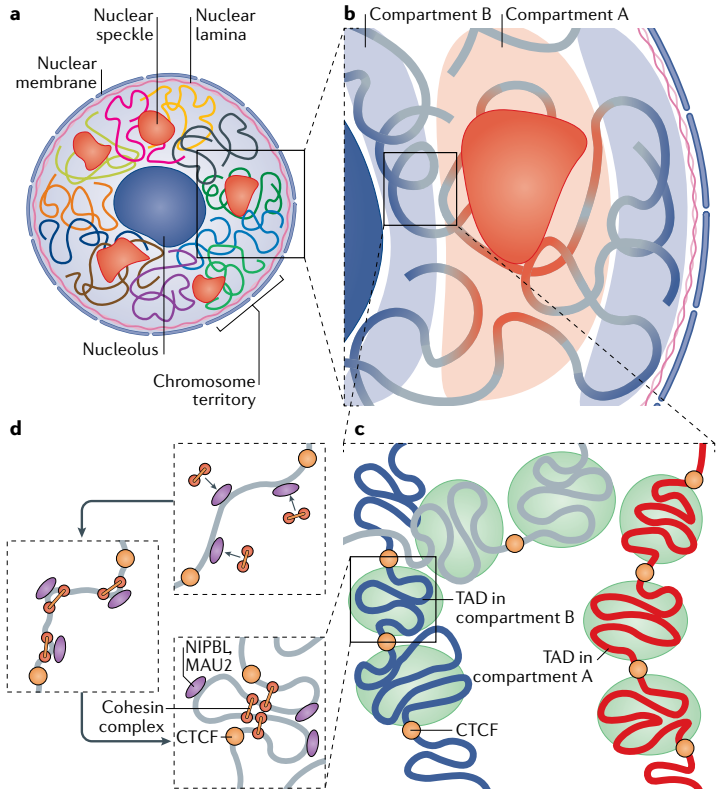

Figure 1.11: Multi-scale nucleome organization. a. Chromosomal territories organize around nuclear landmarks during interphase; b. Euchromatin and heterochromatin separate into distinct compartments; c. Preferentially self-interacting domains exist within compartments; d. Active loop extrusion by cohesin in concert with boundary CTCF elements contribute to domain formation and sub-domain looping. Reproduced from Zheng & Xie [23]

such as liquid-liquid phase separation. For instance, H3K9me-associated constitutive heterochromatin was mechanistically linked with a reader protein of H3K9me, HP1, organizing marked sections of chromatin into liquid-like droplets.[24]. Active processes involving energy consumption also exists as a major force, with a prime example being loop extrusion, where ring-like cohesin complexes act as motors to extrude chromatin loops until their encounter with boundaries bound by proteins CCCTC-binding factor (CTCF).[25] As they organize the very same chromatin fiber, the active and passive forces of disparate origins seldom act in isolation, leading to complex interactions. For example, active cohesin-mediated loop extrusion is known to antagonize a host of passive processes, including compartmentalization of the genome into euchromatin and heterochromatin as well as other condensates such as H3K27me3-enriched polycomb bodies.[27,28] Proper 3D genome organization and nuclear architecture, a healthy nucleome, has also been shown to serve essential physiological functions in view of the wide

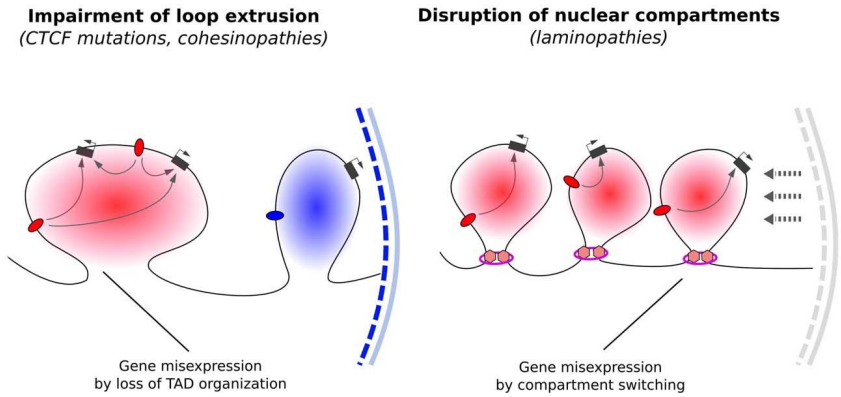

Figure 1.12: Defective higher-order genome architecture. Reproduced from Anania & Lupiáñez [26]

range of diseases associated with defective architectural proteins such as laminopathies and cohesinopathies, often linked to developmental and cognitive anomalies (Fig. 1.12).[26]. Therefore, a simultaneous appreciation of both local one-dimensional (1D) compaction and three-dimensional (3D) global organization, at multiple scales (Fig. 1.13),[29] is necessary to grasp chromatin dynamics and establish a strong grasp of their influence in sickness and health alike.[30]

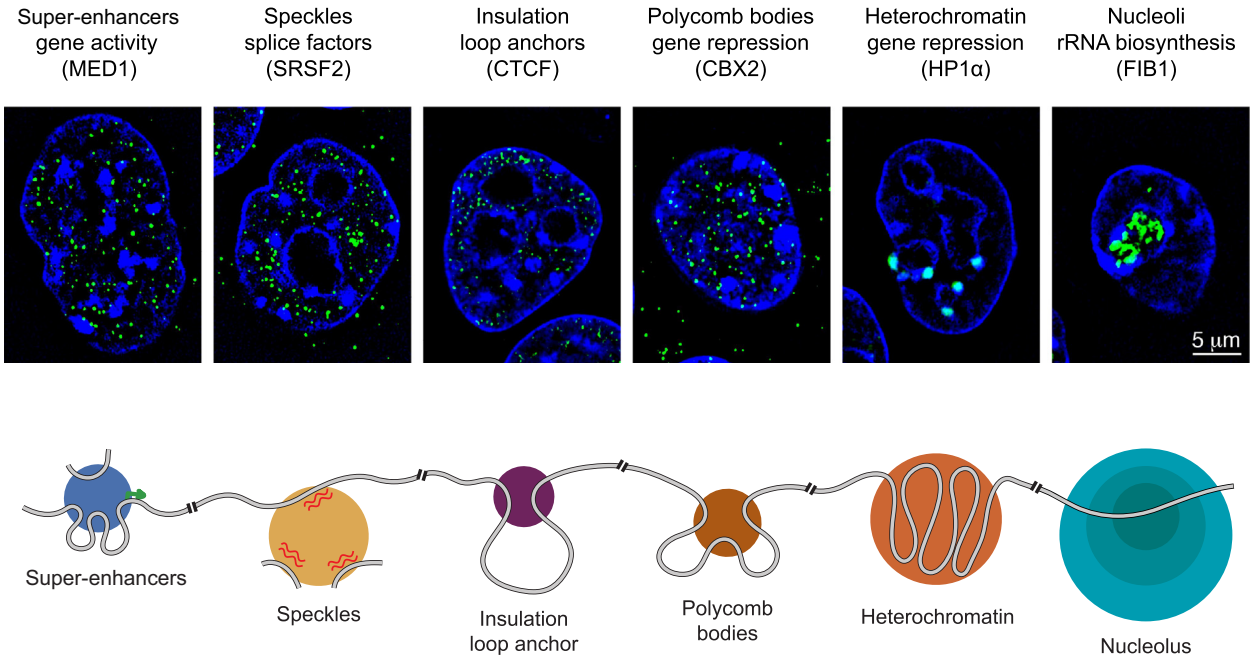

Figure 1.13: Biomolecular condensates of various scales. Reproduced from Sabari *et al.* [29]

Though rapid expansion of the modern genomics toolbox has enabled snapshots of life at unprecedented granularity and depth, technological and analytical barriers siloing discrete data modalities continue to obstruct a complete picture for cellular activity – akin to the parable of the elephant in the dark. Considering the inherent complexity of biological processes based on current knowledge of protein interaction networks and gene regulatory circuits, it's imperative now more than ever to capitalize on the existing and accumulating wealth of multi-omics datasets with integrative approaches to distill holistic insights into specifically the interplay among omics layers (Fig. 1.14).[31] Apart from sharpening our understanding of fundamental principles, an end-to-end comprehension of how changes in a particular aspect propagates through other modalities will additionally supplement novel targets for therapeutic development and thus accelerate translational efforts in precision medicine.

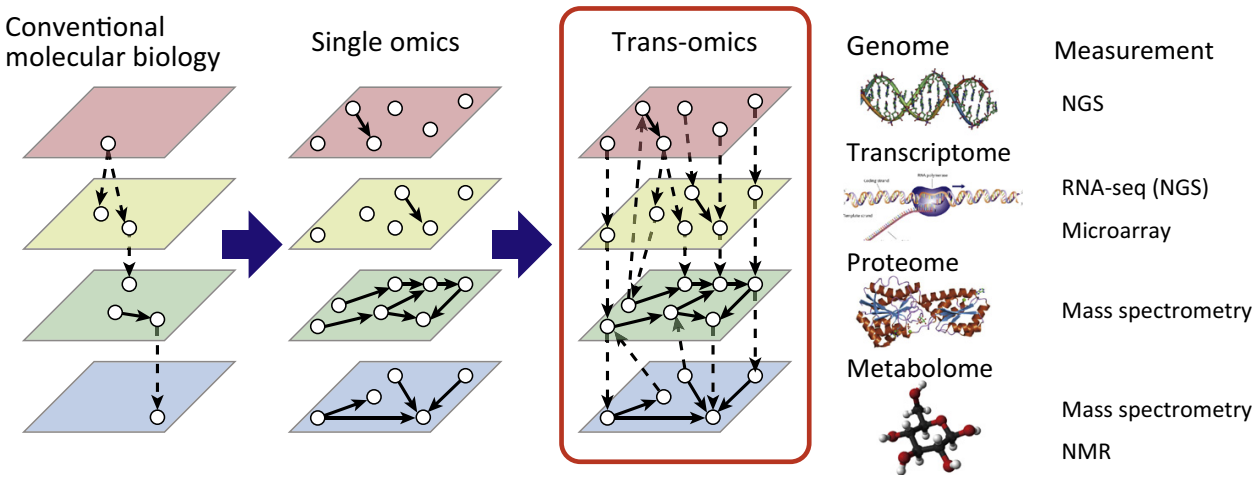

Figure 1.14: Integrative multi-omics. Consideration of information flow within and across omics layers necessary for comprehensive understanding of biological system. Reproduced from Yugi *et al.* [31]

Key multi-omics platforms enabling 3D epigenomics

DNA sequencing technologies, especially next-generation sequencing with their incredible throughput and efficiency, were indispensable in fuelling the explosive growth of early undertakings dissecting genetic variation.[32] Subsequently, ingenious means of encapsulating information from other processes into DNA molecules has been one of the major drivers enabling the detailed characterization and precise quantification of myriad cellular properties and activities. Microscopy and cell imaging has, in parallel, benefitted from advances in optics and fluorophore chemistry and now routinely used to not only provide orthogonal validation of sequencing-based datasets, but also fill in salient gaps such as the spatial and temporal distributions of diverse biomolecules including DNA, RNA, and proteins.[33] Likewise, methodological and computational improvements have also enabled mass spectrometry-based methods to investigate the assortment of proteins present in various samples ("proteome") at increased throughputs without significantly hampering sensitivity and accuracy.[34] Modern studies aiming to molecularly profile specific cellular states thus frequently adopt a multi-pronged approach leveraging many of these technologies in concert, with particularly strong emphasis on three fronts: epigenome, nucleome, and transcriptome (the set of RNA transcripts expressed in a cell).

The epigenome is amenable to a number of methods for dissecting its intricacies from multiple angles (Fig. 1.15).[35] Epigenetic control of chromatin compaction can be evaluated using methods such as assay for transposase-accessible chromatin with sequencing (ATAC-seq) that preferentially enriches for acces-

sible DNA for subsequent sequencing, in the process pinpointing sites of DNA unwound from histones usually driven by transcription factor binding and associated activities. Modifications to DNA itself, specifically methylation of cytosines, can be measured via whole genome bisulfite sequencing (WGBS), where only unmethylated cytosines are converted to thymines while methylated cytosines remain intact, allowing their disambiguation downstream computationally. In contrast, to evaluate the distribution of modifications decorating chromatin across the genome, chromatin immunoprecipitation followed by sequencing (ChIP-seq) draws on the affinity of antibodies for specific targets (e.g., transcription factors or histone modifications) to pull down associated DNA for further analysis. Similarly, western blotting uses antibodies to bind specific targets for quantification. As opposed to focusing on specific targets individually, high-throughput proteomics can also be employed to assay histones and accurately measuring the global abundance of various histone post-translational modifications – therefore complementing sequencing dataset's marker distributional information with precise quantification.[36]

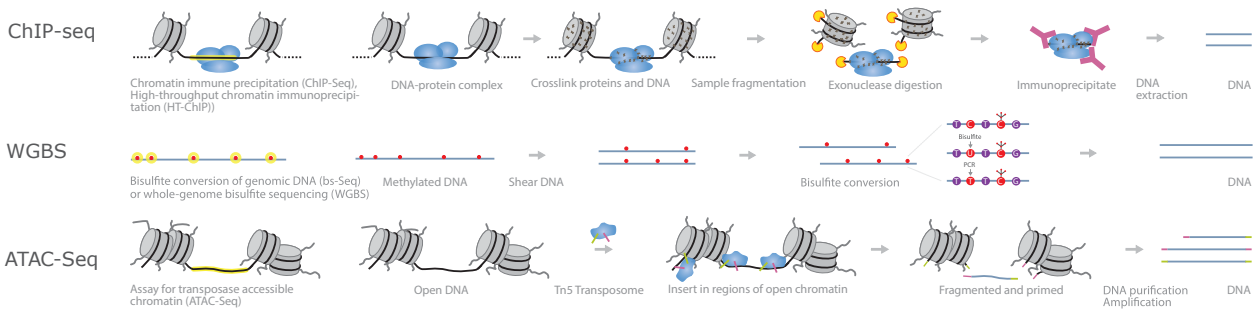

Figure 1.15: Epigenome mapping. Common techniques to investigate different facets of the epigenome. Reproduced from Illumina [37]

Higher-order organization of the DNA can, too, be assessed at multiple resolutions through several orthogonal means (Fig. 1.16).[38] High-throughput chromosome conformation capture (Hi-C) has emerged as a powerful platform by which the contact frequency between all pairwise combination of DNA segments can be deduced, as spatially nearby pieces of chromatin are subjected to proximity ligation and subsequently profiled using paired-end sequencing to enumerate the number of pairs originating from various genomic regions. Although contact probabilities as measured by Hi-C strongly correlate with physical separations in 3D space, there can exist disparities between "contact frequency" versus "average spatial separation" for pairs of genomic loci across a cell population due to non-random folding of chromatin *in vivo* (e.g., as mediated by loop extrusion),[39] proximity ligation is thus frequently

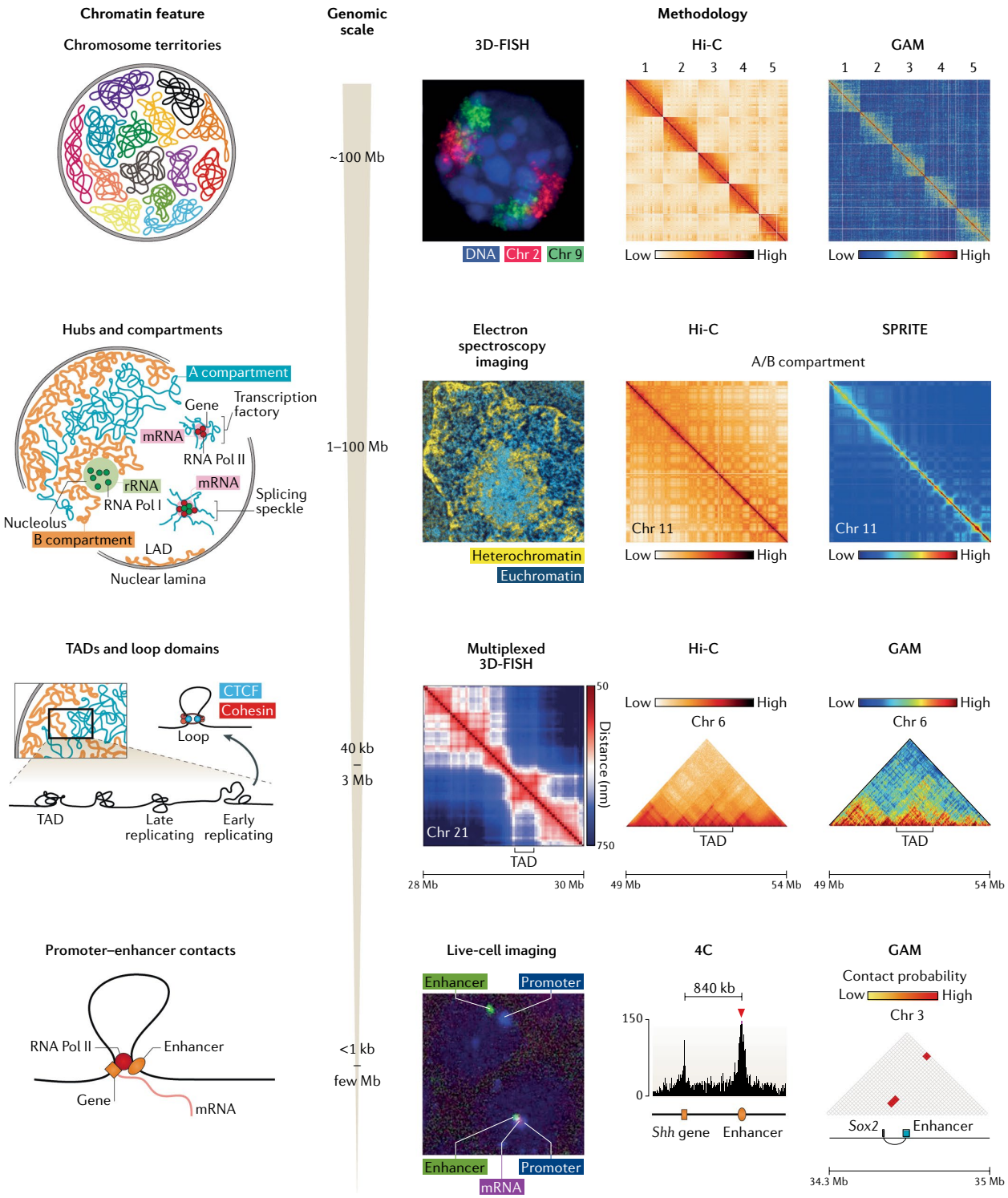

Figure 1.16: Nucleome mapping. Common techniques to investigate different facets of the transcriptome. Reproduced from Kempfer & Pombo [38]

supplemented by fluorescence in situ hybridization (FISH) to label different sequences with targeted probes, after which their true separation can be quantified using microscopy at a single cell resolution. Through recent approaches multiplexing and applying FISH in serial (e.g., in seqFISH+), it's even

possible to evaluate the spatial localization for a large number of targets in the same cells, ranging from histone modifications and proteins to RNAs.[40] Instead of DNA sequences, fluorophore-labelled antibodies are also frequently used in immunofluorescence imaging applications to determine the spatial distribution of nuclear structures such as lamina-associated heterochromatin or nucleolus-associated euchromatin.

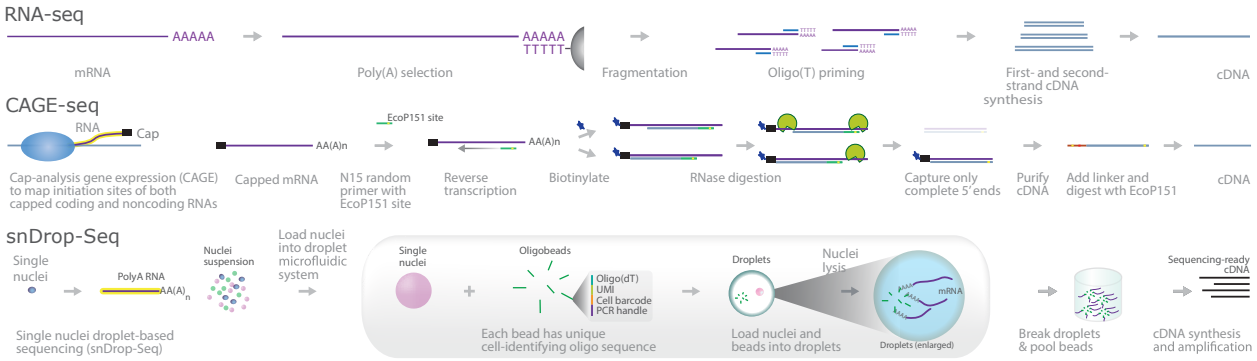

Figure 1.17: Transcriptome mapping. Reproduced from Illumina [41]

Linking chromatin dynamics to downstream outcomes is no less significant than understanding the upstream processes themselves, with one of the most frequently adopted read-outs for phenotypic consequences being gene expression (Fig. 1.17). Although reverse transcription can readily convert RNA into DNA that is ready to be sequenced, the diversity of RNA species introduces additional complexities. Apart from protein-coding messenger RNA (mRNA), there exists a variety of non-coding classes of RNA (ncRNA) molecules such as ribosomal RNA (rRNA) and long noncoding RNA (lncRNA) that can fulfill various biological functions without necessarily being translated.[42] As a result, typical RNA sequencing (RNA-seq) methods usually explore only a subset of total RNA via strategies such as rRNA depletion and poly(A) selection to enrich for mRNA, tagging the 5' cap of mRNAs to map transcription initiation sites, or pulling down RNA polymerase II (RNAPII)-associated RNA to examine nascent transcripts.[43] Many techniques can be further augmented with single cell barcoding to tag molecules from the same cell with unique sequences that can be analytically decoded and enable transcriptomic characterization of individual cells to disentangle the inter-cellular heterogeneity of complex samples.

Despite the richness of information afforded by individual modalities, studies usually stand to gain from a more holistic approach combining signals across omics layers. Besides helping overcome the

inherently noisy nature of biological data by means of pinpointing consistent trends across orthogonal methods, multi-omics datasets importantly facilitate the use of data-hungry unsupervised data mining methods to reveal unexpected patterns – critical to elucidating elaborate processes such as development and tumorigenesis.

Charting 3D epigenome dynamics towards totipotency

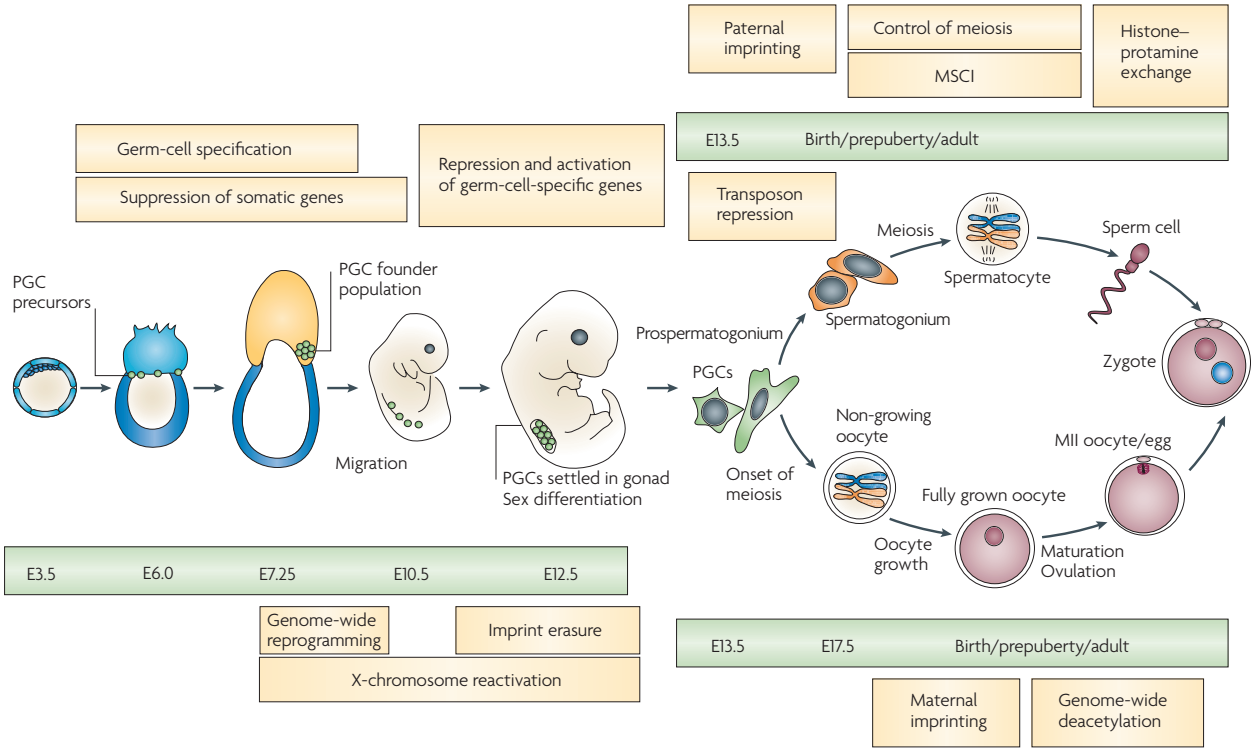

Figure 1.18: Mouse germ-cell development. Reproduced from Sasaki & Matsui [44]

Genetic information is specifically transmitted across generations through the germline, making gametogenesis not only a fascinating system to unravel from a basic biology perspective of understanding the path towards totipotency, but also bear relevance for deciphering candidate mechanisms underlying reproductive disorders. (Fig. 1.18).[44] Apart from the three primary germ layers arising from the epiblast that eventually differentiates into various somatic tissue, primordial germ cell (PGC) specification also occurs in the epiblast and marks one of the earliest conclusive cell fate decisions.[45] A hallmark event that soon ensues is epigenetic reprogramming, a process by which global DNA de-methylation occurs before becoming re-established in a sexual dimorphic manner: largely prenatal for prospermatogonia

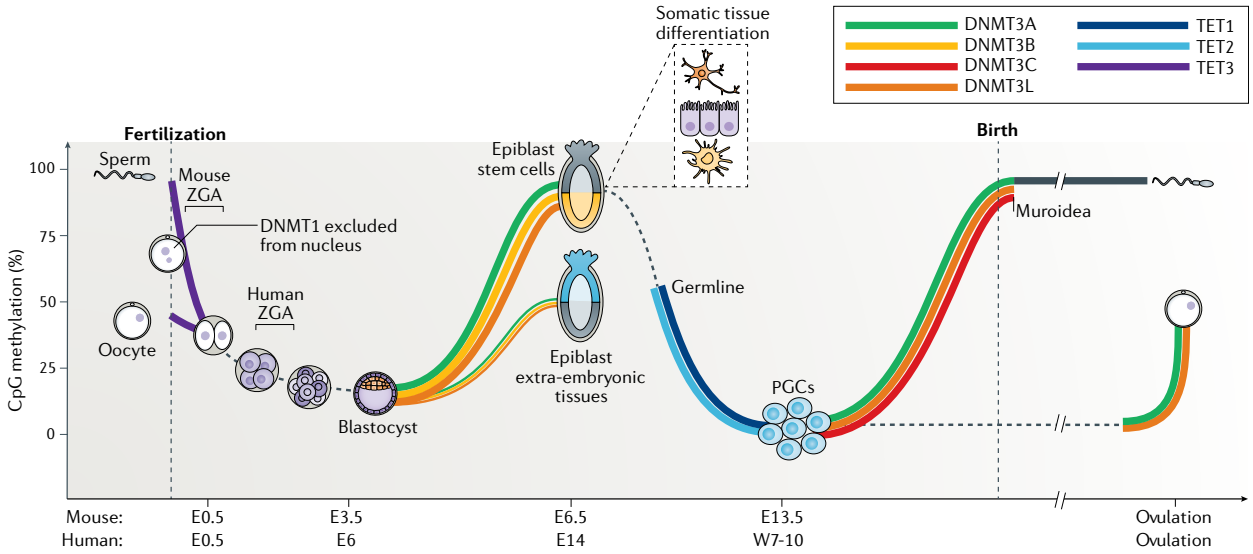

Figure 1.19: Mammalian embryonic epigenome remodelling. Dynamic DNA methylation landscape during early development. Reproduced from Greenberg & Bourc'his [9]

and gradually after birth for growing oocytes (Fig. 1.19).[9] The dramatic chromatin remodeling that takes place during this unique lineage has thus garnered substantial interest from developmental and chromatin biologists alike. However, the meagre population of germ cells *in vivo* has been a roadblock for conventional assays, as it imposes a difficult burden on obtaining sufficient input material. Towards circumventing this obstacle, *in vitro* reconstitution systems have been developed that can faithfully produce functional oocytes and spermatozoa entirely from embryonic stem cells in a dish, empowering a thorough examination of chromatin dynamics during the course of germ cell development.

Meiotic development up until fertilization and early zygotic stages have specifically been intensively investigated to begin unravelling the foundation of totipotency (Fig. 1.20).[46] For instance, oocytes were noted for their 3D genome's lack of compartmentalization and insulation, with gradual emergence of domain and loop structures only taking place once zygotic genome activation begins in early embryos.[47] Additionally, the polycomb system is also known to exhibit unique dynamics including the allele-specific distributions of H3K27me3 and H2AK119ub immediately before and following fertilization,[48] as well as the transient strengthening of interactions between polycomb domains in growing oocytes.[49] Yet mitotic germline development has remained less understood and needs to be explored in greater detail.

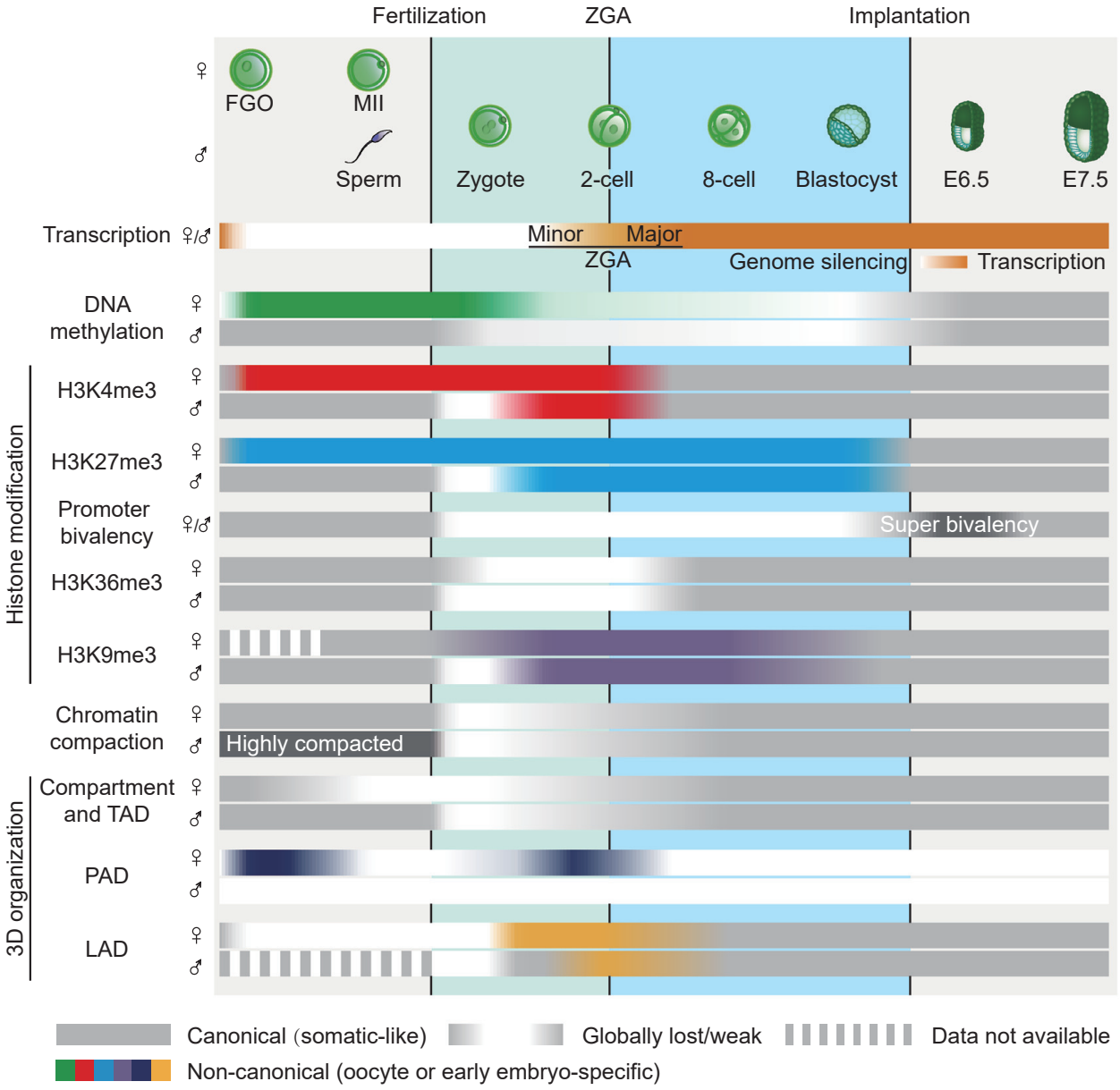

Figure 1.20: 3D epigenome dynamics during early embryogenesis. Reproduced from Xia & Xie [46]

Effects of polycomb re-organization on the 3D epigenome and beyond

While the epigenome undergoes extensive remodelling extensively during development, similarly dramatic transformations can likewise take place during pathogenesis, especially for cancer. Accompanying the growth in sequencing technologies for basic research, clinical applications of genetic and epigenetic profiling to cancers have revealed the existence of molecularly distinct subtypes within the more traditional tumor categories broadly based on anatomical location. These classifications are

particularly important due to high variability in treatment responses, posing an urgent need for finer patient stratification and more tailored selection of therapeutic strategies – the aim of precision medicine. Although the irony of personalized medicine lies in the necessity of massive datasets to detect exquisite differentiators separating individuals, global efforts fortunately heeded these calls with the requisite scale.[51] Consequently, it became apparent that driver mutations in chromatin modifiers or histone themselves constitute a formidable subgroup of their own, often leaving notable epigenomic as well as transcriptomic footprints in addition to characteristic genetic alterations.[52] Given the established role of epigenetic regulation in cellular differentiation, the link between mutations in chromatin regulators with impaired differentiation or aberrant de-differentiation in the course of tumorigenesis came as less than surprising (Fig. 1.21).[50] But beyond mutations in epigenetic modifiers, the canvas itself – chromatin – has also been found to possess characteristic mutations, with the most prominent ones entirely localized on the tail of histone H3 (Fig. 1.22).[53] Such oncogenic histone mutants ("oncohistones"), including histone H3 lysine (27)-to-methionine (H3K27M) and H3K36M, are believed to dominantly exert an inhibitory influence on the corresponding methyltransferases (e.g., PRC2, NSD1/2) in *trans*, causing the genome-wide depletion of methylation on the mutated residue, even for wild-type histones.[52]

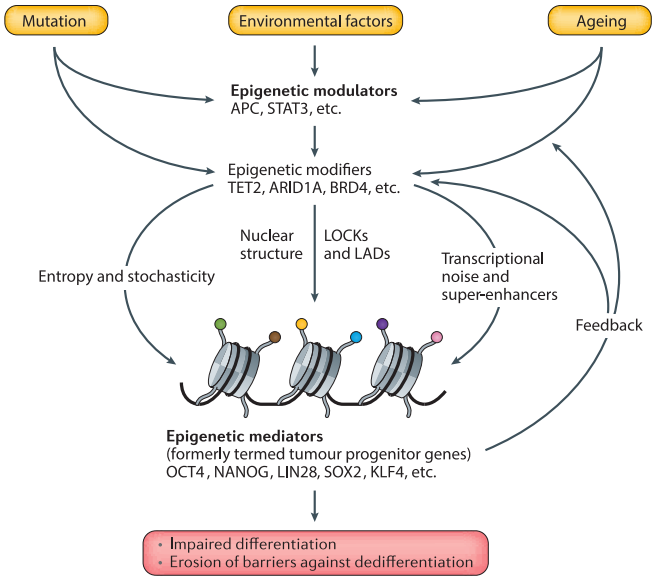

Figure 1.21: Cancer-linked epigenetic genes. Reproduced from Feinberg *et al.* [50]

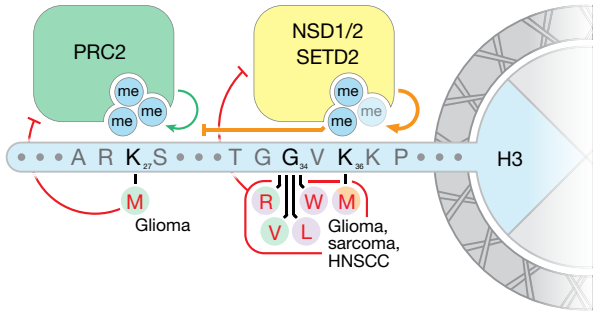

Figure 1.22: Oncohistone H3 mutations. Reproduced from Nacev *et al.* [53]

Whether it be through cell-intrinsic or -extrinsic mechanisms, tumorigenic mutations, especially those in chromatin modifiers, can show high levels of specificity to particular cancer types, and H3K27M is no exception. As one of the most common pediatric malignancies, childhood brain tumors have remained deeply troubling in view of potential long-term complications associated with surgically operating on the brain;[55] and among the diverse patient population, a epigenetically distinct subset of pediatric high-grade gliomas (pHGGs) was identified to specifically possess H3K27M as a driver mutation.[56] Following the initial discovery of H3K27M-associated pHGGs, a previously uncharacterized protein that is over-expressed in posterior fossa type A ependymomas (PFA-EPNs) was revealed to contain a H3K27M-like peptide subsequence, and was therefore named Enhancer of Zeste Homologs Inhibitory Protein (EZHIP). This name stemmed from the discovery that while H3K27M/EZHIP by and large does not affect the recruitment of PRC2 to chromatin, they significantly impair the spreading PRC2 through binding to its catalytic subunit EZH2; the result of H3K27M mutation and EZHIP over-expression is thus the contraction of repressive broad H3K27 methylation domains and consequent up-regulation of opposing euchromatic modifications such as H3K27 acetylation (Fig. 1.23).[54] While cancer stem cells are thought to be involved across both adult and pediatric cancers, the path through which this state is achieved diverges: adult cancers are generally considered to revert to a stem-like state via de-differentiation, whereas pediatric cancers fail to progress past a certain development stage. In line with this school of thought, it was found that H3K27M glioma stem cells are unresponsive to differentiation stimuli *in vitro*, unlike isogenic comparisons where the mutation was removed via CRISPR-Cas9 that readily proceeds to become mature astrocytes/oligodendrocytes.[57] Indeed, single-cell analysis of both H3K27M pHGGs and EZHIP-overexpressing posterior PFA-EPNs uncovered substantial undifferenti-

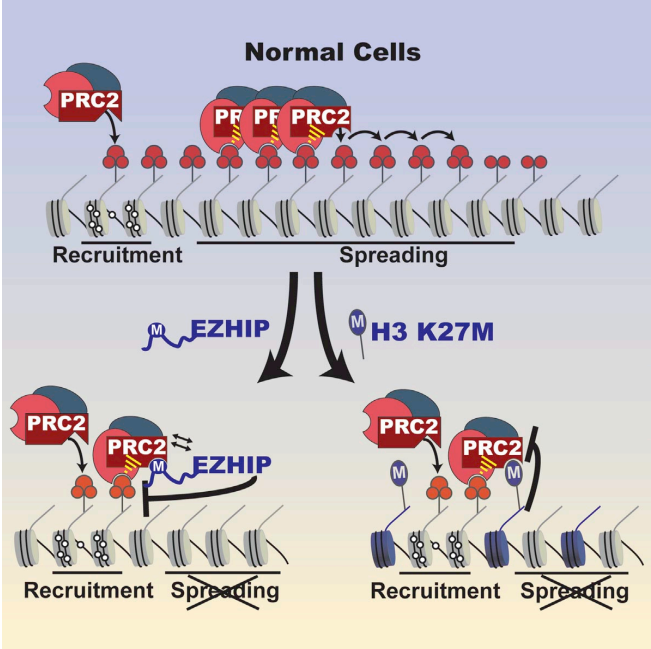

Figure 1.23: PRC2 inhibition by H3K27M/EZHIP. H3K27M oncohistones and EZHIP specifically impede spreading of PRC2. Reproduced from Jain *et al.* [54]

ated progenitor cells – implicating differentiation blockade as the most likely tumorigenic mechanism.[58]

H3K27me3 can also undergo global re-distribution without any direct defects in the Polycomb system itself, as it's been reported that the higher methylation states of H3K27 and H3K36 residues frequently engage in a tug-of-war across a variety of biological contexts ranging from healthy stem cells to malignant cancer cell lines, with their domain edges frequently acting as reciprocal boundaries (Fig. 1.24).[59] As a result, mutations affecting different chromatin modifiers have frequently been linked back to the dysregulation of precisely this balance between H3K36 and H3K27 methylation.[60]. With the genome serving as a consistent backdrop, the expansion of one domain thus compels the encroachment upon another in a zero-sum game,[61] with the competition in force throughout development as well as pathogenesis to orchestrate the coordinated activation and repression of various transcriptional programs.

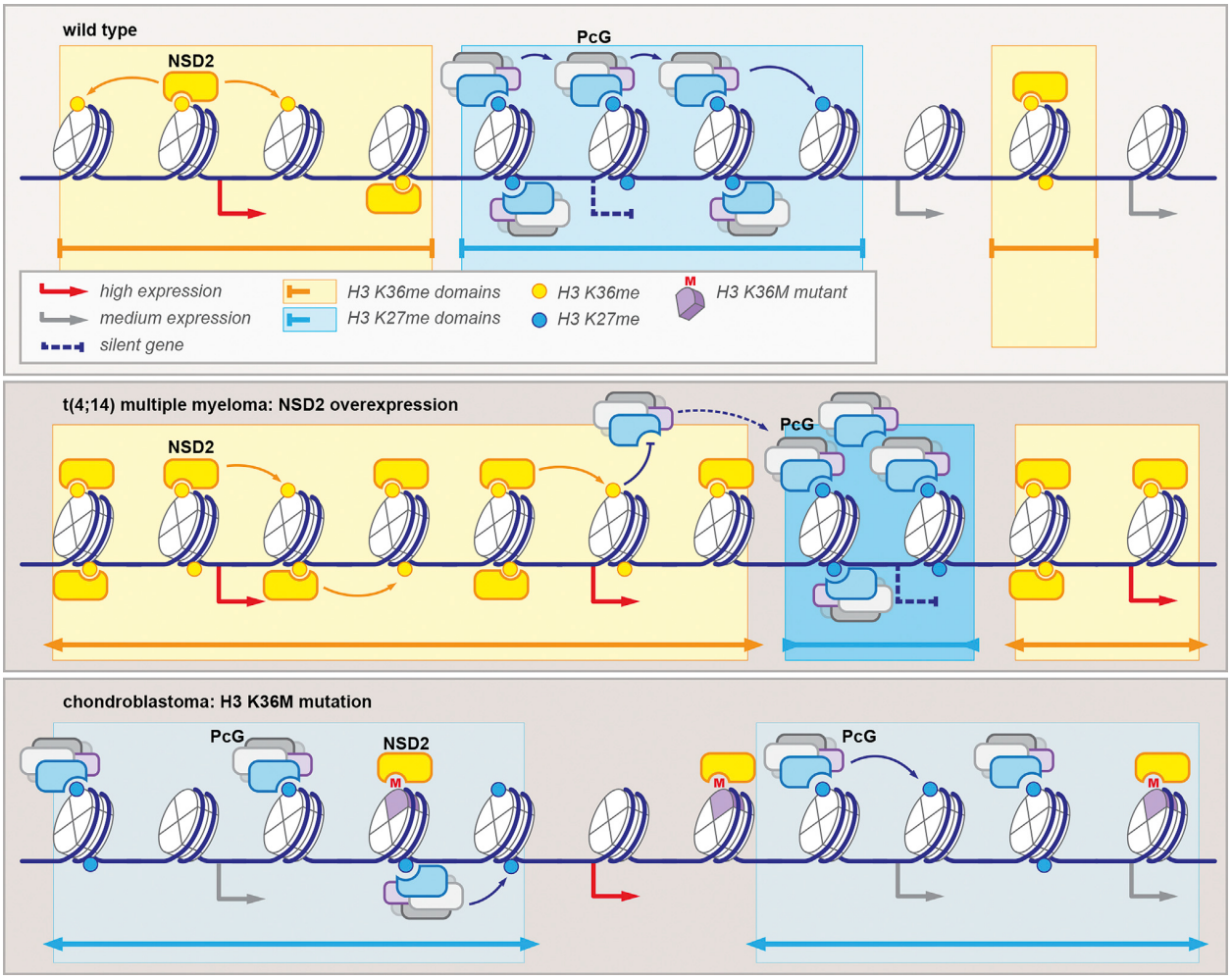

Figure 1.24: Reciprocity of H3K27 vs H3K36 methylation. Reproduced from Soshnev *et al.* [59]

H3K36 methylation, in particular, have been deemed a major force in shaping the epigenome, with mutations to H3K36 methyltransferases such as NSD1 and NSD2 or in histone H3 itself (e.g., H3 lysine(36)-to-methionine, or H3K36M, mutations) leading to not only the dramatic depletion of H3K36 methylation, but also a simultaneous gain of H3K27 methylation and loss of H3K27 acetylation as well as DNA methylation (or vice versa in the case of elevated H3K36me).[62–64] It's therefore evident that a careful maintenance of the balance between H3K27 and H3K36 methylation is necessary for healthy cells, whereas tipping the scales can wreck havoc.

Pinpointing the consequences of 3D epigenomic alterations

In view of the 3D epigenome's emergent importance in health and disease, we resolved to apply multi-omics profiling to normal germ cell differentiation as well as developmentally stalled brain tumors, demonstrating how integrative analytical approaches can step up to the challenge and fulfill unmet gaps in the molecular understanding of chromatin-centric genome regulation.

To tackle the deficit in our understanding of germline mitotic development, we used our *in vitro* differentiation system to closely characterize vital events such as naïve-to-primed transition, primordial germ cell specification, epigenetic reprogramming, and sexual dimorphic germ cell maturation. We hypothesized that a comprehensive 3D epigenomic atlas of male germ cell development will furnish insights into both the physiological idiosyncrasies of the germline and potential points of failure where defects may lead to dire consequences. We thus aimed to build such a compendium through the collection of a time-series multi-omics dataset spanning the nucleome, epigenome, and transcriptome with a range of complementary approaches. Subsequently, we sought to systematically apply genome-wide analytical strategies to quantitatively summarize temporal 3D epigenome variations at multiple scales in an unsupervised fashion, from chromosomal territories and compartmentalization down to domain structures and regulatory elements as well as chromatin loops bridging such regions. Finally, we methodically documented the differences between fully functional and aberrant spermatogonia with impaired spermatogenic potential, paving the path towards understanding the chromatin determinants of reproductive capacity.

On the other hand, based on existing results implicating the dysregulation of H3K27 and H3K36 methylation as driver pathogenic events, we hypothesized that comprehensively profiling the 3D epigenome should provide additional insights into the mechanistic link between primary chromatin alterations targetting H3K27 and H3K36 methylation with downstream phenotypic consequences such as faulty developmental progression. To this end, we set out to assemble a collection of 3D epigenomic datasets from different cell types and biological systems where the balance of H3K27 vs H3K36 is tipped to varying degrees in either direction, including both published resources and newly generated in-house data. We next pursued the specific intermediaries ultimately responsible for alterations in chromatin dynamics through the integration of 1D epigenetic and 3D chromatin conformation datasets. Building on top of the chromatin-based findings, we resolved to identify whether coordinated local and higher-order chromatin changes can be eventually traced to differential gene expression. Following our initial discoveries in cell line models with abundant data, we then validated whether the results are consistent with observations from patient-derived xenografts and primary tumors. Taken the exploratory results altogether, we finally homed in to the most promising co-factors linking upstream chromatin dynamics with downstream transcriptomic alterations for pharmacological perturbation, setting the stage for promising targeted therapeutic strategies.

Most cells contain the same set of genes and yet they are extremely diverse in appearance and functions. Germ cells, stem cells and early embryos all exhibit pluripotency, but each cell type also displays certain unique properties. Mechanisms that regulate this exceptional genomic plasticity and the state of totipotency are being unravelled, and will enhance our ability to manipulate stem cells for therapeutic purposes.

M. Azim Surani

Chapter 2

Nucleome programming for the foundation of totipotency in mammalian germline development

Germ cells are known to undergo epigenetic reprogramming – a highly unique process involving global DNA demethylation as well as other dramatic epigenomic alterations; it is believed that this reset is critical in facilitating the acquisition of totipotency in the next generation. Despite previous microscopic observations of notable nuclear architecture changes accompanying this drastic remodelling event, the mechanisms governing such multi-scale transformations and the functional implications of their interplay with other regulatory modalities remain largely unknown – as the limited number of gonadal germ cells *in vivo* has hindered the application of conventional genome-wide assays. Capitalizing on our murine *in vitro* differentiation system, we here investigated the determinants of nuclear totipotency underlying male germline development. In particular, we assembled a time-series multi-omics compendium of 6 cell types using Hi-C, histone mass spectrometry, ChIP-seq of histone modifications/transcription factors/architectural proteins, ATAC-seq, RNA-seq, NET-CAGE, and WGBS.

Nucleome programming for the foundation of totipotency in mammalian germline development

Masahiro Nagano[1,2,18], Bo Hu[2,3,18], Shihori Yokobayashi[1,2,4], Akitoshi Yamamura[1,2], Fumiya Umemura[1,2], Mariel Coradin[5,6,7], Hiroshi Ohta[1,2], Yukihiro Yabuta[1,2], Yukiko Ishikura[1,2], Ikuhiro Okamoto[1,2], Hiroki Ikeda[4,8,], Naofumi Kawahira[9,10], Yoshiaki Nosaka[1,2], Sakura Shimizu[1,2], Yoji Kojima[1,2,4], Ken Mizuta[1,2], Tomoko Kasahara[1,11], Yusuke Imoto[1], Killian Meehan[1], Roman Stocsits[12], Gordana Wutz[12], Yasuaki Hiraoka[1], Yasuhiro Murakawa[1,11], Takuya Yamamoto[1,4,13], Kikue Tachibana[14,15], Jan-Michel Peters[12], Leonid A Mirny[16], Benjamin A. Garcia[5,6,17], Jacek Majewski[3], Mitinori Saitou[1,2,4]

[1]Institute for the Advanced Study of Human Biology (WPI-ASHBi), [2]Department of Anatomy and Cell Biology, Graduate School of Medicine, Kyoto University, Yoshida-Konoe-cho, Sakyo-ku, Kyoto 606-8501, Japan.

[3]Department of Human Genetics, McGill University, Montreal, Quebec, Canada.

[4]Center for iPS Cell Research and Application (CiRA), Kyoto University, 53 Kawahara-cho, Shogoin, Sakyo-ku, Kyoto 606-8507, Japan.

[5]Department of Biochemistry and Biophysics, [6]Penn Epigenetics Institute, Perelman School of Medicine, University of Pennsylvania, Philadelphia, PA, USA.

[7]Department of Molecular, Cellular, and Developmental Biology, University of Colorado Boulder, Boulder, CO 80309, USA.

[8]Department of Embryology, Nara Medical University, Nara, Japan.

[9]Department of Molecular Cell Developmental Biology, School of Life Science, University of California, Los Angeles, CA, USA.

[10]Laboratory for Developmental Morphogeometry, RIKEN Center for Biosystems Dynamics Research, Kobe, Japan.

[11]RIKEN Center for Integrative Medical Sciences, Yokohama, Kanagawa 230-0045, Japan.

[12]Research Institute of Molecular Pathology, Vienna BioCenter, Vienna, Austria.

[13]Medical-risk Avoidance based on iPS Cells Team, RIKEN Center for Advanced Intelligence Project, Kyoto, Japan.

[14]Institute of Molecular Biotechnology of the Austrian Academy of Sciences, Vienna BioCenter, Vienna, Austria.

[15]Department of Totipotency, Max Planck Institute of Biochemistry, Martinsried, Germany.

[16]Institute for Medical Engineering and Science, and Department of Physics, Massachusetts Institute of Technology, Cambridge, MA, USA.

[17]Department of Biochemistry and Molecular Biophysics, Washington University School of Medicine, 660 S. Euclid Ave., St. Louis, MO 63110-1010, USA.

[18]These authors contributed equally.

Running title: Nucleome Programming for Germ Cells

*Correspondence: Mitinori Saitou, M.D., Ph.D.

E-mail: saitou@anat2.med.kyoto-u.ac.jp; Tel: +81-75-753-4335; Fax: +81-75-751-7286

ABSTRACT

Germ cells are unique in engendering totipotency, yet the mechanisms underlying this capacity remain elusive. Here, we perform comprehensive and in-depth nucleome analysis of mouse germ-cell development in vitro, encompassing pluripotent precursors, primordial germ cells (PGCs) before and after epigenetic reprogramming, and spermatogonia/spermatogonial stem cells (SSCs). Although epigenetic reprogramming, including genome-wide DNA de-methylation, creates broadly open chromatin with abundant enhancer-like signatures, the augmented chromatin insulation safeguards transcriptional fidelity. These insulatory constraints are then erased en masse for spermatogonial development. Notably, despite distinguishing epigenetic programming, including global DNA re-methylation, the PGCs-to-spermatogonia/SSCs development entails further euchromatization. This accompanies substantial erasure of lamina-associated domains (LADs), generating spermatogonia/SSCs with minimal peripheral attachment of chromatin except for pericentromeres—an architecture conserved in primates. Accordingly, faulty nucleome maturation, including persistent insulation and improper euchromatization, leads to impaired spermatogenic potential. Given that PGCs after epigenetic reprogramming serve as oogenic progenitors as well, our findings elucidate a principle for the nucleome programming that creates gametogenic progenitors in both sexes, defining a basis for nuclear totipotency.

INTRODUCTION

Germ cells are the origin of totipotency, which in turn is the foundation for individual development. Mechanisms underlying totipotency have been a focus of intensive investigations, ranging from studies involving somatic-cell nuclear transfer (Gurdon & Wilmut, 2011) to recent efforts exploring the three-dimensional (3D) chromatin organization in zygotes and early embryos (Zheng & Xie, 2019). The latter works involving chromatin conformation capture have revealed a relaxed chromatin configuration in zygotes in part resulting from unique meiotic intermediates, and the progressive maturation of this configuration in early embryos (Alavattam, Maezawa et al., 2019, Battulin, Fishman et al., 2015, Du, Zheng et al., 2017, Flyamer, Gassler et al., 2017, Ke, Xu et al., 2017, Patel, Kang et al., 2019, Vara, Paytuvi-Gallart et al., 2019, Wang, Wang et al., 2019). On the other hand, the manner by which germ cells elaborate the higher-order chromatin organization during their mitotic development, and the founding states for gametogenesis and totipotency, remain poorly understood. In-depth understanding of genome functions requires investigations of the 3D genome organization complemented by thorough epigenome and transcriptome profiling, an approach known as "nucleome" profiling (Dekker, Belmont et al., 2017). While nucleome profiling has been performed in a few somatic lineages (Bonev, Mendelson Cohen et al., 2017, Stadhouders, Vidal et al., 2018, Zhang, Li et al., 2019), studies applying this approach to germ-cell development are lacking.

In mammals, germ cells arise as primordial germ cells (PGCs) during early embryonic development (Saitou & Hayashi, 2021). PGCs undergo migration and colonize the embryonic gonads, where they differentiate either into spermatogonia/spermatogonial stem cells (SSCs), the source for spermatogenesis, or oocytes with an immediate entry into the first prophase of meiosis (Griswold, 2016, Spiller, Koopman et al., 2017, Wen & Tang, 2019). A key event that characterizes PGCs is epigenetic reprogramming, including de-methylation of genome-wide DNA to the point that it contains almost no DNA methylation, as well as histone-modification remodeling, which creates a facultative "naïve" epigenome (Lee, Hore et al., 2014, Tang, Kobayashi et al., 2016). In males, epigenetic reprogramming is followed by the provision of a distinct spermatogenic epigenome, including global DNA re-methylation, for spermatogonia/SSC development, whereas in females, the naïve epigenome serves as a direct precursor

for the oogenic meiotic entry (Lee et al., 2014). Thus, male germ-cell development requires at least one additional epigenetic programming step to create spermatogenic progenitors. Here, to explore the principles that create a basis for gametogenic potential, we performed nucleome profiling of an in vitro system that faithfully reconstitutes mouse germ-cell development from pluripotent precursors to PGCs before and after epigenetic reprogramming and then to spermatogonia/SSCs (Hayashi, Ohta et al., 2011, Kanatsu-Shinohara, Ogonuki et al., 2003, Ohta, Kurimoto et al., 2017, Ohta, Yabuta et al., 2021). We show that the in vitro system recapitulates not only gene-expression and epigenetic properties, but also 3D genome-organization dynamics during germ-cell development in vivo, lending credence to our analyses using scalable materials to provide a more complete picture of nucleome dynamics with high resolution during germ-cell development. In addition, to delineate the functional significance of appropriate nucleome programming, we analyzed the nucleome of an in vitro counterpart of spermatogonia/SSCs with an impaired spermatogenic potential (Ishikura, Yabuta et al., 2016).

RESULTS

Mouse germ-cell development in vitro

We analyzed the following male cell types (Fig 1A): mouse embryonic stem cells (mESCs) derived from blastocysts (Ying, Wray et al., 2008), epiblast-like cells (EpiLCs) (Hayashi et al., 2011), mouse PGC-like cells at day 2 of induction (d2 mPGCLCs) (Hayashi et al., 2011), d4 mPGCLCs expanded in vitro for 7 days for epigenetic reprogramming (d4c7 mPGCLCs) (Ohta et al., 2017, Ohta et al., 2021), and germline stem cells (GSCs) derived from neonatal spermatogonia (Kanatsu-Shinohara et al., 2003). These cells show gene-expression, epigenetic, and functional properties equivalent to those of their in vivo counterparts, i.e., mESCs to epiblast at embryonic day (E) 4.5 with naïve pluripotency (Boroviak, Loos et al., 2014, Marks, Kalkan et al., 2012), EpiLCs to epiblast at ~E6.0 with formative pluripotency (Hayashi et al., 2011), d2 mPGCLCs to mPGCs during their specification at ~E7.0 and before epigenetic reprogramming (Hayashi et al., 2011, Kurimoto, Yabuta et al., 2015), d4c7 mPGCLCs to PGCs at E11.5 after epigenetic reprogramming (Ohta et al., 2017, Ohta et al., 2021), and GSCs to spermatogonia/SSCs (Ishikura et al., 2016). Note that PGCs before E11.5 do not show overt sexual differences in gene-expression and epigenetic properties, except X-chromosome reactivation in females (Jameson, Natarajan et al., 2012, Ohta et al., 2017). Accordingly, male PGCs bear a capacity to form functional oocytes (Evans, Ford et al., 1977), and male mPGCLCs take on the oogenic fate and enter into the meiotic prophase in response to appropriate signals at an efficiency comparable to that of female mPGCLCs (Miyauchi, Ohta et al., 2017, Nagaoka, Nakaki et al., 2020). Thus, while our present analysis focuses on male germ-cell development, male d4c7 mPGCLCs can be considered to bear an oogenic potential as well. In addition, to evaluate the functional relevance of proper nucleome programming, we analyzed GSC-like cells (GSCLCs) that were derived from d4 mPGCLCs in vitro and had an impaired spermatogenic potential (Ishikura et al., 2016) (see the "Nucleome programming engenders gametogenic potential" section).

Higher-order genome organization: maturation towards a highly euchromatized state

We first examined the nuclear morphology of the five cell types (mESCs, EpiLCs, d2 mPGCLCs, d4c7 mPGCLCs, and GSCs) stained with DAPI (4′,6-diamidino-2-phenylindole) using high-resolution

confocal microscopy. Counterintuitive to GSCs' acquisition of a distinct spermatogenic epigenome, including global DNA re-methylation, on the epigenome of naïve PGCs, the areas of high DAPI density (peri-centromeric heterochromatin) (Guenatri, Bailly et al., 2004), the variances of DAPI density (chromatin condensation heterogeneity), and the distances of the DAPI-dense areas from the nuclear periphery (chromosome radial positioning), all exhibited a monotonically decreasing transformation towards GSCs (Fig 1B and C). This indicates that chromatin de-condensation (i.e., euchromatization), as well as peripheral tethering of centromeres, proceeds progressively beyond the canonical epigenetic reprogramming period. Notably, formative EpiLCs showed more discrete chromatin condensation than naïve mESCs, while mESCs and d4c7 mPGCLCs (latent pluripotency) (Surani, Hayashi et al., 2007) exhibited significant differences in chromosome radial positioning (Fig 1B and C). Fluorescence in situ hybridization (FISH) confirmed that, in line with chromatin de-condensation, GSCs bore larger chromosome volumes than mESCs and EpiLCs (Fig 1D, Fig EV1A).

We next analyzed the five cell types by in situ Hi-C (~5 kb resolution) with reproducible biological replicates (Fig EV1B, Table EV1). Consistent with the morphological observations, 3D genome organization was transformed in an unidirectional manner during germ-cell development: the chromosomal contact profile shifted progressively from the conventional proximal contact-enriched state to a more uniform profile with heightened distal interactions (Fig 1E, Fig EV1C, Appendix Fig S1A), and the compartment score distributions and euchromatin-to-heterochromatin balance exhibited a monotonical increase (Fig 1G, Fig EV1D). Notably, while the vast majority (~33.3% genome-wide) of the A compartment in mESCs remained an A compartment, more than one third (~38.9% genome-wide) of the B compartment in mESCs progressively turned into A, with the largest B-compartment fraction (~7.5% genome-wide) turning into A upon the d4c7 mPGCLC-to-GSC transition. In stark contrast, the compartment scores exhibited a gradual decrease during somatic development, including neuronal, B-cell, and cardiomyocyte differentiation (Fig 1G, Appendix Fig S1B) (Bonev et al., 2017, Stadhouders et al., 2018, Zhang et al., 2019). The brief decrease in the compartment score upon EpiLCs-to-d2 mPGCLCs differentiation (Fig 1G) is consistent with the transient activation of a somatic program during mPGCLC specification (Kurimoto et al., 2015). Accordingly, principal component analysis (PCA) of the

compartment scores segregated the germline from somatic development (Appendix Fig S1C). Along with the expansion of the A compartment (Fig 1G, Fig EV1D), euchromatic A-A interactions became less intense, while the reduced B compartment exhibited stronger B-B interactions both within (cis) and between (trans) chromosomes, implying the formation of repressive condensates (Fig 1F).

On a smaller scale, topologically associating domain (TAD) boundaries exhibited a substantial overlap during germ-cell development, with the degree of their conservation being similar to that of somatic lineages (Fig EV1E and F, Appendix Fig S1D). However, inter-TAD interactions involving the simultaneous aggregations of multiple non-neighboring TADs, referred to as "TAD-cliques" (Paulsen, Liyakat Ali et al., 2019), became dramatically less prevalent in the A compartments, while they were over-represented in the B compartments in both d4c7 mPGCLCs and GSCs, which was in stark contrast to their opposite/relatively stable behaviors in somatic lineages (Fig 1H and I, Appendix Fig S1E). Through polymer simulations, we generated representative 3D structures of whole chromosomes (Todd, Todd et al., 2021), which similarly demonstrated the progressive expansion of chromosome volume during germ-cell development (Fig EV1G, Appendix Fig S1F, Movie EV1).

To examine whether the five cell types recapitulate their in vivo counterparts at the 3D genome organization level, we retrieved published Hi-C data of the inner cell mass at ~E4.0, epiblast at E6.5, PGCs at E11.5, and spermatogonia in adults, which were generated from small numbers of samples (Du et al., 2017, Du, Zheng et al., 2020, Luo, Wang et al., 2020). Remarkably, not only at the transcriptomic and epigenomic level that we reported previously (Hayashi et al., 2011, Ishikura et al., 2016, Ohta et al., 2017), the in vitro cell types exhibited a strong concordance with their in vivo counterparts at the 3D genome organization level (Fig EV1C and E) (despite the elevated noise of contact matrices from in vivo samples), with unsupervised hierarchical clustering (UHC) and PCA using compartment scores consistently placing corresponding cell types next to one another (Fig EV1H and I). Thus, the in vitro system faithfully captures the nucleome dynamics of in vivo germ-cell development, further empowering our strategy for using scalable in vitro materials to delineate a more complete picture of nucleome dynamics during germ-cell development. We conclude that, beyond the canonical epigenetic

reprogramming period, higher-order genome organization undergoes a continuous maturation and culminates in a largely euchromatic genome and peripherally positioned centromeres in spermatogonia/SSCs (GSCs). Thus, global DNA methylation and euchromatization are separable events. Moreover, our findings revealed that, despite their profound epigenomic differences, PGCs (d4c7 mPGCLCs) with both oogenic and spermatogenic potential and spermatogonia/SSCs (GSCs) show relatively similar higher-order genome organization.

Epigenome profiling: epigenetic reprogramming for highly open chromatin with enhanced insulation

To explore the mechanism underlying the higher-order genome organization unique to the germ line, we conducted comprehensive epigenome profiling of the five cell types. We performed mass spectrometry (MS) of histones; chromatin immunoprecipitation followed by deep sequencing (ChIP-seq) of 13 different targets, including 9 histone modifications; assay for transposase-accessible chromatin with deep sequencing (ATAC-seq) for open chromatin; and native elongating transcript–cap analysis of gene expression (NET-CAGE) for transcribed cis regulatory elements (Table EV1). For some assays, we analyzed d4 mPGCLCs, which are in the middle of epigenetic reprogramming, as an intermediate between d2 and d4c7 mPGCLCs and mouse embryonic fibroblasts (MEFs) as a somatic control.

MS revealed dynamic changes in histone-modification levels with high reproducibility (Fig 2A, Table EV2). Consistent with previous observations (Kurimoto et al., 2015, Ohta et al., 2017), histone H3 lysine 9 di-methylation (H3K9me2) was substantially reduced and H3K27 tri-methylation (H3K27me3) was strongly up-regulated in d4c7 mPGCLCs (Fig 2A, Fig EV2A and B). With respect to active modifications, H3K27 acetylation (H3K27ac: active cis-regulatory elements) and H3K18ac were the most abundant in EpiLCs, whereas H3K4 mono-methylation (H3K4me1: poised enhancers), H3K14ac, and H3K23ac were the most adundant in d4c7 mPGCLCs, and, interestingly, H3K4me3 (promoters) was the least prevalent in d4c7 mPGCLCs (Fig 2A). UHC based on H3-modification abundance segregated each cell type with their unique sets of associated H3 modifications (Fig 2B), and PCA demonstrated characteristic transitions of epigenetic properties, with the transition from d2 to d4c7 mPGCLCs representing the

epigenetic reprogramming to a latent pluripotency and the transition from d4c7 mPGCLCs to GSCs signifying the acquisition of a spermatogenetic epigenome (Fig 2C). We proceeded to normalize all histone modification ChIP-seq signals with MS-based scaling factors for subsequent analyses (Fig EV2C and D) (Farhangdoost, Horth et al., 2021).

We first scrutinized the open-chromatin landscape. Consistent with d4c7 mPGCLCs being globally DNA demethylated (~5%) (Fig 1A) (Ohta et al., 2017, Ohta et al., 2021), they exhibited a pervasively open chromatin with coincident up-regulation of H3K4me1, bearing large open domains in a genome-wide manner (Fig 2D and E). Indeed, among a diverse panel of mouse fetal tissues (Gorkin, Barozzi et al., 2020), d4c7 mPGCLCs showed the highest degree of openness (Fig EV2E). Consistent with the analysis of the abundance of H3 modifications (Fig 2C), PCA with the most variable open sites (Fig EV2F) and UHC revealed that d4c7 mPGCLCs share open sites for pluripotency with mESCs and those for germ-cell identity with GSCs: the former (clusters 1, 2, 4) being enriched in transcription-factor (TF)-binding sites for POU5F1, NANOG, SOX2, ZIC2/3, and KLF3/12, and the latter (clusters 3, 7) in those for DMRTs (Fig EV2G, Table EV3).

Despite their genome-wide DNA demethylation, PGCs and d4c7 mPGCLCs do not exhibit transcriptional hyperactivity or promiscuousness (Ohta et al., 2017, Ohta et al., 2021, Seisenberger, Andrews et al., 2012). To explore higher-order regulatory mechanisms, we identified enhancer-promoter (E-P) pairs using the activity-by-contact model by integrating ATAC-seq, H3K27ac, and Hi-C data (Fig EV3A) (Fulco, Nasser et al., 2019). Notably, d4c7 mPGCLCs showed a reduced number and range of active E-P pairs as compared to the other cell types (Fig 2F, Fig EV3B). Furthermore, NET-CAGE revealed an under-representation of E-P co-transcription in d4c7 mPGCLCs (Fig EV3C). d4c7 mPGCLCs were also predicted to bear the largest numbers of insulating TAD boundaries (Fig 2G, Fig EV3D) and exhibited the broadest compartment profile (Fig EV3E), in agreement with the notion that heightened insulation can mask smaller compartments (Schwarzer, Abdennur et al., 2017). While CTCF and RAD21, a key component of cohesin, exhibited comparable enrichment at TAD boundaries across the five cell types (Fig EV3F) (we discuss the CTCF depletion in GSCs below), ATAC-seq revealed that

d4c7 mPGCLCs uniquely exhibited lower chromatin information content around regions with co-localized CTCF/RAD21 bindings (Fig EV3G), suggesting that d4c7 mPGCLCs bore a shorter CTCF/RAD21 residence time (D'Oliveira Albanus, Kyono et al., 2021). Taken together, these findings support the idea that, due to a reduced residence time of the loop extrusion machinery with no major changes in global binding sites, d4c7 mPGCLCs bear shorter chromatin loops and enhanced insulation (Fig EV3H and I). We conclude that PGCs with a naïve epigenome bear a highly open chromatin, but undergo enhanced insulation to ensure their transcriptional integrity.

Insulation erasure for spermatogonia development and oogenesis

We next classified ATAC-seq peaks (open sites) based on their combinatorial epigenetic states. Building on the Ensembl Regulatory Build and ENCODE's registry of candidate Cis-Regulatory Elements (cCREs), we applied uniform manifold approximation and projection (UMAP) in combination with hierarchical density-based spatial clustering of applications with noise (HDBSCAN) in a semi-supervised manner through iterative sub-clustering (Tables EV4 and EV5). This framework classified the open sites into 19 distinct sets (Fig 3A), which we grouped into 6 broader categories (Fig 3B, Fig EV4A). While d4c7 mPGCLCs showed the largest number of enhancer elements (clusters 5, 6, 15, 18) (Fig 3B and C), GSCs exhibited a relatively large number (~ >10,000) of non-promoter bivalent open sites (clusters 8, 9, 10, 13). Additionally, we uncovered a set of open sites with unique trivalency of H3K4me3, H3K27ac and H3K9me3 that were enriched in EpiLCs (cluster 19) (Fig 3B) and overlapped not only with the promoter of long interspersed nuclear elements 1 (LINE1) but also with the binding site of YY1 (Fig EV4B, Table EV5), underscoring the capacity of our epigenetic compendium for uncovering biologically distinct regulatory regions. A vast majority of enhancers were cell-type specific, whereas most CTCF bindings were conserved upon each cell-fate transition until d4c7 mPGCLCs; strikingly, however, a majority of CTCF-bound sites in d4c7 mPGCLCs were lost in GSCs (Fig 3C) (see below).

We performed the same analyses for promoters (Fig EV4D-F, Table EV4). In accord with our previous finding (Kurimoto et al., 2015), EpiLCs bore the largest number of bivalent promoters (Fig EV4F). Evaluation of the promoter-promoter (P-P) interactions revealed that active as well as bivalent promoters

exhibited significantly enriched interactions in all cell types, but to lesser extents in d4c7 mPGCLCs bearing elevated insulation (Fig 2G, Fig EV4G).

We next explored the depletion of CTCF binding upon d4c7 mPGCLCs-to-GSCs transition (Fig 3C). In GSCs, decreased CTCF protein expression accompanied a dramatic reduction in the number of CTCF peaks (Fig 3D-F). In particular, CTCF was depleted from relatively weak binding sites (Fig 3E and F). These CTCF-depleted sites exhibited elevated DNA methylation as well as enrichment of H3K9me2/me3 and H3K36me2/me3, whereas CTCF peaks enriched in GSCs showed divergent patterns (Fig 3G, Fig EV4H). Importantly, despite relatively weak bindings, CTCF depletion from such sites resulted in a reduction in insulation (Fig 3G), leading to a rewiring of neighboring cis-regulatory interactions as exemplified for Ddx4, a key gene up-regulated upon d4c7 mPGCLCs-to-GSCs transition, whose promoter strengthened its long-range interaction with a distal enhancer (Fig 3H, Fig EV4I). We then systematically identified E-P pairs straddling CTCF sites depleted in GSCs and ranked the target genes according to coordinated expression up-regulation and increased E-P interactions (Fig EV4J). Genes with coordinated activation were enriched in gene ontology (GO) functional terms such as "homologous chromosome pairing at meiosis," and "piRNA metabolic process," and included Ddx4, Mael, Piwil2, Piwil4, Zbtb16, Sycp1, Syce3, Mei4, and Prdm9 (Fig 3I, Table EV6) [these genes are referred to as "germline genes" (Borgel, Guibert et al., 2010) ; also, see below], indicating a critical role of the insulation erasure in spermatogonia development and the acquisition of meiotic competence.

To explore whether insulation erasure may also occur upon oogenesis, we re-analyzed published Hi-C data for E11.5 PGCs (d4c7 mPGCLC counterparts) and E13.5 germ cells initiating their male or female differentiation (Du et al., 2017, Du et al., 2020). We found that a majority of E13.5 male germ cells were still in the mitotic phase and bear similar properties to E11.5 PGCs, whereas most E13.5 female germ cells were in the leptotene stage of the meiotic prophase (Nagaoka et al., 2020, Western, Miles et al., 2008). Consistent with our comprehensive analyses (Fig 2 and 3), the point of fastest decline in the chromosomal cis-contact decay rate, an index for TAD width (preprint: Polovnikov, Belan et al., 2022), occurred at the smallest genomic separation in E11.5 PGCs and d4c7 mPGCLCs (Fig 2H, Fig EV3J and

K), suggesting that, similar to d4c7 mPGCLCs, E11.5 PGCs bear enhanced insulation. Notably, while the fastest point of decline of E13.5 male germ cells was in a range comparable to E11.5 PGCs and d4c7 mPGCLCs, that in E13.5 female germ cells occurred at a much longer distance, suggesting a rapid weakening of insulation upon the initiation of oogenesis. We conclude that insulation erasure occurs both for spermatogonia development and oogenesis, with the latter having an earlier onset.

Mechanism for euchromatization: dynamics of LADs, pericentromeric heterochromatin, and H3K9 methylation

We next explored potential mechanisms for the progressive euchromatization unique to germ-cell development (Fig 1G). While the five cell types exhibited relatively conserved correlations between their compartment scores and epigenetic modification profiles, there nevertheless existed cell-type specific variations (Fig 4A). We noted that the binding profiles of lamin B1, which forms the nuclear lamina and tethers chromosomes to create lamina-associated domains (LADs) (Guelen, Pagie et al., 2008), were the strongest predictor for compartment-score differences between mESCs and GSCs (Fig 4B), and the LADs changed dramatically with a sweeping reduction across regions that undergo euchromatinization in GSCs (Fig 4C). Consequently, among a number of other cell types (Peric-Hupkes, Meuleman et al., 2010, Poleshko, Shah et al., 2017, Robson, de Las Heras et al., 2016, Yattah, Hernandez et al., 2020), GSCs bore the smallest genomic coverage of LADs (~10%) (Fig 4D), a vast majority of which were a subset of constitutive LADs found across all other cell types (Fig 4E and F). Indeed, GSCs exhibited low lamin B1 levels and enrichments (Fig 4G and H). Thus, GSCs constitute a cell type with minimal LADs.

While LADs were prominent toward the distal ends of long arms in mESCs and EpiLCs, they became more uniformly distributed in d2/d4c7 mPGCLCs with a reduction in their coverage in d4c7 mPGCLCs, and they eventually become depleted around the distal ends of long (q) arms in GSCs, where they were only retained towards the opposing (p/short) end, i.e., around centromeres of the telocentric mouse chromosomes (Fig 4C, I, and J). This is consistent with the progression of nuclear peripheral association of DAPI-dense areas along germ-cell development (Fig 1B and C). Accordingly, DNA FISH for major satellite repeats, a pericentromere marker, revealed that while such regions were localized mainly within

the nuclear interior in EpiLCs, they were predominantly positioned around the nuclear periphery in GSCs (Fig 4L).

To explore whether the peripherally positioned centromeres and extensive euchromatization in other chromosomal regions in GSCs are a conserved feature in mouse spermatogonia in vivo and in other mammals such as primates, we re-analyzed relevant published datasets (Du et al., 2020, Wang et al., 2019). The distributions of chromosome-wide compartment-score differences between GSCs and EpiLCs were very similar to those between spermatogonia and fibroblasts in both mice and rhesus monkeys, with spermatogonia showing the lowest compartment score around centromeres and widespread euchromatization across other regions (note that rhesus monkeys bear metacentric chromosomes) (Fig EV5A and B). We conclude that higher-order genome organization in GSCs is conserved in spermatogonia in vivo and, through evolution, in monkeys.

As a mechanism that gives rise to the minimal LADs, we noted significant changes in the abundance and distributions of H3K9me2/me3, hallmarks of chromatin anchored to the nuclear lamina (Bian, Khanna et al., 2013, Chen, Yammine et al., 2014, Harr, Luperchio et al., 2015). The abundance of both H3K9me2/me3 increased progressively from mESCs to d2 mPGCLCs, and then decreased dramatically in d4c7 mPGCLCs (Fig 2A). While the low abundance of H3K9me2 persisted in GSCs, the abundance of H3K9me3 increased in GSCs to the highest level among the five cell types (Fig 2A). The distributions of H3K9me2 were widespread across the chromosomes and well conserved among the five cell types except in d4c7 mPGCLCs, which, unlike the other cell types, retained H3K9me2 at a relatively high level around the pericentromeres (Fig 4K). On the other hand, in all cell types, H3K9me3 showed a unique and conserved distribution with a characteristic enrichment around the pericentromeres, with GSCs bearing broader/expanded H3K9me3 domains that bridge several peaks present in other cell types (Fig 4K, 5A and B). Notably, consistent with the increased B-B interactions, the broad H3K9me3 domains in GSCs exhibited elevated intra- as well as inter-domain aggregations (Fig 5C).

LADs consistently showed positive correlations with both H3K9me2/me3, except in GSCs, which had

minimal LADs showing a positive correlation only with H3K9me3 (Fig 5D). IF analysis verified that GSCs showed a nuclear peripheral enrichment of H3K9me3 but not me2, while EpiLCs bore peripheral H3K9me2 but not me3 enrichment (Fig 5E). Interestingly, regions constitutively enriched with H3K9me3 across all five cell types, i.e., putative nucleation sites for H3K9me3 expansion in GSCs, were enriched with evolutionarily young transposable elements (TEs) including ERVK, ERV1 and LINE1 (Fig 5F, Fig EV5C, Table EV5). Accordingly, the densities of these TEs were highly predictive of the minimal LADs in GSCs (Fig 5G, Fig EV5D). Thus, minimal LADs in GSCs are the regions that show consistent attachment to the nuclear lamina across all cell types, likely contributing to the continued repression of evolutionarily young TEs and the maintenance of genome fidelity. Collectively, these results indicate that, during germ-cell development, LADs progressively remodel toward a minimal state, positionally shifting from the distal ends of long arms predominantly associated with H3K9me2 to the opposite ends of the chromosomes, the centromeres. These pericentromeric regions, with newfound peripheral attachment in GSCs, are predominantly associated with H3K9me3 and are populated with evolutionarily young TEs, enabling extensive euchromatization on the opposing chromosome arm (long/q arm).

Next, to gain insights into the mechanisms underlying H3K9 methylome dynamics, we examined the expression of major H3K9 methyltransferases (K9MTases). At the transcriptional level, Suv39h1 and h2, which are responsible for the H3K9 methylation in the peri-centromeric heterochromatin and other B compartment regions (Fukuda, Shimura et al., 2021), showed progressive up-regulation, whereas Setdb1, Ehmt1 (Glp1), and Ehmt2 (G9a), which are involved in the H3K9 methylation in both A and B compartments (Fukuda et al., 2021), were gradually repressed until d4c7 mPGCLCs and then up-regulated in GSCs (Fig 5H). At the protein level, SETDB1, EHMT1 and EHMT2 were repressed until d4c7 mPGCLCs and remained at a low level in GSCs as well (we were not able to determine the SUV39H1/H2 levels due to the lack of appropriate antibodies) (Fig 5I). These findings are consistent with the dynamics of the H3K9me2/me3 levels and distributions, suggesting that the H3K9 methylome is regulated at least in part by the differential expression of K9MTases.

Additionally, we explored the impact of the global remodeling of H3K9me3 on gene expression. In particular, we noted that during the d2-to-d4c7 mPGCLC transition, 728 promoters showed H3K9me3 down-regulation (Fig 5J), and they were enriched with GO terms such as "multi-organism reproductive process," "sexual reproduction," and "gamete generation," and included Dazl, Ddx4, Sycp1, Sohlh2, and Mael (Fig 5J, Table S6). These genes, which included many subject to insulation erasure upon spermatogonia development (Fig 3I and J), are referred to as "germline genes" (Borgel et al., 2010), and are known to be repressed by DNA methylation in somatic cells and by H3K27me3 and H3K9me2 in mPGCLCs (Borgel et al., 2010, Kurimoto et al., 2015). Furthermore, a recent report has shown that the germline genes were repressed in EpiLCs with H3K9me3 imposed by Setdb1 (Mochizuki, Sharif et al., 2021). In good agreement, the transcriptional start sites (TSSs) of germline genes repressed by Setdb1 up-regulated H3K9me3 in EpiLCs and, more prominently, in d2 mPGCLCs, and lost it in d4c7 mPGCLCs (Fig 5K and L). The TSSs of germline genes defined in another study (Kurimoto et al., 2015) exhibited a comparable reduction of H3K9me3 during d2-to-d4c7 mPGCLC transition (Fig 5M). Thus, the germline genes are endowed with multiple layers of mechanisms, including higher-order genome organization involving the insulation by CTCF and compound repressive epigenetic modifications, to prevent their activation in somatic cells, and such mechanisms are exempted in a stepwise manner—i.e., erasure of DNA and H3K9 methylation occurs first and then release from H3K27me3/H2AK119u1 and CTCF insulation ensues—during germ-cell development.

Heterochromatin compaction excludes H3K36me2 to create PMDs and Y-chromosome hypomethylation

A unique epigenetic characteristic of male germ cells (pro-spermatogonia, spermatogonia and spermatozoa) is the presence of large partially methylated domains (PMDs) in intergenic regions (Kubo, Toh et al., 2015). PMDs can be defined as broad genomic domains with a comparatively lower methylation level than the rest of the genome and typically cover a substantial fraction of the genome (Lister, Pelizzola et al., 2009). They were first identified in a human cultured cell line (Lister et al., 2009) and subsequently found to be prevalent in cancers, aged cells, and tissues such as placenta (Hansen, Timp et al., 2011, Hon, Hawkins et al., 2012, Schroeder, Blair et al., 2013). While evidence suggests that PMDs

arise from an imperfect maintenance of methylation during mitosis (Salhab, Nordstrom et al., 2018), the mechanism that engenders PMDs in mitotically arrested pro-spermatogonia and their subsequent maintenance in male germ cells remains unclear.

We found that GSCs bore PMDs larger than 140 Mb in total, a majority (~86%) of which were overlapped with those in spermatogonia (Fig 6A) (Kubo et al., 2015). The PMDs in GSCs consisted almost entirely of B compartments and were enriched with heterochromatic modifications such as H3K9me3, while depleted of active modifications including H3K36me2, H3K27ac and H3K4me1/3 (Appendix Fig S2). The epigenomic profiles revealed that the epigenome of d4c7 mPGCLCs exhibited the greatest predictive power for PMDs in GSCs (greater than that of the epigenome of GSCs themselves) (Fig 6B), and among individual epigenetic markers, H3K9me2/me3 and lamin B1 in d4c7 mPGCLCs were the strongest negative predictors (Fig 6C), suggesting that the constitutive heterochromatin in d4c7 mPGCLCs contributes to the subsequent formation of PMDs. Accordingly, we found that H3K36me2, which is catalyzed by NSD1 and serves as a recruiter of the androgenetic DNA methylome (Shirane, Miura et al., 2020), showed a specific depletion in the B compartments and the regions retaining H3K9me3, but not H3K27me3, in d4c7 mPGCLCs (Fig 6D-F), resulting in an exquisite concordance of H3K36me2 with the A compartments and a near-complete exclusion from LADs in d4c7 mPGCLCs (Fig 6G). We found that the TADs involved in larger-sized TAD cliques in d4c7 mPGCLCs exhibited the greatest H3K9me3 enrichment (Fig 6H). Given that the heterochromatic TAD-cliques become dominant in d4c7 mPGCLCs and GSCs (Fig 1H and I), these findings suggest that an increased aggregation of constitutive heterochromatin in d4c7 mPGCLCs may exclude the recruitment of NSD1 and hence the deposition of H3K36me2, leading to the formation of PMDs in GSCs.

In this regard, we noted that, as compared to the autosomes and the X chromosomes, the Y chromosomes, which bear a highly repetitive structure (Soh, Alfoldi et al., 2014), were the most enriched with H3K9me3 in all five cell types, and interestingly, exhibited a progressive enrichment of lamin B1 during germ-cell development, with the Y chromosomes in GSCs showing the highest lamin B1 enrichment level (Fig 6I). In addition, we found that the Y chromosome in GSCs was hypo-methylated

across almost its entire length, with ~75% of it identified as falling within PMDs—a much greater proportion than in autosomes (4%) or the X chromosome (21%) (Fig 6J, L, and M). Indeed, by alternatively mapping directly to the consensus repeat sequences of the Y chromosome, we found that all repetitive units demonstrate reduced methylation levels in GSCs as compared to EpiLCs (Appendix Fig S3A and B). Consistent with the de-condensation of chromatin in GSCs (Fig 1B-D), the Y chromosomes in GSCs exhibited loose structures and were associated with the nuclear periphery with a lower sphericity (Fig 6K), indicating greater surface contact with the nuclear lamina through chromosome elongation. Thus, the Y chromosome in GSCs achieves chromosome-wide hypomethylation likely via a convergent mechanism with PMDs in autosomes. Together, these results lead us to conclude that the unique 3D epigenomic character of the progenitors (d4c7 mPGCLCs) serves as a blueprint for the formation of PMDs in male germ cells.

Nucleome programming engenders gametogenic potential

To delineate the functional significance of a proper nucleome for gametogenesis, we performed nucleome analyses (morphology; in situ Hi-C; MS; ChIP-seq for 13 targets; ATAC-seq; and NET-CAGE) of GSC-like cells (GSCLCs), which were derived from d4 mPGCLCs with their differentiation into spermatogonia-like cells in reconstituted testes followed by expansion under a GSC derivation condition (Ishikura et al., 2016) (Fig 7A). GSCLCs derived under this condition bore a morphology, transcriptome, and DNA methylome similar to those of GSCs, but showed a severely impaired capacity for spermatogenesis for unclear reasons (Ishikura et al., 2016) (Appendix Fig S4A). We hypothesized that aberrant nucleome programming during the derivation of GSCLCs might underlie their impaired function.

GSCLCs were similar to GSCs in terms of the areas of high DAPI density and the distances of the DAPI-dense areas from the nuclear periphery, but showed greater variances of DAPI density than GSCs (Fig 7B and C), indicating that GSCLCs bear a more heterogeneous chromatin de-condensation. In situ Hi-C revealed that, compared to GSCs, GSCLCs exhibited a depletion in long-range interactions, indicative of incomplete chromatin uniformalization (Fig 7D, Appendix Fig S4B), and notably, failed to acquire

the positively skewed compartment score distribution characteristic of GSCs (Fig 7E). A multi-scale model dividing the genome into the eight subcompartments with distinct epigenetic properties (Liu, Nanni et al., 2021) revealed that major difference between GSCLCs and GSCs were localized to intermediate compartments, with GSCLCs bearing fewer and more intermediate A and B sub-compartments, respectively (Fig 7F and G, Appendix Fig S4C).

Accordingly, MS revealed that GSCLCs bore an elevated level of H3K27me3 and H3K9me2, which are associated with a state intermediate between compartments A and B (Johnstone, Reyes et al., 2020) (Fig 7H). The regions with higher H3K27me3 in GSCLCs were enriched in promoters and CpG islands (CGIs) (Appendix Fig S4D, Table EV6), which were, importantly, associated with pathways such as "male meiotic nuclear division," and "recombinatorial repair," and included Ddx4, Dmrt1, Dmc1, Stag3, and Spo11 (Fig 7I and J, Table EV6). These genes bore higher levels of H3K27me3 on their gene bodies as well (Fig 7I, Appendix Fig S4E). In contrast, the regions with higher levels of H3K9me2 in GSCs were enriched in enhancers and distal active regulatory elements (Appendix Fig S4F and G), and were associated with pathways such as "response to ciliary neurotrophic factor," "rod bipolar cell differentiation," and "adrenal cortex formation" (Appendix Fig S4H, Table EV6).

Moreover, GSCLCs bore a larger number of the CTCF-binding peaks coinciding with insufficient accumulation of H3K9me3 (Fig 7K, Appendix Fig S4I and J), and indeed GSCLCs developed higher intra-TAD interaction strength compared to GSCs (Fig 7L), indicating that the chromatin of GSCLCs is more insulated than that of GSCs. In a megabase-scale domain encompassing Ddx4, the insulating CTCF peak separating the Ddx4 promoter from one of its potential enhancers was removed only partially in GSCLCs, resulting in a reduced activation as evidenced by the comparatively lower H3K36me3 levels on Ddx4 (Fig 7M). Collectively, these results lead us to conclude that GSCLCs exhibit aberrant nucleome programming, including insulation erasure and epigenome programming, with partial retention of the properties of d4c7 mPGCLCs, resulting in their impaired spermatogenic potential.

DISCUSSION

Germ-cell development lays the groundwork for nuclear totipotency, creating sexually dimorphic haploid gametes, the oocytes and the spermatozoa, which unite to form totipotent zygotes. PGCs bear naïve epigenome after epigenetic reprogramming and can serve as a direct precursor for oocyte differentiation; they can also acquire a distinct spermatogenic epigenome, including global DNA re-methylation, to differentiate into spermatogonia/SSCs, a direct precursor for spermatozoa differentiation (Lee et al., 2014). PGCs and spermatogonia/SSCs therefore exhibit dimorphic epigenomic properties and have been thought to represent highly distinct cellular states. Contrary to this notion, our nucleome analyses have uncovered a smooth and unidirectional maturation of higher-order genome organization from pluripotent precursors (mESCs/EpiLCs) to PGCs (d2/d4/d4c7 mPGCLCs) and then to spermatogonia/SSCs (GSCs), involving progressive euchromatization and radial chromosomal re-positioning (Fig 1 and 8). This finding delineates a common nuclear-architectural foundation towards gamete generation in both sexes, a coordination not found in somatic lineages. This widespread euchromatization might underlie the potential of GSCs to de-differentiate into pluripotent stem cells, albeit at a low frequency (Kanatsu-Shinohara, Inoue et al., 2004). Thus, germ-cell development entails mechanisms that create and preserve a broadly euchromatic genome, while simultaneously accommodating essential epigenetic orchestrations. Our findings also demonstrate that global DNA methylation and euchromatization are dissociable events.

As a key mechanism for global euchromatization, we have shown that germ-cell development distinctly down-regulates H3K9me2, an aggregative force for heterochromatin formation (Poleshko, Smith et al., 2019), and progressively restricts LADs to around centromeres (Fig 2 and 4). These events would be mediated at least in part through the repression of SETDB1 and EHMT1, K9MTases acting in both the A and B compartments (Fukuda et al., 2021), as well as lamin B1 itself. On the other hand, germ cells up-regulate Suv39h1 and h2, K9MTases specific to the B compartment and particularly for pericentromeric regions. This results in an expansion of H3K9me3 into broad domains in GSCs with an appreciable increase in both local and distal compaction among such domains (Fig 5), consistent with the notion of a critical threshold of H3K9me3 domain width for phase separation to take place via HP1 (Sanulli, Trnka

et al., 2019). This compaction would also contribute to the formation of PMDs, and most remarkably, those on the Y chromosome, likely by physically excluding spermatogenesis-associated NSD1 and preventing H3K36me2 depositions (Fig 6). Thus, typical LADs mediated by H3K9me2, which are seen in pluripotent precursors as well as in most somatic lineages, are progressively re-organized into a minimal state marked by H3K9me3 during germ-cell development. Importantly, the positional preference of H3K9me3-associated minimal LADs is in part attributable to the density of evolutionarily young TEs that are enriched near centromeres (Fig 5, Fig EV5), indicating a critical role of inherent genomic properties in shaping the fundamental nuclear architecture. In good agreement with this concept, cell-type specific LADs have been reported to be enriched in such TEs (preprint: Keough, Shah et al., 2021). The involvement of H3K9 demethylases and the interplay among associated machineries for LAD formation warrant further investigation.

Despite adopting a highly permissive epigenome with abundant enhancer-like open sites, d4c7 mPGCLCs strengthened their chromatin insulation to thwart spurious distal activation, which, combined with a mechanism to ensure low H3K4me3 levels, would prevent the pervasive poised enhancers from realizing their potential (Fig 2 and 3). Thus, epigenetic reprogramming creates PGCs that have almost no DNA methylation and a highly open epigenome, but that are protected by elevated H3K27me3 (Ohta et al., 2017) and CTCF insulation against hyper-transcription. As to a possible mechanism for the enhanced insulation, we revealed a reduced residence time of the loop extrusion machinery at TAD boundaries in d4c7 mPGCLCs (Fig EV3H-J). Such a reduction in residence time could be achieved through multiple mechanisms, including the use of variant cohesin complexes and modulating the balance between cohesin loading/release factors (Cuadrado, Gimenez-Llorente et al., 2019, Wutz, Varnai et al., 2017). Clarification of these potential mechanisms warrants future investigation.

On the other hand, such protective mechanisms must be at least partly disentangled upon male and female germ-cell specification to eventually achieve full activation of the gametogenic program. Accordingly, a failure of such unraveling and a partial retention/aberrant development of the PGC-like nucleome together contributed to the limited spermatogenic capacities of GSCLCs (Fig 6, Appendix Fig

S4). In the original GSCLC induction strategy, d4 mPGCLCs, which are in the middle of epigenetic reprogramming and bear ~50% genome-wide DNA methylation, were aggregated with embryonic testicular somatic cells for differentiation into spermatogonia-like cells (Ishikura et al., 2016). We speculate that precocious testicular sex-determining signals on mPGCLCs might be a reason for mis-organized nucleome in the originally reported GSCLCs. In good agreement with this speculation, we have recently succeeded in deriving fully functional GSCLCs using d4c5 mPGCLCs, which have an almost fully complete epigenetic reprogramming, as starting materials for aggregation culture with embryonic testicular somatic cells (Ishikura, Ohta et al., 2021). The nucleome analysis of these newly established GSCLCs would be important to confirm this hypothesis.

The nucleome programming for germ-cell development that we have delineated herein, which involves progressive euchromatization with peripheral centromere positioning, is reminiscent of climbing up the Waddington's landscape of epigenesis (Fig 8), and we propose that it constitutes at least part of the mechanism for creating nuclear totipotency, including meiotic potential. Elucidation of the nucleome programming during germ-cell development in other mammals, including humans, will be crucial for a more comprehensive understanding of nuclear totipotency and its evolutionary divergence. The rich datasets we have assembled would be invaluable as a benchmark for mammalian in vitro gametogenesis studies (Saitou & Hayashi, 2021) and for future studies aiming to identify unifying principles for the acquisition of unique cellular identities across lineages. Further, they could contribute to the development of powerful computational frameworks, which in turn could help integrate time-series multi-omics datasets and unveil hidden insights.

ACKNOWLEDGMENTS

We thank the members of our laboratory for their helpful input on this study. We are grateful to Y. Nagai, N. Konishi, E. Tsutsumi, and M. Kawasaki of the Saitou Laboratory, to the DNAFORM genetic analysis department for NET-CAGE library preparation and sequencing, to the Single-Cell Genome Information Analysis Core (SignAC) in ASHBi for their technical assistance and help with all the other sequencing experiments, to R. Maeda of the Tachibana Laboratory for helpful suggestions for ChIP-seq, to S. Nagaoka and K. Kurimoto of the Kurimoto Laboratory and G. Bourque of the Bourque Laboratory for thoughtful discussions on the data analysis, and to C. Horth from the Majewski Laboratory for her assistance with histone extraction. This work was supported in part by a Grant-in-Aid for Specially Promoted Research from JSPS (17H06098), a JST-ERATO Grant (JPMJER1104), a Grant from HFSP (RGP0057/2018), Grants from the Pythias Fund and Open Philanthropy Project to M.S., JSPS KAKENHI Grants (JP18H02613, JP20H05387) to S.Y., and NIH grants (CA196539, NS111997) to B.A.G. M.N. is a fellow of the Takeda Science Foundation. B.H. is supported by studentship awards from the Canadian Institutes of Health Research and the Fonds de recherche du Québec – Santé.

AUTHOR CONTRIBUTIONS

M.N., B.H., S.Y., and M.S. conceived the project and designed experiments. M.N. performed all cell cultures and inductions with assistance from H.O., Y.I. and Y.N. M.N. performed immunofluorescence and its analysis with assistance from H.O., N.K. and K.M. M.N. and F.U. performed western blot and its analysis with assistance from Y.N., S.S., and Y.K. M.N. performed FISH with assistance from I.O. M.N. performed histone extraction and M.C. performed mass spectrometry under the supervision of B.A.G. M.N. and A.Y. performed ChIP-seq with assistance from S.Y. and T.Y. M.N. performed ATAC-seq with assistance from S.Y., H.I., and T.Y. M.N. performed in situ Hi-C with assistance from S.Y., R.S., G.W., K.T., J-M.P., and L.A.M. M.N. performed NET-CAGE with assistance from T.K. under the supervision of Y.M. M.N. and B.H. performed all data analysis with assistance from Y.Y. and J.M. B.H. performed polymer simulation and analysis with assistance from Y.I., K.M., and Y.H. M.N., B.H.,

and M.S. wrote the manuscript with input from all co-authors. S.Y., J.M., and M.S. supervised the project.

CONFLICT OF INTEREST

The authors declare no conflicting interests.

MATERIALS AND METHODS

Reagents and Tools Table

Reagent/Resource	Reference or Source	Identifier or Catalog Number
Experimental Models		
AAG 129/B6 GSC2 (Acrosin-EGFP; beta-Actin-EGFP, 129Sv×C57BL/6, P7 spermatogonia, Germline stem cell line)	Ishikura et al., 2016	https://doi.org/10.1016/j.celrep.2016.11.026
AAG 129/B6 GSCLC16_1 (Acrosin-EGFP; beta-Actin-EGFP, 129SvJ×C57BL6, Germline stem cell-like line, derived from mESCs)	Ishikura et al., 2016	https://doi.org/10.1016/j.celrep.2016.11.026
BVSC BDF1-2-1 mESCs (Blimp1-mVenus; Stella-ECFP , DBA/2×C57BL/6, embryonic stem cell line)	Ohta et al., 2021	https://doi.org/10.1093/biolre/ioaa195
m220-5 (sub-cloned from Sl/Sl4-m220, resistant to mitomycin C, expressing membrane-bound SCF, stromal cell)	Ohta et al., 2021	https://doi.org/10.15252/embj.201695862
MEF (ICR, mitomycinC-treated mouse embryonic fibroblasts prepared from E12.5 fetuses)	N/A	N/A
Antibodies		
Anti-CTCF	CST	#3418
Anti-G9a	R&D Systems	PP-A8620A-00
Anti-GFP(Rat IgG2a), Monoclonal(GF090R), CC	Nacalai Tesque	04404-84
Anti-GLP	R&D Systems	PP-B0422-00
Anti-H2Aub	CST	#8240
Anti-H3	CST	#9715
Anti-H3K27ac	MBL	MABI0309
Anti-H3K27me3	MBL	MABI0323
Anti-H3K27me3	Merk	07-449
Anti-H3K36me2	CST	#2901
Anti-H3K36me3	Active Motif	61101
Anti-H3K4me1	CST	#5326
Anti-H3K4me3	MBL	MABI0304
Anti-H3K9me2	MBL	MABI0317
Anti-H3K9me3	MBL	MABI0318
Anti-Laminb1	Proteintech	12987-1-AP
Anti-Laminb1	Abcam	ab16048

Anti-mouse IgG (whole molecule)–peroxidase antibody produced in sheep affinity isolated antibody, buffered aqueous solution	Sigma	A5906-1ML
Anti-normal mouse IgG	Santa Cruz	sc-2025
Anti-normal rabbit IgG	Santa Cruz	sc-2027
Anti-rabbit IgG (whole molecule)–peroxidase antibody produced in goat affinity isolated antibody, buffered aqueous solution	Sigma	A6154-1ML
Anti-Rad21	Abcam	ab992
Anti-Ring1b	CST	#5694
Anti-Setdb1	Proteintech	11231-1-AP
Anti-α-tubulin	Sigma	T9026
Anti-β-actin	MBL	M177-3
Goat anti-mouse IgG (H+L) highly cross-adsorbed secondary antibody, Alexa Fluor 568	Invitrogen	A-11031
Goat anti-rabbit IgG (H+L) cross-adsorbed secondary antibody, Alexa Fluor 568	Invitrogen	A-11011
Goat anti-rat IgG (H+L) cross-adsorbed secondary antibody, Alexa Fluor 488	Invitrogen	A-11006
Oligonucleotides and sequence-based reagents		
XMP 1 orange	MetaSystems	D-1401-050-OR
XMP 16 orange	MetaSystems	D-1416-050-OR
XMP Y orange	MetaSystems	D-1421-050-OR
Chemicals, enzymes, and other reagents		
16% Formaldehyde solution	Thermo Fisher Scientific	28906
2-Mercaptoethanol	Nacalai Tesque	21438-82
20xSCC	Sigma	S6639
37% Formaldehyde(FA)	Sigma	252549
4% Paraformaldehyde	Nacalai Tesque	26126-25
4X Laemmli sample buffer	Bio-Rad	#1610747
Activin A (human/mouse/rat)	Peprotech	120-14
AlbuMaxI	Gibco	11020062
Amanitin 1mg	Wako	1022961
Apo transferrin	Sigma	T1147
Axygen® AxyPrep MAG PCR Clean-Up Kit	Corning	MAG-PCR-CL-250
B27	Thermo Fisher Scientific	12587010

bFGF	Invitrogen	13256029
Biotin-14-dATP	Thermo Fisher Scientific	19524-016
Bovine serum albumin cold ethanol fraction, pH 5.2, ≥96%	Sigma	A4503-10G
BSA fraction V	Gibco	15260-037
CHIR99021	Bio Vision	4423
cOmplete™, protease inhibitor cocktail	Roche	4693116001
cOmplete™, EDTA-free protease inhibitor cocktail	Roche	11873580001
cOmplete™, mini, EDTA-free	Roche	4693159001
Cyclosporin A	Sigma	30024
DAPI	Wako	342-07431
Difco™ skim milk	BD Biosciences	232100
Digitonin	Promega	G9441
DMEM/F12	Gibco	11330-057
DMEM/F12 (phenol red free)	Thermo Fisher Scientific	21041025
DNA polymerase I, large (Klenow) fragment	NEB	M0210S
DNaseI 1 unit/ul, RNase-free	Thermo Fisher Scientific	89836
DpnII	NEB	R0543L
DTT 100 ul	Promega	P1171
Dynabeads M-280 sheep anti-mouse IgG	Thermo Fisher Scientific	DB11201
Dynabeads protein A	Thermo Fisher Scientific	DB10001
Dynabeads® MyOne™ Streptavidin C1	Thermo Fisher Scientific	65001
EGF, mouse, recombinant, carrier-free	RSD	2028EG
Fetal bovine serum (FBS)	Hyclone	SH30910.03
Fibronectin (human)	Merck Millipore	FC010
Formamide	Nacalai Tesque	16228-05
Forskolin	Sigma	F3917
GDNF, rat, recombinant	RSD	512GF
Glasgow's MEM (GMEM)	Thermo Fisher Scientific	11710035
GlutaMAX supplement	Life Technologies	35050061
Immobilon-P PVDF membrane	Merck Millipore	IPVH00010
Insulin	Sigma	#I-1882
Insulin-transferrin-selenium (ITS)-G	Gibco	41400045
KnockOut™ serum replacement	Gibco	10828028
L-Glutamine	Thermo Fisher Scientific	25030149
Laminin	BD Bioscience	354232

LIF(ESGRO®)	Merck Millipore	ESG1107
MEM non-essential amino acids solution	Thermo Fisher Scientific	11140-050
Minimum Essential Medium (MEM) Vitamin Solution	Thermo Fisher Scientific	11120052
Mitomycin C	kyowakirin	KWN-057039107
NEBNext High-Fidelity 2x PCR Master Mix	NEB	M0541S
Neurolbasal™ medium	Invitrogen	2113-049
Nuclei EZ Prep	Sigma	NUC101
Orange-dUTP	Abbott	02N33-050
PD325901	Stemgent	04-2006
Penicillin-Streptomycin (10,000 units/mL, 10,000 μg/mL)	Thermo Fisher Scientific	15140148
PhosSTOP™	Roche	4906837001
Pierce™ Protease Inhibitor Mini Tablets, EDTA-free	Thermo Fisher Scientific	A32955
Poly-L-ornithine	Sigma	P3655
Progesterone	Sigma	P8783
Proteinase K solution	Thermo Fisher Scientific	AM2546
Putrescine	Sigma	P5780
Recombinant Human BMP-4	RSD	314BP01M
Recombinant Mouse SCF	RSD	455MC
RIPA lysis buffer system 50ml	Santa Cruz	SC-24948
RNase A	Thermo Fisher Scientific	EN0531
Rolipram	Abcam	AB120029
Sodium pyruvate	Thermo Fisher Scientific	11360-070
Sodium selenate	Sigma	S5261
StemPro™-34 SFM (1X)	Gibco	10639011
SUPERase	Thermo Fisher Scientific	AM2694
T4 DNA ligase 1U/ μl	Thermo Fisher Scientific	15224090
T4 DNA polymerase	NEB	M0203L
Tks Gflex™ DNA Polymerase	Takara	R060A
TryPLE-Express	Thermo Fisher Scientific	12604-021
VECTASHIELD® Antifade Mounting Medium	Vector Laboratories	H-1000-10
β-Mercaptoethanol	Thermo Fisher Scientific	21985023
Software		
ABC commit 7fd69b0	Fulco et al., 2019	https://github.com/broadinstitute/ABC-Enhancer-Gene-Prediction
BEDTools v2.29.2	Quinlan et al., 2010	https://github.com/arq5x/bedtools2

Bismark v0.22.1	Krueger et al., 2011	https://www.bioinformatics.babraham.ac.uk/projects/bismark/
Bowtie2 v2.3.4.1	Langmead et al., 2012	http://bowtie-bio.sourceforge.net/bowtie2/index.shtml
CAGEfightR v1.7.6	Thodberg et al., 2019	https://bioconductor.org/packages/release/bioc/html/CAGEfightR.html
CAGEr v1.32.0	Haberle et al., 2015	https://www.bioconductor.org/packages/release/bioc/html/CAGEr.html
CALDER commit 32220e8	Liu et al., 2021	https://github.com/CSOgroup/CALDER
Chrom3D	Paulsen et al., 2017	https://github.com/Chrom3D/pipeline
ChromA v2.1.1	Gabitto et al., 2020	https://github.com/marianogabitto/ChromA
Chromosight v1.5.1	Matthey-Doret et al., 2020	https://github.com/koszullab/chromosight
cooler v0.8.10	Abdennur et al., 2020	https://github.com/open2c/cooler
coolpup.py v0.9.7	Flyamer et al., 2020	https://github.com/open2c/coolpuppy
cooltools v0.4.0	Venev et al., 2021	https://github.com/open2c/cooltools
CSynth commit 26e21fb	Todd et al., 2021	https://github.com/csynth/csynth
Cutadapt v1.9.1	Martin et al., 2011	https://cutadapt.readthedocs.io/en/stable/
dcHiC commit 7b1727f	Wang et al., 2021	https://github.com/ay-lab/dcHiC
deepTools v3.5.0	Ramirez et al., 2016	https://github.com/deeptools/deepTools
DESeq2 v1.28.1	Love et al., 2014	https://bioconductor.org/packages/release/bioc/html/DESeq2.html
DiffBind v3.0.13	Ross-Innes et al., 2012	https://bioconductor.org/packages/release/bioc/html/DiffBind.html
EDD v1.1.19	Lund et al., 2014	https://github.com/CollasLab/edd
epic2 v0.0.41	Stovner et al., 2019	https://github.com/biocore-ntnu/epic2
EpiProfile v2.0	Yuan et al., 2018	https://github.com/zfyuan/EpiProfile2.0_Family
FACSDiva Software	BD Biosciences	N/A
FAN-C v0.9.13	Kruse et al., 2020	https://github.com/vaquerizaslab/fanc
fastp v0.21.0	Chen et al., 2018	https://github.com/OpenGene/fastp
GimmeMotifs v0.15.3	Bruse et al., 2018	https://github.com/vanheeringen-lab/gimmemotifs
HDBSCAN v0.8.27	Campello et al., 2013	https://github.com/scikit-learn-contrib/hdbscan
HiCKey commit 6e282b9	Xing et al., 2021	https://github.com/YingruWuGit/HiCKey
HiCRep.py v0.2.3	Lin et al., 2021	https://github.com/Noble-Lab/hicrep
HiCRes v1.1	Marchal et al., 2020	https://github.com/ClaireMarchal/HiCRes
HiCSeg v1.1	Levy-Leduc et al., 2014	https://cran.r-project.org/web/packages/HiCseg/index.html
HiCUP v0.8.0	Wingett et al., 2015	https://github.com/StevenWingett/HiCUP
IDR2D v1.4.0	Krismer et al., 2020	https://github.com/kkrismer/idr2d
Imaris v9.1.2	N/A	https://imaris.oxinst.com/
Juicer tools v1.22.01	Durand et al., 2016	https://github.com/aidenlab/juicer
MACS v2.1.1	Zhang et al., 2008	https://github.com/macs3-project/MACS
OnTAD v1.2	An et al., 2019	https://github.com/anlin00007/OnTAD
Picard Tools v2.18.23	N/A	https://broadinstitute.github.io/picard/
Python v3.8.8	N/A	https://www.python.org/
R (v4.0.3)	https://www.r-project.org/	https://www.r-project.org/

RobusTAD	Dali et al., 2018	https://github.com/rdali/RobusTAD
S3V2-IDEAS commit b7cc2d5	Xiang et al., 2021	https://github.com/guanjue/S3V2_IDEAS_ESMP
Salmon v1.4.0	Patro et al., 2017	https://github.com/COMBINE-lab/salmon
SAMtools v1.7	Li et al., 2009	https://github.com/samtools/samtools
SpectralTAD v1.4.0	Cresswell et al., 2020	https://github.com/dozmorovlab/SpectralTAD
TADpole 0.0.0.9000	Soler-Vila et al., 2020	https://github.com/3DGenomes/TADpole
TopDom v0.10.1	Shin et al., 2016	https://github.com/HenrikBengtsson/TopDom
Trim-Galore! v0.6.3	Krueger et al., 2021	https://www.bioinformatics.babraham.ac.uk/projects/trim_galore/
tximport v1.16.1	Soneson et al., 2015	https://github.com/mikelove/tximport
UMAP v0.5.1	Mcinnes et al., 2018	https://github.com/lmcinnes/umap
Other		
Chemi-Lumi One Super	Nacalai Tesque	02230-14
FastGene Adapter Kit	FastGene	FG-NGSAD24
Illumina Tagment DNA Enzyme and Buffer, Small Kit	Illumina	20034197
KAPA Hyper Prep Kit	KAPA	KK8504
KAPA Library Quantification Kit	KAPA	KK4824
MinElute PCR purification Kit (50)	QIAGEN	28004
miRNeasy Mini Kit 50	QIAGEN	217004
NEBNext® Multiplex Oligos for Illumina® (Index Primers Set 1)	NEB	E7335S
NEBNext® Ultra™ II DNA Library Prep Kit for Illumina®	NEB	E7645S
NextSeq 500/550 High Output Kit v2.5 (150 Cycles)	Illumina	20024907
NextSeq 500/550 High Output Kit v2.5 (75 Cycles)	Illumina	20024906
NextSeq 500/550 High-Output v2 Kit (150 cycles)	Illumina	FC-404-2002
NextSeq 500/550 High-Output v2 Kit (75 cycles)	Illumina	FC-404-2005
NextSeq 500/550 Mid Output Kit v2.5 (150 Cycles)	Illumina	20024904
NextSeq 500/550 Mid-Output v2 Kit (150 cycles)	Illumina	FC-404-2001
NovaSeq 6000 S1 Reagent Kit (200 cycles)	Illumina	20012864
NovaSeq 6000 SP Reagent Kit (200 cycles)	Illumina	20040326
QIAquick PCR Purification Kit (50)	QIAGEN	28104
Qubit RNA HS Assay Kit	Thermo Fisher Scientific	Q32855
RNase-Free DNase Set	QIAGEN	79254

Film-bottom dish	Matsunami Glass	FD10300
MAS-GP type A	Matsunami Glass	S9901-9905

Methods and Protocols

Culture of mESCs

The BDF1-2-1 mouse mESCs bearing Blimp1-mVenus and Stella-ECFP (BVSC) transgenes (Ohta et al., 2021) were cultured as described previously (Hayashi et al., 2011). Briefly, mESCs were maintained in N2B27 medium supplemented with PD0325901 (0.4 uM) (Stemgent, 04-2006), CHIR99021 (3 uM) (Bio Vision, 4423), and leukemia inhibitory factor (LIF) (1000 U/ml) (Merck Millipore, ESG1107) on a 12-well plate coated with poly-L-ornithine (0.01%) (Sigma, P3655) and laminin (10 ng/ml) (BD Biosciences, 354232). In this study, all cells were cultured at 37°C under an atmosphere of 5% CO_2 in air.

Induction of EpiLCs and mPGCLCs

Induction of EpiLCs and PGCLCs was performed as described previously (Hayashi et al., 2011) with minor modifications. Briefly, the EpiLCs were induced by plating 8×10^4 mESCs on a well of a 12-well plate coated with human plasma fibronectin (16.7 mg/ml) (Merck Millipore, FC010) in N2B27 medium containing activin A (20 ng/ml) (Peprotech, 120-14), bFGF (12 ng/ml, 13256029) (Invitrogen), and KSR (1%) (Gibco, 10828028). mPGCLCs were induced from d2 EpiLCs (2 days after induction) under a floating condition in wells of a low-cell-binding U-bottom 96-well plate in GMEM medium (Thermo Fisher Scientific, 11710035) containing 15% KSR (Gibco, 10828028), 0.1 mM NEAA (Thermo Fisher Scientific, 11140-050), 1 mM sodium pyruvate (Thermo Fisher Scientific, 11360-070), 0.1 mM β-mercaptoethanol (Thermo Fisher Scientific, 21985023), 100 U/ml penicillin, 0.1 mg/ml streptomycin (Thermo Fisher Scientific, 15140148) and 2 mM L-glutamin (Thermo Fisher Scientific, 25030149) supplemented with BMP4 (500 ng/ml) (RSD, 314BP01M), LIF (1000 U/ml) (Merck Millipore, ESG1107), SCF (100 ng/ml) (RSD, 455MC), and EGF (50 ng/ml) (RSD, 2028EG).

Expansion culture of mPGCLCs

The expansion culture of mPGCLCs was performed as previously described (Ohta et al., 2021). Briefly, following incubation in TrypLE™ Express (Gibco, 12604-021) for 10 min, the aggregates of d4 mPGCLCs (PGCLCs induced for 4 days) were dissociated into single cells by rigorous pipetting. Subsequently, BV-positive cells were sorted with a FACSAria III cell sorter. Purified d4 mPGCLCs were cultured on m220-5 cells as the feeder cells in GMEM (Gibco, 11710035) containing 10% KSR (Gibco, 10828028), 0.1 mM NEAA (Thermo Fisher Scientific, 11140-050), 1 mM sodium pyruvate (Thermo Fisher Scientific, 11360-070), 0.1 mM β-mercaptoethanol (Thermo Fisher Scientific, 21985023), 100 U/ml penicillin, 0.1 mg/ml streptomycin (Thermo Fisher Scientific, 15140148), 2 mM L-glutamin (Thermo Fisher Scientific, 25030149), 2.5% FBS (Hyclone, SH30910.03), SCF (100 ng/ml) (RSD, 455MC), 10 mM forskolin (Sigma, F3917), 10 uM rolipram (Abcam, AB120029), and 5 uM CsA (Sigma, 30024). Half of the culture medium was changed every two days.

Culture of GSCs and GSCLCs

GSCs and GSCLCs bearing Acrosin-EGFP and beta-Actin-EGFP (AAG) transgenes (Ohta et al., 2000) were cultured as described previously (Ishikura et al., 2016). Briefly, cells were cultured in Stempro-34 SFM supplemented with Stempro Supplement (Gibco, 10639011), with 0.1 mM β-mercaptoethanol (Thermo Fisher Scientific, 21985023), 1% FBS (Hyclone, SH30910.03), 1×MEM vitamin solution (Thermo Fisher Scientific, 11120052), 5.0 mg/ml AlbMAXI (Gibco, 11020062), 0.1 mM NEAA (Thermo Fisher Scientific, 11140-050), 1 mM sodium pyruvate (Thermo Fisher Scientific, 11360-070), 0.1 mM β-mercaptoethanol (Thermo Fisher Scientific, 21985023), 100 U/ml penicillin, 0.1 mg/ml streptomycin (Thermo Fisher Scientific, 15140148), 2 mM L-glutamin (Thermo Fisher Scientific, 25030149), 1×Insulin-Transferrin-Selenium (ITS-G) (Gibco, 41400045), 10 ng/ml bFGF (Invitrogen, 13256029), 20 ng/ml GDNF rat recombinant (RSD, 512GF), 20 ng/ml EGF (RSD, 2028EG), and 1000 U/ml LIF (Merck Millipore, ESG1107) in a well of a 6-well plate on mouse embryonic fibroblast cells (MEFs) as feeder cells. Half of the medium was replaced every two or three days.

Immunofluorescence staining

The following primary antibodies were used at the indicated dilutions: rabbit anti-Laminb1 (1/1000; Abcam ab16048); mouse anti-H3K9me2 (1/500; MBL, MABI0317); mouse anti-H3K9me3 (1/500; MBL, MABI0318); and mouse anti-H3K27me3 (1/500; Merk, 07-449).

The following secondary antibodies from Thermo Fisher Scientific were used at a 1/500 dilution: Alexa Fluor 568 goat anti-rabbit IgG; Alexa Fluor 488 goat anti-rabbit IgG; and Alexa Fluor 568 goat anti-mouse IgG.

Immunofluorescence (IF) staining was performed as previously described (Ohta et al., 2017) with minor modifications. Briefly, cells were fixed in 4% PFA (paraformaldehyde) (Nacalai Tesque, 26126-25) for 30 min at RT. After fixation, cells were washed in PBS three times and then permeabilized in 1% Triton-X100/PBS for 5 min on ice. Then, they were washed in PBS three times and incubated in 1% BSA (Sigma, A4503-10G)/PBS for 1 h. The cells were incubated with primary antibodies in 1% BSA/PBS overnight. After incubation with primary antibodies, the cells were washed in PBS three times and then incubated for 2 h with secondary antibodies and DAPI (1 mg/ml) (Wako, 342-07431) at RT. Then, they were washed three times in PBS and mounted in VECTOR SHIELD (Vector Laboratories, H-1000-10). Images were captured with a confocal microscope (LSM780 or LSM980 with Airyscan2; Zeiss).

Probe preparation for DNA-FISH against major satellite repeats

The probe against major satellite repeats was generated as previously described (Anton, 2014) with some modifications. DNA fragments were amplified with forward (5'-GCGAGAAAACTGAAAATCAC-3') and reverse (5'-TCAAGTCGTCAAGTGGATG-3') primers using mouse genomic DNA as a template, and purified using a QIA quick PCR purification kit (QIAGEN, 28104). 500 ng of the PCR product was labeled with Orange-dUTP (Abbott, 02N33-050) using a Nick translation kit (Roche, 10976776001).

DNA-FISH

DNA-FISH was performed as described previously (Okamoto et al., 2005). Briefly, cells were cultured in a film-bottom dish (Matsunami Glass, FD10300) and fixed in 3% PFA/PBS (Nacalai Tesque, 26126-25) for 10 min at RT. After a brief wash in PBS, cells were permeabilized in 0.5% Triton-X100 in PBS for 5 min on ice and stored in 70% ethanol at −30°C by the day of use. Then, the DNA was denatured in 50% FA (formamide) (Nacalai Tesque, 16228-05)/2×SSC pH 7.4 (Sigma, S6639) for 40 min at 80°C and dehydrated through an ice-cold ethanol series. Hybridization with probes was performed at 37°C overnight. After incubation, the samples were washed in 50% FA/2×SSC followed by 2×SSC. The samples were counterstained with DAPI (1 mg/ml) (Wako, 342-07431), and mounted and viewed under a confocal microscope (Zeiss LSM980 with Airyscan2). Images were analyzed using Imaris 9.1.2 software (Bitplane).

Western blot analysis

The following primary antibodies were used at the indicated dilutions: rabbit anti-Lamin b1 (1/1000; Abcam ab16048); mouse anti-H3K9me2 (1/500; MBL, MABI0317); mouse anti-H3K9me3 (1/500; MBL, MABI0318); and mouse anti-H3K27me3 (1/500; MBL, MABI0323); rabbit anti-H3 (1/10000; CST, #9715); rabbit anti-CTCF (1/500; CST, #3418); mouse anti-G9a (1/500; R&D, PP-A8620A-00); mouse anti-GLP (1/500; R&D, PP-B0422-00); rabbit anti-Setdb1 (1/1000; Proteintech, 11231-1-AP); mouse anti-α-tubulin (1/5000; Merk, T9026); and mouse anti-β-actin (1/5000; MBL, M177-3).

The following secondary antibodies from Merk were used at the indicated dilutions: goat anti-rabbit IgG conjugated with peroxidase (1/8000); and sheep anti-mouse IgG conjugated with peroxidase (1/10000).

Western blot was performed as previously described (Hayashi et al., 2011) with slight modifications. Briefly, cells were lysed by RIPA buffers (Santa Cruz, SC-24948). After incubation for 30 min at 4°C with rotation, the lysates were sonicated by Bioruptor using 10 cycles of 30 s on/30 s off. Then, the lysates were spun down at 14000 rpm for 15 min at 4°C and the supernatant was collected. A BCA assay was performed using a Pierce™ BCA Protein Assay Kit (Thermo Fisher Scientific, 23227) to measure the

protein concentration. For western blot, 4.5 mg of whole cell lysate or 2.25 mg of chromatin fraction was loaded onto each lane. After addition of 4×Laemmli buffer (Bio-Rad, #1610747), the sample was run by SDS-PAGE, followed by blotting to PVDF membrane (pore size: 0.45 mm) (Millipore, IPVH00010) in CAPS buffer (10 mM CAPS-NaOH pH 11, 5% methanol). After blotting, the membrane was incubated for 1 h in 0.1% Tween-20/PBS (PBST) with 1% skim milk (BD Bioscience, 232100). After blocking, the membrane was incubated overnight with the primary antibodies in 0.1% PBST with 1% skim milk. The membrane was washed in 0.1% PBST, followed by incubation for 2 h with the secondary antibodies in the 0.1% PBST with 1% skim milk. After washing in 0.1% PBST three times, secondary antibodies were detected by Chemilumi One Super (Nacalai Tesque, 02230-14) using Fusion solo 4S (Vilber). Quantification analysis of the signal intensity was performed in ImageJ v2.1.0 (NIH). Target protein signals were normalized by the loading control.

Chromatin fraction isolation

Chromatin fractionation was performed as previously described (Wutz et al., 2017). In brief, cells were resuspended in extraction buffer (20 mM Tris-HCl pH 7.5, 100 mM NaCl, 5 mM $MgCl_2$, 2 mM NaF, 10% glycerol, 0.2% NP-40, 20 mM β-glycerophosphate, 0.5 mM DTT, and protease inhibitor cocktail (Roche, 11873580001)). The chromatin pellet was fractionated by centrifugation at 2000 g for 5 min and washed in the same buffer three times. Then, the chromatin pellet was resuspended in RIPA buffer (Santa Cruz, SC-24948) and processed along with the whole cell lysate by a downstream BCA assay (Thermo Fisher Scientific, 23227) followed by western blot.

Visualization and analysis of nuclei by DAPI staining

All cells except d2 mPGCLCs were cultured in a film-bottom dish (Matsunami Glass, FD10300). d2 mPGCLCs were attached on a slide glass (MATSUNAMI, S9901-9905) using Cyto Spin 4 (Thermo Fisher Scientific) as previously described (Ohta et al., 2017). Cells were fixed in 4% PFA (Nacalai Tesque, 26126-25) at RT for 30 min and washed in PBS three times. For permeabilization, cells were incubated on ice in 0.5% TritonX-100/PBS for 5 min. Then, cells were incubated in DAPI solution (1 mg/ml) (Wako, 342-07431) for 8 min, mounted and viewed under a fluorescence microscope. Confocal z-series

images with an interval of 0.14 μm were captured by Zeiss LSM980 with Airyscan2 using a 405 nm wavelength and a 63×objective oil-immersion lens. For DAPI-staining analysis, cells were attached to slides using Cyto Spin 4 (Thermo Fisher Scientific) as previously described (Ohta et al., 2017) in order to avoid the effect of differences in their colony shapes. DAPI-staining and image acquisition were performed as described above. Acquired images were processed as follows. The nuclear mask, nuclear rim, and DAPI dense regions were defined in each z-slice using ImageJ custom script as previously described (Miura et al., 2020). Then, the slice showing the maximum diameter was decided for each cell as a representative slice, and the representative slice ±5 slices for each cell (i.e., 11 slices/cell) were used in the downstream analysis. Approximately 20–30 cells were analyzed in each cell type. The parameters presented in the Figures were calculated using R custom script.

Histone extraction for mass spectrometry

Frozen cell pellets containing 3 million cells were lysed in nuclear isolation buffer (15 mM Tris pH 7.5, 60 mM KCl, 15 mM NaCl, 5 mM $MgCl_2$, 1 mM $CaCl_2$, 250 mM sucrose, 10 mM sodium butyrate, 0.1% v/v b-mercaptoethanol (Nacalai Tesque, 21438-82), commercial phosphatase and protease inhibitor cocktail tablets (Roche, 4906837001; Thermo Fisher Scientific, A32955)) containing 0.3% NP-40 alternative on ice for 5 min. Nuclei were washed in the same solution without NP-40 twice and the pellet was slowly resuspended while vortexing in chilled 0.4 N H_2SO_4, followed by 3 h of rotation at 4°C. After centrifugation, the supernatants were collected and proteins were precipitated in 20% TCA overnight at 4°C, washed once with 0.1% HCl (v/v) acetone and then twice with acetone only, and resuspended in deionized water. Acid-extracted histones (20–50 μg) were resuspended in 100 mM ammonium bicarbonate pH 8, derivatized using propionic anhydride and digested with trypsin as previously described (Sidoli et al., 2016). After the second round of propionylation, the resulting histone peptides were desalted using C18 Stage Tips, dried using a centrifugal evaporator and reconstituted using 0.1% formic acid in preparation for liquid chromatography-mass spectrometry (LC–MS) analysis.

LC/LC-MS

Nanoflow liquid chromatography was performed using a Thermo Fisher Scientific Dionex UltiMate 3000 LC system equipped with a 300mm ID x 0.5-cm trap column (Thermo) and a 75 mm ID x 20-cm analytical column packed in-house using Reprosil-Pur C18-AQ (3 mm; Dr. Maisch). Buffer A was 0.1% formic acid and Buffer B was 0.1% formic acid in 80% acetonitrile. Peptides were resolved using a two-step linear gradient from 5% B to 33% B over 45 min, then from 33% B to 90% B over 10 min at a flow rate of 300 nL min^{-1}. The HPLC was coupled online to an Orbitrap QE-HF mass spectrometer operating in the positive mode using a Nanospray Flex Ion Source (Thermo Fisher Scientific) at 2.3 kV. Two full mass spectrometry scans (m/z 300–1,100) were acquired in the Orbitrap Fusion mass analyzer with a resolution of 120,000 (at 200 m/z) every 8 data-independent acquisition tandem mass spectrometry (MS/MS) events, using isolation windows of 50 m/z each (for example, 300–350, 350–400, 650–700). MS/MS spectra were acquired in the ion trap operating in normal mode. Fragmentation was performed using collision-induced dissociation in the ion trap mass analyzer with a normalized collision energy of 35. The automatic gain control target and maximum injection time were 5×10^5 and 50 ms for the full mass spectrometry scan, and 3×10^4 and 50 ms for the MS/MS scan, respectively. Raw files were analyzed using EpiProfile 2.0 (Yuan et al., 2018). The area for each modification state of a peptide was normalized against the total signal for that peptide to give the relative abundance of the histone modification.

ChIP-seq library preparation and sequencing

The ChIP-seq library preparation was performed as previously described (Lee, 2006) with minor modifications. We used harvested mESCs and EpiLCs, and FACS-sorted BV-positive cells for d2 mPGCLCs and d4c7 mPGCLCs samples, and FACS-sorted AAG-positive cells for GSCs and GSCLCs samples. Briefly, the harvested cells were crosslinked with 1% formaldehyde (Thermo Fisher Scientific, 28906)/PBS for 10 min at RT and quenched with 125 mM glycine. Crosslinked cells were lysed consecutively using LB1 (50 mM HEPES-KOH pH 7.5, 1 mM EDTA, 140 mM NaCl, 10% glycerol, 0.5% NP-40, 0.25% Triton-100, protease inhibitors (Roche, 11873580001)), LB2 (10 mM Tris-HCl pH 8.0, 1 mM EDTA, 0.5 mM EGTA, 200 mM NaCl, protease inhibitors), and LB3 (50 mM Tris-HCl pH 8.0, 1 mM EDTA, 0.5 mM EGTA, 100 mM NaCl, 0.1% Na-deoxycholate, 0.5% N-lauroylsarcosine, protease inhibitors) and then sonicated by a picoruptor to achieve a mean DNA fragment size of around 200–

400 bp. Sonicated chromatin was incubated with Dynabeads M-280 Sheep anti-Mouse IgG beads (Thermo Fisher Scientific, DB11201) or Dynabeads ProteinA beads (Thermo Fisher Scientific, DB10001) for 35 min at 4°C for preclear. Precleared chromatin was then incubated with antibodies that were preincubated with the appropriate Dynabeads in 0.5% BSA (Gibco, 15260-037) in PBS as follows: a chromatin equivalent of 5×10^5 cells with anti-H3K4me1 (rabbit monoclonal, CST, #5326, 5 μl), anti-H3K9me2 (mouse monoclonal, MBL, MABI0317, 5 μl), anti-H3K27me3 (mouse monoclonal, MBL, MABI0323, 5 μl); 1×10^6 cells with anti-H3K4me3 (mouse monoclonal, MBL, MABI0304, 5 μl), anti-H3K9me3 (mouse monoclonal, MBL, MABI0318, 5 μl), anti-H3K36me2 (rabbit monoclonal, CST, #2901, 5 μl), anti-H2AK119ub1 (rabbit monoclonal, #8240, 10 μl), anti-H3K36me3 (rabbit polyclonal, Active Motif, 61101, 2 μl); 1.5×10^6 cells with anti-H3K27ac (mouse monoclonal, MBL, MABI0309, 5 μl); 2×10^6 cells with anti-CTCF (rabbit monoclonal, CST, #3418, 5 μl), anti-Laminb1 (rabbit polyclonal, Proteintech, 12987-1-AP, 10 μl); 4×10^6 cells with anti-Ring1b (rabbit monoclonal, CST, #5694, 10 μl); and 4.5×10^6 cells with anti-Rad21 (rabbit monoclonal, ab992, 5 μl).

After incubation for 6 h at 4°C, the beads were washed 4 times in wash buffer 1 (20 mM Tris-HCl pH 8.0, 2 mM EDTA, 150 mM NaCl, 1% TritonX-100, 0.1% SDS), 2 times in wash buffer 2 (20 mM Tris-HCl pH 8.0, 2 mM EDTA, 500 mM NaCl, 1% TritonX-100, 0.1% SDS), and 2 times in wash buffer 3 (10 mM Tris-HCl pH 8.0, 1 mM EDTA, 250 mM LiCl, 1% Na-Deoxycolate, 1% NP-40). Then, the washed beads were eluted in 10 mM Tris-HCl pH 8.0, 5 mM EDTA, 300 mM NaCl, and 1% SDS, and crosslinks were reversed overnight at 65°C. Input samples were treated in a similar manner. The following day, the IP and Input samples were incubated with RNaseA (Thermo Fisher Scientific, EN0531) and proteinase K (Thermo Fisher Scientific, AM2546). IP or Input DNA was purified using a QIA quick PCR purification kit (QIAGEN, 28104).

ChIP-seq libraries were prepared using a KAPA Hyper Prep Kit (KAPA, KK8504) following the manufacturer's guidelines. An adaptor kit (Fastgene, FG-NGSAD24) was used for the sample indexes. The average size and concentration of libraries were analyzed using LabChIP GX (PerkinElmer) and a KAPA library Quantification kit (KAPA, KK4824), respectively. Libraries were sequenced as 75 bp

single-end reads on an Illumina NextSeq 500/550 platform with a NextSeq 500/550 High Output kit (75 cycles) (Illumina, 20024906).

ATAC-seq library preparation and sequencing

The ATAC-seq experiment was performed as described previously (Corces et al., 2017, Buenrostro et al., 2013) with minor modifications. We used FACs-sorted viable cells for mESCs and EpiLCs; FACS-sorted BV-positive cells for d2 mPGCLCs, d4 mPGCLCs, and d4c7 mPGCLCs; and FACS-sorted AAG-positive cells for GSCs and GSCLCs. 50,000 cells were permeabilized in cold lysis buffer 1 (10 mM Tris-HCl pH8.0, 10 mM NaCl, 3 mM $MgCl_2$, 0.1% NP-40, 0.1% Tween20, 0.1% Digitonin (Promega, G9441)) for 3 min followed by addition of 1 ml of cold lysis buffer 2 (10 mM Tris-HCl pH8.0, 10 mM NaCl, 3 mM $MgCl_2$, 0.1% Tween20). Nuclei were centrifuged and resuspended with 50 ml of transposase reaction mixture (25 ul of 2×TD buffer (Illumina, 20034197), 2.5 ml of Transposase (Illumina, 20034197), 16.5 ml of PBS, 0.5 ml of Digitonin, and 0.5 ml of Tween-20, 5 ul of DDW). After incubation at 37°C for 30 min, the tagged DNA was purified using a Minelute PCR purification kit (QIAGEN, 28004). The purified DNA was amplified for 8 cycles by a PCR reaction (NEB, M0541S) followed by size selection using AMPure XP beads (Corning, MAG-PCR-CL-250) to remove primer dimers. Libraries were sequenced as 2×75bp paired-end reads on an Illumina NextSeq 500/550 platform with a NextSeq 500/550 Mid Output Kit (150 cycles) (Illumina, 20024904) or NextSeq 500/550 High Output Kit (150 cycles, 20024907) (Illumina).

In situ Hi-C library preparation and sequencing

In situ Hi-C library preparation was performed as described previously (Belaghzal et al., 2017, Rao et al., 2014) with minor modifications. We used the whole harvested cells for mESCs and EpiLCs; FACS-sorted BV-positive cells for d2 mPGCLCs and d4c7 mPGCLCs; and FACS-sorted AAG-positive cells for GSCs and GSCLCs. 2.5×10^6 cells were used for one replicate. The cells were fixed by 1% formaldehyde (Sigma, 252549)/HBSS and lysed in lysis buffer (10 mM Tris-HCl pH 8.0, 10 mM NaCl, 0.2% NP-40) for 30 min on ice with frequent inversion. The cells were digested by 500 U of DpnII (NEB, R0543L) overnight at 37°C. Following biotin filling (Thermo Fisher Scientific, 19524-016; NEB, M0210S), proximity ligation

(Thermo Fisher Scientific, 15224090) and reverse crosslinking, DNA was purified by ethanol precipitation and sheared to 200-400 bp fragments using a Covaris E220 sonicator (Covaris) at 4°C (10% Duty Factor, 200 cycles/burst, 175 W Peak Incident Power, 110 s). Ligation fragments containing biotin were immobilized on MyOne Streptavidin T1 beads (Thermo Fisher Scientific, 65001) followed by library preparation using a NEB library preparation kit (NEB, E7645S; NEB, E7335S) according to the manufacturer's guidelines. The libraries were amplified in 8 cycles and DNA fragments of 300–800 bp were selected using AMPure XP beads (Corning, MAG-PCR-CL-250). Libraries were sequenced as 2×100bp paired-end reads on an Illumina NovaSeq 6000 platform with a NovaSeq 6000 S1 Reagent Kit (200 cycles) (Illumina, 20012864).

NET-CAGE library preparation and sequencing

NET-CAGE library preparation was performed as described previously (Hirabayashi et al., 2019) with minor modifications. For extraction of nascent RNA, cells were first lysed with 1400 μl of Buffer A, which is Nuclei EZ Lysis Buffer (Sigma, NUC101-1KT) supplemented with 25 μM α-amanitin (Wako, 1022961), 1×cOmplete Protease Inhibitor Cocktail (Roche, 4693116001) and SUPERase•IN RNase Inhibitor (20 units; Thermo Fisher Scientific, AM2694), and then incubated on ice for 10 min and centrifuged at 800 g for 5 min at 4°C followed by washing once with the same buffer. Washed pellets were resuspended in 200 μl of Buffer B, containing 1% NP-40, 20 mM HEPES pH 7.5, 300 mM NaCl, 2 M urea, 0.2 mM EDTA, 1 mM dithiothreitol (DTT) (Promega, P1171), 25 μM α-amanitin, 1×cOmplete Protease Inhibitor Cocktail and SUPERase•IN RNase Inhibitor (20 units), and incubated for 10 min on ice. The suspension was centrifuged at 3,000g for 2 min at 4°C. After removing the supernatant, the nuclear insoluble fraction was washed once with 100 μl of Buffer B. DNase I solution (50 μl) containing DNase I (10 units; Thermo Fisher Scientific, 89836), 1×DNase I Buffer (Thermo Fisher Scientific) and SUPERase•IN RNase Inhibitor (20 units) was added to the pellets. The samples were incubated for 30 min at 37°C while being pipetted up and down several times at 10-min intervals. QIAzol (700 μl) was then added and the solution was thoroughly mixed. RNA was extracted with an miRNeasy Mini kit (QIAGEN, 217004) according to the manufacturer's instructions. On-column DNase I digestion was carried out with an RNase-free DNase set (QIAGEN, 79254). RNA was eluted in 30 μl RNase-free water,

and its quality and quantity were measured with a Qubit RNA HS assay kit (Thermo Fisher Scientific, Q32855) and 2100 BioAnalyzer (Agilent). cDNA was synthesized from 200 ng of nascent RNA. CAGE libraries were generated according to the no amplification non-tagging CAGE libraries for Illumina next-generation sequencers (nAnT-iCAGE) protocol (Murata et al., 2014) with PCR amplifications (Takara, R060A). All CAGE libraries were sequenced in 75 bp single-end reads on an Illumina NextSeq 500 platform.

ChIP-seq data processing

Single-end reads were processed using Trim-Galore! v0.4.1/cutadapt v1.9.1 (Krueger et al., 2021, Martin et al., 2011) to remove adaptor sequences. The truncated reads were then aligned to (GRCm38p3) using Bowtie2 v2.3.4.1 (Langmead et al., 2012) with the "-very-sensitive" option. Reads aligned to chromosomes 1 to 19, X, and Y were converted to the BAM format by SAMtools v1.7 (Li et al., 2009). BED files were obtained from the BAM files using the bamtobed command of BEDTools v2.29.2 (Quinlan et al., 2010). BigWig files were generated from the BAM files using bamcoverage for raw count with the "--normalizeUsing CPM -bs 25" or bamcompare for IP/Input command with the "--pseudocount 1 -bs 1000" option of deepTools v3.5.0 (Ramirez et al., 2016) In both cases, the blacklist regions (Amemiya et al., 2019) were excluded.

The regions enriched by epigenetic marks were identified using peak calling tools. For CTCF peaks, MACS v2.1.1 (Zhang et al., 2008) was used with the "-q 0.01 --nomodel --keep-dup all --extsize 200" option. For H3K9me3 domains, epic2 v0.0.41 (Stovner et al., 2019) was used with "-kd -fdr 0.01" option. The number of IP or Input reads in 10/25/50/100 kb genomic windows were counted by the intersect command of BEDTools v2.29.2, and normalized by total million mapped reads (FPM) and transformed to Log2(IP/Input) for the downstream analysis. The bins in which no reads were detected in the Input samples were excluded.

ATAC-seq data processing

ATAC-seq data processing including public data was performed as previously described (Buenrostro et al., 2013) with minor modifications. First, adaptor sequences were trimmed from the reads using TrimGalore! v0.4.1/cutadapt v1.9.1. These reads were aligned using Bowtie2 v2.3.4.1 to GRCm38p3 with the "--very-sensitive -X 2000" option. The properly mapped reads with the flag (99, 147, 83 or 163) were extracted by awk, and mitochondrial reads were excluded. Duplicated reads were removed using the MarkDuplicates command of Picard Tools v2.18.23 (https://broadinstitute.github.io/picard/). These de-duplicated reads were then filtered for high quality (MAPQ≧30). The reads with an insert size of less than 100 bp were extracted as nucleosome free region (NFR) reads. Bed files for downstream analysis were generated by the bamtobed command of BEDTools v2.29.2 with the "-bedpe" option. BigWig files were generated from the BAM files using bamcoverage for raw count with the "--normalizeUsing CPM -bs 25" option of deepTools v3.5.0. The blacklist regions (https://www.encodeproject.org/files/ENCFF999QPV/) were excluded.

Peak calling was performed using MACS v2.1.1 with the "--nomodel --shift -100 --extsize 200 --keep-dup all" option after shifting NFR reads with the offset by +4 bp in the + strand and by -5 bp in the - strand. Then, confident peak sets in each cell type were obtained by the IDR method (https://www.encodeproject.org/software/idr/) using two replicates.

PBAT data processing

Public read data processing of the methylation levels was performed as described previously (Shirane et al., 2016). In brief, all reads were processed with Trim-Galore! v0.4.1/cutadapt v1.9.1 with the "--clip_R1 4," "--trim1" and "-a AGATCGGAAGAGC" options. Output reads were mapped onto the mouse genome, GRCm38.p6, using Bismark v0.22.1 (Krueger et al., 2011)/Bowtie2 v2.3.4.1 with the "--pbat" option. All public WGBS data were obtained from DDBJ or NCBI SRA ftp sites and processed as described above. Conversion rates were calculated as follows: output reads after Trim-Galore were mapped onto the lambda phage DNA sequence using Bismark v0.22.1/Bowtie2 v2.3.4.1 with the "--pbat" option. From the Bismark's statistics, conversion rates were determined as 1 - ([total mC counts] / [total

C and mC counts]). All CpG sites with a read depth of between 4 and 200 were used for the %mC calculations.

3-prime RNA sequencing data processing

Raw 3' RNA-seq data were directly used with Salmon v1.4.0 (Patro et al., 2017) with default parameters and --noLengthCorrection to quantify the expression of GENCODE vM25 features on GRCm38.p6. Gene-level expression estimates were aggregated from transcript-level abundance using tximport v1.16.1 (Soneson et al., 2015).

In situ Hi-C data processing

Sequences were first trimmed using fastp v0.21.0 (Chen et al., 2018) with default options and the --detect_adapter_for_pe flag. Trimmed sequences were then processed using HiCUP v0.8.0 {Wingett, 2015 #3503} with default options and the di-tag length range set to 0–800, with bowtie v2.4.2 as the aligner. hicup2juicer was then used to produce pairs files, which were subsequently ingested with Juicer tools v1.22.01 (Durand et al., 2016) for the creation of .hic files. The same set of pairs files were also used to create multi-resolution cooler files using cooler v0.8.10 (Abdennur et al., 2020) with default options. Additionally, HiCSR commit b13ac41 (Dimmick et al., 2020)was used to de-noise 10 kb-resolution contact maps for visualization. In particular, pooled mESC data from (Bonev et al., 2017) after 10× down-sampling were used for training with default parameters; inference was then performed using default parameters. FAN-C v0.9.13 (Kruse et al., 2020) was finally used for the normalization (with default parameters) and subsequent visualization of the enhanced 10 kb matrices, including virtual 4C profiles.

NET-CAGE data processing

Sequences were first trimmed using fastp v0.21.0 and then aligned with STAR 2.7.6a (Dobin et al., 2013) using default options. Uniquely mapped reads were converted to coverage bigWig tracks with G-bias correction using CAGEr v1.32.0 (Haberle et al., 2015) with default options. Tag clusters were identified using CAGEfightR v1.7.6 (Thodberg et al., 2019) with pooledCutoff = 0.1 and mergeDist = 20 for unidirectional clusters as well as balanceThreshold = 0.8 for bidirectional clusters. These clusters were

subsequently filtered to require at least 1 sample demonstrating an expression level exceeding 1 TPM. Unidirectional clusters (putative promoters) were removed if they overlapped bidirectional clusters (putative enhancers), and the two region sets were subsequently combined to identify coordinately regulation enhancer-promoter co-transcription across stages. In particular, Kendall correlation was used to find putative enhancers within 1 mb of putative promoters that exhibited correlated expression patterns, with TPM as the expression unit.

Global Hi-C metrics

HiCRes v1.1 (Marchal et al., 2020) with default parameters was used for the resolution of contact maps following the definition in (Rao et al., 2014). Matrix similarity scores were computed using HiCRep.py v0.2.3 (Lin et al., 2021) with --binSize=50000 --dBPMax=5000000 --h=3. Contact probability decay (i.e., the average contact frequency across different genomic separation distances) was assessed using the compute-expected and logbin-expected modules from cooltools v0.4.0 (Venev et al., 2021) at all resolutions, in both cis and trans. 3D models of individual chromosomes were produced using CSynth commit 26e21fb (Todd et al., 2021) with balanced 50 kb cis matrices, whose coordinates are normalized to achieve unit backbone length (i.e., the sum of Euclidean distance between adjacent beads being 1); and the size of these predicted structures are taken to be the volume of their 3D convex hulls.

Compartment-related analysis

For analyses involving data across multiple studies, eigendecomposition was performed at 100 kb resolution using the call-compartments module from cooltools v0.4.0 with GC content for orientating the track sign to achieve a positive correlation. For analyses strictly focusing on data generated within this study, dcHiC commit 7b1727f (Wang et al., 2021) was used with default parameters to perform simultaneous compartment score calculation across all samples at 50 kb resolution to facilitate statistical comparison across cell types while integrating replicate data. Though the values produced by dcHiC showed high correlation with those generated by cooltools, dcHiC was not applied to public datasets due to a lack of replication in certain datasets. Quantile-binned saddle plots were produced using dcHiC-generated compartment scores and the outputs of compute-expected described above at 50 kb resolution.

Binarization of compartment score tracks was carried out using A := score > 0 and B := score < 0. PCA of compartment scores to contrast lineages was done using 100 kb resolution data and bins non-masked in all samples. The average size of compartments was assessed using an auto-correlation function, where the signal profile is shifted and correlated against the original, using the acf function from R library stats 4.0.3 with na.action = na.pass.

Subcompartment-related analysis

8-state subcompartment labels were assigned to 50 kb bins with balanced contact frequencies using CALDER commit 32220e8 (Liu et al., 2021). The strength of epigenetic signals in each subcompartment was subsequently examined by converting enrichment values to Z-scores genome-wide, after which the average across all bins with the same label was computed. Significant differences in subcompartment proportions were evaluated using the prop.test function from R library stats 4.0.3.

TAD-related analysis

Insulation scores were computed at 10 kb resolution with a window size of 100 kb using the diamond-insulation module of cooltools v0.4.0. Consensus TADs in each dataset were derived by taking the set of bins with boundary prominence scores >0.2 in at least half the cell types present and subsequently pairing neighboring boundaries, with those exceedingly 2mb filtered out, consistently yielding ~4000–5000 domains for each dataset. The significance and strength of TAD-TAD interactions were evaluated using a non-central hypergeometric (NCHG) test implemented as a part of the Chrom3D pipeline (Paulsen et al., 201). Biological replicates (the two deepest ones in case there were more than two) were then used to identify highly reproducible TAD-TAD interactions using IDR2D v1.4.0 (Krismer et al., 2020) with default parameters. In particular, TAD-TAD interactions with NCHG p-value > 0.01 were first filtered out, and then the odds ratio was used as the ranking statistic for IDR analysis, with the final filter criteria being IDR p-value < 0.01. Treating significant TAD-TAD interactions as edges of a graph, cliques were identified using the max_cliques function from R library igraph v1.2.6 (Csardi et al., 2006). The over-representation of A-A vs B-B clique interactions was compared against an expected value based on the proportion of A vs B TADs across all TADs, with the identity of compartment assignment of

TADs based on having more 25 kb bins labelled as one compartment versus the other. Confidence intervals were derived from bootstrapping the set of clique interactions. The degree of TAD boundary conservation was evaluated using a permutation test, where the number of boundaries being shared across cell types was compared against a background derived from merging the list of boundaries and shuffling cell type labels. Additionally, 9 other TAD identification algorithms (Rao et al., 2014, Matthey-Doret et al., 2020, Xing et al., 2021, Levy-Leduc et al., 2014, An et al., 2019, Dali et al., 2018, Cresswell et al., 2020, Soler-Vila et al., 2020, Shin et al., 2016) were used with default parameters to validate trends observed with insulation scores, all at 50 kb resolution.

Histone mass spectrometry analysis

Single histone modification abundances are summed from their individual occurrences as well as co-occurrences (e.g., H3K27me3 = H3K27me3 + H3K27me3&H3K36me1 + H3K27me3&H3K36me2 + H3K27me3&H3K36me3). PCA of these relative abundance measures for all quantifiable H3 modifications (at least one sample exhibiting abundance >0.1%) were used as input for PCA using the prcomp function from the R library stats v4.0.3 with default parameters to assess epigenome-wide tendencies. Abundance measures were further Z-score transformed for hierarchical clustering using the hclust function from R library stats v4.0.3 with default parameters.

Normalization of epigenetic signals

Histone mass spectrometry-derived abundances were used to scale corresponding ChIP-seq tracks by directly multiplying the library-size normalized (counts/million mapped reads) values with the relative abundance. For targets lacking mass spectrometry data (e.g., transcription factors), we applied S3V2-IDEAS commit b7cc2d5 (Xiang et al., 2021) to derive scaling factors using default parameters at a bin size of 200 bp.

ATAC-seq analysis

The union set of peaks across all cell types was taken as features against which reads were counted, and the resulting count matrix was further normalized via FPKM to account for variations in peak widths

and sequence depth. PCA was then performed on the 10000 most variable peaks to assess global accessome trends. The 2000 most variable peaks were additionally clustered by using the hclust function from R library stats v4.0.3 with default parameters; visual inspection of the resulting dendrogram suggested 7 as a reasonable number of clusters for cutting. Global openness was assessed by first fitting a two-component gaussian mixture model to the log2(FPKM + 1) distribution across the union peak set and then assessing the number of sites exceeding the higher component's mean versus those below the lower component's mean.

Motif enrichment analysis

Over-representation of known transcription factor motifs was assessed in an ensemble manner by combining multiple frameworks (e.g., HOMER, MEME) as implemented in GimmeMotifs v0.15.3 (Bruse et al., 2018) using default options. Differential enrichment of motifs between different region sets (e.g., open sites with distinct chromatin states) was examined using the maelstrom module of GimmeMotifs with default options.

Enhancer-promoter pairing

Cis-regulatory elements were associated with putative target genes using "activity-by-contact" (ABC) commit 7fd69b0 (Fulco et al., 2019). KR-normalized matrices at 5 kb resolution were combined with H3K27ac and ATAC-seq data to calculate ABC scores quantile-normalized to K562 data, after which a stringent cut-off of 0.02 was applied — corresponding to 70% recall and 60% precision based on previous CRISPRi-FlowFISH validation (Fulco et al., 2019). Alternatively, enhancer-promoter pairs identified based on co-regulated NET-CAGE tag clusters, as described above, were assessed for their degree of coordination. Specifically, a permutation test was used to compare the number of co-expressed (>1 TPM in a specific cell type) enhancer-promoter pairs versus that of background sets generated by sampling from all tag clusters. Differential interactions between enhancer-promoter pairs identified by ABC scores were investigated using R library HiCDCPlus v0.99.12 (Sahin et al., 2021) using default parameters at 10 kb resolution. The degree of coordinated differential promoter interaction and differential expression was quantified through the application of RRHO2 v1.0 (Cahill et al., 2018) to

gene lists ranked by DESeq2 test statistics; for promoters involved in multiple ABC E-P pairs, the mean test statistic was used for ranking.

ChIP-seq analysis

The domain size distributions of histone modifications were determined using MCORE (Molitor et al., 2017) with the maximum shift size set to the chromosome lengths and other parameters kept at their defaults. Resulting cross-correlation values between replicates were averaged using a cubic spline via the function smooth.spline from R library stats v4.0.3 with default parameters, after which Gardner transformations were applied to decompose the decay spectrum into component exponential functions corresponding to different domain sizes and quantify their contribution. Differential ChIP-seq analysis was performed using DiffBind (Ross-Innes et al., 2012) for targets with narrow signals and csaw for broad ones. DiffBind v3.0.13 was applied with union peak sets resized to 500 bp around the summits of MACS peak calls and other options kept at their defaults using both edgeR (Robinson et al., 2010) and DESeq2 (Love et al., 2014) for the underlying statistical framework, after which only concordant results were retained (e.g., up-regulated with both methods). Unless otherwise stated, "constitutive"/"conserved" peaks refer to the intersection of MACS peak calls between cell types. csaw v1.24.3 (Lun et al., 2016) was applied with default settings with edgeR as the underlying statistical framework at both a coarse (2 kbp windows with a 500 bp step size for H3K27me3; 10 kbp windows with a 2 kbp step size for H3K9me2) and a fine resolution (500 bp windows with a 100 bp step size for H3K27me3; 1 kb windows with a 200 bp step size for H3K9me2), after which the results were consolidated, allowing for a gap size of 100 bp. The domain expansion/contraction kinetics were characterized using ChromTime commit a332dbb (Fiziev et al., 2018) with default settings in broad mode, with a post-hoc filter applied to exclude regions <10 kb. Aggregate plots were generated using the module computeMatrix from deepTools v3.5.0 with default options, in scale-regions mode for domains and reference-point mode for focal features such as peaks. Differential H3K9me3 promoters (+/- 1kb from TSS) were defined using the mass spectrometry-derived coefficient-normalized log2-transformed FPKM signal with the threshold (log2(FPKM) >1 in either cell type and log2(FPKM) difference >1).

Epigenome-based clustering of cis-regulatory elements

The log2(enrichment over input) values of ChIP-seq signals and log2(FPKM + 1) for ATAC-seq signals in promoters (+/- 2.5kb from TSS) or reproducible accessible sites identified using ChromA v2.1.1 (Gabitto et al., 2020) (resized to +/- 500 bp surrounding the summit) were used as input for dimension reduction through UMAP v0.5.1 (Mcinnes et al., 2018) and subsequently clustered through HDBSCAN v0.8.27 (Campello et al., 2013). For UMAP, manhattan distances were used for promoters and correlation distances for open sites; a grid search over min_dist of [0.0, 0.01, 0.1], n_neighbors of [15, 30, 50] and n_components of 2–10 were all subjected to HDBSCAN clustering to identify epigenetically distinct clusters via visual inspection. For HDBSCAN, a grid search over min_cluster_size and min_samples over [50, 100, 200, 500, 1000, 2000, 5000, 10000] were tested. In a semi-supervised fashion, individual clusters were isolated and subjected to further sub-clustering until the embedding no longer exhibited distinct segregation of data points for any individual epigenetic signal.

Pathway enrichment analysis

Associations of specific gene lists with particular biological pathways were evaluated using the gost function from R library gprofiler2 v0.2.0 (Kolberg et al., 2020) with default options. The enrichment of pathways towards the extremes of ranked gene lists, on the other hand, was assessed using the fgseaMultilevel function from R library fgsea 1.17.1 (Korotkevich et al., 2021) with the boundary parameter eps set to 0 and others kept at their default values; redundant terms were collapsed by using collapsePathways with an adjusted p-value threshold of 0.05. To obtain gene lists ranked by multiple metrics (e.g., differential expression and promoter interaction), the mean test statistic was used to rank genes independently for each metric, and an aggregated ranking was then obtained using p-values produced by the aggregateRanks function from R library RobustRankAggreg v1.1 (Kolde et al., 2012).

Overlap enrichment analysis

The overlap between genomic regions and annotated intervals was examined using Fisher's exact tests as implemented in the R library LOLA v1.19.1 (Sheffield et al., 2016). Ensembl Regulatory build annotations v20180516 were sourced directly from Ensembl; RepeatMasker annotations were obtained

from the rmsk table hosted on the UCSC Genome Browser. ENCODE cCRE annotations were downloaded from SCREEN v13 (http://screen.encodeproject.org/).

Pile-up analysis

Interaction between specific regions (e.g., promoters of a similar chromatin state) were quantified using the ObsExpSnipper function from cooltools v0.4.0 with default parameters and using the aforementioned diagonal-wise expected values. For pile-up of domains (e.g., TADs or broad H3K9me3 domains) rescaled to the same size, coolpup.py v0.9.7 (Flyamer et al., 2020) was used with the option --rescale and optionally --local when assessing on-diagonal patterns, and with all other options kept at their defaults.

Lamin B1-related analysis

EDD v1.1.19 (Lund et al., 2014) was used to identify lamina-associated domains from lamin B1 ChIP-seq with a bin size of 10 kb, gap penalty set to 20, and all others options kept at their defaults. LADetector v8122016 (Harr et al., 2015) was used instead for lamin B1 DamID, with a bin size of 10 kb and max dip size of 25 kb. Generalized linear models with 50 basis functions were used to visualize chromosome-scale patterns using REML for smoothness selection as implemented in the gam function of R library mgcv v1.8-31 (Wood et al., 2011).

Partially methylated domains-related analysis

PMDs were identified by calculating median mCG/CG values using a 100 kb sliding window and identifying those falling below 85%; after merging adjacent regions, those wider than 500 kb were called as PMDs. The binary status of whether a bin falls within a GSC PMD or not was modelled using three methods: (1) gradient boosted tree (gbm), (2) neural network (nnet), and (3) elastic net (glmnet), each with 10x10 cross validation using a 70/30 train/test split as implemented in the R library caret v6.0-86 (Kuhn et al., 2008}. Model performance for predicting PMDs was then assessed on the held-out test set using the roc function from R library pROC v1.16.2 (Robin et al., 2011).

Mapping to the Y chromosome

Ampliconic sequences on the murine Y chromosome were retrieved from an earlier report describing its assembly (Soh et al., 2014), and were directly used as the reference for alignment. Otherwise, data was processed as described in "PBAT data processing".

Statistical considerations

P-values were mapped to symbols as follows: 0 (****) 0.0001 (***) 0.001 (**) 0.01 (*) 0.05 (ns) 1. Wilcoxon rank-sum tests and T-tests were carried out using the functions wilcox.test and t.test, respectively, from the R library stats v4.0.3. Bootstrap confidence intervals were computed using the function boot with 100000 replicates followed by boot.ci from the R library boot 1.3-28 (Davison et al., 1997) using default options. For all box plots (i.e., box-and-whiskers plots), the lower and upper hinge correspond to the first and third quartile, and the upper whiskers extend to the largest value % 1.5 * IQR and vice versa for the lower whiskers.

Data Availability

The accession number for all the sequencing data generated in this study is GSE183828 (the GEO database). Scripts used to generate the presented results and additional raw data underlying figures are available at https://github.com/bhu/germ_nucleome.

REFERENCES

Abdennur N, Mirny LA (2020) Cooler: scalable storage for Hi-C data and other genomically labeled arrays. Bioinformatics 36: 311-316

Alavattam KG, Maezawa S, Sakashita A, Khoury H, Barski A, Kaplan N, Namekawa SH (2019) Attenuated chromatin compartmentalization in meiosis and its maturation in sperm development. Nat Struct Mol Biol 26: 175-184

Amemiya HM, Kundaje A, Boyle AP (2019) The ENCODE Blacklist: Identification of Problematic Regions of the Genome. Scientific reports 9: 9354

An L, Yang T, Yang J, Nuebler J, Xiang G, Hardison RC, Li Q, Zhang Y (2019) OnTAD: hierarchical domain structure reveals the divergence of activity among TADs and boundaries. Genome Biol 20: 282

Anton T, Bultmann S, Leonhardt H, Markaki Y (2014) Visualization of specific DNA sequences in living mouse embryonic stem cells with a programmable fluorescent CRISPR/Cas system. Nucleus 5: 163-72

Battulin N, Fishman VS, Mazur AM, Pomaznoy M, Khabarova AA, Afonnikov DA, Prokhortchouk EB, Serov OL (2015) Comparison of the three-dimensional organization of sperm and fibroblast genomes using the Hi-C approach. Genome Biol 16: 77

Belaghzal H, Dekker J, Gibcus JH (2017) Hi-C 2.0: An optimized Hi-C procedure for high-resolution genome-wide mapping of chromosome conformation. Methods 123: 56-65

Bian Q, Khanna N, Alvikas J, Belmont AS (2013) beta-Globin cis-elements determine differential nuclear targeting through epigenetic modifications. J Cell Biol 203: 767-83

Bonev B, Mendelson Cohen N, Szabo Q, Fritsch L, Papadopoulos GL, Lubling Y, Xu X, Lv X, Hugnot JP, Tanay A, Cavalli G (2017) Multiscale 3D Genome Rewiring during Mouse Neural Development. Cell 171: 557-572 e24

Borgel J, Guibert S, Li Y, Chiba H, Schubeler D, Sasaki H, Forne T, Weber M (2010) Targets and dynamics of promoter DNA methylation during early mouse development. Nat Genet 42: 1093-100

Boroviak T, Loos R, Bertone P, Smith A, Nichols J (2014) The ability of inner-cell-mass cells to self-renew as embryonic stem cells is acquired following epiblast specification. Nat Cell Biol 16: 516-28

Bourque G, Leong B, Vega VB, Chen X, Lee YL, Srinivasan KG, Chew JL, Ruan Y, Wei CL, Ng HH, Liu ET (2008) Evolution of the mammalian transcription factor binding repertoire via transposable elements. Genome Res 18: 1752-62

Bruse N, Heeringen SJV (2018) GimmeMotifs: an analysis framework for transcription factor motif analysis. bioRxiv: https://doi.org/10.1101/474403

Buenrostro JD, Giresi PG, Zaba LC, Chang HY, Greenleaf WJ (2013) Transposition of native chromatin for fast and sensitive epigenomic profiling of open chromatin, DNA-binding proteins and nucleosome position. Nat Methods 10: 1213-8

Cahill KM, Huo Z, Tseng GC, Logan RW, Seney ML (2018) Improved identification of concordant and discordant gene expression signatures using an updated rank-rank hypergeometric overlap approach. Scientific reports 8: 9588

Campello R, Moulavi D, Sander J (2013) Density-Based Clustering Based on Hierarchical Density Estimates. In Advances in Knowledge Discovery and Data Mining, pp 160-172. Springer

Chen S, Zhou Y, Chen Y, Gu J (2018) fastp: an ultra-fast all-in-one FASTQ preprocessor. Bioinformatics 34: i884-i890

Chen X, Yammine S, Shi C, Tark-Dame M, Gondor A, Ohlsson R (2014) The visualization of large organized chromatin domains enriched in the H3K9me2 mark within a single chromosome in a single cell. Epigenetics 9: 1439-45

Corces MR, Trevino AE, Hamilton EG, Greenside PG, Sinnott-Armstrong NA, Vesuna S, Satpathy AT, Rubin AJ, Montine KS, Wu B, Kathiria A, Cho SW, Mumbach MR, Carter AC, Kasowski M, Orloff LA, Risca VI, Kundaje A, Khavari PA, Montine TJ et al. (2017) An improved ATAC-seq protocol reduces background and enables interrogation of frozen tissues. Nat Methods 14: 959-962

Cresswell KG, Stansfield JC, Dozmorov MG (2020) SpectralTAD: an R package for defining a hierarchy of topologically associated domains using spectral clustering. BMC Bioinformatics 21: 319

Csardi G, Nepusz T (2006) The igraph software package for complex network research. InterJournal, Complex Systems 1695

Cuadrado A, Gimenez-Llorente D, Kojic A, Rodriguez-Corsino M, Cuartero Y, Martin-Serrano G,

Gomez-Lopez G, Marti-Renom MA, Losada A (2019) Specific Contributions of Cohesin-SA1 and Cohesin-SA2 to TADs and Polycomb Domains in Embryonic Stem Cells. Cell reports 27: 3500-3510 e4

D'Oliveira Albanus R, Kyono Y, Hensley J, Varshney A, Orchard P, Kitzman JO, Parker SCJ (2021) Chromatin information content landscapes inform transcription factor and DNA interactions. Nat Commun 12: 1307

Dali R, Bourque G, Blanchette M (2018) RobusTAD: A Tool for Robust Annotation of Topologically Associating Domain Boundaries. bioRxiv: https://doi.org/10.1101/293175

Davison AC, Hinkley DV (1997) Boostrap methods and their application. Cambridge University Press

Dekker J, Belmont AS, Guttman M, Leshyk VO, Lis JT, Lomvardas S, Mirny LA, O'Shea CC, Park PJ, Ren B, Politz JCR, Shendure J, Zhong S, Network DN (2017) The 4D nucleome project. Nature 549: 219-226

Di Giammartino DC, Kloetgen A, Polyzos A, Liu Y, Kim D, Murphy D, Abuhashem A, Cavaliere P, Aronson B, Shah V, Dephoure N, Stadtfeld M, Tsirigos A, Apostolou E (2019) KLF4 is involved in the organization and regulation of pluripotency-associated three-dimensional enhancer networks. Nat Cell Biol 21: 1179-1190

Dimmick MC, Lee LJ, Frey BJ HiCSR: a Hi-C super-resolution framework for producing highly realistic contact maps. Bioinformatics

Dobin A, Davis CA, Schlesinger F, Drenkow J, Zaleski C, Jha S, Batut P, Chaisson M, Gingeras TR (2013) STAR: ultrafast universal RNA-seq aligner. Bioinformatics 29: 15-21

Du Z, Zheng H, Huang B, Ma R, Wu J, Zhang X, He J, Xiang Y, Wang Q, Li Y, Ma J, Zhang X, Zhang K, Wang Y, Zhang MQ, Gao J, Dixon JR, Wang X, Zeng J, Xie W (2017) Allelic reprogramming of 3D chromatin architecture during early mammalian development. Nature 547: 232-235

Du Z, Zheng H, Kawamura YK, Zhang K, Gassler J, Powell S, Xu Q, Lin Z, Xu K, Zhou Q, Ozonov EA, Veron N, Huang B, Li L, Yu G, Liu L, Au Yeung WK, Wang P, Chang L, Wang Q et al. (2020) Polycomb Group Proteins Regulate Chromatin Architecture in Mouse Oocytes and Early Embryos. Mol Cell 77: 825-839 e7

Durand NC, Shamim MS, Machol I, Rao SS, Huntley MH, Lander ES, Aiden EL (2016) Juicer Provides

a One-Click System for Analyzing Loop-Resolution Hi-C Experiments. Cell Syst 3: 95-8

Evans EP, Ford CE, Lyon MF (1977) Direct evidence of the capacity of the XY germ cell in the mouse to become an oocyte. Nature 267: 430-1

Farhangdoost N, Horth C, Hu B, Bareke E, Chen X, Li Y, Coradin M, Garcia BA, Lu C, Majewski J (2021) Chromatin dysregulation associated with NSD1 mutation in head and neck squamous cell carcinoma. Cell reports 34: 108769

Fiziev P, Ernst J (2018) ChromTime: modeling spatio-temporal dynamics of chromatin marks. Genome Biol 19: 109

Flyamer IM, Gassler J, Imakaev M, Brandao HB, Ulianov SV, Abdennur N, Razin SV, Mirny LA, Tachibana-Konwalski K (2017) Single-nucleus Hi-C reveals unique chromatin reorganization at oocyte-to-zygote transition. Nature 544: 110-114

Flyamer IM, Illingworth RS, Bickmore WA (2020) Coolpup.py: versatile pile-up analysis of Hi-C data. Bioinformatics 36: 2980-2985

Fukuda K, Shimura C, Miura H, Tanigawa A, Suzuki T, Dohmae N, Hiratani I, Shinkai Y (2021) Regulation of mammalian 3D genome organization and histone H3K9 dimethylation by H3K9 methyltransferases. Commun Biol 4: 571

Fulco CP, Nasser J, Jones TR, Munson G, Bergman DT, Subramanian V, Grossman SR, Anyoha R, Doughty BR, Patwardhan TA, Nguyen TH, Kane M, Perez EM, Durand NC, Lareau CA, Stamenova EK, Aiden EL, Lander ES, Engreitz JM (2019) Activity-by-contact model of enhancer-promoter regulation from thousands of CRISPR perturbations. Nat Genet 51: 1664-1669

Gabitto MI, Rasmussen A, Wapinski O, Allaway K, Carriero N, Fishell GJ, Bonneau R (2020) Characterizing chromatin landscape from aggregate and single-cell genomic assays using flexible duration modeling. Nat Commun 11: 747

Gorkin DU, Barozzi I, Zhao Y, Zhang Y, Huang H, Lee AY, Li B, Chiou J, Wildberg A, Ding B, Zhang B, Wang M, Strattan JS, Davidson JM, Qiu Y, Afzal V, Akiyama JA, Plajzer-Frick I, Novak CS, Kato M et al. (2020) An atlas of dynamic chromatin landscapes in mouse fetal development. Nature 583: 744-751

Griswold MD (2016) Spermatogenesis: The Commitment to Meiosis. Physiol Rev 96: 1-17

Guelen L, Pagie L, Brasset E, Meuleman W, Faza MB, Talhout W, Eussen BH, de Klein A, Wessels L, de Laat W, van Steensel B (2008) Domain organization of human chromosomes revealed by mapping of nuclear lamina interactions. Nature 453: 948-51

Guenatri M, Bailly D, Maison C, Almouzni G (2004) Mouse centric and pericentric satellite repeats form distinct functional heterochromatin. J Cell Biol 166: 493-505 Gurdon JB, Wilmut I (2011) Nuclear transfer to eggs and oocytes. Cold Spring Harb Perspect Biol 3

Haberle V, Forrest AR, Hayashizaki Y, Carninci P, Lenhard B (2015) CAGEr: precise TSS data retrieval and high-resolution promoterome mining for integrative analyses. Nucleic Acids Res 43: e51

Hansen KD, Timp W, Bravo HC, Sabunciyan S, Langmead B, McDonald OG, Wen B, Wu H, Liu Y, Diep D, Briem E, Zhang K, Irizarry RA, Feinberg AP (2011) Increased methylation variation in epigenetic domains across cancer types. Nat Genet 43: 768-75

Harr JC, Luperchio TR, Wong X, Cohen E, Wheelan SJ, Reddy KL (2015) Directed targeting of chromatin to the nuclear lamina is mediated by chromatin state and A-type lamins. J Cell Biol 208: 33-52

Hayashi K, Ohta H, Kurimoto K, Aramaki S, Saitou M (2011) Reconstitution of the mouse germ cell specification pathway in culture by pluripotent stem cells. Cell 146: 519-32

Hirabayashi S, Bhagat S, Matsuki Y, Takegami Y, Uehata T, Kanemaru A, Itoh M, Shirakawa K, Takaori-Kondo A, Takeuchi O, Carninci P, Katayama S, Hayashizaki Y, Kere J, Kawaji H, Murakawa Y (2019) NET-CAGE characterizes the dynamics and topology of human transcribed cis-regulatory elements. Nat Genet 51: 1369-1379

Hon GC, Hawkins RD, Caballero OL, Lo C, Lister R, Pelizzola M, Valsesia A, Ye Z, Kuan S, Edsall LE, Camargo AA, Stevenson BJ, Ecker JR, Bafna V, Strausberg RL, Simpson AJ, Ren B (2012) Global DNA hypomethylation coupled to repressive chromatin domain formation and gene silencing in breast cancer. Genome Res 22: 246-58

Ishikura Y, Ohta H, Sato T, Murase Y, Yabuta Y, Kojima Y, Yamashiro C, Nakamura T, Yamamoto T, Ogawa T, Saitou M (2021) In vitro reconstitution of the whole male germ-cell development from mouse pluripotent stem cells. Cell Stem Cell 28: 2167-2179 e9

Ishikura Y, Yabuta Y, Ohta H, Hayashi K, Nakamura T, Okamoto I, Yamamoto T, Kurimoto K, Shirane K, Sasaki H, Saitou M (2016) In Vitro Derivation and Propagation of Spermatogonial Stem Cell Activity

from Mouse Pluripotent Stem Cells. Cell reports 17: 2789-2804

Jameson SA, Natarajan A, Cool J, DeFalco T, Maatouk DM, Mork L, Munger SC, Capel B (2012) Temporal transcriptional profiling of somatic and germ cells reveals biased lineage priming of sexual fate in the fetal mouse gonad. PLoS Genet 8: e1002575

Johnstone SE, Reyes A, Qi Y, Adriaens C, Hegazi E, Pelka K, Chen JH, Zou LS, Drier Y, Hecht V, Shoresh N, Selig MK, Lareau CA, Iyer S, Nguyen SC, Joyce EF, Hacohen N, Irizarry RA, Zhang B, Aryee MJ et al. (2020) Large-Scale Topological Changes Restrain Malignant Progression in Colorectal Cancer. Cell 182: 1474-1489 e23

Kanatsu-Shinohara M, Inoue K, Lee J, Yoshimoto M, Ogonuki N, Miki H, Baba S, Kato T, Kazuki Y, Toyokuni S, Toyoshima M, Niwa O, Oshimura M, Heike T, Nakahata T, Ishino F, Ogura A, Shinohara T (2004) Generation of pluripotent stem cells from neonatal mouse testis. Cell 119: 1001-12

Kanatsu-Shinohara M, Ogonuki N, Inoue K, Miki H, Ogura A, Toyokuni S, Shinohara T (2003) Long-term proliferation in culture and germline transmission of mouse male germline stem cells. Biol Reprod 69: 612-6

Karimi MM, Goyal P, Maksakova IA, Bilenky M, Leung D, Tang JX, Shinkai Y, Mager DL, Jones S, Hirst M, Lorincz MC (2011) DNA methylation and SETDB1/H3K9me3 regulate predominantly distinct sets of genes, retroelements, and chimeric transcripts in mESCs. Cell Stem Cell 8: 676-87

Ke Y, Xu Y, Chen X, Feng S, Liu Z, Sun Y, Yao X, Li F, Zhu W, Gao L, Chen H, Du Z, Xie W, Xu X, Huang X, Liu J (2017) 3D Chromatin Structures of Mature Gametes and Structural Reprogramming during Mammalian Embryogenesis. Cell 170: 367-381 e20

Keough KC, Shah PP, Gjoni K, Santini GT, Wickramasinghe NM, Dundes CE, Karnay A, Chen A, Salomon REA, Walsh PJ, Nguyen SC, Whalen S, Joyce EF, Loh KM, Dubois N, Pollard KS, Jain R (2021) An atlas of lamina-associated chromatin across twelve human cell types reveals an intermediate chromatin subtype. bioRxiv

Kolberg L, Raudvere U, Kuzmin I, Vilo J, Peterson H (2020) gprofiler2 -- an R package for gene list functional enrichment analysis and namespace conversion toolset g:Profiler. F1000Res 9

Kolde R, Laur S, Adler P, Vilo J (2012) Robust rank aggregation for gene list integration and meta-analysis. Bioinformatics 28: 573-80

Korotkevich G, Sukhov V, Budin N, Shpak B, Artyomov MN, Sergushichev A Fast gene set enrichment analysis.

Krismer K, Guo Y, Gifford DK (2020) IDR2D identifies reproducible genomic interactions. Nucleic Acids Res 48: e31

Krueger F, Andrews SR (2011) Bismark: a flexible aligner and methylation caller for Bisulfite-Seq applications. Bioinformatics 27: 1571-2

Krueger F, James F, Ewels P, Afyounian E, Schuster-Boeckler B (2021) FelixKrueger/TrimGalore: v0.6.7. Zenodo.

Kruse K, Hug CB, Vaquerizas JM (2020) FAN-C: a feature-rich framework for the analysis and visualisation of chromosome conformation capture data. Genome Biol 21: 303

Kubo N, Toh H, Shirane K, Shirakawa T, Kobayashi H, Sato T, Sone H, Sato Y, Tomizawa S, Tsurusaki Y, Shibata H, Saitsu H, Suzuki Y, Matsumoto N, Suyama M, Kono T, Ohbo K, Sasaki H (2015) DNA methylation and gene expression dynamics during spermatogonial stem cell differentiation in the early postnatal mouse testis. BMC Genomics 16: 624

Kuhn M (2008) Building Predictive Models in R Using the caret Package. J Stat Soft 28: 1-26

Kurimoto K, Yabuta Y, Hayashi K, Ohta H, Kiyonari H, Mitani T, Moritoki Y, Kohri K, Kimura H, Yamamoto T, Katou Y, Shirahige K, Saitou M (2015) Quantitative Dynamics of Chromatin Remodeling during Germ Cell Specification from Mouse Embryonic Stem Cells. Cell Stem Cell 16: 517-32

Langmead B, Salzberg SL (2012) Fast gapped-read alignment with Bowtie 2. Nat Methods 9: 357-9

Lee HJ, Hore TA, Reik W (2014) Reprogramming the methylome: erasing memory and creating diversity. Cell Stem Cell 14: 710-9

Lee TI, Johnstone SE, Young RA (2006) Chromatin immunoprecipitation and microarray-based analysis of protein location. Nature protocols 1: 729-48

Levy-Leduc C, Delattre M, Mary-Huard T, Robin S (2014) Two-dimensional segmentation for analyzing Hi-C data. Bioinformatics 30: i386-92

Li H, Handsaker B, Wysoker A, Fennell T, Ruan J, Homer N, Marth G, Abecasis G, Durbin R, Genome

Project Data Processing S (2009) The Sequence Alignment/Map format and SAMtools. Bioinformatics 25: 2078-9

Lin D, Sanders J, Noble WS (2021) HiCRep.py : Fast comparison of Hi-C contact matrices in Python. Bioinformatics

Lister R, Pelizzola M, Dowen RH, Hawkins RD, Hon G, Tonti-Filippini J, Nery JR, Lee L, Ye Z, Ngo QM, Edsall L, Antosiewicz-Bourget J, Stewart R, Ruotti V, Millar AH, Thomson JA, Ren B, Ecker JR (2009) Human DNA methylomes at base resolution show widespread epigenomic differences. Nature 462: 315-22

Liu Y, Nanni L, Sungalee S, Zufferey M, Tavernari D, Mina M, Ceri S, Oricchio E, Ciriello G (2021) Systematic inference and comparison of multi-scale chromatin sub-compartments connects spatial organization to cell phenotypes. Nat Commun 12: 2439

Love MI, Huber W, Anders S (2014) Moderated estimation of fold change and dispersion for RNA-seq data with DESeq2. Genome Biol 15: 550

Lun AT, Smyth GK (2016) csaw: a Bioconductor package for differential binding analysis of ChIP-seq data using sliding windows. Nucleic Acids Res 44: e45

Lund E, Oldenburg AR, Collas P (2014) Enriched domain detector: a program for detection of wide genomic enrichment domains robust against local variations. Nucleic Acids Res 42: e92

Luo Z, Wang X, Jiang H, Wang R, Chen J, Chen Y, Xu Q, Cao J, Gong X, Wu J, Yang Y, Li W, Han C, Cheng CY, Rosenfeld MG, Sun F, Song X (2020) Reorganized 3D Genome Structures Support Transcriptional Regulation in Mouse Spermatogenesis. iScience 23: 101034

Marchal C, Singh N, Corso-Díaz X, Swaroop A (2020) HiCRes: a computational method to estimate and predict the resolution of HiC libraries. bioRxiv: https://doi.org/10.1101/2020.09.22.307967

Marks H, Kalkan T, Menafra R, Denissov S, Jones K, Hofemeister H, Nichols J, Kranz A, Francis Stewart A, Smith A, Stunnenberg HG (2012) The transcriptional and epigenomic foundations of ground state pluripotency. Cell 149: 590-604

Martin M (2011) Cutadapt removes adapter sequences from high-throughput sequencing reads. EMBnetjournal 17: 10

Matthey-Doret C, Baudry L, Breuer A, Montagne R, Guiglielmoni N, Scolari V, Jean E, Campeas A, Chanut PH, Oriol E, Meot A, Politis L, Vigouroux A, Moreau P, Koszul R, Cournac A (2020) Computer vision for pattern detection in chromosome contact maps. Nat Commun 11: 5795

Mcinnes L, Healy J, Saul N, Großberger L (2018) UMAP: Uniform Manifold Approximation and Projection. Journal of Open Source Software 3: 861

Miura K (2020) Measurements of Intensity Dynamics at the Periphery of the Nucleus. In Bioimage Data Analysis Workflows, pp 9-32. Springer International Publishing

Miyauchi H, Ohta H, Nagaoka S, Nakaki F, Sasaki K, Hayashi K, Yabuta Y, Nakamura T, Yamamoto T, Saitou M (2017) Bone morphogenetic protein and retinoic acid synergistically specify female germ-cell fate in mice. EMBO J 36: 3100-3119

Mochizuki K, Sharif J, Shirane K, Uranishi K, Bogutz AB, Janssen SM, Suzuki A, Okuda A, Koseki H, Lorincz MC (2021) Repression of germline genes by PRC1.6 and SETDB1 in the early embryo precedes DNA methylation-mediated silencing. Nat Commun 12: 7020

Molitor J, Mallm JP, Rippe K, Erdel F (2017) Retrieving Chromatin Patterns from Deep Sequencing Data Using Correlation Functions. Biophys J 112: 473-490

Murata M, Nishiyori-Sueki H, Kojima-Ishiyama M, Carninci P, Hayashizaki Y, Itoh M (2014) Detecting expressed genes using CAGE. Methods Mol Biol 1164: 67-85

Nagaoka S, I., Nakaki F, Miyauchi H, Nosaka Y, Yabuta Y, Kurimoto K, Hayashi K, Nakamura T, Yamamoto T, Saitou M (2020) ZGLP1 is a determinant for the oogenic fate in mice. Science 367

Ohta H, Kurimoto K, Okamoto I, Nakamura T, Yabuta Y, Miyauchi H, Yamamoto T, Okuno Y, Hagiwara M, Shirane K, Sasaki H, Saitou M (2017) In vitro expansion of mouse primordial germ cell-like cells recapitulates an epigenetic blank slate. EMBO J 36: 1888-1907

Ohta H, Yabuta Y, Kurimoto K, Nakamura T, Murase Y, Yamamoto T, Saitou M (2021) Cyclosporin A and FGF signaling support the proliferation/survival of mouse primordial germ cell-like cells in vitrodagger. Biol Reprod 104: 344-360

Ohta H, Yomogida K, Yamada S, Okabe M, Nishimune Y (2000) Real-time observation of transplanted 'green germ cells': proliferation and differentiation of stem cells. Dev Growth Differ 42: 105-12

Okamoto I, Arnaud D, Le Baccon P, Otte AP, Disteche CM, Avner P, Heard E (2005) Evidence for de novo imprinted X-chromosome inactivation independent of meiotic inactivation in mice. Nature 438: 369-73

Patel L, Kang R, Rosenberg SC, Qiu Y, Raviram R, Chee S, Hu R, Ren B, Cole F, Corbett KD (2019) Dynamic reorganization of the genome shapes the recombination landscape in meiotic prophase. Nat Struct Mol Biol 26: 164-174

Patro R, Duggal G, Love MI, Irizarry RA, Kingsford C (2017) Salmon provides fast and bias-aware quantification of transcript expression. Nat Methods 14: 417-419

Paulsen J, Liyakat Ali TM, Nekrasov M, Delbarre E, Baudement MO, Kurscheid S, Tremethick D, Collas P (2019) Long-range interactions between topologically associating domains shape the four-dimensional genome during differentiation. Nat Genet 51: 835-843

Paulsen J, Sekelja M, Oldenburg AR, Barateau A, Briand N, Delbarre E, Shah A, Sorensen AL, Vigouroux C, Buendia B, Collas P (2017) Chrom3D: three-dimensional genome modeling from Hi-C and nuclear lamin-genome contacts. Genome Biol 18: 21

Peric-Hupkes D, Meuleman W, Pagie L, Bruggeman SW, Solovei I, Brugman W, Graf S, Flicek P, Kerkhoven RM, van Lohuizen M, Reinders M, Wessels L, van Steensel B (2010) Molecular maps of the reorganization of genome-nuclear lamina interactions during differentiation. Mol Cell 38: 603-13

Poleshko A, Shah PP, Gupta M, Babu A, Morley MP, Manderfield LJ, Ifkovits JL, Calderon D, Aghajanian H, Sierra-Pagan JE, Sun Z, Wang Q, Li L, Dubois NC, Morrisey EE, Lazar MA, Smith CL, Epstein JA, Jain R (2017) Genome-Nuclear Lamina Interactions Regulate Cardiac Stem Cell Lineage Restriction. Cell 171: 573-587 e14

Poleshko A, Smith CL, Nguyen SC, Sivaramakrishnan P, Wong KG, Murray JI, Lakadamyali M, Joyce EF, Jain R, Epstein JA (2019) H3K9me2 orchestrates inheritance of spatial positioning of peripheral heterochromatin through mitosis. Elife 8

Polovnikov K, Belan S, Imakaev M, Brand HB, A. ML (2022) Fractal polymer with loops recapitulates key features of chromosome organization. bioRxiv

Quinlan AR, Hall IM (2010) BEDTools: a flexible suite of utilities for comparing genomic features. Bioinformatics 26: 841-2

Ramirez F, Ryan DP, Gruning B, Bhardwaj V, Kilpert F, Richter AS, Heyne S, Dundar F, Manke T (2016) deepTools2: a next generation web server for deep-sequencing data analysis. Nucleic Acids Res 44: W160-5

Rao SS, Huntley MH, Durand NC, Stamenova EK, Bochkov ID, Robinson JT, Sanborn AL, Machol I, Omer AD, Lander ES, Aiden EL (2014) A 3D map of the human genome at kilobase resolution reveals principles of chromatin looping. Cell 159: 1665-80

Robin X, Turck N, Hainard A, Tiberti N, Lisacek F, Sanchez JC, Muller M (2011) pROC: an open-source package for R and S+ to analyze and compare ROC curves. BMC Bioinformatics 12: 77

Robinson MD, McCarthy DJ, Smyth GK (2010) edgeR: a Bioconductor package for differential expression analysis of digital gene expression data. Bioinformatics 26: 139-40

Robson MI, de Las Heras JI, Czapiewski R, Le Thanh P, Booth DG, Kelly DA, Webb S, Kerr ARW, Schirmer EC (2016) Tissue-Specific Gene Repositioning by Muscle Nuclear Membrane Proteins Enhances Repression of Critical Developmental Genes during Myogenesis. Mol Cell 62: 834-847

Ross-Innes CS, Stark R, Teschendorff AE, Holmes KA, Ali HR, Dunning MJ, Brown GD, Gojis O, Ellis IO, Green AR, Ali S, Chin SF, Palmieri C, Caldas C, Carroll JS (2012) Differential oestrogen receptor binding is associated with clinical outcome in breast cancer. Nature 481: 389-93

Sahin M, Wong W, Zhan Y, Van Deynze K, Koche R, Leslie CS (2021) HiC-DC+ enables systematic 3D interaction calls and differential analysis for Hi-C and HiChIP. Nat Commun 12: 3366

Saitou M, Hayashi K (2021) Mammalian in vitro gametogenesis. Science 374: eaaz6830

Salhab A, Nordstrom K, Gasparoni G, Kattler K, Ebert P, Ramirez F, Arrigoni L, Muller F, Polansky JK, Cadenas C, J GH, Lengauer T, Manke T, Consortium D, Walter J (2018) A comprehensive analysis of 195 DNA methylomes reveals shared and cell-specific features of partially methylated domains. Genome Biol 19: 150

Sanulli S, Trnka MJ, Dharmarajan V, Tibble RW, Pascal BD, Burlingame AL, Griffin PR, Gross JD, Narlikar GJ (2019) HP1 reshapes nucleosome core to promote phase separation of heterochromatin. Nature 575: 390-394

Sasaki K, Yokobayashi S, Nakamura T, Okamoto I, Yabuta Y, Kurimoto K, Ohta H, Moritoki Y, Iwatani

C, Tsuchiya H, Nakamura S, Sekiguchi K, Sakuma T, Yamamoto T, Mori T, Woltjen K, Nakagawa M, Yamamoto T, Takahashi K, Yamanaka S et al. (2015) Robust In Vitro Induction of Human Germ Cell Fate from Pluripotent Stem Cells. Cell Stem Cell 17: 178-94

Schroeder DI, Blair JD, Lott P, Yu HO, Hong D, Crary F, Ashwood P, Walker C, Korf I, Robinson WP, LaSalle JM (2013) The human placenta methylome. Proc Natl Acad Sci U S A 110: 6037-42

Schwarzer W, Abdennur N, Goloborodko A, Pekowska A, Fudenberg G, Loe-Mie Y, Fonseca NA, Huber W, Haering CH, Mirny L, Spitz F (2017) Two independent modes of chromatin organization revealed by cohesin removal. Nature 551: 51-56

Seisenberger S, Andrews S, Krueger F, Arand J, Walter J, Santos F, Popp C, Thienpont B, Dean W, Reik W (2012) The dynamics of genome-wide DNA methylation reprogramming in mouse primordial germ cells. Mol Cell 48: 849-62

Sheffield NC, Bock C (2016) LOLA: enrichment analysis for genomic region sets and regulatory elements in R and Bioconductor. Bioinformatics 32: 587-9

Shin H, Shi Y, Dai C, Tjong H, Gong K, Alber F, Zhou XJ (2016) TopDom: an efficient and deterministic method for identifying topological domains in genomes. Nucleic Acids Res 44: e70

Shirane K, Kurimoto K, Yabuta Y, Yamaji M, Satoh J, Ito S, Watanabe A, Hayashi K, Saitou M, Sasaki H (2016) Global Landscape and Regulatory Principles of DNA Methylation Reprogramming for Germ Cell Specification by Mouse Pluripotent Stem Cells. Dev Cell 39: 87-103

Shirane K, Miura F, Ito T, Lorincz MC (2020) NSD1-deposited H3K36me2 directs de novo methylation in the mouse male germline and counteracts Polycomb-associated silencing. Nat Genet 52: 1088-1098

Sidoli S, Bhanu NV, Karch KR, Wang X, Garcia BA (2016) Complete Workflow for Analysis of Histone Post-translational Modifications Using Bottom-up Mass Spectrometry: From Histone Extraction to Data Analysis. Journal of Visualized Experiments

Soh YQ, Alfoldi J, Pyntikova T, Brown LG, Graves T, Minx PJ, Fulton RS, Kremitzki C, Koutseva N, Mueller JL, Rozen S, Hughes JF, Owens E, Womack JE, Murphy WJ, Cao Q, de Jong P, Warren WC, Wilson RK, Skaletsky H et al. (2014) Sequencing the mouse Y chromosome reveals convergent gene acquisition and amplification on both sex chromosomes. Cell 159: 800-13

Soler-Vila P, Cusco P, Farabella I, Di Stefano M, Marti-Renom MA (2020) Hierarchical chromatin organization detected by TADpole. Nucleic Acids Res 48: e39

Soneson C, Love MI, Robinson MD (2015) Differential analyses for RNA-seq: transcript-level estimates improve gene-level inferences. F1000Res 4: 1521

Spiller C, Koopman P, Bowles J (2017) Sex Determination in the Mammalian Germline. Annu Rev Genet 51: 265-285

Stadhouders R, Vidal E, Serra F, Di Stefano B, Le Dily F, Quilez J, Gomez A, Collombet S, Berenguer C, Cuartero Y, Hecht J, Filion GJ, Beato M, Marti-Renom MA, Graf T (2018) Transcription factors orchestrate dynamic interplay between genome topology and gene regulation during cell reprogramming. Nat Genet 50: 238-249

Stovner EB, Saetrom P (2019) epic2 efficiently finds diffuse domains in ChIP-seq data. Bioinformatics 35: 4392-4393

Surani MA, Hayashi K, Hajkova P (2007) Genetic and epigenetic regulators of pluripotency. Cell 128: 747-62

Tang WW, Kobayashi T, Irie N, Dietmann S, Surani MA (2016) Specification and epigenetic programming of the human germ line. Nat Rev Genet 17: 585-600

Thodberg M, Thieffry A, Vitting-Seerup K, Andersson R, Sandelin A (2019) CAGEfightR: analysis of 5'-end data using R/Bioconductor. BMC Bioinformatics 20: 487

Todd S, Todd P, McGowan SJ, Hughes JR, Kakui Y, Leymarie FF, Latham W, Taylor S (2021) CSynth: an interactive modelling and visualization tool for 3D chromatin structure. Bioinformatics 37: 951-955

Vara C, Paytuvi-Gallart A, Cuartero Y, Le Dily F, Garcia F, Salva-Castro J, Gomez HL, Julia E, Moutinho C, Aiese Cigliano R, Sanseverino W, Fornas O, Pendas AM, Heyn H, Waters PD, Marti-Renom MA, Ruiz-Herrera A (2019) Three-Dimensional Genomic Structure and Cohesin Occupancy Correlate with Transcriptional Activity during Spermatogenesis. Cell reports 28: 352-367 e9

Venev S, Abdennur N, Goloborodko A, Flyamer I, Fudenberg G, Nuebler J, Galitsyna A, Akgol B, Abraham S, Kerpedjiev P, Imakaev M (2021) open2c/cooltools: v0.4.1. Zenodo.

Wang J, Chakraborty A, Ay F (2021) dcHiC: differential compartment analysis of Hi-C datasets. bioRxiv:

https://doi.org/10.1101/2021.02.02.429297

Wang Y, Wang H, Zhang Y, Du Z, Si W, Fan S, Qin D, Wang M, Duan Y, Li L, Jiao Y, Li Y, Wang Q, Shi Q, Wu X, Xie W (2019) Reprogramming of Meiotic Chromatin Architecture during Spermatogenesis. Mol Cell 73: 547-561 e6

Wen L, Tang F (2019) Human Germline Cell Development: from the Perspective of Single-Cell Sequencing. Mol Cell 76: 320-328

Western PS, Miles DC, van den Bergen JA, Burton M, Sinclair AH (2008) Dynamic regulation of mitotic arrest in fetal male germ cells. Stem Cells 26: 339-47

Wingett S, Ewels P, Furlan-Magaril M, Nagano T, Schoenfelder S, Fraser P, Andrews S (2015) HiCUP: pipeline for mapping and processing Hi-C data. F1000Res 4: 1310 Wood SN (2011) Fast stable restricted maximum likelihood and marginal likelihood estimation of semiparametric generalized linear models. J R Statist Soc B 73: 3-36

Wutz G, Varnai C, Nagasaka K, Cisneros DA, Stocsits RR, Tang W, Schoenfelder S, Jessberger G, Muhar M, Hossain MJ, Walther N, Koch B, Kueblbeck M, Ellenberg J, Zuber J, Fraser P, Peters JM (2017) Topologically associating domains and chromatin loops depend on cohesin and are regulated by CTCF, WAPL, and PDS5 proteins. EMBO J 36: 3573-3599

Xiang G, Giardine BM, Mahony S, Zhang Y, Hardison RC (2021) S3V2-IDEAS: a package for normalizing, denoising and integrating epigenomic datasets across different cell types. Bioinformatics

Xing H, Wu Y, Zhang MQ, Chen Y (2021) Deciphering hierarchical organization of topologically associated domains through change-point testing. BMC Bioinformatics 22: 183

Yattah C, Hernandez M, Huang D, Park H, Liao W, Casaccia P (2020) Dynamic Lamin B1-Gene Association During Oligodendrocyte Progenitor Differentiation. Neurochem Res 45: 606-619

Ying QL, Wray J, Nichols J, Batlle-Morera L, Doble B, Woodgett J, Cohen P, Smith A (2008) The ground state of embryonic stem cell self-renewal. Nature 453: 519-23

Yuan ZF, Sidoli S, Marchione DM, Simithy J, Janssen KA, Szurgot MR, Garcia BA (2018) EpiProfile 2.0: A Computational Platform for Processing Epi-Proteomics Mass Spectrometry Data. J Proteome Res 17: 2533-2541

Zhang Y, Li T, Preissl S, Amaral ML, Grinstein JD, Farah EN, Destici E, Qiu Y, Hu R, Lee AY, Chee S, Ma K, Ye Z, Zhu Q, Huang H, Fang R, Yu L, Izpisua Belmonte JC, Wu J, Evans SM et al. (2019) Transcriptionally active HERV-H retrotransposons demarcate topologically associating domains in human pluripotent stem cells. Nat Genet 51: 1380-1388

Zhang Y, Liu T, Meyer CA, Eeckhoute J, Johnson DS, Bernstein BE, Nusbaum C, Myers RM, Brown M, Li W, Liu XS (2008) Model-based analysis of ChIP-Seq (MACS). Genome Biol 9: R137

Zheng H, Xie W (2019) The role of 3D genome organization in development and cell differentiation. Nat Rev Mol Cell Biol 20: 535-550

Figure 1

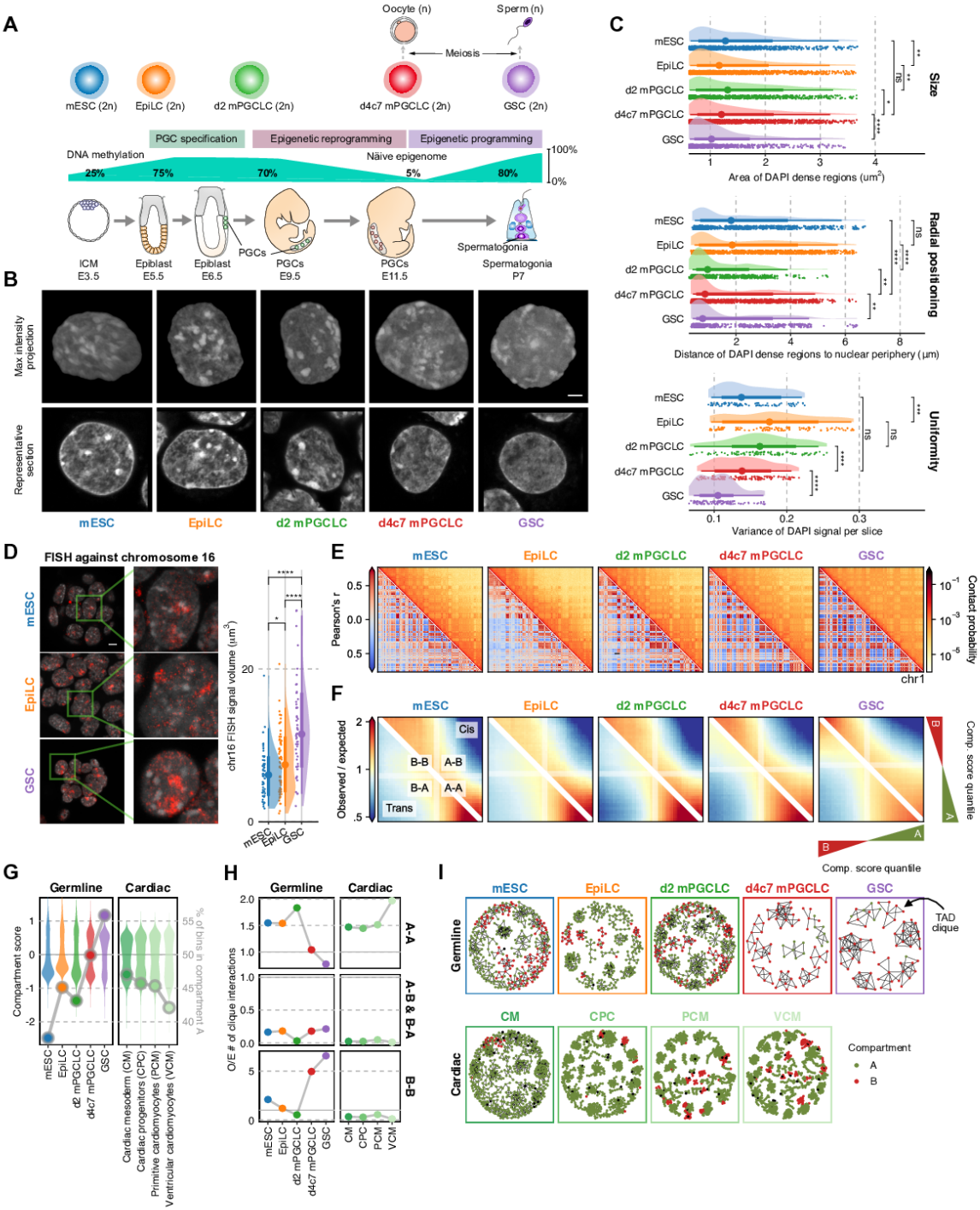
A
Oocyte (n)
Sperm (n)
Meiosis
mESC (2n)
EpiLC (2n)
d2 mPGCLC (2n)
d4c7 mPGCLC (2n)
GSC (2n)
PGC specification
Epigenetic reprogramming
Epigenetic programming
DNA methylation
Naïve epigenome
25%
75%
70%
5%
80%
100%
0%
ICM E3.5
Epiblast E5.5
Epiblast E6.5
PGCs E9.5
PGCs E11.5
Spermatogonia P7
B
Max intensity projection
Representative section
mESC
EpiLC
d2 mPGCLC
d4c7 mPGCLC
GSC
C
Size
Area of DAPI dense regions (um2)
Radial positioning
Distance of DAPI dense regions to nuclear periphery (µm)
Uniformity
Variance of DAPI signal per slice
D
FISH against chromosome 16
chr16 FISH signal volume (um3)
E
Pearson's r
Contact probability
chr1
F
Observed / expected
Cis
B-B
A-B
B-A
A-A
Trans
Comp. score quantile
G
Germline
Cardiac
Compartment score
% of bins in compartment A
Cardiac mesoderm (CM)
Cardiac progenitors (CPC)
Primitive cardiomyocytes (PCM)
Ventricular cardiomyocytes (VCM)
H
O/E # of clique interactions
A-A
A-B & B-A
B-B
I
TAD clique
CM
CPC
PCM
VCM
Compartment
A
B

Figure 1. 3D genome programming.

(A) Scheme for mouse germ-cell development in vitro (top) and in vivo (bottom), with dynamics of genome-wide DNA methylation levels (middle).

(B) Maximum intensity projections (top) and representative sections (bottom) of typical nuclei of the indicated cell types stained with DAPI. Bars, 3 μm.

(C) Areas of DAPI-dense regions (top), distance of DAPI-dense regions from the nuclear periphery (middle), and variance of DAPI signals (bottom). The point marks the median while the thick and thin lines correspond to 66% and 95% intervals, respectively. Number of DAPI dense regions = 950/1450/839/1535/736 and number of slices = 90/115/95/135/110 for mESC/EpiLC/d2/d4c7 mPGCLC/GSC. P-values are computed using Wilcoxon rank-sum tests. Wilcoxon rank-sum test p-values (top to bottom): 4.37e-3, 1.62e-3, 2.99e-2, 2.03e-10, 4.03e-1, <2.2e-16, 1.31e-3, 8.94e-3, 1.06e-4, 5.62e-2, 4.63e-5, 7.65e-13.

(D) (left) Fluorescence in situ hybridization (FISH) against chromosome 16 (red) with DAPI staining (grey). Z-stacked representative images are paired with magnified views. (right) Distributions of surface volumes for chr16. The point marks the median while the thick and thin lines correspond to 66% and 95% intervals, respectively. n = 51/68/53 for mESC/EpiLC/GSC. Bars, 5 μm. P-values are computed using Wilcoxon rank-sum tests. Wilcoxon rank-sum test p-values (left to right): 4.16e-2, 4.33e-6, 8.68e-9.

(E) Hi-C maps of chromosome 1. (upper) 250 kb-resolution balanced contact probability matrices; (lower) matching Pearson's correlation matrices.

(F) Compartmentalization saddle plots for the average interaction frequency between pairs of 50 kb genomic bins belonging to various compartment-score quantiles in cis (upper) and trans (lower).

(G) Transitions in euchromatin-vs-heterochromatin bias during the development of different lineages (cardiomyocyte differentiation (Zhang et al., 2019)) at 100 kb resolution. (left axis: violin plots) Distribution of compartment scores; (right axis: dots) ratio of A:B compartment bins.

(H) Enrichment of TAD-TAD interactions involved in max cliques (size ≥3) during the development of different lineages. A dispersal of active hubs was specifically observed during epigenetic reprogramming. Inter-compartmental TAD-TAD interactions are under-represented in all cases.

(I) Network representation of TAD cliques and their compartment identity during germ cell and cardiomyocyte differentiation.

Figure 2

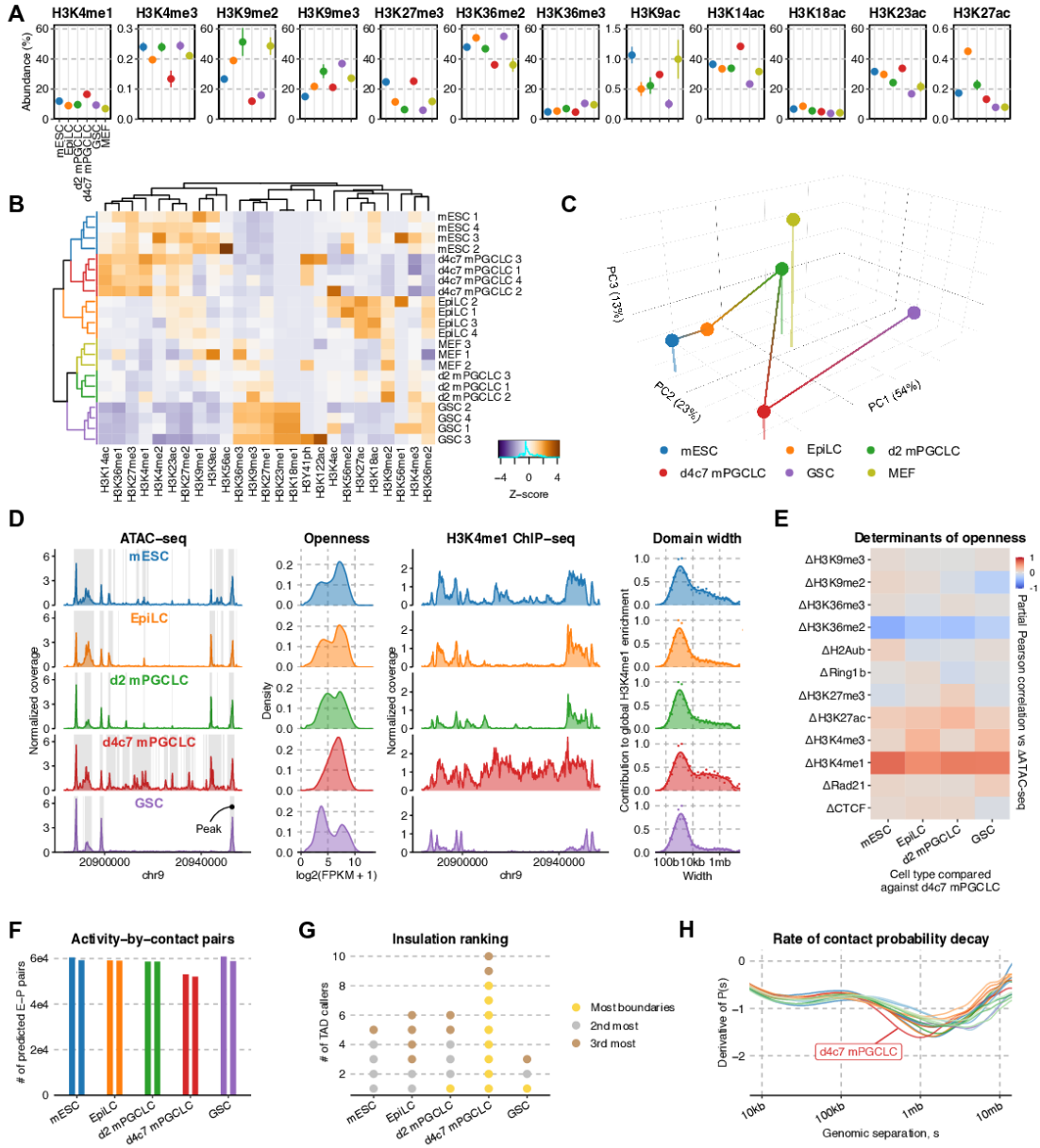
A
H3K4me1
H3K4me3
H3K9me2
H3K9me3
H3K27me3
H3K36me2
H3K36me3
H3K9ac
H3K14ac
H3K18ac
H3K23ac
H3K27ac
Abundance (%)
mESC
EpiLC
d2 mPGCLC
d4c7 mPGCLC
GSC
MEF
B
mESC 1
mESC 4
mESC 3
mESC 2
d4c7 mPGCLC 3
d4c7 mPGCLC 1
d4c7 mPGCLC 4
d4c7 mPGCLC 2
EpiLC 2
EpiLC 1
EpiLC 3
EpiLC 4
MEF 3
MEF 1
MEF 2
d2 mPGCLC 3
d2 mPGCLC 1
d2 mPGCLC 2
GSC 2
GSC 4
GSC 1
GSC 3
Z–score
C
PC3 (13%)
PC2 (23%)
PC1 (54%)
mESC
EpiLC
d2 mPGCLC
d4c7 mPGCLC
GSC
MEF
D
ATAC–seq
Openness
H3K4me1 ChIP–seq
Domain width
Normalized coverage
Density
Contribution to global H3K4me1 enrichment
Peak
chr9
log2(FPKM + 1)
Width
E
Determinants of openness
ΔH3K9me3
ΔH3K9me2
ΔH3K36me3
ΔH3K36me2
ΔH2Aub
ΔRing1b
ΔH3K27me3
ΔH3K27ac
ΔH3K4me3
ΔH3K4me1
ΔRad21
ΔCTCF
Partial Pearson correlation vs ΔATAC-seq
Cell type compared against d4c7 mPGCLC
F
Activity–by–contact pairs
# of predicted E–P pairs
G
Insulation ranking
# of TAD callers
Most boundaries
2nd most
3rd most
H
Rate of contact probability decay
Derivative of P(s)
d4c7 mPGCLC
Genomic separation, s

Figure 2. Epigenome profiles and CTCF insulation.

(A) Relative abundance (%) of key histone modifications as measured by mass spectrometry. The point marks the mean while error bars indicate standard errors. Three biological replicates in each cell type were analyzed.

(B) UHC of H3 modification abundances. Numeric suffixes indicate biological replicates.

(C) PCA of average H3 modifications abundances in each cell type.

(D) Chromatin accessibility landscape throughout germline development. (left) ATAC-seq coverage tracks at a representative locus, with peaks highlighted; (second left) distribution of read counts per each in the union peak set; (second right) H3K4me1 ChIP-seq coverage tracks at the same locus; (right) Distribution of domain widths for H3K4me1-enriched regions based on cross-correlation, as implemented in MCORE.

(E) Partial Pearson correlation matrix for inter-cell type ATAC-seq differences against d4c7 mPGCLCs versus differences in other epigenetic signals.

(F) Number of E-P pairs with ABC score > 0.02 (Fulco et al., 2019). Two biological replicates in each cell type were analyzed.

(G) Cell type insulation ranking. 10 different TAD-calling algorithms were used to determine the cell types rank in terms of insulation (gold: most insulated; silver: 2nd most insulated; bronze: 3rd most insulated).

(H) Slope of contact decay (P(s)) curves as a function of genomic separation in log-log space for the germline, neural induction (Bonev et al., 2017), B cell reprogramming (Stadhouders et al., 2018), and cardiomyocyte differentiation (Zhang et al., 2019) datasets.

Figure 3

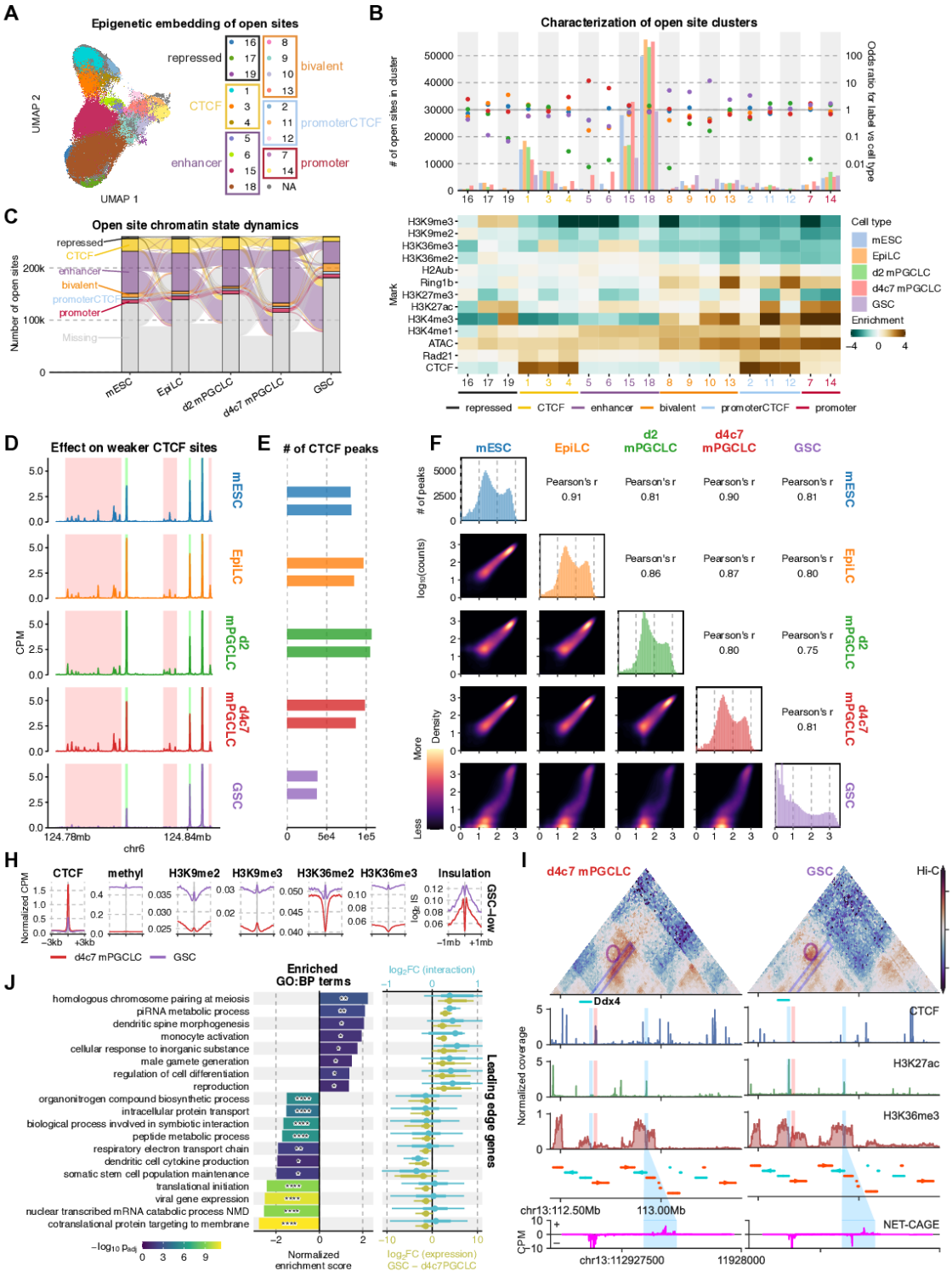
A
Epigenetic embedding of open sites
repressed
CTCF
enhancer
bivalent
promoterCTCF
promoter
NA
UMAP 1
UMAP 2
B
Characterization of open site clusters
# of open sites in cluster
Odds ratio for label vs cell type
Mark
H3K9me3
H3K9me2
H3K36me3
H3K36me2
H2Aub
Ring1b
H3K27me3
H3K27ac
H3K4me3
H3K4me1
ATAC
Rad21
CTCF
Cell type
mESC
EpiLC
d2 mPGCLC
d4c7 mPGCLC
GSC
Enrichment
C
Open site chromatin state dynamics
Number of open sites
Missing
mESC
EpiLC
d2 mPGCLC
d4c7 mPGCLC
GSC
D
Effect on weaker CTCF sites
CPM
chr6
E
# of CTCF peaks
F
# of peaks
Pearson's r
Density
More
Less
G
H
CTCF
methyl
H3K9me2
H3K9me3
H3K36me2
H3K36me3
Insulation
Normalized CPM
log2 IS
GSC–low
d4c7 mPGCLC
GSC
I
d4c7 mPGCLC
GSC
Hi-C
log(O/E)
Ddx4
CTCF
H3K27ac
H3K36me3
Normalized coverage
chr13:112.50Mb
113.00Mb
NET-CAGE
CPM
chr13:112927500
11928000
J
Enriched GO:BP terms
homologous chromosome pairing at meiosis
piRNA metabolic process
dendritic spine morphogenesis
monocyte activation
cellular response to inorganic substance
male gamete generation
regulation of cell differentiation
reproduction
organonitrogen compound biosynthetic process
intracellular protein transport
biological process involved in symbiotic interaction
peptide metabolic process
respiratory electron transport chain
dendritic cell cytokine production
somatic stem cell population maintenance
translational initiation
viral gene expression
nuclear transcribed mRNA catabolic process NMD
cotranslational protein targeting to membrane
−log10 Padj
Normalized enrichment score
log2FC (interaction)
log2FC (expression)
GSC – d4c7PGCLC
Leading edge genes

Figure 3. Open-site characterizations and CTCF release.

(A) 2D UMAP embedding based on epigenetic signals in ATAC-seq peaks for each cell type, with labels derived from semi-supervised HDBSCAN.

(B) Association between open-site clusters and cell types. (top) Number of open sites per cell type in each cluster (left axis: bars) and their enrichment as odds ratios (right axis: dots); (bottom) enrichment of epigenetic signals in each cluster.

(C) Dynamics of open site classes. Classification of the same open sites peak are compared between adjacent stages and shown as flows. Open sites that could not be reliably clustered or were not called as peaks are labelled as "Missing."

(D) ChIP-seq coverage tracks of CTCF in each cell type.

(E) Number of CTCF peaks called in each cell type. GSCs have considerably fewer CTCF peaks. Two biological replicates in each cell type were analyzed.

(F) Correlograms of CTCF binding in the union peak set. (Upper) Pearson's correlation coefficients between log2 transformed signals. (Diagonal) Histograms of CTCF signal intensity in the union peak set. (Lower) 2D density plots of CTCF binding in pairs of cell types.

(G) Aggregate plots of ChIP-seq enrichment for various targets and insulation score (IS) around CTCF-binding sites depleted in GSCs as compared to d4c7 mPGCLCs. n = 39408.

(H) 3D epigenetic landscape re-wiring near Ddx4. Observed/expected contact maps at 10 kb resolution for d4c7 mPGCLCs and GSCs are shown alongside select ChIP-seq and NET-CAGE coverage tracks. A strong insulating CTCF peak (orange) upstream of the Ddx4 TSS is lost in GSCs, facilitating the interaction between the Ddx4 promoter and an active enhancer demonstrating pronounced bidirectional nascent transcription (bottom).

(I) GSEA using genes ranked by concomitant differential expression and promoter interaction. (left) ABC-defined E-P pairs overlapping GSC-depleted CTCF peaks are used to rank genes based on coordinated E-P interaction and expression differences; (right) log2 fold changes for leading-edge genes of enriched gene sets.

Figure 4

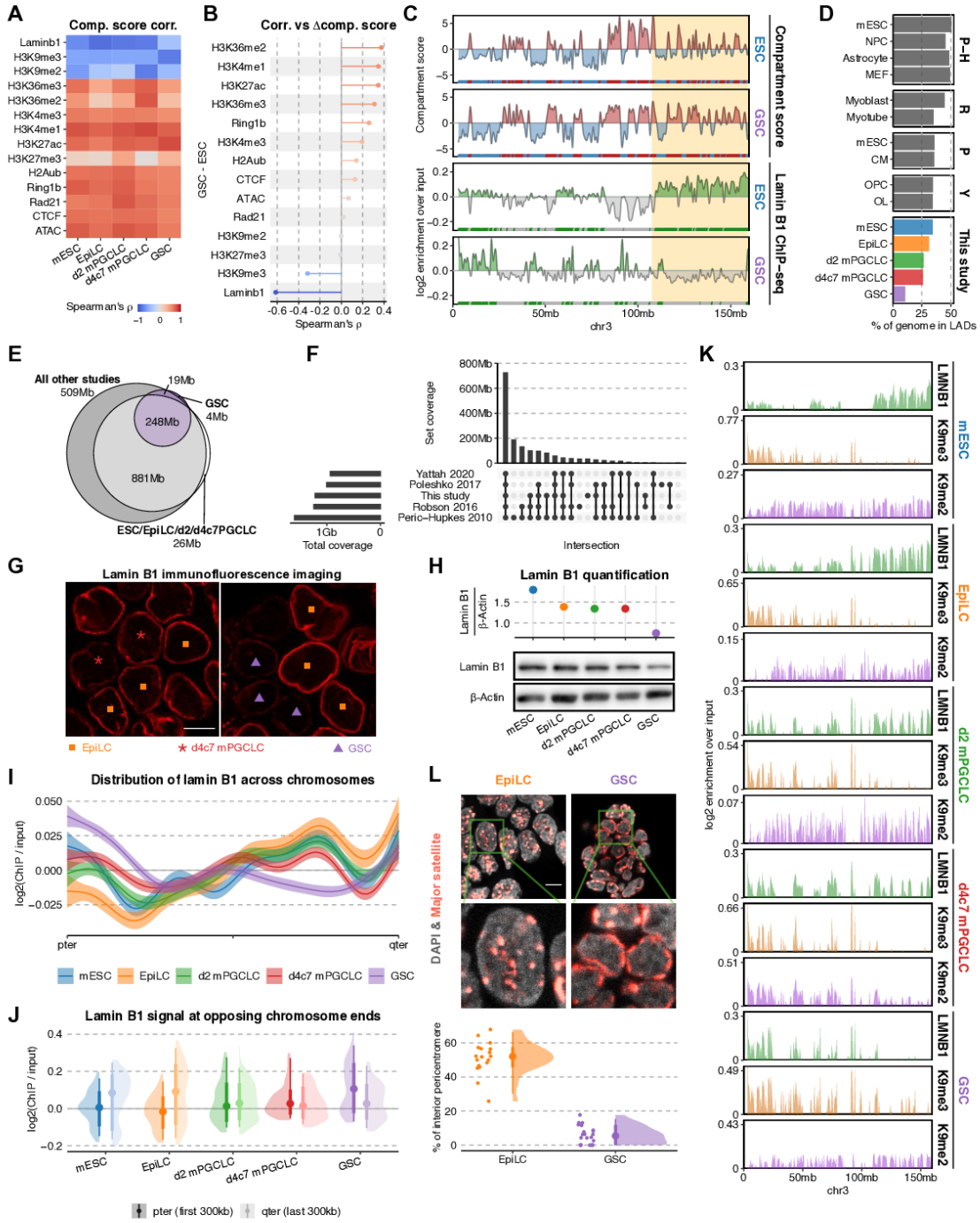
A
Comp. score corr.
Laminb1
H3K9me3
H3K9me2
H3K36me3
H3K36me2
H3K4me3
H3K4me1
H3K27ac
H3K27me3
H2Aub
Ring1b
Rad21
CTCF
ATAC
mESC
EpiLC
d2 mPGCLC
d4c7 mPGCLC
GSC
Spearman's ρ
B
Corr. vs Δcomp. score
GSC - ESC
Spearman's ρ
C
Compartment score
ESC
GSC
Lamin B1 ChIP-seq
log2 enrichment over input
chr3
D
P–H
R
P
Y
This study
% of genome in LADs
E
All other studies
509Mb
19Mb
GSC
4Mb
248Mb
881Mb
ESC/EpiLC/d2/d4c7PGCLC
26Mb
F
Set coverage
Yattah 2020
Poleshko 2017
This study
Robson 2016
Peric–Hupkes 2010
Intersection
Total coverage
G
Lamin B1 immunofluorescence imaging
EpiLC
d4c7 mPGCLC
GSC
H
Lamin B1 quantification
Lamin B1
β-Actin
I
Distribution of lamin B1 across chromosomes
log2(ChIP / input)
pter
qter
J
Lamin B1 signal at opposing chromosome ends
pter (first 300kb)
qter (last 300kb)
K
LMNB1
H3K9me3
H3K9me2
mESC
EpiLC
d2 mPGCLC
d4c7 mPGCLC
GSC
log2 enrichment over input
chr3
L
EpiLC
GSC
DAPI & Major satellite
% of interior pericentromere

Figure 4. Generation of minimal LADs.

(A) Correlation between compartment score and ChIP-seq enrichment at 50 kb resolution.

(B) Correlation between differential compartment score and differential ChIP-seq enrichment between mESCs and GSCs at 50kb resolution.

(C) Representative chromosome-wide distributions of compartment score and lamin B1 enrichment for mESCs and GSCs.

(D) LAD occupancies in different cell types (Peric-Hupkes et al., 2010, Poleshko et al., 2017, Robson et al., 2016, Yattah et al., 2020).

(E) Venn diagram of LADs called in GSCs, union of LADs called in all other cell types in this study, and union of LADs identified from all other studies (Peric-Hupkes et al., 2010, Poleshko et al., 2017, Robson et al., 2016, Yattah et al., 2020).

(F) UpSet plot for the union set of LADs in different studies (Peric-Hupkes et al., 2010, Poleshko et al., 2017, Robson et al., 2016, Yattah et al., 2020). A majority of regions correspond to constitutive LADs.

(G) IF analysis for lamin B1 in (left) EpiLCs and d4c7 mPGCLCs, as well as (right) EpiLCs and GSCs. Symbols for each cell type are as indicated. Bars, 10 μm.

(H) Western blot for lamin B1 in different cell types (bottom) and quantification normalized by β-actin (top).

(I) Average distributions of lamin B1 enrichment across all chromosomes (1–19, X). Ribbons correspond to 95% confidence intervals of fitted GAMs.

(J) Lamin B1 ChIP-seq enrichment in the first (left/p-ter) and the last (right/q-ter) 300 Kb of each chromosome. The point marks the median while the thick and thin lines correspond to 66% and 95% intervals, respectively.

(K) Representative chromosome-wide distributions of ChIP-seq enrichment for lamin B1 and H3K9me3/me2.

(L) (top) Representative images of FISH against major satellite repeats in EpiLCs and GSCs. Bars, 10 μm; (bottom) percentage of the pericentromeres detached from the nuclear lamina in EpiLCs and GSCs. The point marks the median while the thick and thin lines correspond to 66% and 95% intervals, respectively. Number of cells = 18/22 for EpiLC/GSC.

Figure 5

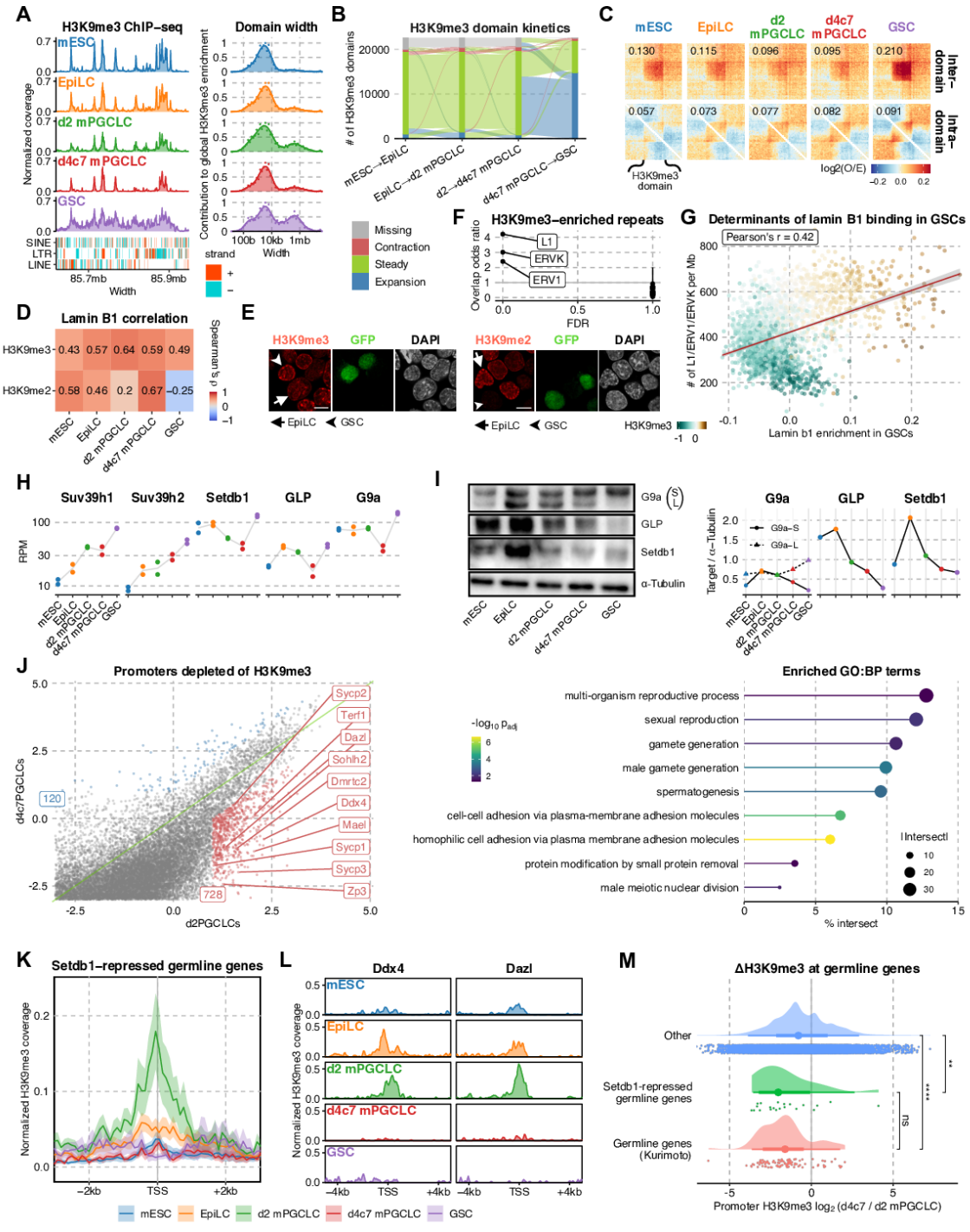
A
H3K9me3 ChIP–seq
Domain width
mESC
EpiLC
d2 mPGCLC
d4c7 mPGCLC
GSC
Normalized coverage
Contribution to global H3K9me3 enrichment
SINE
LTR
LINE
85.7mb
85.9mb
Width
strand
100b 10kb 1mb
B
H3K9me3 domain kinetics
# of H3K9me3 domains
mESC→EpiLC
EpiLC→d2 mPGCLC
d2→d4c7 mPGCLC
d4c7 mPGCLC→GSC
Missing
Contraction
Steady
Expansion
C
mESC
EpiLC
d2 mPGCLC
d4c7 mPGCLC
GSC
0.130
0.115
0.096
0.095
0.210
0.057
0.073
0.077
0.082
0.091
Inter–domain
Intra–domain
H3K9me3 domain
log2(O/E)
D
Lamin B1 correlation
H3K9me3
H3K9me2
0.43 0.57 0.64 0.59 0.49
0.58 0.46 0.2 0.67 −0.25
Spearman's ρ
E
H3K9me3
GFP
DAPI
H3K9me2
EpiLC
GSC
F
H3K9me3–enriched repeats
Overlap odds ratio
L1
ERVK
ERV1
FDR
G
Determinants of lamin B1 binding in GSCs
Pearson's r = 0.42
# of L1/ERV1/ERVK per Mb
Lamin b1 enrichment in GSCs
H
Suv39h1
Suv39h2
Setdb1
GLP
G9a
RPM
I
G9a (S) (L)
GLP
Setdb1
α-Tubulin
G9a–S
G9a–L
Target / α–Tubulin
J
Promoters depleted of H3K9me3
d4c7PGCLCs
d2PGCLCs
120
728
Sycp2
Terf1
Dazl
Sohlh2
Dmrtc2
Ddx4
Mael
Sycp1
Sycp3
Zp3
Enriched GO:BP terms
-log10 padj
multi-organism reproductive process
sexual reproduction
gamete generation
male gamete generation
spermatogenesis
cell-cell adhesion via plasma-membrane adhesion molecules
homophilic cell adhesion via plasma membrane adhesion molecules
protein modification by small protein removal
male meiotic nuclear division
Intersect
% intersect
K
Setdb1–repressed germline genes
Normalized H3K9me3 coverage
−2kb
TSS
+2kb
L
Ddx4
Dazl
−4kb
+4kb
M
ΔH3K9me3 at germline genes
Other
Setdb1-repressed germline genes
Germline genes (Kurimoto)
ns
Promoter H3K9me3 log2 (d4c7 / d2 mPGCLC)

Figure 5. Heterochromatin re-organization.

(A) (left) H3K9me3 ChIP-seq tracks, with TEs in different classes shown below; (right) Distribution of domain widths for H3K9me3-enriched regions based on cross-correlation, as implemented in MCORE.

(B) Spatial-temporal dynamics of H3K9me3 domains (>10 Kb) analyzed using ChromTime. c, Enrichment of interaction between (top) and within (bottom) broad H3K9me3 domains (>50 Kb; identified in GSCs and overlap peaks in other cell types). (C) (Top) Enrichment of interaction between (upper) and within (lower) broad H3K9me3 domains (>50 Kb; identified in GSCs and overlap peaks in all other cell types).

(D) Correlation between H3K9me2/3 and lamin B1 ChIP-seq enrichment.

(E) IF analysis for H3K9me3 (top) and H3K9me2 (bottom) in EpiLCs and GSCs. Arrowheads: GFP+ GSCs; arrows: EpiLCs. Bars, 10 μm.

(F) Odds ratio and significance of overlap between H3K9me3 domains conserved across all cell types and different repeat families.

(G) Scatter plot of lamin B1 enrichment in GSCs vs the aggregated density of select TEs (L1, ERV1 and ERVK) in 1mb bins, with points colored by H3K9me3 enrichment in GSCs.

(H) Expression of H3K9 methyltransferases as measured by RNA-seq (Ishikura et al., 2016, Ohta et al., 2021, Sasaki, Yokobayashi et al., 2015). Two biological replicates in each cell type were analyzed.

(I) (left) Western blot for G9a, GLP, Setdb1 and α-tubulin; (right) quantification normalized by α-Tubulin.

(J) (left) Scatter plot of H3K9me3 enrichment across all promoters in d2 mPGCLCs and d4c7 mPGCLCs, with 728 genes (red) showing substantially higher H3K9me3 levels in d2 mPGCLCs than d4c7 mPGCLCs; (right) pathway enrichment of the 728 genes using g:Profiler.

(K) Aggregate plot of H3K9me3 around the TSSs of Setdb1-repressed germline genes (Karimi, Goyal et al., 2011). The thick line marks the mean while the upper and lower limits indicate standard errors.

(L) Normalized H3K9me3 tracks around the TSSs of Dazl and Ddx4.

(M) Distribution of differences in promoter H3K9me3 between d2 and d4c7 mPGCLCs for germline genes (Kurimoto et al., 2015), Setdb1-repressed germline genes (Karimi et al., 2011) and other genes. The point marks the median while the thick and thin lines correspond to 66% and 95% intervals, respectively.

From top to bottom, n = 19559, 21, 99. P-values are computed using Wilcoxon rank-sum tests. Wilcoxon rank-sum test p-values (top to bottom): 2.36e-3, 1.14e-9, 4.43e-1.

Figure 6

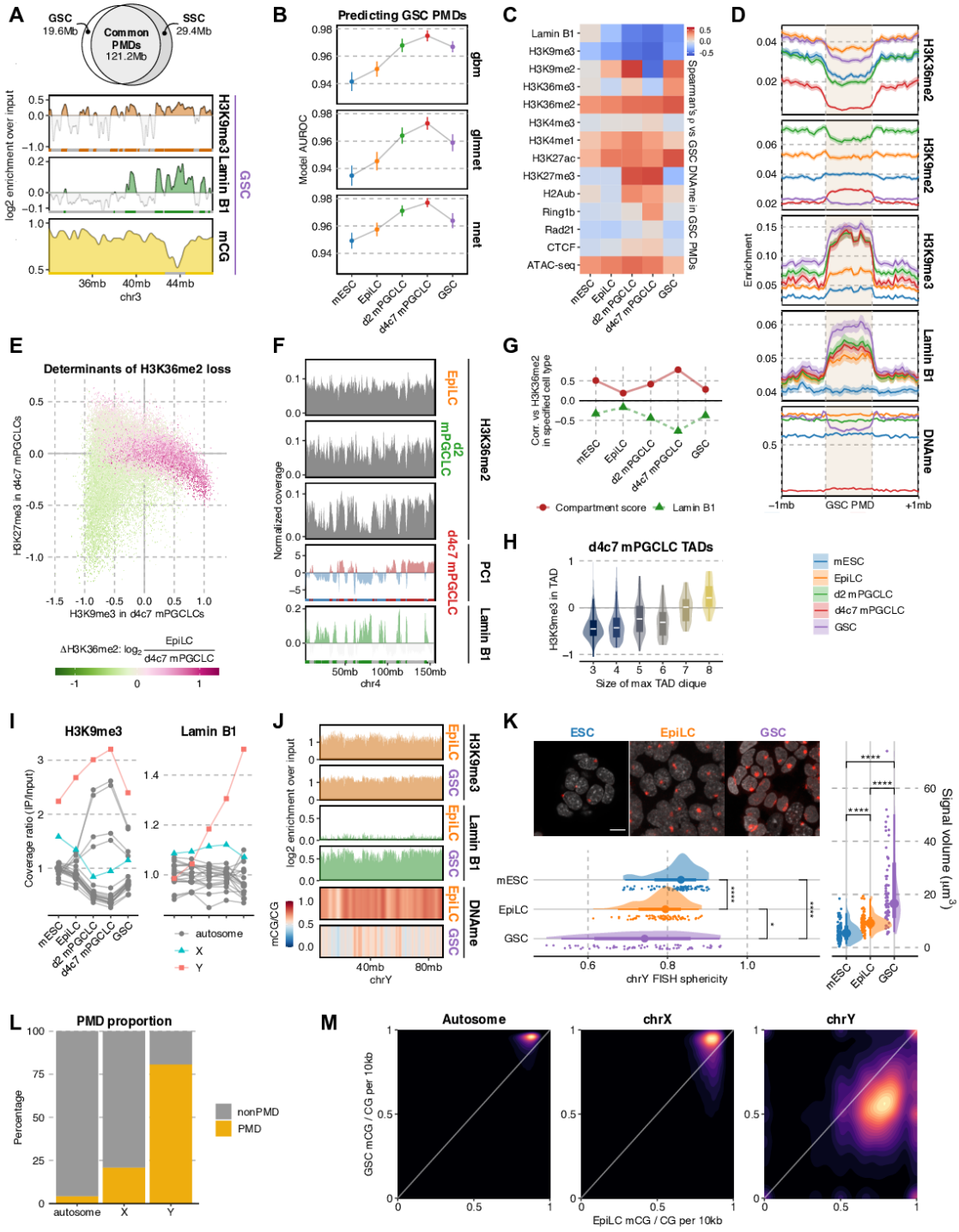
A
GSC
19.6Mb
Common PMDs
121.2Mb
SSC
29.4Mb
log2 enrichment over input
H3K9me3
Lamin B1
mCG
GSC
36mb
40mb
44mb
chr3
B
Predicting GSC PMDs
Model AUROC
gbm
glmnet
nnet
mESC
EpiLC
d2 mPGCLC
d4c7 mPGCLC
GSC
C
Lamin B1
H3K9me3
H3K9me2
H3K36me3
H3K36me2
H3K4me3
H3K4me1
H3K27ac
H3K27me3
H2Aub
Ring1b
Rad21
CTCF
ATAC-seq
Spearman's ρ vs GSC DNAme in GSC PMDs
D
H3K36me2
H3K9me2
H3K9me3
Lamin B1
DNAme
Enrichment
−1mb
GSC PMD
+1mb
E
Determinants of H3K36me2 loss
H3K27me3 in d4c7 mPGCLCs
H3K9me3 in d4c7 mPGCLCs
ΔH3K36me2: log2 EpiLC / d4c7 mPGCLC
F
EpiLC
d2 mPGCLC
d4c7 mPGCLC
H3K36me2
PC1
Lamin B1
Normalized coverage
50mb
100mb
150mb
chr4
G
Corr. vs H3K36me2 in specified cell type
Compartment score
Lamin B1
H
d4c7 mPGCLC TADs
H3K9me3 in TAD
Size of max TAD clique
mESC
EpiLC
d2 mPGCLC
d4c7 mPGCLC
GSC
I
H3K9me3
Lamin B1
Coverage ratio (IP/Input)
autosome
X
Y
J
log2 enrichment over input
mCG/CG
H3K9me3
Lamin B1
DNAme
40mb
80mb
chrY
K
ESC
EpiLC
GSC
mESC
EpiLC
GSC
chrY FISH sphericity
Signal volume (μm3)
L
PMD proportion
Percentage
nonPMD
PMD
autosome
X
Y
M
Autosome
chrX
chrY
GSC mCG / CG per 10kb
EpiLC mCG / CG per 10kb

Figure 6. Mechanism of PMD formation via balancing H3K36me2 vs H3K9me-marked LADs and Y chromosome hypomethylation.

(A) (top) Overlap of PMDs between spermatogonia (Kubo et al., 2015) and GSCs; (bottom) Representative locus demonstrating colocalization of H3K9me3 and lamin B1 enrichment wit DNA hypomethylation.

(B) The area under the receiver operating characteristic (AUROC) of classifiers predicting 50 kb bins as either PMD or not in GSCs using each cell type's own epigenome.

(C) Correlation of GSCs' DNA methylation levels in GSC LADs with epigenetic signals in different cell types.

(D) Aggregate plots of H3K36me2, H3K9me2, H3K9me3, and lamin B1 enrichment as well as DNA methylation around PMDs in GSCs. The thick line marks the mean while the upper and lower limits indicate standard errors.

(E) Scatter plot of d4c7 mPGCLCs' H3K9me3 and H3K27me3 enrichment in 50 kb bins colored by differential H3K36me2 (EpiLCs–d4c7 mPGCLCs).

(F) Representative chromosome-wide distributions of compartment score, lamin B1 enrichment, and H3K36me2 coverage.

(G) Correlation between H3K36me2 and compartment scores or lamin B1 enrichment in 50 kb bins.

(H) Relationship between the max clique size involving a given TAD and the average H3K9me3 enrichment in that TAD in d4c7 mPGCLCs.

(I) IP/input ratio of H3K9me3 and lamin B1 alignments per chromosome.

(J) Enrichment tracks of H3K9me3 and lamin B1 as well as DNA methylation in EpiLCs and d4c7 mPGCLCs on chromosome Y.

(K) (top) FISH against the Y chromosome; (bottom) sphericity of the Y chromosome FISH signals; (right) distributions Y chromosome surface volumes. The point marks the median while the thick and thin lines correspond to 66% and 95% intervals, respectively. n = 89/76/69 for mESC/EpiLC/GSC. Bar, 10 μm. P-values are computed using Wilcoxon rank-sum tests.

(L) Proportion of the genome occupied by PMDs in GSCs with stratification by chromosome.

(M) 2D density plots of DNA methylation level (mCG/CG) between EpiLCs and GSCs in 10 kb bins.

Figure 7

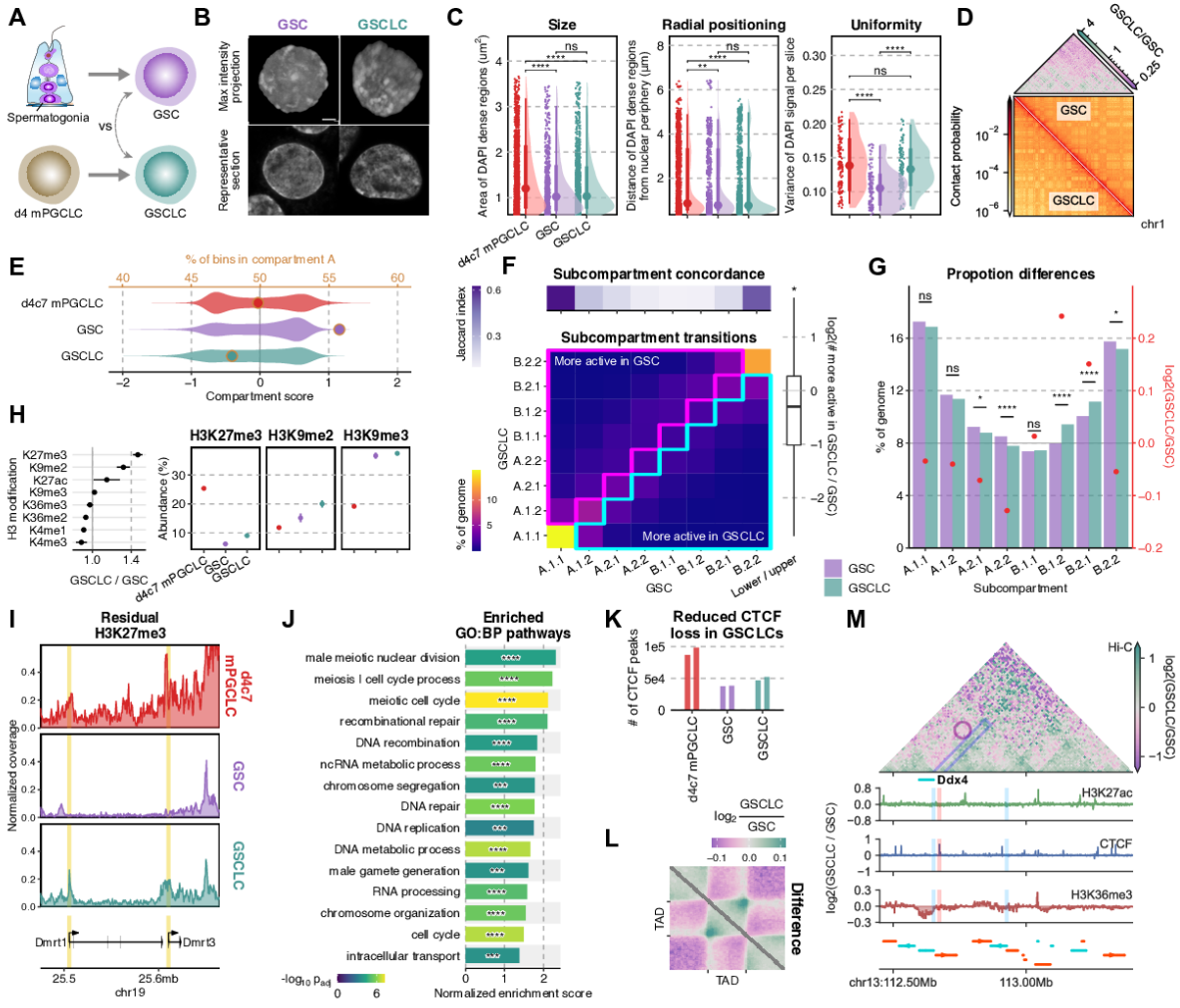
A
Spermatogonia
GSC
vs
d4 mPGCLC
GSCLC
B
GSC
GSCLC
Max intensity projection
Representative section
C
Size
Radial positioning
Uniformity
Area of DAPI dense regions (um²)
Distance of DAPI dense regions from nuclear periphery (µm)
Variance of DAPI signal per slice
ns
****
**
d4c7 mPGCLC
GSC
GSCLC
D
GSCLC/GSC
GSC
GSCLC
Contact probability
chr1
E
% of bins in compartment A
d4c7 mPGCLC
GSC
GSCLC
Compartment score
F
Subcompartment concordance
Jaccard index
Subcompartment transitions
More active in GSC
More active in GSCLC
% of genome
log2(# more active in GSCLC / GSC)
Lower / upper
G
Propotion differences
% of genome
log2(GSCLC/GSC)
Subcompartment
H
H3K27me3
H3K9me2
H3K9me3
K27me3
K9me2
K27ac
K9me3
K36me3
K36me2
K4me1
K4me3
H3 modification
Abundance (%)
GSCLC / GSC
I
Residual H3K27me3
d4c7 mPGCLC
GSC
GSCLC
Normalized coverage
Dmrt1
Dmrt3
chr19
J
Enriched GO:BP pathways
male meiotic nuclear division
meiosis I cell cycle process
meiotic cell cycle
recombinational repair
DNA recombination
ncRNA metabolic process
chromosome segregation
DNA repair
DNA replication
DNA metabolic process
male gamete generation
RNA processing
chromosome organization
cell cycle
intracellular transport
Normalized enrichment score
K
Reduced CTCF loss in GSCLCs
# of CTCF peaks
L
TAD
Difference
M
Hi-C
Ddx4
H3K27ac
CTCF
H3K36me3
chr13:112.50Mb
113.00Mb

Figure 7. Nucleome differences between GSCs and GSCLCs.

(A) Scheme for the derivation of GSCs and GSCLCs.

(B) Maximum intensity projections (top) and representative sections (bottom) of typical nuclei of GSCs and GSCLCs stained with DAPI. Bars, 3 μm.

(C) Areas of DAPI-dense regions (left), distance of DAPI-dense regions from the nuclear periphery (middle), and variance of DAPI signals (right). The point marks the median while the thick and thin lines correspond to 66% and 95% intervals, respectively. Number of DAPI dense regions = 1535/736/1227 and number of slices = 135/110/120 for d4c7 mPGCLC/GSC/GSCLC.

(D) (bottom) 250 kb resolution balanced contact probability matrices of chromosome 1 in GSCs (upper) and GSCLCs (lower); (top) fold change (GSCLCs/GSCs) of contact probability, showing an attenuation of distal interactions in GSCLCs.

(E) Distribution of compartment scores (bottom axis: violin plots) and ratio of A:B compartment bins (top axis: dots) at 100 kb resolution.

(F) Differential subcompartmentalization between GSCs and GSCLCs at 50 kb resolution. (top) Jaccard index between genomic bins belonging to each subcompartment in GSCs vs GSCLCs. (bottom) Comparison of subcompartment labels between cell types reveals a greater proportion of the genome belongs to the upper triangle, in line with GSCLCs being more repressive. (right) Quantification of matched bins in the upper vs lower triangle.

(G) Comparison of overall subcompartment proportions in GSCs vs GSCLCs. Most significant changes are again observed mostly for the intermediate states and not active euchromatin (A.1) or constitutive heterochromatin (B.2). P-values are computed using two-proportions z-tests.

(H) (left) Fold change (GSCLCs/GSCs) of different H3 modifications as measured by mass spectrometry, with confidence intervals denoting standard errors; (right) full data for select modifications.

(I) Normalized H3K27me3 coverage tracks around Dmrt1 and Dmrt3.

(J) GSEA results for promoters ranked by preferential enrichment in GSCLCs as compared to GSCs.

(K) Number of CTCF peaks in each cell type. Two biological replicates in each cell type were analyzed.

(L) Pile-up plots of intra-TAD interactions in GSCs and GSCLCs.

(M) 3D epigenetic landscape rewiring near Ddx4. Differential (GSCLCs/GSCs) contact maps and ChIP-seq coverage at the Ddx4 locus are shown. The insulating CTCF peak separating Ddx4 from one of its enhancers is not completely removed in GSCLCs.

Figure 8

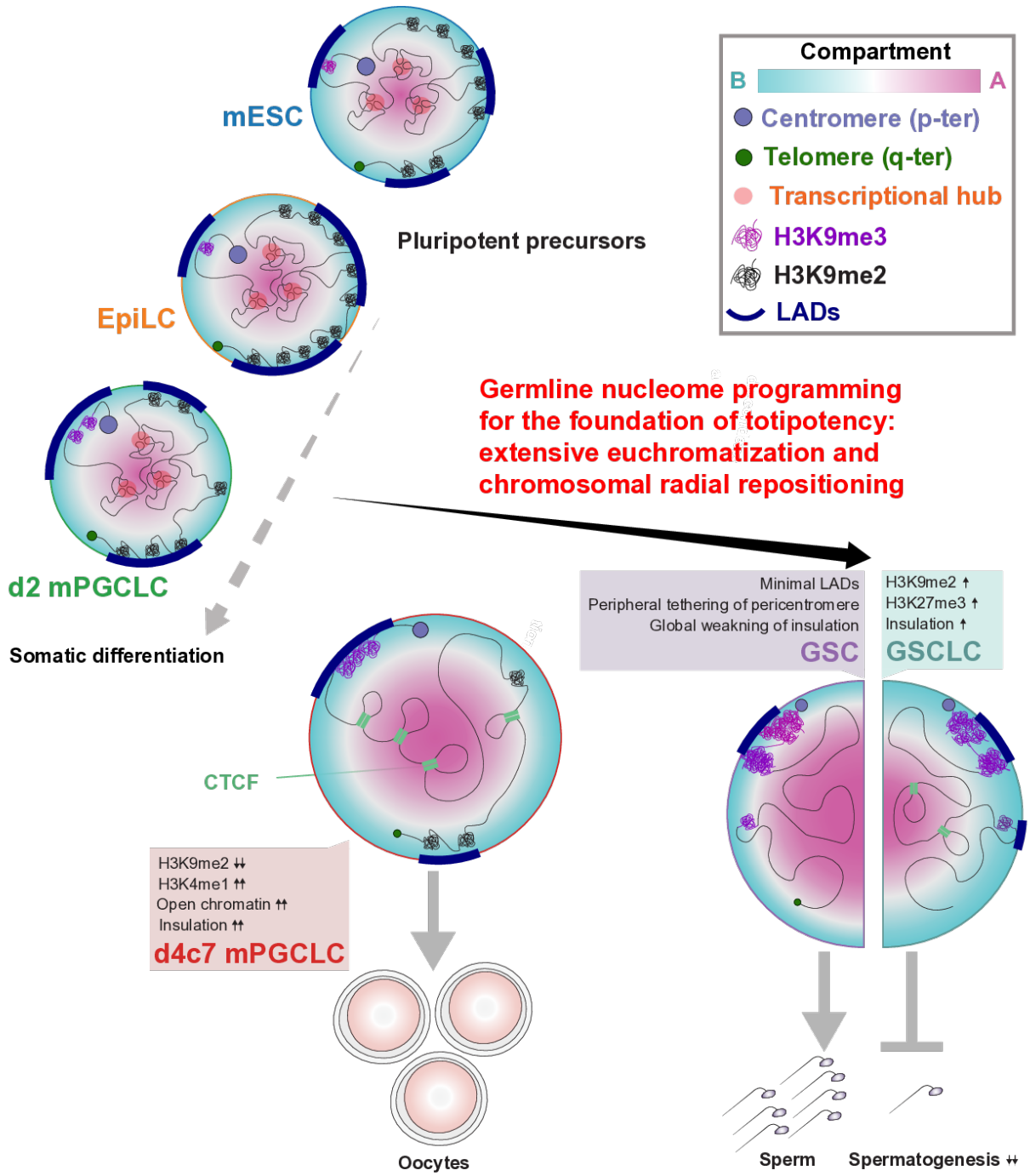
Compartment
B
A
Centromere (p-ter)
Telomere (q-ter)
Transcriptional hub
H3K9me3
H3K9me2
LADs
mESC
Pluripotent precursors
EpiLC
d2 mPGCLC
Germline nucleome programming
for the foundation of totipotency:
extensive euchromatization and
chromosomal radial repositioning
Somatic differentiation
Minimal LADs
Peripheral tethering of pericentromere
Global weakning of insulation
GSC
H3K9me2 ↑
H3K27me3 ↑
Insulation ↑
GSCLC
CTCF
H3K9me2 ↓↓
H3K4me1 ↑↑
Open chromatin ↑↑
Insulation ↑↑
d4c7 mPGCLC
Oocytes
Sperm
Spermatogenesis ↓↓

Figure 8. A model for the nucleome programming during mouse germ-cell development.

Unlike somatic fates, germline nucleome programming entails extensive euchromatization, which is associated with radial re-positioning of pericentromeres and peripheral de-attachment elsewhere. Augmented insulation helps to maintain transcriptional fidelity during global DNA hypomethylation in PGCs (PGCs bear oogenic potential as well). Insulators are subsequently erased en masse to activate gametogenic program during the PGCs-to-spermatogonia/SSC development. Faulty nucleome maturation involving intermediate compartment states leads to impaired spermatogenic capacity.

Figure EV1

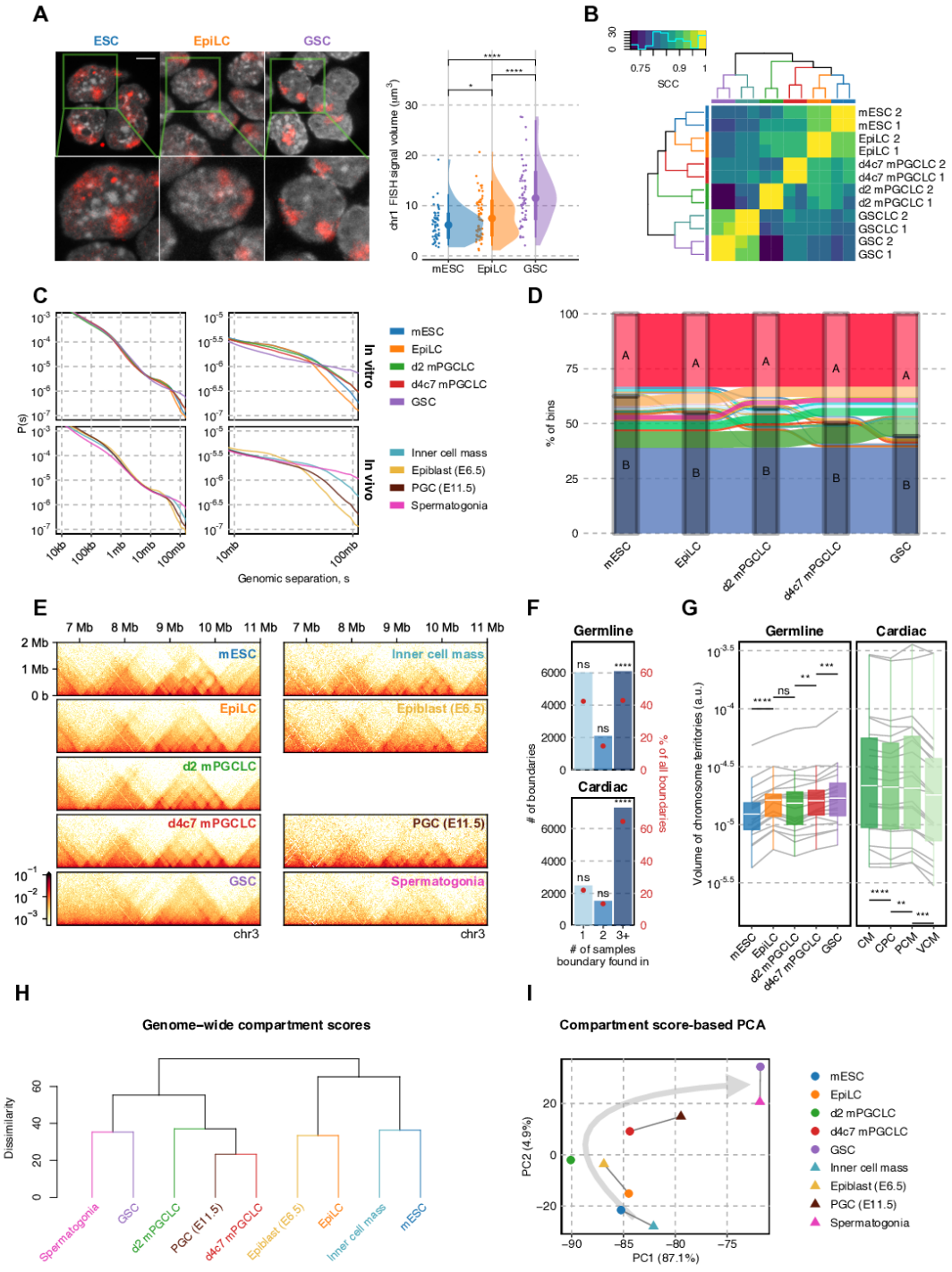
A
ESC
EpiLC
GSC
chr1 FISH signal volume (μm³)
mESC
EpiLC
GSC
B
SCC
mESC 2
mESC 1
EpiLC 2
EpiLC 1
d4c7 mPGCLC 2
d4c7 mPGCLC 1
d2 mPGCLC 2
d2 mPGCLC 1
GSCLC 2
GSCLC 1
GSC 2
GSC 1
C
P(s)
In vitro
In vivo
mESC
EpiLC
d2 mPGCLC
d4c7 mPGCLC
GSC
Inner cell mass
Epiblast (E6.5)
PGC (E11.5)
Spermatogonia
Genomic separation, s
D
% of bins
E
mESC
EpiLC
d2 mPGCLC
d4c7 mPGCLC
GSC
Inner cell mass
Epiblast (E6.5)
PGC (E11.5)
Spermatogonia
chr3
F
Germline
Cardiac
# of boundaries
% of all boundaries
# of samples boundary found in
G
Germline
Cardiac
Volume of chromosome territories (a.u.)
CM
CPC
PCM
VCM
H
Genome–wide compartment scores
Dissimilarity
I
Compartment score-based PCA
PC2 (4.9%)
PC1 (87.1%)

Figure EV1. Investigation of global nuclear architecture dynamics through Hi-C and FISH.

(A) Fluorescence in situ hybridization (FISH) against chromosome 1 (red) with DAPI counterstaining (grey). Z-stacked representative images (top left) are paired with magnified views (top right). (Bottom) The distribution of "surface" volumes for chr1, as seen for chr16, validates chromosomal decondensation in GSCs. n = 51/68/53 for mESC/EpiLC/GSC. P-values are computed using Wilcoxon rank-sum tests. Wilcoxon rank-sum test p-values (left to right): 4.16e-2, 4.33e-6, 8.68e-9.

(B) Hierarchical clustering of stratum-adjusted correlation coefficients (SCC) between samples validating the reproducibility of biological replicates.

(C) Contact probability decay across different inter-loci separation distances for various cell types throughout in vivo and in vitro germ cell differentiation, demonstrating a gain of distal interactions along differentiation, especially at distances >50 Mb.

(D) Sankey diagram of compartment identities in 50 kb bins across cell types. Compartment A regions newly acquired by GSCs are formed through a unidirectional switch of B-A with relatively little reversal.

(E) 25 kb-resolution balanced contact maps spanning chr3:5–12.5 mb.

(F) Degree of TAD boundary conservation in different lineages. Consistent across different lineages, more than 40% TAD boundaries are significantly conserved across differentiation. One-sided permutation tests were carried out by shuffling sample labels 100000 times, with p-values (left to right, top to bottom): 1, 1, 1e-5, 1, 1, 1e-5.

(G) Convex hull volumes of CSynth-produced chromosome 3D models during the development of different lineages, after normalization to unit backbone length. n = 22/19 for cardiac/germline. P-values are computed using Wilcoxon rank-sum tests. Wilcoxon signed-rank test p-values (left to right): 1.91e-6, 1.89e-1, 1.69e-3, 2.61e-4, 4.77e-6, 1.86e-3, 2.93e-4.

(H) UHC based on Euclidean distance between 100 kb compartment score tracks for cell types from in vitro and in vivo germ cell differentiation, with comparable stages consistently grouped together.

(I) PCA of compartment scores at 100 kb resolution for various cell types throughout in vivo and in vitro germ cell differentiation, with comparable stages consistently grouped together.

Figure EV2

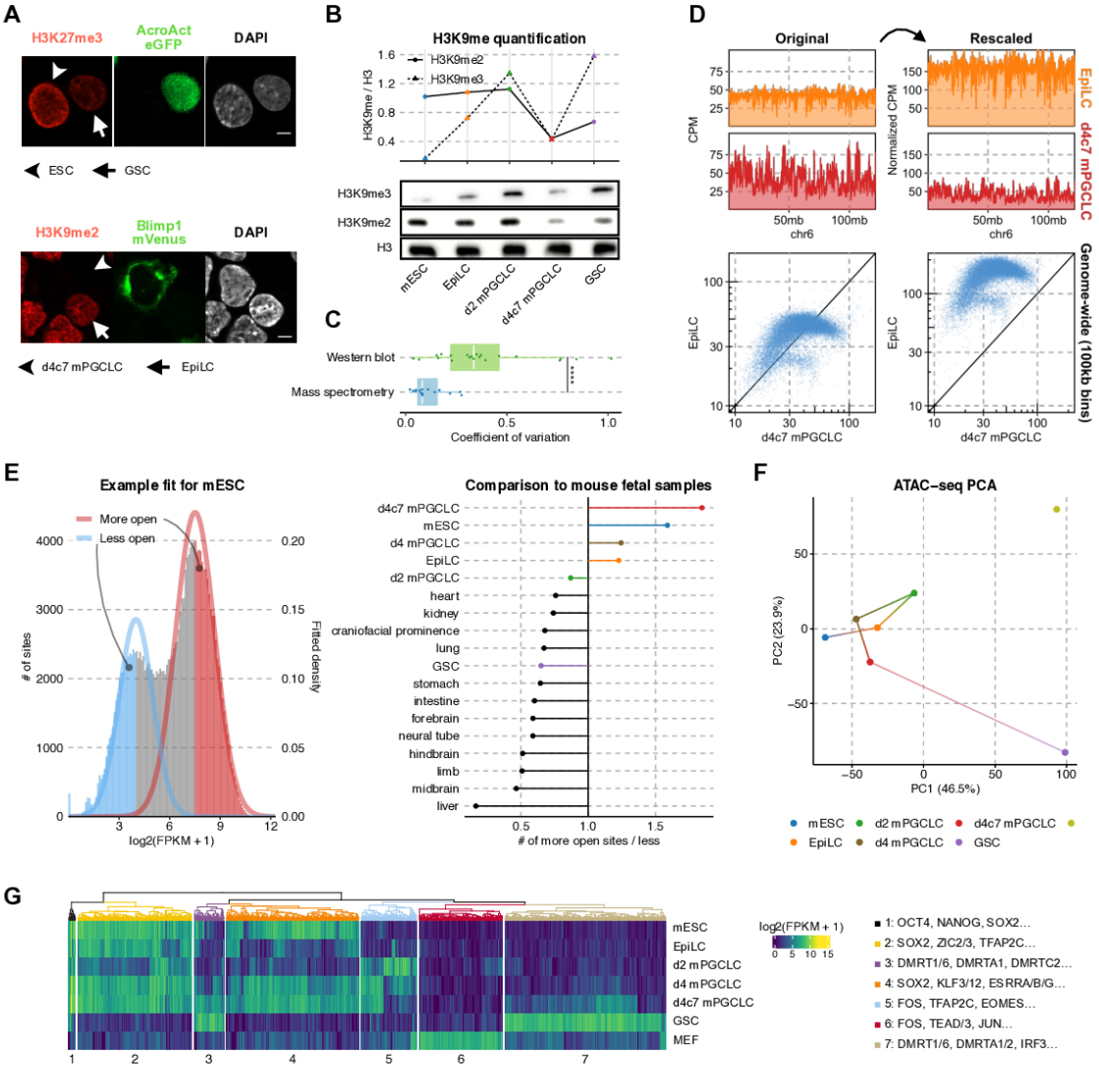
A
H3K27me3
AcroAct eGFP
DAPI
ESC
GSC
H3K9me2
Blimp1 mVenus
DAPI
d4c7 mPGCLC
EpiLC
B
H3K9me quantification
H3K9me2
H3K9me3
H3K9me / H3
H3K9me3
H3K9me2
H3
mESC
EpiLC
d2 mPGCLC
d4c7 mPGCLC
GSC
C
Western blot
Mass spectrometry
Coefficient of variation
D
Original
Rescaled
CPM
Normalized CPM
EpiLC
d4c7 mPGCLC
50mb
100mb
chr6
Genome-wide (100kb bins)
d4c7 mPGCLC
E
Example fit for mESC
More open
Less open
# of sites
Fitted density
log2(FPKM + 1)
Comparison to mouse fetal samples
d4c7 mPGCLC
mESC
d4 mPGCLC
EpiLC
d2 mPGCLC
heart
kidney
craniofacial prominence
lung
GSC
stomach
intestine
forebrain
neural tube
hindbrain
limb
midbrain
liver
# of more open sites / less
F
ATAC–seq PCA
PC2 (23.9%)
PC1 (46.5%)
mESC
d2 mPGCLC
d4c7 mPGCLC
EpiLC
d4 mPGCLC
GSC
G
mESC
EpiLC
d2 mPGCLC
d4 mPGCLC
d4c7 mPGCLC
GSC
MEF
log2(FPKM + 1)
1: OCT4, NANOG, SOX2…
2: SOX2, ZIC2/3, TFAP2C…
3: DMRT1/6, DMRTA1, DMRTC2…
4: SOX2, KLF3/12, ESRRA/B/G…
5: FOS, TFAP2C, EOMES…
6: FOS, TEAD/3, JUN…
7: DMRT1/6, DMRTA1/2, IRF3…

Figure EV2. Quantitative epigenome analysis by mass spectrometry and chromatin accessibility analysis by ATAC-seq.

(A) (Top) Immunofluorescence against H3K27me3 in mESCs and GSCs; the shaftless arrowhead marks a GFP+ GSCs and the arrow indicates mESCs. (Bottom) Immunofluorescence against H3K9me2 in EpiLCs and d4c7 mPGCLCs; the shaftless arrowhead marks a Blimp1-mVenus+ d4c7 mPGCLCs and the arrow indicates EpiLCs. Scale bars = 10 μm.

(B) Western blot against H3K9me3, H3K9me2, and histone H3 in each cell type (bottom) and H3-normalized quantification (top).

(C) Coefficients of variation across replicates of histone modification abundance as measured by quantitative histone mass spectrometry versus western blot for H3K9me2, H3K9me3, and H3K27me3. Mass spectrometry measurements consistently exhibit higher reproducibility. n = 15/21 for mass spectrometry/western blot. P-value computed using Wilcoxon rank-sum test. Wilcoxon rank-sum test p-value: 5.34e-5.

(D) Schematic of normalizing histone modification ChIP-seq via mass spectrometry-derived coefficients. With only depth-normalization (left), EpiLCs and d4c7 mPGCLCs appear to have comparable H3K9me2 profiles both in terms of coverage tracks and in a pairwise scatter plot comparing the two cell types; after multiplication of their relative abundances based on mass spectrometry, the comparatively lower levels of H3K9me2 in d4C7GCLCs become apparent (right).

(E) Comparison of regions with greater ("more open") and reduced ("less open") accessibility in the union peak set of germline samples and E14.5 mouse fetal tissues (Gorkin et al., 2020). Through fitting two-component gaussian mixture models, d4c7 mPGCLCs stand out as possessing the most permissive genome.

(F) PCA of ATAC-seq signals in the top 10,000 most variable peaks from the union peak set including MEFs (Di Giammartino, Kloetgen et al., 2019).

(G) UHC of the top 2,000 most variable ATAC-seq peaks in the union peak set including MEFs. (left) Clustered ATAC-seq enrichment heatmap; (right) overrepresented TF-binding motifs in each cluster.

Figure EV3

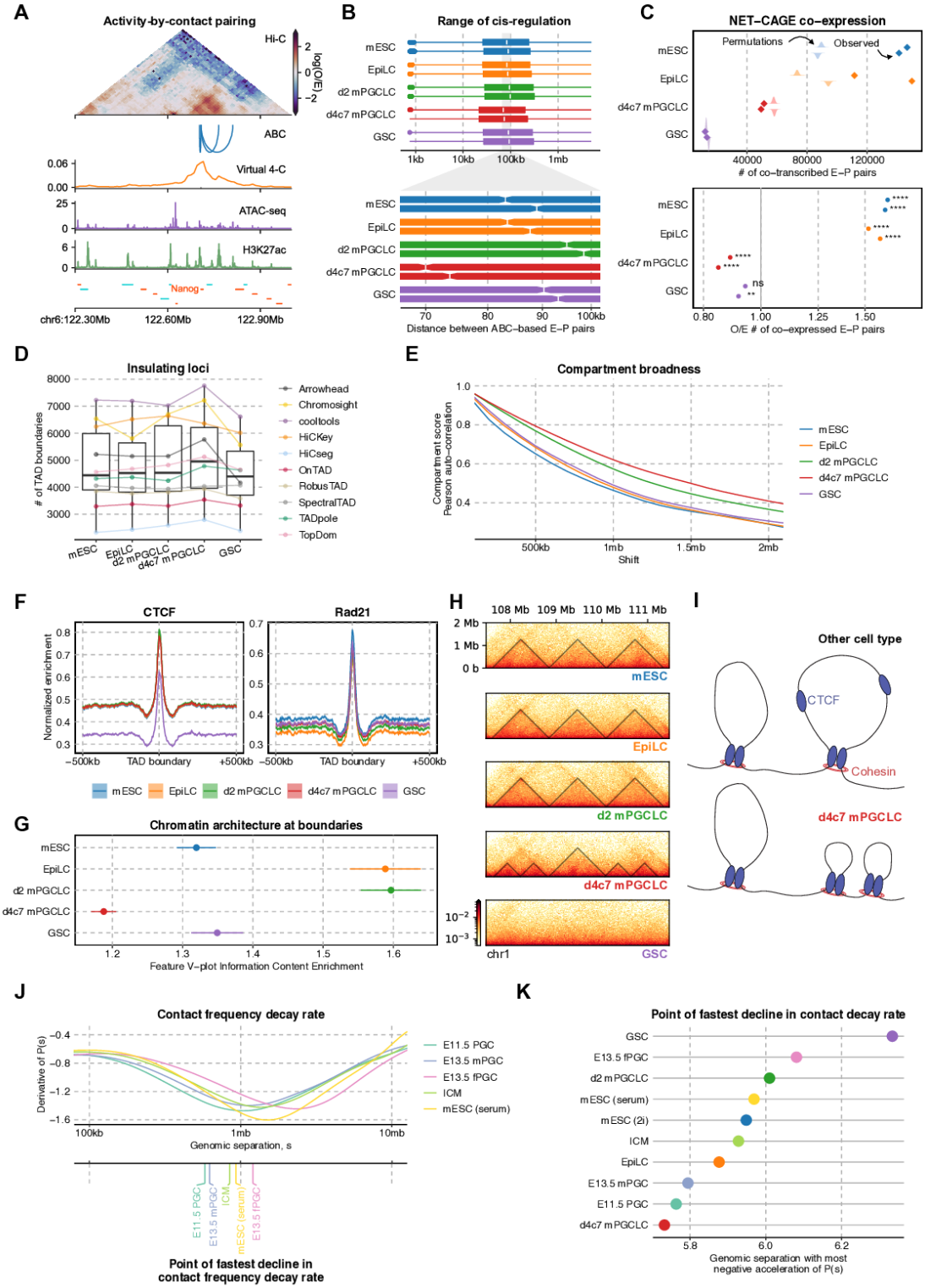
A
Activity-by-contact pairing
Hi-C
log(O/E)
ABC
Virtual 4-C
ATAC-seq
H3K27ac
Nanog
chr6:122.30Mb
122.60Mb
122.90Mb
B
Range of cis-regulation
mESC
EpiLC
d2 mPGCLC
d4c7 mPGCLC
GSC
1kb
10kb
100kb
1mb
70
80
90
100kb
Distance between ABC-based E–P pairs
C
NET–CAGE co–expression
Permutations
Observed
40000
80000
120000
# of co–transcribed E–P pairs
ns
0.80
1.00
1.25
1.50
O/E # of co–expressed E–P pairs
D
Insulating loci
# of TAD boundaries
Arrowhead
Chromosight
cooltools
HiCKey
HiCseg
OnTAD
RobusTAD
SpectralTAD
TADpole
TopDom
E
Compartment broadness
Compartment score Pearson auto-correlation
500kb
1mb
1.5mb
2mb
Shift
F
CTCF
Rad21
Normalized enrichment
–500kb
TAD boundary
+500kb
G
Chromatin architecture at boundaries
Feature V–plot Information Content Enrichment
H
108 Mb
109 Mb
110 Mb
111 Mb
2 Mb
1 Mb
0 b
chr1
I
Other cell type
CTCF
Cohesin
d4c7 mPGCLC
J
Contact frequency decay rate
Derivative of P(s)
100kb
1mb
10mb
Genomic separation, s
E11.5 PGC
E13.5 mPGC
E13.5 fPGC
ICM
mESC (serum)
Point of fastest decline in contact frequency decay rate
K
Point of fastest decline in contact decay rate
mESC (2i)
5.8
6.0
6.2
Genomic separation with most negative acceleration of P(s)

Figure EV3. Exploration of cis-regulatory element by NET-CAGE combined with Hi-C and comparison against public Hi-C datasets.

(A) An example of enhancer-promoter interactions for Nanog in mESCs as predicted by ABC, all of which correspond to known associations including super-enhancers.

(B) (Top) Distribution of distances separating ABC-predicted enhancer-promoter pairs in each replicate. Notches correspond to 1.58 * interquartile range of distances / (# of 1/2 E-P pairs) , comparable to 95% confidence intervals around the median. d4c7 mPGCLCs' E-P pairs are significantly shorter in range than those of other cell types. (Bottom) Magnified view from 60 kb to 100 kb.

(C) (Left) Co-transcription of enhancer-promoter pairs with correlated NET-CAGE expression. The observed number of correlated E-P pairs involving tag clusters transcribed (TPM > 1) in a given cell type (points) are compared against a permuted background in which tag clusters are sampled from the union tag cluster set. (Right) Observed / expected number of E-P pairs with correlated NET-CAGE expression and co-expressed (>1 TPM) in a given cell type. Two-sided permutation tests were carried out by sampling 100000 times from the set of elements expressed in at least 1 cell type, with p-values (left to right): 2e-5, 2e-5, 2e-5, 2e-5, 2e-5, 2e-5, 6.44e-3, 7.64e-2. Two biological replicates in each cell type were analyzed.

(D) Number of TAD boundaries in each cell type across 10 different algorithms. Dots correspond to values produced by a specific algorithm for a given cell type and are grouped into lines by algorithm.

(E) Auto-correlation of compartment scores (25 kb bins), with a slower decay indicative of broader compartments.

(F) Aggregate plots of S3V2-normalized ChIP-seq profiles for CTCF and Rad21 around the union set of TAD boundaries.

(G) Mean f-VICE across replicates (error bars indicate standard errors) for CTCF motifs overlapping both Rad21 and CTCF peaks within the union set of TAD boundaries.

(H) representative locus demonstrating the emergence of smaller insulated domains in d4c7 mPGCLCs within otherwise homogeneous wider TADs observed in earlier stages. (I) proposed mechanism for

elevated insulation via the reduction of loop extrusion factor's residence time, leading to shorter loops and domains.

(J) (Top) Slope of contact decay (P(s)) curves as a function of genomic separation in log-log space for in vivo germline development (Du et al., 2017, Du et al., 2020); (bottom) genomic separation with the most negative second derivative of P(s) in log-log space, corresponding to distance of fastest decline in contact frequency.

(K) Genomic separation with fastest decline in contact frequency for cell types across in vivo and in vitro germ cell differentiation.

Figure EV4

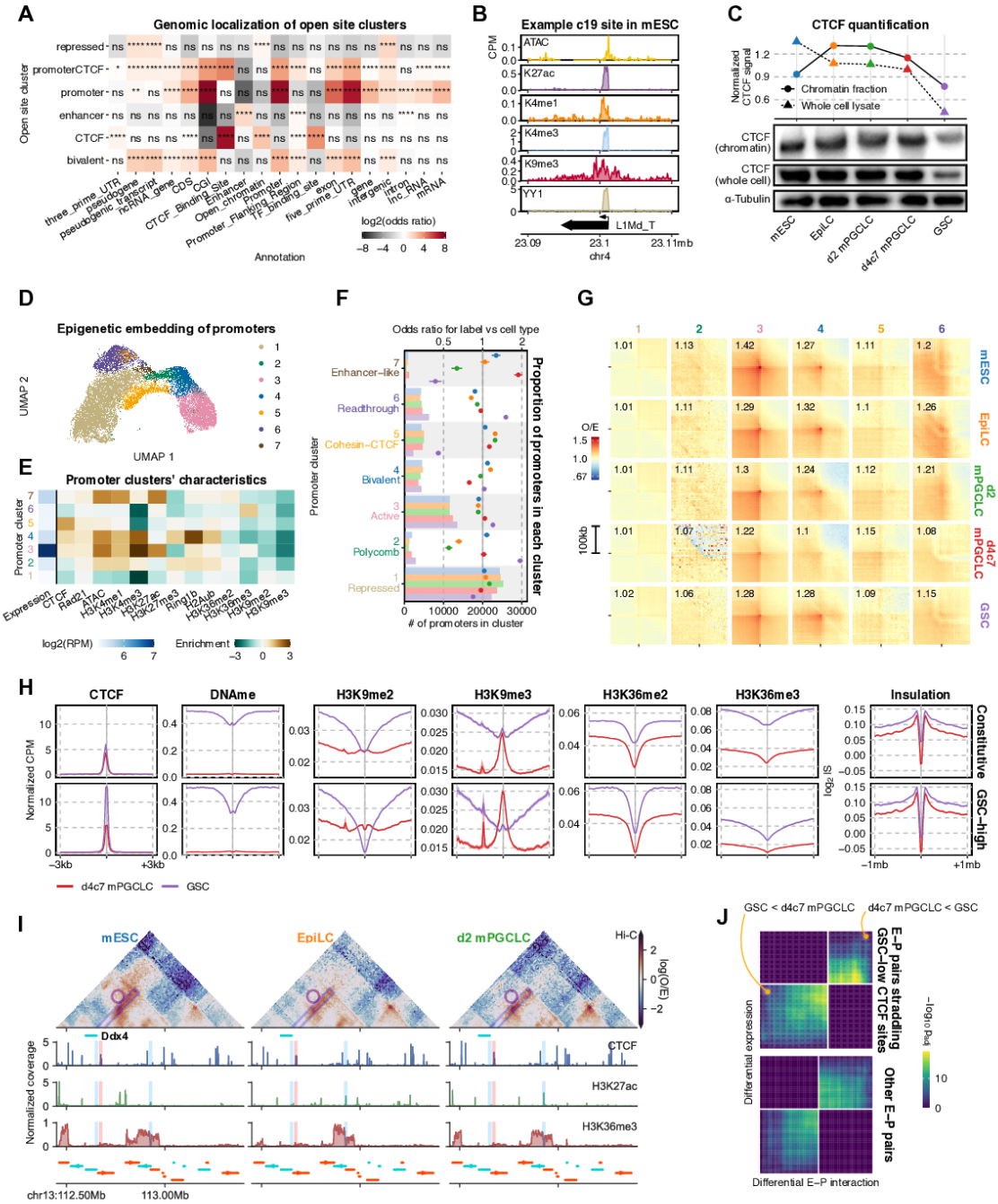
A
Genomic localization of open site clusters
Open site cluster
repressed
promoterCTCF
promoter
enhancer
CTCF
bivalent
Annotation
log2(odds ratio)
B
Example c19 site in mESC
CPM
ATAC
K27ac
K4me1
K4me3
K9me3
YY1
L1Md_T
chr4
C
CTCF quantification
Normalized CTCF signal
Chromatin fraction
Whole cell lysate
CTCF (chromatin)
CTCF (whole cell)
α-Tubulin
mESC
EpiLC
d2 mPGCLC
d4c7 mPGCLC
GSC
D
Epigenetic embedding of promoters
UMAP 2
UMAP 1
E
Promoter clusters' characteristics
Promoter cluster
Expression
CTCF
Rad21
ATAC
H3K4me1
H3K4me3
H3K27ac
H3K27me3
Ring1b
H2AUb
H3K36me2
H3K36me3
H3K9me2
H3K9me3
log2(RPM)
Enrichment
F
Odds ratio for label vs cell type
Enhancer–like
Readthrough
Cohesin–CTCF
Bivalent
Active
Polycomb
Repressed
Proportion of promoters in each cluster
# of promoters in cluster
G
O/E
100kb
mESC
EpiLC
d2 mPGCLC
d4c7 mPGCLC
GSC
H
CTCF
DNAme
H3K9me2
H3K9me3
H3K36me2
H3K36me3
Insulation
Normalized CPM
log2 IS
Constitutive
GSC–high
–3kb
+3kb
–1mb
+1mb
d4c7 mPGCLC
GSC
I
mESC
EpiLC
d2 mPGCLC
Hi-C
log(O/E)
Ddx4
CTCF
H3K27ac
H3K36me3
Normalized coverage
chr13:112.50Mb
113.00Mb
J
GSC < d4c7 mPGCLC
d4c7 mPGCLC < GSC
E–P pairs straddling GSC–low CTCF sites
Other E–P pairs
Differential expression
Differential E–P interaction
−log10 Padj

Figure EV4. Open site chromatin state dynamics and differential CTCF binding throughout germ cell differentiation.

(A) Overlap enrichment analysis of consolidated open site clusters against annotations from the Ensembl Regulatory build.

(B) Select ChIP-seq coverage tracks around a representative cluster 2 loci.

(C) Western blot against CTCF in the chromatin-bound fraction (top row) and whole cell lysate (middle row) as well as α-tubulin (bottom row) in each cell type. The signals of CTCF from whole cell lysates were normalized by α-Tubulin, while those of the chromatin-bound fraction were normalized by the mean across all cell types (top panel). (D) 2D UMAP embedding based on epigenetic signals in promoters for each cell type, with labels derived from semi-supervised HDBSCAN.

(E) Enrichment of epigenetic signals in each promoter cluster and expression of the cognate gene.

(F) Association between promoter clusters and cell types, as described in (B).

(G) Pile-up plots of intra-class promoter-promoter interactions.

(H) Contributors of differential CTCF binding. The aggregate plot of various ChIP-seq enrichment signals (left) as well as the insulation score (right) near CTCF-binding sites found both in cell types ("constitutive") or only GSCs but not in d4c7 mPGCLCs ("GSC-high") appear largely identical in their chromatin state yet distinct from those lost in GSCs. n = 35692/13364 for constitutive/GSC-high peaks.

(I) 3D epigenetic landscape rewiring near Ddx4. Observed/expected contact maps at 10 kb resolution for mESCs, EpiLCs and d2 mPGCLCs are shown alongside select ChIP-seq coverage tracks. A strongly insulating CTCF peak (highlighted in orange) upstream of Ddx4's TSS is found in all earlier stages and prevents spurious activation. (J) Coordinated differential expression and E-P looping between d4c7 mPGCLCs and GSCs. Strong correlation was observed when applying stratified rank-rank hypergeometric overlap to genes ranked by differential expression versus differential E-P interactions straddling sites depleted of CTCF binding in GSCs. While increased E-P looping is correlated with elevated expression regardless of whether the interaction spans differential CTCF-bound sites, the degree of coordination is stronger (i.e., more significant / brighter) for those that do straddle GSC-depleted sites.

Figure EV5

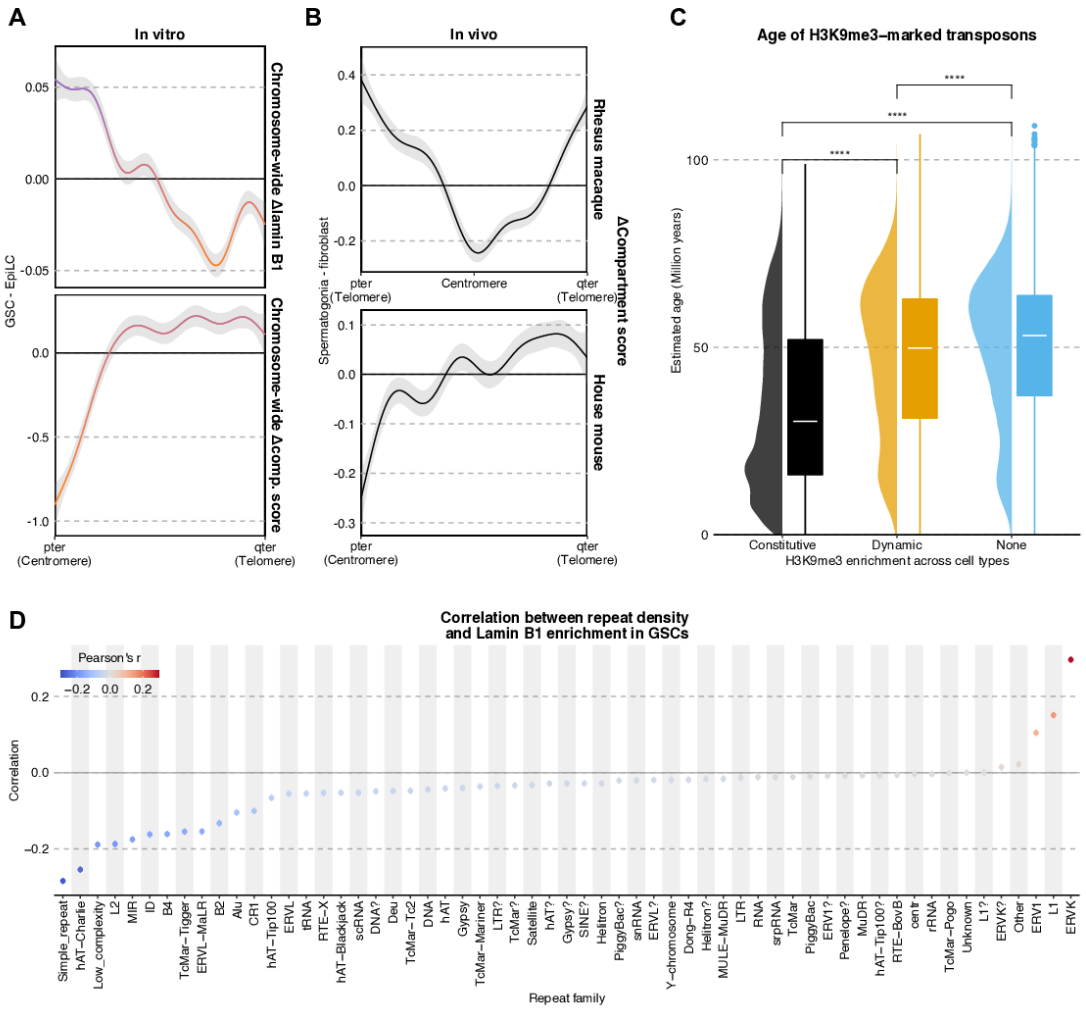
A
In vitro
Chromosome-wide Δlamin B1
Chromosome-wide Δcomp. score
GSC - EpiLC
pter (Centromere)
qter (Telomere)
B
In vivo
Rhesus macaque
House mouse
ΔCompartment score
Spermatogonia - fibroblast
pter (Telomere)
Centromere
qter (Telomere)
C
Age of H3K9me3–marked transposons
Estimated age (Million years)
Constitutive
Dynamic
None
H3K9me3 enrichment across cell types
D
Correlation between repeat density and Lamin B1 enrichment in GSCs
Pearson's r
Correlation
Repeat family

Figure EV5. Inter-species comparison of germ-cell specific chromatin structure and characterization of H3K9me3-enriched repeats.

(A) Average distributions of differential (GSC – EpiLC) lamin B1 enrichment (top) or compartment score (bottom) across all chromosomes (1–19, X). Ribbons correspond to 95% confidence intervals of fitted GAMs.

(B) Average distributions of compartment score (spermatogonia – fibroblast) across all chromosomes (excluding Y) for Macaca mulatta (top) and Mus musculus (bottom).

(C) Estimated age of families overlapping H3K9me3 domains based on age = divergence/substitution rate with 4.5×10-9 as the rate and milliDiv from RepeatMasker as the divergence (Bourque, Leong et al., 2008). P-values are computed using Wilcoxon rank-sum tests.

(D) Correlation between lamin B1 enrichment and density for different repeat families.

Non-mutational epigenetic reprogramming will come to be accepted as a bona fide enabling characteristic that serves to facilitate the acquisition of hallmark capabilities, distinct from that of genomic DNA instability and mutation. Notably, it can be anticipated that non-mutational epigenetic reprogramming will prove to be integrally involved in enabling the provisional new hallmark capability of phenotypic plasticity

Douglas Hanahan

Chapter 3

H3K27me3 spreading organizes canonical PRC1 chromatin architecture to regulate developmental transcriptional program

Having established the importance of nuclear architecture throughout germline development in the previous chapter, we now turn our attention to possible faulty 3D epigenome dynamics in disease. Polycomb group proteins, in particular, have a storied past as the archetypal mediator of epigenetic transcriptional regulation and serves critical functions in the proper orchestration of various early developmental programs.[65] For instance, germ-cell differentiation entails dynamic expression of germline-specific Polycomb-related factors such as SCML2 and EZHIP whose loss can lead to infertility.[66,67] Accumulating evidence suggests that Polycomb-mediated regulation can take shape both within local chromatin domains as well as across large genomic separations via distal chromatin looping. Recent results highlighting the importance of these processes in early development thus lead us to re-examine the effect of epigenetic dysregulation on 3D genome organization in several disease states studied by our labs.

Broadly, the Polycomb Repressive Complexes exist as critical machineries regulating transcription through inducing facultative heterochromatinization by means of depositing histone modifications such as H3K27me3 and H2AK119ub, the target of which are often key developmental regulators dynamically expressed during the course of differentiation. But the set of associated factors also form an intricate interaction network given their dual reader-writer capacities for diverse epigenetic markers. As the counterpart to Polycomb, a collection of SET domain-containing enzymes catalyzing H3K36 methylation such as NSD1 mediates the deposition of euchromatic H3K36 methylome, in turn shaping the facultative heterochromatin landscape through their mutual antagonism. With the factors governing this euchromatin-heterochromatin balance dynamically shifted during development and perturbed in a variety of diseases, we here holistically assess the impact of these events on the 3D epigenome through applying Hi-C, ChIP-seq, RNA-seq to assay stem and cancer cells.

H3K27me3 spreading organizes canonical PRC1 chromatin architecture to regulate developmental transcriptional program

Brian Krug[1,18], Bo Hu[1,2,3,18], Haifen Chen[1,2,18], Kristjan H. Gretarsson[4,18], Nisha Kabir[1,5], Xiao Chen[4], Shriya Deshmukh[6], Elias Jabbour[1], Ashot Harutyunyan[1], John J. Y. Lee[7,8,9], Damien Faury[10], Caterina Russo[10], Michael J. Johnston[11,12], Marco Gallo[11,12,13], Michael D. Taylor[7,8,9,14,15], Claudia L. Kleinman[1,5], Chao Lu[4,16], Jacek Majewski[1,2], Nada Jabado[1,6,10,17]

[1]Department of Human Genetics, McGill University, Montreal, QC H3A 1B1, Canada
[2]McGill University Genome Centre, Montreal, QC H3A 0G1, Canada
[3]Department of Anatomy and Cell Biology, Graduate School of Medicine, Kyoto University, Yoshida-Konoe-cho, Sakyo-ku, Kyoto 606-8501, Japan.
[4]Department of Genetics and Development, Columbia University Irving Medical Center, New York, NY 10032, USA
[5]The Lady Davis Institute, Jewish General Hospital, Montreal, QC H3T 1E2, Canada
[6]Division of Experimental Medicine, Department of Medicine, McGill University, Montreal, QC H4A 3J1, Canada
[7]The Arthur and Sonia Labatt Brain Tumor Research Center, The Hospital for Sick Children, Toronto, ON M5G 0A4, Canada
[8]Developmental & Stem Cell Biology Program, The Hospital for Sick Children, Toronto, ON M5G 0A4, Canada
[9]Department of Laboratory Medicine and Pathobiology, University of Toronto, Toronto, ON M5G 1L7, Canada
[10]Department of Pediatrics, McGill University, The Research Institute of the McGill University Health Center, Montreal, QC H4A 3J1, Canada
[11]Arnie Charbonneau Cancer Institute, Cumming School of Medicine, University of Calgary, Calgary, Alberta T2N 1N4, Canada
[12]Alberta Children's Hospital Research Institute, Cumming School of Medicine, University of Calgary, Calgary, Alberta T2N 1N4, Canada
[13]Department of Molecular Biology and Biochemistry, Cumming School of Medicine, University of Calgary, Calgary, Alberta T2N 1N4, Canada
[14]Department of Medical Biophysics, University of Toronto, Toronto, ON M5G 1L7, Canada
[15]Division of Neurosurgery, The Hospital for Sick Children, Toronto, ON M5G 1L7, Canada
[16]Herbert Irving Comprehensive Cancer Center, Columbia University Irving Medical Center, New York, NY 10032, USA
[17]The Research Institute of the McGill University Health Center, Montreal, H4A 3J, Canada

[18]These authors contributed equally.

Corresponding authors:
cl3684@cumc.columbia.edu
jacek.majewski@mcgill.ca
nada.jabado@mcgill.ca

Abstract

Polycomb Repressive Complex 2 (PRC2) nucleates and propagates H3K27me3 to recruit canonical PRC1 (cPRC1), establishing repressive heterochromatin at developmental genes. Mechanisms that either broaden or restrain spatial distributions of H3K27me3 are dysregulated in several pediatric cancers and developmental syndromes. Higher order cPRC1 chromatin looping has been observed in stem and progenitor cell types that resolves upon cell differentiation despite increasing levels of H3K27me3. It remains unclear, however, how cPRC1 interactions are dynamically regulated and how they affect the silencing of polycomb genes during development. We show that focal H3K27me3 confinement in histone H3 Lys-27-Met (H3K27M) mutant gliomas concentrates chromatin occupancy of cPRC1 complexes. This results in long-range chromatin interactions and aggregates anchored in polycomb bodies mirroring patterns found in stem cells. Conversely, pervasive spreading of H3K27me3 following loss of the H3K36 methyltransferase NSD1 in pluripotent stem cells leads to cPRC1 dilution and disrupts polycomb body architecture. Inhibition of H3K27me3 spreading by H3K27M causes sustained repression of genes tethered to polycomb bodies, which associates with self-renewing progenitor states that drive tumour development in isogenic patient-derived xenograft models. This effect depends on H3K27me3 recognition by cPRC1, as chemical allosteric modulation of chromodomains can alleviate repression of transcription and promote differentiation. These results suggest that polycomb gene expression programs orchestrating developmental transitions are controlled by the dissolution of repressive 3D loop architecture. The writer-reader relationship between PRC2/1 therefore shapes a tradeoff in the quality versus quantity of chromatin silencing and its imbalance explains disease states caused by altered H3K27me3 spread.

Introduction

Polycomb repressive complexes are essential and conserved writers (PRC2) and readers (PRC1) of histone H3 lysine 27 methylation (H3K27me).[1] Facultative heterochromatin is established and inherited via chromatin nucleation of PRC2 and the spreading of a histone post-translational modification (PTM): H3K27me3.[2] Chromodomain subunits of canonical PRC1 (cPRC1) recognize H3K27me3 and contribute to promoter silencing by chromatin compaction of self-associating domains.[3] H3K27me3-enriched regions have been implicated as distal silencers, with their excision leading to up-regulation of target genes.[4] Over the course of development, controlled de-repression of master-regulatory transcription factors is required for lineage specification and differentiation.[5] PRC2 spread of H3K27me3 is cooperatively regulated by diverse factors including H3K36 di/trimethylation (H3K36me2/3), 5-methylcytosine, PRC2 subunit composition and allosteric stimulation from EED.[6] Driver mutations found in several types of cancers display effects converging to alter H3K27me3 spread.[7]

Spatial segregation of chromatin loop structures containing PRC2/1, termed polycomb bodies, are observed in primed pluripotent stem cells and several progenitor cell types.[4, 8] Furthermore, cohesin depletion can enhance long-range interactions between polycomb targets while diminishing interactions of cohesin binding sites, distinguishing polycomb-mediated nuclear architecture from conventional cohesin-mediated loop extrusion.[9, 10] However, the transcriptional effects and downstream physiological consequences of long-range H3K27me3 spread and polycomb body architecture are unclear. We ask whether the relationship between PRC2 spread and 3D genome organization may contribute to abnormal developmental outcomes in disease.

Confined H3K27me3 deposition associates with enhanced chromatin looping

The histone H3 Lys-K27-Met (H3K27M) driver mutation of pediatric midline high-grade gliomas (HGGs) shares structural resemblance to EZH Inhibitory Protein (EZHIP), whose ectopic expression defines posterior-fossa group A ependymomas (PFA-EPN). Both oncogenic proteins are potent

inhibitors of H3K27me3 spread from PRC2 nucleation sites, leading us to investigate these tumours to understand relationships with chromatin architecture. They contribute to tumour initiation linked to impaired differentiation potential and elevated cycling progenitor states.[11, 12] These tumours are critically dependent on residual H3K27me3, distinguishing H3K27M/EZHIP-associated malignancies from those displaying complete loss of PRC2 function.[13] Their patterns of PRC2 distribution strongly resembles that of primed pluripotent stem cells (PSCs), wherein focal H3K27me3 domains repress target genes to preserve self-renewal and are associated with the formation of polycomb bodies. We therefore sought to investigate these tumours to understand relationships between H3K27me3 and polycomb-associated chromatin architecture.

We generated global comparisons of chromatin states and architecture by integrating ChIP/CUT&RUN-seq and Hi-C chromatin conformation capture data. Isogenic patient tumour-derived cell lines in which we either expressed H3K27M, or knocked out endogenous mutant alleles (KO) allowed us to delineate the mutation's effect in disease-relevant contexts.[14, 15] We also compared PFA-EPN-derived cell cultures expressing EZHIP when maintained in hypoxia to those losing EZHIP in normal oxygen levels.[16] These brain tumour datasets were compared to developmental contexts of altered H3K27me3 spread (Figure 1A). We tested human induced pluripotent stem cells (hiPSC) and mouse embryonic stem cell (mESC) differentiation to neural progenitor cells (NPCs), and mESCs cultured in naïve (2i/LIF media) or primed (serum media) pluripotency conditions. Entrance to primed pluripotency from the naïve ground state was previously described to confine H3K27me3 and heighten polycomb loop architecture, both of which diminish when exiting pluripotency upon differentiation.[17] We adapted quantitative metrics of H3K27me3 confinement to evaluate genome-wide distributions across each model (Figure S1A-D). This approach consistently quantifies the observed H3K27me3 confinement in H3K27M/EZHIP-expressing tumours and PSCs (Figure 1A-C). Published H3K27me3 ChIP-seq data from mouse embryonic brain demonstrate diminishing confinement scores between E10-E15 time points (Figure S1E). In resembling patterns of PSC to NPC transitions, this confirms that H3K27me3 spreading is a feature of *in vivo* differentiation and early development.

Limited H3K27me3 spread is universally linked with greater 3D contacts between H3K27me3 sites. We pile up evaluated pairwise interaction between CGIs enriched for H3K27me3, which revealed that such interactions are specifically enriched in H3K27M/EZHIP-expressing gliomas and PSCs that confine H3K27me3 spread (Figure 1D-E). Notably, H3K27M does not appreciably alter the number of CTCF ChIP-seq peaks or contact frequencies among these sites (Figure S2A-B), precluding their identity as conventional cohesin/CTCF-associated loops. At the Homeobox D (HOXD) cluster, H3K27M mutants display multiple distal loop contacts between H3K27me3 peaks, that are lost in KO lines when H3K27me3 spreads over extended domains (Figure 1F). Strengthened interaction between two otherwise insulated domains is especially evident in the 3D structures predicted from the same locus (Figure 1G). As these types of chromatin loops can span tens of megabases, cross TAD boundaries, and anchor multiple sites at one location, they stand in stark contrast to typical loop extrusion associated structures typically on a sub-megabase scale. By assessing which transcriptional regulator's binding sites are over-represented among regions participating in differential chromatin interactions between isogenic H3K27M/KO comparisons, we instead find PRC2 components emerge as the most strongly associated with H3K27M-specific interactions (Figure S2C). Additionally, changes in compartment or insulation scores across isogenic pairs derived from different cell lines show limited concordance (Figure S2D), suggesting that H3K27M-associated changes in H3K27me3 does not substantially alter compartmentalization and domain architectures. Indeed, when comparing the Hi-C profiles of various brain tumors subtypes, we found that H3K27M tumors did not constitute its own unique subgroup through the lens of compartment and insulation scores (Figure S3).

The link between H3K27me3 confinement and 3D chromatin architecture is also observed in several other cancers. We sampled published datasets of matched comparisons of H3K27me3 profiles and Hi-C. Gain of NSD2 expression or loss of histone H1 impairs H3K27me3 spread in multiple myeloma and lymphoma models, respectively.[18, 19] Loss of the tumour-suppressor and H2AK119 deubiquitylase BAP1 increases H3K27me3 spread in mESCs.[20] We further considered heterozygous and homozygous

loss of NSD1 in mouse and human PSCs in which H3K27me3 spreads upon H3K36me2 loss (Figure S4A-B). In each scenario, greater H3K27me3 confinement associated with increased contact frequencies between CGIs (Figure S4C-G). This suggests that H3K27me3 spread establishing chromatin architecture is a broadly applicable organizing principle in contexts of oncogenic transformation.

Confined H3K27me3 concentrates canonical PRC1 to drive polycomb body compaction

We sought to delineate mechanisms of polycomb loop architecture by charting PRC1 localization and activity. Canonical PRC1 links Chromobox (CBX2/4/6/7/8) recognition of H3K27me3 to spatial chromatin organization via SAM domain oligomerization between PHC1, PHC2 or PHC3 subunits and phase separation properties of the CBX2 subunit.[21] We profiled pools of PRC1 complexes by ChIP-seq of the RING1B core subunit, and CBX2 that is unique to cPRC1 and robustly expressed across cell lines (Figure S5A). H2AK119ub ChIP-seq portrays catalytic activity of PRC1 complexes.

Focal H3K27me3 confinement uniquely concentrates the canonical subset of PRC1 complexes. Using a peak-calling approach, we noted that a minority of H3K27me3 and RING1B peaks overlap at CpG islands, marking dual PRC2 and PRC1 enrichment. CBX2 peaks show large overlap with these intersection sites, which identifies canonical PRC1 (containing CBX2) as the reader for a subset of H3K27me3, while non canonical PRC1 (lacking CBX2) is widely distributed outside of PRC2 domains (Figure 2A-B, S5B-C). Sites of H3K27me3, RING1B and CBX2 overlap displayed significantly higher H3K27M-enriched contact frequencies compared to other peak categories (Figure 2A), suggesting a link between cPRC1 and the formation of polycomb looping in H3K27M cells. Substantial RING1B enrichment can also exist at H3K27ac-marked sites devoid of H3K27me3, displaying 3D interactions characteristic of active enhancers (Figure S5D).[22] We subsequently sought to quantify how H3K27M affects cPRC1 signal intensity. When H3K27me3 spread is confined, the retainment of H3K27me3 enrichment at specific CGIs correlates with several-fold higher signals of RING1B and CBX2 enrichment (Figure 2C), indicating RING1B and CBX2 are concentrated specifically in regions where H3K27me3 is confined. We can additionally recapitulate this redistribution in other H3K27M glioma cells as well as

by expressing H3K27M in WT glioma cells to show the mutation reversibly drives these effects (Figure S6). In contrast, cPRC1 redistribution did not appreciably alter tumour H2AK119ub profiles (Figure 2B, D, S6A, C, H), corroborating observations that this PTM is largely deposited by variant PRC1 complexes in somatic cell types.[23]

Links between H3K27me3 confinement and polycomb-associated chromatin looping motivated our investigation of opposing scenarios of heightened PRC2 spread. The H3K36me2 PTM limits H3K27me3 deposition in euchromatin regions. Mutations of the H3K36 dimethylase Nuclear Receptor Binding SET Domain Protein 1 (NSD1) or histone H3 Lys-36-Met (H3K36M) result in loss of H3K36me2 and increased H3K27me3 spread in stem cells and cancers.[24, 25] Somatic NSD1 or rare H3K36M mutations underlie a subgroup of head and neck squamous cell carcinoma (HNSCC),[26] and H3K36M is the predominant driver of chondroblastoma tumours.[27] Germline loss of NSD1 function also defines Sotos syndrome, wherein patients display precocious developmental progression and overgrowth,[28] yet the effect of chromatin perturbations is unclear. We profiled chromatin conformation in PSCs harboring either heterozygous NSD1 loss (human iPSCs) or homozygous knockout (mESCs). In WT PSCs, H3K27me3 and RING1B peak overlap largely correspond with CBX2 peaks (Figure 2E-F, S7A-B). The loss of NSD1 leads to decreased H3K36me2 and increased spread of H3K27me3 deposition (Figure 2F-G, S4A-B). Regions with decreased cPRC1 binding due to complete or partial loss of NSD1 coincide with strongly H3K27me3-enriched regions in WT cells that subsequently see substantial decreases (Figure 2G-H, S7C-D). Taken together, cPRC1 dilution from CGIs upon NSD1 loss resulted in decreased contact enrichment specifically at sites of PRC2/1 overlap (Figure 2E, S7A). Consequently, in pluripotent states, polycomb bodies are sensitive to disruption by abolishing H3K36me2 that confines H3K27me3 spreading and preserves cPRC1 concentration at nucleation sites.

Distinctive features of polycomb bodies in pluripotency and cancer

We next integrated high-dimensional profiles for a greater variety of chromatin modifiers and PTMs to comprehensively characterize the distinct chromatin states of polycomb bodies. We examine ChIP-seq

datasets of several active (H3K27ac, H3K4me3, H3K36me2/3), repressive (H3K27me3, PRC2/1, H3K9me3) and architectural (CTCF, SMC1) features. We used UMAP projections in combination with HDBSCAN clustering to stratify signal enrichment at CGIs and promoters, as they organize locations of cis-regulatory elements (Figure 3A,E,G). This holistic classification reaffirms overlap of a subset of H3K27me3-enriched sites with RING1B and CBX2 signals in tumours, mESCs and hiPSCs (Figure 3A-B, E-F, G-H). We next divided CGIs and promoters into 4 main clusters; 1) Active (H3K27ac, H3K4me3), 2) cPRC1 (CBX2, RING1B, H3K27me3), 3) PRC2 (H3K27me3, SUZ12, absent CBX2) and 4) Other (lacking distinctive enrichment). Although the non-active clusters broadly represent non-expressed genes, cPRC1 targets were noted to experience the greatest level of repression (Figure S8A). The active and other site classification is largely conserved among 3 different H3K27M tumour-derived cultures, while cPRC1 and PRC2 sites display greater diversity (Figure S8B). Differential contact frequencies are predominantly found in cPRC1 targets (Figure 3D, I, S8C), confirming our earlier findings. As expected, cPRC1 target genes associate with pathways of developmental specification, including processes such as neural differentiation (Figure S8D).

A subset of promoters in several cell states are described as bivalent; dually carrying H3K27me3 and H3K4me3, wherein productive transcription is absent but can be rapidly activated upon change in stimuli.[29] Our mESC and hiPSC datasets substantiate H3K4me3 bivalency throughout PRC2 and cPRC1 clusters (Figure 3E-F,G-H). Differential contact frequencies confirm the predicted loop architecture driven by NSD1 is specific to the cPRC1 cluster (Figure 3I). Previous H3K27M glioma models were reported to alter expression of bivalent genes.[30, 31] H3K4me3 marked approximately half of cPRC1 and PRC2 cluster sites of tumours (Figure 3A). We subdivide the bimodal distributions into H3K4me3-: absent of H3K4me3 enrichment, and H3K4me3+: enriched for bivalent H3K4me3 signal (Figure 3C). Importantly, differential contact frequencies caused by H3K27M were specific to cPRC1 H3K4me3- sites and not H3K4me3+ ones (Figure 3D, S8C). Furthermore, this loop architecture is conserved between cell cultures and patient tumours: consensus cluster cPRC1 H3K4me3- sites among tumour-derived lines show elevated contact frequencies in H3K27M HGGs and PFA-EPNs, compared

to normal fetal and adult brain and WT HGGs (Figure S9A). Absence of H3K4me3 at nearly half of cPRC1 targets in H3K27M HGGs distinguishes them from wholly bivalent patterns found in primed pluripotency. Moreover, cPRC1 can be concentrated at hundreds of target sites, but this does not compact loops when sites are accessible to H3K4me3 deposition. This heterogeneity in architecture among cPRC1 sites likely reflects the preservation of chromatin states from tumours' lineage of origin.

Accumulated findings posit that competition between PRC1/2 and the H3K4 methyltransferases Complex of Proteins Associated with Set1 (COMPASS) controls promoter expression.[32] We find cPRC1 H3K4me3- sites specifically gain H3K4me3 enrichment when H3K27M is lost (Figure 4A). Distal loop compaction thus predicts diminished H3K4me3 deposition, which rises when polycomb bodies are dissolved. This decompaction and acquisition of transcription associated H3K4me3 led us to profile consequences of chromatin architecture on gene expression.

Aggregation of polycomb bodies represses target expression

Differential compaction of polycomb bodies further predicts the absence of transcription in primary tumours. We surveyed single cell RNA sequencing cohorts from H3K27M and histone-WT HGGs, and normal human fetal brain. Using consensus promoter classification derived from three cell lines, we found that genes associated to the active cluster are similarly expressed at a high level across tumor types, while cPRC1 H3K4me3- targets are specifically repressed in H3K27M glioma tumour cells (Figure 4B). When portraying mean expression of cPRC1 H3K4me3- targets among heterogeneous cell populations, we observed that they were homogeneously silenced in H3K27M tumour cells, whereas the same gene set was variably expressed in H3WT HGG and fetal brain cells (Figure 4C). In contrast, H3K4me3+ cluster 2B genes are expressed at equivalent levels, indicating some cPRC1 sites can remain expressed when not compacted by H3K27M (Figure 4B). We can further demarcate cell type categories using signatures that portray continuums of cell lineage differentiation among scRNA-seq datasets. Cluster 2A expression is not biased towards specific cell types or by differentiation or progenitor status, indicating this broad group of genes includes regulators of several lineages (Figure S9B).

To test the functional significance of repressive chromatin compaction, we examine experimental models of H3K27M's tumourigenic potential. Among isogenic cell cultures, H3K27M is required to maintain cells' tumour-forming competence when engrafted into orthotopic sites of mice.[14] We found H3K27M-KO lines, despite the absence of tumour development, survive and engraft to contribute a substantial proportion of cells in the murine brain (Figure 4D, S9C). We labeled and recovered matched pairs of H3K27M and KO engrafted cells from mice and use scRNA-seq to profile *in vivo* cell states. In three model systems, H3K27M diminishes expression of mature glia signature genes and representation of these cell populations, instead favouring glial progenitor cell types (Figure 4E). H3K27M-mutant tumour cells recurrently form lethal tumours containing a substantial fraction of cells resembling radial glial progenitors, which are largely lost in engrafted KO cells that fail to form tumours (Figure 4F, S9D). Other than other, examination of cluster 2A expression revealed that H3K27M repression acts across all cell type subpopulations (Figure 4F, S9D). Reversal of cPRC1 concentration and polycomb body decompaction can therefore restore potential for greater transcription of target genes. These relevant models identify cPRC1 repression occurring during impaired differentiation that forms the basis of H3K27M tumour development (Figure 4F).

We also determined the transcriptomic effects of aberrant polycomb body loss by NSD1 depletion in PSCs. Comparison of differential intra-class long-range interaction versus differential expression revealed that only cPRC1 target genes experience robust up-regulation upon decreased looping (Figure S10). Genes significantly de-repressed in NSD1-haploinsufficient iPSCs (NSD1+/-) include cPRC1-compacted targets relevant to development, including the HOXB cluster, GATA4 and EVX2. Therefore, polycomb chromatin looping is required for stable silencing of cPRC1 target genes. These effects are reminiscent of iPSCs that de-repress strong polycomb targets when PRC2 spread is enhanced by the formation of PRC2.2 subcomplexes instead of PRC2.1.[33]

Obstructing chromodomain recognition of H3K27me3 alleviates differentiation blockade

We next assessed the transcriptomic consequences of polycomb bodies in different cell culture conditions. Routine maintenance of the lines in media conditions favouring neural stem cell self-renewal promotes the growth of both H3K27M and KO lines. We previously demonstrated H3K27M dramatically impairs cells' differentiation status that only emerges upon application of culture media promoting glial fate acquisition.[11] Although select few genes (including PRDM13) gain expression in KO lines after loss of polycomb looping (Figure 5A-B), overall we observe relatively minor repressive effects of H3K27M on the expression of cluster 2A targets in stem cell media (Figure 5C, S11A). However, differentiation media conditions further accentuate differences in expression, reflecting continued H3K27M repression and specific upregulation of cluster 2A in differentiated KO lines (Figure 5C, S11A). Transcription of cPRC1 target genes is thus conditional on signaling stimuli applied to cell cultures. These stimuli are required to recapitulate the expression differences observed in xenograft models and patient tumours compared to normal brain tissue. This was not surprising, since polycomb bodies undergo substantial remodeling during developmental transitions.

Finally, we sought to test whether cPRC1 concentration is causal to target repression and impaired differentiation potential due to H3K27M. cPRC1 recruitment and residence time on chromatin depends on chromodomain affinity for H3K27me3 substrate recognition.[34] Chemical probes have been developed that selectively obstruct the chromodomain reading of H3K27me3 by various CBX proteins. These allosteric modulators (CBX-AM) can dilute cPRC1 occupancy at H3K27me3-marked targets and can promote their expression.[35] These compounds precisely reverse cPRC1 concentration we show to nucleate polycomb body architecture of H3K27M mutants. We thus tested whether these compounds overcome target repression and the associated differentiation impairment.

We added the CBX-AM UNC4976 to H3K27M-mutant cultures at the onset of differentiation stimuli and observed specific de-repression of cluster 2A (Figure 5D, S11B). This effect argues that H3K27M-driven concentration of cPRC1 via chromodomain reading of H3K27me3 forms the basis of target repression, as RING1B and CBX2 is specifically diluted from cPRC1 targets (Figure 5E). This repression

is thus reversible through cPRC1 dilution due to either loss of H3K27M and spread of H3K27me3, or obstruction of CBX reading of H3K27me3. Subsequently, we profiled cultures for markers of differentiation; the astrocyte marker glial fibrillary acidic protein (GFAP) in DIPGXIII and the OPC marker SRY-Box Transcription Factor 10 (SOX10) in BT245. CBX-AM treatment raised GFAP and SOX10 protein signals to intermediate or comparable levels of that of KO lines (Figure 5E, S11C-D). cPRC1 dilution and target de-repression therefore endow competence for greater differentiation to mature glia. Differentially expressed genes significantly correlate when comparing the H3K27M transcriptome to either CBX-AM treatment or H3K27M-KO (Figure S11D), corroborating cell states marked by patterns of GFAP and SOX10. These effects argue that chromodomain localization determines downstream gene expression and cPRC1 repression plays a key role in restricting tumour cell differentiation. Our *in vitro*, *in vivo*, and patient tumour systems support this mechanism as central to H3K27M mutants' process of oncogenic transformation.

Discussion

Loss and gain of function alterations to PRC2/1 can promote cancers or genetic disorders, yet we lack a unified understanding connecting them with disease development. We identify features of PRC2/1 that explain their functional outcomes; 1) Nucleation and spread of PRC2 depositing H3K27me3 are separate sequential processes, 2) the pool of cPRC1 complexes read the genome-wide H3K27me3 distribution, but it is limited in the amount available to bind chromatin, and 3) cPRC1 target repression depends on higher order aggregation, which in turn requires a sufficiently high local concentration in space. We show that the extent of H3K27me3 spread from PRC2 nucleation sites can be broadly categorized into confined versus diffuse patterns, and that this dichotomy further determines chromatin architecture as confinement of H3K27me3 concentrates cPRC1 to facilitate self-association of cPRC1. Enhanced or impaired spread of PRC2 trimethylase activity can thus modulate the means through which its role as an epigenetic repressor manifest. Target genes often orchestrate developmental fate specification, and the concentration of cPRC1 can 'freeze' cell architecture to stall differentiation programs in select cancers. We further show tumour progenitor cell polycomb bodies exclude H3K4me3, unique from stem cell

bivalency. This architectural feature lends understanding to proposed models of bi-phasic switches in promoter activity arising from competition between Polycomb group and Trithorax group members.[36]

Our findings suggest a mechanism for the phenotypic resemblance between Sotos syndrome and a family of Weaver syndrome-related overgrowth disorders that include mutations in EZH2, SUZ12 or EED subunits of PRC2.[37, 38] The Weaver syndrome EZH2-K634E variant located in the pocket sensing H3K36me2/3 increases H3K27 methylation on H3K36-methylated substrates.[39] Enhanced H3K27me3 spread is therefore plausible in the same disease as loss of PRC2 activity. Both effects could dilute cPRC1 repression in progenitor cells and parallel the effects of NSD1 mutations. Precocious polycomb body dissolution may thus contribute to Sotos syndrome patients' characteristic accelerated growth rates from early childhood and advanced morphological and molecular aging markers.[40]

Hox gene clusters are prototypical polycomb targets that are altered in cancers and Sotos syndrome.[41-43] They begin as silenced in pluripotency and then segmentally lose PRC2/1 repression during spatial axial patterning and temporal maturation.[44] H3K27M tumours only express select anterior segments of Hox clusters, which can evolve towards developmentally 'aged' states after loss of H3K27M-driven compaction of posterior segments. We propose the inaccessibility of master-regulatory posterior Hox codes may contribute to stalling differentiation of tumours. Many cancers depend on PRC2/1 activity, motivating the design of targeted therapies against them. The universal association of H3K27me3 confinement with loop architecture facilitates predicting whether oncogenic H3K27me3 alterations will either repress or activate polycomb targets. Understanding cPRC1 functional complexity will require the study of subunit expression across cell types, their stochiometric composition and the variety of cofactors recruiting them to chromatin. These careful considerations serve to identify therapeutic agents with the potential to overcome self-renewal in numerous cancers.

Acknowledgements

This work was supported by a Large-Scale Applied Research Project grant from Genome Quebec, Genome Canada, the Government of Canada, and Ministère de l'Économie, de la Science et de l'Innovation du Québec, with the support of the Ontario Research Fund through funding provided by the Government of Ontario to N.J., J.M. and C.L.K.; the Canadian Institutes for Health Research (CIHR; grants PJT-156086 to C.L.K., and MOP-286756 and FDN-154307 to N.J.); the National Sciences and Engineering Research Council (NSERC; grant RGPIN-2016-04911 to C.L.K.). J.M. and N.J. is supported by funding from the United States National Institutes of Health (NIH) Grant P01-CA196539; C. L. is supported by funding from NIH Grant R35GM138181 and the Pew-Stewart Scholars for Cancer Research Award; B. A. G. is supported by NIH grants CA196539 and AI118891, and the St. Jude Children's Hospital Chromatin Consortium; B. H. is supported by the Canadian Institutes of Health Research (CIHR) Banting and Best Graduate Scholarship. C.L.K. is supported by a salary award from Fonds de recherche du Québec (FRQS). N.J. is a member of the Penny Cole Laboratory and holds a Canada Research Chair Tier 1 in Pediatric Oncology from CIHR. This work was performed within the context of the International Childhood Astrocytoma Integrated Genomic and Epigenomic (ICHANGE) consortium. We are especially grateful for the generous philanthropic donation of the Charles Bruneau Foundation, the WeLoveYouConnie Foundation, and the Cedars/Sarah Cook funds.

Competing interests

The authors declare no competing interests

Methods

Patient samples and clinical information. This study was approved by the Institutional Review Board of the respective institutions from which the samples were collected. We thank Keith Ligon and Michelle Monje for generously sharing primary tumor cell lines established from patients with high-grade glioma.

Cell culture. Tumor-derived cell lines were maintained in Neucult NS-A proliferation media (StemCell Technologies) supplemented with bFGF (10 ng/mL) (StemCell Technologies), rhEGF (20 ng/mL) (StemCell Technologies), and heparin (0.0002%) (StemCell Technologies) on plates coated in poly-L-ornithine (0.01%) (Sigma) and laminin (0.01 mg/mL) (Sigma). HEK293T cells (ATCC) were cultured in DMEM containing 4.5 g/L glucose, L-glutamine, phenol red, and 10% FBS (Wisent). All lines tested negative for mycoplasma contamination, checked monthly using the MycoAlert Mycoplasma Detection Kit (Lonza). Tumor-derived cell lines (Supplementary Table 1) were confirmed to match original samples by STR fingerprinting. Lines were cultured to become differentiated glioma cells by adaptation to media of DMEM (4.5 g l−1 glucose, with l-glutamine, sodium pyruvate and phenol red) (Wisent) supplemented with 10% FBS (Wisent) for 2 weeks, while maintained on poly-l-ornithine- and laminin-coated plates.

Mouse orthotopic xenograft. All mice were housed, bred and subjected to listed procedures according to the McGill University Health Center Animal Care Committee and were in compliance with the guidelines of the Canadian Council on Animal Care. Brain tumour cells culture were transduced with lentiviruses constitutively expressing GFP and luciferase. Female NOD SCID mice (4-6 weeks) were used for xenograft experiments. Mice were injected with the following cell lines at a density of $7x10^5$ cells in the caudate putamen for BT245 and in the pons for DIPG-XIII. The Robot Stereotaxic machine from Neurostar was used for stereotaxic injections. Mice were monitored daily for over a year, for neurological symptoms of brain tumors: weight loss, epilepsy, altered gait, lethargy. Mice brains were imaged by MRI when symptoms appeared. They were euthanized immediately when clinical endpoint is reached. The brains were removed and sectioned into pieces. A proportion of tumour or normal brain was dissociated for each animal using the MACS Brain Tumor Dissociation Kit (Miltenyi Biotec). Dissociated cells were cryopreserved in CryoStor CS10 (StemCell Technologies), followed by thawing, PBS washing and sorting for GFP+ cells using flow cytometry platform at the McGill University Health Centre Research Institute. Collected GFP+ cells were used as input for scRNA library prep beginning with 5000 viable cells per sample.

Chromatin immunoprecipitation sequencing. Cells (cell lines or dissociated tumor cells) were fixed with 1% formaldehyde (Sigma). Fixed cell preparations were washed, pelleted and stored at -80°C. Sonication of lysed nuclei (lysed in a buffer containing 1% SDS) was performed on a BioRuptor UCD-300 for 18-30 cycles, 30s on 30s off, centrifuged every 15 cycles, chilled by 4°C water cooler. Samples were checked for sonication efficiency using the criteria of 150-500bp by gel electrophoresis. After the sonication, the chromatin was diluted to reduce SDS level to 0.1% and before ChIP reaction 2% of sonicated drosophila S2 cell chromatin was spiked-in the samples for quantification of total levels of histone mark after the sequencing (see below).

ChIP reaction for histone modifications was performed on a Diagenode SX-8G IP-Star Compact using Diagenode automated Ideal ChIP-seq Kit. 25ul Dynabeads Protein A beads (Invitrogen) Dynabaeds M-280 Sheep anti-Mouse IgG beads (Invitrogen) were washed and then incubated with antibodies (anti-H3K27me3 (1:40, CST 9733), anti-H3K4me3 (1:40, CST 9751), anti-H2AK119ub (1:40, CST 8240), anti-H3K27ac (1:100, Diagenode C15410196), anti-H3K36me2 (1:50, CST 2901)). One-two million cells of sonicated cell lysate combined with protease inhibitors for 10 hr, followed by 20 min wash cycle with provided wash buffers.

ChIP reactions for SUZ12, RING1B, CBX2 and CTCF were performed as follows: antibodies (anti-SUZ12 (1:150, CST 3737), anti-RING1B (1:200, Active Motif 39663), anti-CBX2 (Bethyl A302-524 1:200), anti-CTCF (1:400, Diagenode C15410210)) were conjugated by incubating with 40ul protein A or G beads at 4°C for 6 hours, then chromatin from 5-10 million cells was added in RIPA buffer, incubated at 4°C o/n, washed using buffers from Ideal ChIP-seq Kit (1 wash with each buffer, corresponding to RIPA, RIPA+500mM NaCl, LiCl, TE), eluted from beads by incubating with Elution buffer for 30 minutes at room temperature.

Reverse cross linking took place on a heat block at 65°C for 4 hr. ChIP samples were then treated with 2ul RNase Cocktail at 65°C for 30 min followed by 2ul Proteinase K at 65°C for 30 min. Samples were then purified with QIAGEN MiniElute PCR purification kit as per manufacturers' protocol. In parallel,

input samples (chromatin from about 50,000 cells) were reverse crosslinked and DNA was isolated following the same protocol.

Library preparation was carried out using Kapa HTP Illumina library preparation reagents. Briefly, 25ul of ChIP sample was incubated with 45ul end repair mix at 20°C for 30 min followed by Ampure XP bead purification. A tailing: bead bound sample was incubated with 50ul buffer enzyme mix for 30°C 30 min, followed by PEG/NaCl purification. Adaptor ligation: bead bound sample was incubated with 45ul buffer enzyme mix and 5ul of different TruSeq DNA adapters (Illumina) for each sample, for 20°C 15 min, followed by PEG/NaCl purification (twice). Library enrichment: 12 cycles of PCR amplification. Size selection was performed after PCR using a 0.6x/0.8x ratio of Ampure XP beads (double size selection) set to collect 250-450bp fragments. ChIP libraries were sequenced using Illumina HiSeq 2000, 2500 or 4000 or NovaSeq 6000 platforms at 50 or 100 bp single reads.

High-throughput chromosome conformation capture. *In situ* Hi-C libraries were generated from patient-derived glioma cell lines (5 million cells each), and murine embryonic brain tissue (1-3 million cells per sample), as described previously with minor modifications.[45] Briefly, in situ Hi-C was performed in 7 steps: (1) crosslinking cells with formaldehyde, (2) digesting DNA using a 4-cutter restriction enzyme (DpnII) within intact permeabilized nuclei, (3) filling in, biotinylating the resulting 5′ overhangs and ligating the blunt ends, (4) shearing the DNA, (5) pulling down biotinylated ligation junctions with streptavidin beads, (6) library amplification and (7) analyzing fragments using paired end sequencing. As quality control (QC) steps, efficient sonication was checked by agarose DNA gel electrophoresis and for appropriate size selection by Agilent Bioanalyzer profiles for libraries. For final QC, we performed superficial sequencing on the Illumina Hiseq 2500 (~30M reads/sample) to assess quality of the libraries using percent of reads passing filter, percent of chimeric reads, and percent of forward-reverse pairs. Hi-C libraries were sequenced (paired-end, 125 bp) on the Illumina HiSeq2500 platform.

Bulk RNA sequencing. Total RNA was extracted from cell pellets and mouse tumors using the AllPrep DNA/RNA/miRNA Universal Kit (Qiagen) according to instructions from the manufacturer. Library preparation was performed with ribosomal RNA (rRNA) depletion according to instructions from the manufacturer (Epicentre) to achieve greater coverage of mRNA and other long non-coding transcripts. Paired-end sequencing (100 bp) was performed on the Illumina HiSeq 2500 or 4000 platform.

Single cell RNA-seq. The concentration of the single-cell suspension was assessed with a Trypan blue count. Approximately 5000 cells per sample were loaded on the Chromium Single Cell 3′ system (10X Genomics). GEM-RT, DynaBeads cleanup, PCR amplification and SPRIselect beads cleanup were performed using Chromium Single Cell 3′ Gel Bead kit. Indexed single-cell libraries were generated using the Chromium Single Cell 3′ Library kit and the Chromium i7 Multiplex kit. Size, quality, concentration and purity of the complementary DNAs and the corresponding 10X library were evaluated by the Agilent 2100 Bioanalyzer system. The 10X libraries were sequenced in the Illumina 2500 sequencing platform.

Droplet Digital PCR. RNA was extracted from cells using the Aurum Total RNA Mini Kit (Bio-Rad) and concentration was quantified on the BioDrop uLite (Montreal Biotech). cDNA was generated using iScript Reverse Transcription Supermix (Bio-Rad). Target concentration was determined using the QX200 ddPCR EvaGreen Supermix assay (Bio-Rad) using 20 uL per reaction containing 5 ng of cDNA, using manufacturer's protocol cycling conditions with a 58 degrees annealing temperature and 40 cycles. Droplets were assayed using the QX200 Droplet Reader (Bio-Rad) and manually scored for positive signal using QuantaSoft Software (Bio-Rad). The concentration of positive droplets per target was normalized to the concentration of GAPDH.

Histone mass spectrometry. The complete workflow for histone extraction, LC/MS, and data analysis was previously described.[46, 47] Briefly, cell pellets (~1 × 10^6 cells) were lysed on ice in nuclear isolation buffer supplemented with 0.3% NP-40 alternative. Isolated nuclei were incubated with 0.4 N

H_2SO_4 for 3 h at 4°C with agitation. 100% trichloroacetic acid (w/v) was added to the acid extract to a final concentration of 20% and samples were incubated on ice overnight to precipitate histones. The resulting histone pellets were rinsed with ice cold acetone + 0.1% HCl and then with ice cold acetone before resuspension in water and protein estimation by Bradford assay. Approximately 20 μg of histone extract was then resuspended in 100 mM ammonium bicarbonate and derivatized with propionic anhydride. 1 μg of trypsin was added and samples were incubated overnight at 37°C. After tryptic digestion, a cocktail of isotopically-labeled synthetic histone peptides was spiked in at a final concentration of 250 fmol/μg and propionic anhydride derivatization was performed for second time. The resulting histone peptides were desalted using C18 Stage Tips, dried using a centrifugal evaporator, and reconstituted using 0.1% formic acid in preparation for nanoLC-MS analysis.

nanoLC was performed using a Thermo ScientificTM Easy nLCTM 1000 equipped with a 75 μm × 20 cm in-house packed column using Reprosil-Pur C18-AQ (3 μm; Dr. Maisch GmbH, Germany). Buffer A was 0.1% formic acid and Buffer B was 0.1% formic acid in 80% acetonitrile. Peptides were resolved using a two-step linear gradient from 5 to 33% B over 45 min, then from 33 to 90% B over 10 min at a flow rate of 300 nL/min. The HPLC was coupled online to an Orbitrap Elite mass spectrometer operating in the positive mode using a Nanospray FlexTM Ion Source (Thermo Scientific) at 2.3 kV. Two full MS scans (m/z 300–1100) were acquired in the orbitrap mass analyzer with a resolution of 120,000 (at 200 m/z) every 8 DIA MS/MS events using isolation windows of 50 m/z each (e.g., 300–350, 350–400, ...,650–700). MS/MS spectra were acquired in the ion trap operating in normal mode. Fragmentation was performed using collision-induced dissociation (CID) in the ion trap mass analyzer with a normalized collision energy of 35. AGC target and maximum injection time were 10^6 and 50 ms for the full MS scan, and 10^4 and 150 ms for the MS/MS can, respectively. Raw files were analyzed using EpiProfile.[48]

Western blotting. Histone lysates were extracted using the Histone Extraction kit (Abcam). Lysate protein concentration was determined with the Bradford assay reagent (Bio-Rad). Ten micrograms of

protein was separated on SDS-PAGE gels (10% acrylamide) and wet-transferred to a PVDF membrane (GE Healthcare). Membrane blocking was performed with 5% skimmed milk in Tris-buffered saline (50 mM Tris, 150 mM NaCl, 0.1% Tween-20, pH 7.4) (TBST) for 1 h. Membranes were incubated overnight with primary antibody (GAPDH Advanced ImmunoChemical Inc 2-RGM2 1:1000 dilution, or SOX10 ab212843 1:1000 dilution) in 1% skimmed milk in TBST. Membranes were washed three times in TBST, and the secondary antibody (ECL anti-mouse IgG horseradish peroxidase linked whole antibody) (GE Healthcare) was applied for 1 h in 1% skimmed milk in TBST. Membranes were washed three times and the signal was resolved with Amersham ECL Prime Western Blotting Detection Reagent (GE Healthcare) and imaged on a ChemiDoc MP Imaging System (Bio-Rad).

Immunofluorescence. Cells were plated in a Nunc Lab-Tek II Chamber slide system (ThermoFisher Scientific). Slides were fixed with 4% paraformaldehyde in PBS for 20 min at room temperature, followed by washing three times with PBS. Cells were permeabilized by Triton X-100 (0.05% DIPGXIII, 0.2% BT245), 2% BSA, 5% normal goat serum (NGS) in PBS followed by three PBS washes. Slides were blocked with 2% BSA, 5% NGS in PBS for 1 h, followed by overnight incubation with primary antibody (anti-GFAP rabbit monoclonal antibody Cell Signaling, catalog no. 12389 at 1:200 dilution, or anti-SOX10 ThermoFisher Scientific cat. no. 703439 at 1:200 dilution) in blocking solution. Cells were washed three times with PBS and incubated for 1 h with 1:100 dilution of goat anti-rabbit IgG cross-adsorbed secondary antibody, Alexa Fluor 488 (ThermoFisher Scientific) in blocking solution. Slides were washed three times in PBS and Prolong Gold antifade reagent with DAPI (Invitrogen) was applied. Slides were photographed with a Zeiss LSM780 Laser Scanning Confocal Microscope at ×20 and ×63 magnification. Each image had the protein of interest (SOX10/GFAP) quantified by fluorescence signal normalized to nucleus count value using ImageJ software.

ChIP-seq data processing. Raw sequences were first trimmed using fastp v0.22.0 with default settings before alignment using bwa-mem2 v2.2.1 to a combined reference of hg38+dm6 or mm10+dm6 with default settings. After identification of duplicates using picard v2.26.2's "MarkDuplicates" module with default settings, alignments with MAPQ>3 mapping to each species was extracted into separate

BAM files using samtools v1.14's "view" module. Alignments overlapping different genomic intervals (e.g., 10kb bins, promoters, CpG islands) were subsequently tabulated using bedtools v2.30.0's "intersect" module. Depth-normalized coverage tracks were generated using deepTools v3.5.1's bamCoverage module with parameters "--normalizeUsing CPM --centerReads -e 200".

Quantification of ChIP-seq signal confinement. Parameters were fitted using the H3K27me3 track and peak calls from a K27M pHGG cell line with default parameters, after which the peak widths were increased to simulate spreading. Signal breadth of experimental and simulated ChIP-seq datasets was quantified using the FCS metric from ssp, specifically FCS computed at 10kb, a range chosen based on the typical width of H3K27me3 peaks.

Identification of ChIP-seq peaks. Regions with focal ChIP-seq enrichment with respect to input controls were identified using MACS v2.2.7.1 with settings "—broad --broad-cutoff 0.1". Differential ChIP-seq enrichment across conditions were assessed using DiffBind v3.4.0.

Chromatin-state classification of genomic regions. The union set of GENCODE (v36/vM25) annotated TSSs and mid points of CpG islands from the UCSC Genome Browser were expanded to +/-2.5kb and used as the reference set of promoter / CGIs. The log fold enrichment of ChIP-seq over input for alignments overlapping these intervals were then computed for various targets, producing a table with the rows being promoter / CGI intervals and columns being different ChIP-seq signal sources. Dimension reduction was then performed using UMAP with correlation distance, minimum distance of 0.01 and neighbourhood size from (15, 30, 50, 100) depending on the number of datapoints. HDBSCAN was adopted for clustering of datapoints in UMAP embeddings (of dimensions 5-10) with similar chromatin states, with minimum cluster and sample sizes from (500, 1000, 5000) depending on the number of datapoints. Dimension reduction and clustering was performed iteratively to refine subclusters.

Hi-C data processing. Raw sequences were processed using Juicer v1.6 with default parameters against hg38 or mm10. Additional, Juicer .hic files were converted to cooler .mcool files using hic2cool v0.8.3, after which bias vectors were re-computed using the balance module of cooler v0.8.11 with default settings. Additionally, CNV-aware bias vectors were determined using NeoLoopFinder v0.2.4 with default settings.

Compartment- and domain-level analysis. Compartment scores were computed using the call-compartments module of cooltools v0.4.1 with GC content as the phasing track. Insulation scores were computed at 25kb resolution with a window size of 1mb using the diamond-insulation module of cooltools. Interaction between genomic ranges with various ranges of compartment scores was then assessed using compute-saddle module of cooltools with quantile binning into 50 intervals. Embeddings were generated using genome-wide binned signals as input (e.g., insulation score, compartment score) and correlation as the metric for UMAP, while silhouette scores were computed using inter-sample (1 - Pearson's r) as the distance with genome-wide binned signals.

Assessment of loop strength. Aggregate peak analysis was performed using coolpup.py v0.9.5 with default settings to assess the average interaction strength between pairs of genomic intervals. Alternatively, the looping strength of individual pairs of regions was quantified using chromosight v1.6.1's quantify module at 10kb resolution with default settings. Transcriptional regulators associated with differential looping were identified using BART3D v1.0 for each pair of isogenic K27M vs K27M-KO samples, after which the ranked (by significance) list of factors was integrated using RobustRankAggreg v1.1.

Bulk RNA-seq data processing. Raw sequences were trimmed using fastp with default settings, after expression quantification was performed using salmon v1.4.0 with default settings against GENCODE annotations (v36/vM25). Transcript-level counts were collated to genes using tximport to produce gene-level count matrices.

Differential gene expression analysis. DESeq2 v1.34.0 was ran with default settings with gene expression count matrices to identify differentially expressed genes. Gene set enrichment analysis was performed using fgsea v1.20.0 with default settings and taking Wald test statistics as the ranking metric. Gene set over-representation analysis was instead carried out using Enrichr v3.0. Concordance of differential gene expression.

scRNA-seq data processing. Cell Ranger (10X Genomics, v3.1.0) was used with default parameters to demultiplex and align sequencing reads, distinguish cells from background, and obtain gene counts per cell. Alignment was performed using a joint hg19+mm10 genome reference build, coupled with Ensembl transcriptome build GRCh37 v.82 for hg19 and GRCm38 v.84 for mm10. Intronic counts were excluded. Human cells were extracted if cells were either assigned as human by Cell Ranger or the cell contained greater than 75% of total reads mapping to hg19 in order to obtain adequate numbers of cells per sample. Quality control and normalization was performed using the R package Seurat (v3.1.0). Cells were filtered based on the following quality control metrics: mitochondrial content (indicative of cellular damage), number of genes and number of unique molecular identifiers (UMIs). Filtering thresholds were set on a per-sample basis where cells were excluded if they had greater than 50% of total reads mapping to mitochondrial read counts, had less than 500 total genes or UMIs, or were outside 2 standard deviations from the mean number of genes or UMIs, respectively. Libraries were scaled to 10,000 UMIs per cell and natural log-normalized. Log normalized counts were used for computing correlations of gene expression and assessing expression of specific genes. Samples were combined by cell line, without any additional transformation of the data.

Identification of nearest normal cell types in xenograft samples. To assign a nearest-normal cell type to individual cells, Spearman correlation of the log-normalized counts with a reference expression matrix was computed inn base R with parameter 'complete.obs' to compute covariances. The reference expression matrix was a developmental murine forebrain and pons single cell atlas with average

expression values per cluster, as described in the original study (Jessa et al, 2019, Nature Genetics). For each cell, the cluster label with the highest correlation was assigned as the nearest normal cell type.

Quantification of cPRC1 target expression in single cell data. To assess for enrichment of cPRC1 gene signatures in single cell data, ssGSEA was run To assess enrichment of cPRC1 gene signatures in single cell data, single-sample gene set enrichment analysis (ssGSEA) was run using raw counts per cell and gene sets derived from x (this is how you derived the gene sets). For xenograft samples, gene sets derived from clusters in x seq data for the corresponding cell line were used as input. For tumor samples, only genes common to gene sets per cluster in both cell lines (BT245, DIPG13) were kept as input. ssGSEA code was adapted from the GVSA package using parameters 'alpha = 0.75, normalize = FALSE'. For visualization, proportions were calculated as the fraction of cells of total cells. In cases where only glial cells were visualized, proportions were calculated using fractions of total glial cells.

Visualization. ChIP-seq coverage tracks were imported using rtracklayer and subsequently displayed using ggplot2 v3.3.5. Gene annotations were similarly imported and shown through gggenes. Balanced Hi-C matrices were further processed using VEHiCLE with default settings before being imported via RcppCNPy v0.2.10 and similarly visualized using ggplot2. 3D structures were predicted from balanced contact matrices using CSynth with default settings. Intersections were shown through Euler diagrams with eulerr v6.1.1.

Statistical consideration. Unless otherwise stated, Wilcoxon rank-sum tests were used to compare the distribution of metrics between two conditions. When appropriate (e.g., matched isogenic cell lines), a paired instead independent test is performed. P-values are represented as: 0 (****) 0.0001 (***) 0.001 (**) 0.01 (*) 0.05 (ns) 1.

Public datasets accessed. H3K27me3 ChIP-seq and Hi-C datasets were sourced from: Bonev 2017 (GSE96107), Gorkin 2020 (ENCODE), McLaughlin 2019 (GSE124342), Conway 2021 (GSE162739),

Yusufova 2020 (GSE143293), Lhoumaud 2019 (GSE131651), Won 2016 (GSE77565). Bulk RNA-seq datasets were sourced from: Harutyunyan 2019 (GenAP), Krug 2019 (GSE128745), Weinberg 2019 (GSE118785). Single cell RNA-seq datasets were sourced from: Jessa 2019 (GSE133531), Jessa 2021 (GSE).

References

1. Piunti, A. and A. Shilatifard, *The roles of Polycomb repressive complexes in mammalian development and cancer.* Nat Rev Mol Cell Biol, 2021. **22**(5): p. 326-345.

2. Laugesen, A., J.W. Hojfeldt, and K. Helin, *Molecular Mechanisms Directing PRC2 Recruitment and H3K27 Methylation.* Mol Cell, 2019. **74**(1): p. 8-18.

3. Plys, A.J., et al., *Phase separation of Polycomb-repressive complex 1 is governed by a charged disordered region of CBX2.* Genes Dev, 2019. **33**(13-14): p. 799-813.

4. Zhang, X., et al., *Large DNA Methylation Nadirs Anchor Chromatin Loops Maintaining Hematopoietic Stem Cell Identity.* Mol Cell, 2020. **78**(3): p. 506-521 e6.

5. Atlasi, Y. and H.G. Stunnenberg, *The interplay of epigenetic marks during stem cell differentiation and development.* Nat Rev Genet, 2017. **18**(11): p. 643-658.

6. Finogenova, K., et al., *Structural basis for PRC2 decoding of active histone methylation marks H3K36me2/3.* Elife, 2020. **9**.

7. Zhao, S., C.D. Allis, and G.G. Wang, *The language of chromatin modification in human cancers.* Nat Rev Cancer, 2021. **21**(7): p. 413-430.

8. Boyle, S., et al., *A central role for canonical PRC1 in shaping the 3D nuclear landscape.* Genes Dev, 2020. **34**(13-14): p. 931-949.

9. Rhodes, J.D.P., et al., *Cohesin Disrupts Polycomb-Dependent Chromosome Interactions in Embryonic Stem Cells.* Cell Rep, 2020. **30**(3): p. 820-835 e10.

10. Bsteh, D., et al., *Loss of Cohesin regulator PDS5A reveals repressive role of Polycomb loops.* bioRxiv, 2021.

11. Jessa, S., et al., *Stalled developmental programs at the root of pediatric brain tumors.* Nat Genet, 2019. **51**(12): p. 1702-1713.

12. Vladoiu, M.C., et al., *Childhood cerebellar tumours mirror conserved fetal transcriptional programs.* Nature, 2019. **572**(7767): p. 67-73.

13. Jain, S.U., et al., *PFA ependymoma-associated protein EZHIP inhibits PRC2 activity through a H3 K27M-like mechanism.* Nat Commun, 2019. **10**(1): p. 2146.

14. Harutyunyan, A.S., et al., *H3K27M induces defective chromatin spread of PRC2-mediated repressive H3K27me2/me3 and is essential for glioma tumorigenesis.* Nat Commun, 2019. **10**(1): p. 1262.

15. Krug, B., et al., *Pervasive H3K27 Acetylation Leads to ERV Expression and a Therapeutic Vulnerability in H3K27M Gliomas.* Cancer Cell, 2019. **35**(5): p. 782-797 e8.

16. Michealraj, K.A., et al., *Metabolic Regulation of the Epigenome Drives Lethal Infantile Ependymoma.* Cell, 2020. **181**(6): p. 1329-1345 e24.

17. McLaughlin, K., et al., *DNA Methylation Directs Polycomb-Dependent 3D Genome Re-organization in Naive Pluripotency.* Cell Rep, 2019. **29**(7): p. 1974-1985 e6.

18. Lhoumaud, P., et al., *NSD2 overexpression drives clustered chromatin and transcriptional changes in a subset of insulated domains.* Nat Commun, 2019. **10**(1): p. 4843.

19. Yusufova, N., et al., *Histone H1 loss drives lymphoma by disrupting 3D chromatin architecture.* Nature, 2021. **589**(7841): p. 299-305.

20. Conway, E., et al., *BAP1 enhances Polycomb repression by counteracting widespread H2AK119ub1 deposition and chromatin condensation.* Mol Cell, 2021. **81**(17): p. 3526-3541 e8.

21. Blackledge, N.P. and R.J. Klose, *The molecular principles of gene regulation by Polycomb repressive complexes.* Nat Rev Mol Cell Biol, 2021. **22**(12): p. 815-833.

22. Loubiere, V., et al., *Widespread activation of developmental gene expression characterized by PRC1-dependent chromatin looping.* Sci Adv, 2020. **6**(2): p. eaax4001.

23. Barbour, H., et al., *Polycomb group-mediated histone H2A monoubiquitination in epigenome regulation and nuclear processes.* Nat Commun, 2020. **11**(1): p. 5947.

24. Lu, C., et al., *Histone H3K36 mutations promote sarcomagenesis through altered histone methylation landscape.* Science, 2016. **352**(6287): p. 844-9.

25. Streubel, G., et al., *The H3K36me2 Methyltransferase Nsd1 Demarcates PRC2-Mediated H3K27me2 and H3K27me3 Domains in Embryonic Stem Cells.* Mol Cell, 2018. **70**(2): p. 371-379 e5.

26. Papillon-Cavanagh, S., et al., *Impaired H3K36 methylation defines a subset of head and neck squamous cell carcinomas.* Nat Genet, 2017. **49**(2): p. 180-185.

27. Behjati, S., et al., *Distinct H3F3A and H3F3B driver mutations define chondroblastoma and giant cell tumor of bone.* Nat Genet, 2013. **45**(12): p. 1479-82.

28. Kurotaki, N., et al., *Haploinsufficiency of NSD1 causes Sotos syndrome.* Nat Genet, 2002. **30**(4): p. 365-6.

29. Blanco, E., et al., *The Bivalent Genome: Characterization, Structure, and Regulation.* Trends Genet, 2020. **36**(2): p. 118-131.

30. Chan, K.M., et al., *The histone H3.3K27M mutation in pediatric glioma reprograms H3K27 methylation and gene expression.* Genes Dev, 2013. **27**(9): p. 985-90.

31. Larson, J.D., et al., *Histone H3.3 K27M Accelerates Spontaneous Brainstem Glioma and Drives Restricted Changes in Bivalent Gene Expression.* Cancer Cell, 2019. **35**(1): p. 140-155 e7.

32. Schuettengruber, B., et al., *Genome Regulation by Polycomb and Trithorax: 70 Years and Counting.* Cell, 2017. **171**(1): p. 34-57.

33. Youmans, D.T., et al., *Competition between PRC2.1 and 2.2 subcomplexes regulates PRC2 chromatin occupancy in human stem cells.* Mol Cell, 2021. **81**(3): p. 488-501 e9.

34. Huseyin, M.K. and R.J. Klose, *Live-cell single particle tracking of PRC1 reveals a highly dynamic system with low target site occupancy.* Nat Commun, 2021. **12**(1): p. 887.

35. Lamb, K.N., et al., *Discovery and Characterization of a Cellular Potent Positive Allosteric Modulator of the Polycomb Repressive Complex 1 Chromodomain, CBX7.* Cell Chem Biol, 2019. **26**(10): p. 1365-1379 e22.

36. Sneppen, K. and L. Ringrose, *Theoretical analysis of Polycomb-Trithorax systems predicts that poised chromatin is bistable and not bivalent.* Nat Commun, 2019. **10**(1): p. 2133.

37. Cohen, A.S., et al., *Weaver Syndrome-Associated EZH2 Protein Variants Show Impaired Histone Methyltransferase Function In Vitro.* Hum Mutat, 2016. **37**(3): p. 301-7.

38. Tatton-Brown, K. and N. Rahman, *The NSD1 and EZH2 overgrowth genes, similarities and differences.* Am J Med Genet C Semin Med Genet, 2013. **163C**(2): p. 86-91.

39. Jani, K.S., et al., *Histone H3 tail binds a unique sensing pocket in EZH2 to activate the PRC2 methyltransferase.* Proc Natl Acad Sci U S A, 2019. **116**(17): p. 8295-8300.

40. Brennan, K., et al., *NSD1 mutations deregulate transcription and DNA methylation of bivalent developmental genes in Sotos syndrome.* Hum Mol Genet, 2022.

41. Wang, G.G., et al., *NUP98-NSD1 links H3K36 methylation to Hox-A gene activation and leukaemogenesis.* Nat Cell Biol, 2007. **9**(7): p. 804-12.

42. Parreno, V., A.M. Martinez, and G. Cavalli, *Mechanisms of Polycomb group protein function in cancer.* Cell Res, 2022. **32**(3): p. 231-253.

43. Tauchmann, S. and J. Schwaller, *NSD1: A Lysine Methyltransferase between Developmental Disorders and Cancer.* Life (Basel), 2021. **11**(9).

44. Ringrose, L. and R. Paro, *Epigenetic regulation of cellular memory by the Polycomb and Trithorax group proteins.* Annu Rev Genet, 2004. **38**: p. 413-43.

45. Rao, S.S., et al., *A 3D map of the human genome at kilobase resolution reveals principles of chromatin looping.* Cell, 2014. **159**(7): p. 1665-80.

46. Karch, K.R., S. Sidoli, and B.A. Garcia, *Identification and Quantification of Histone PTMs Using High-Resolution Mass Spectrometry.* Methods Enzymol, 2016. **574**: p. 3-29.

47. Sidoli, S., et al., *Complete Workflow for Analysis of Histone Post-translational Modifications Using Bottom-up Mass Spectrometry: From Histone Extraction to Data Analysis.* J Vis Exp, 2016(111).

48. Yuan, Z.F., et al., *EpiProfile 2.0: A Computational Platform for Processing Epi-Proteomics Mass Spectrometry Data.* J Proteome Res, 2018. **17**(7): p. 2533-2541.

Figure 1

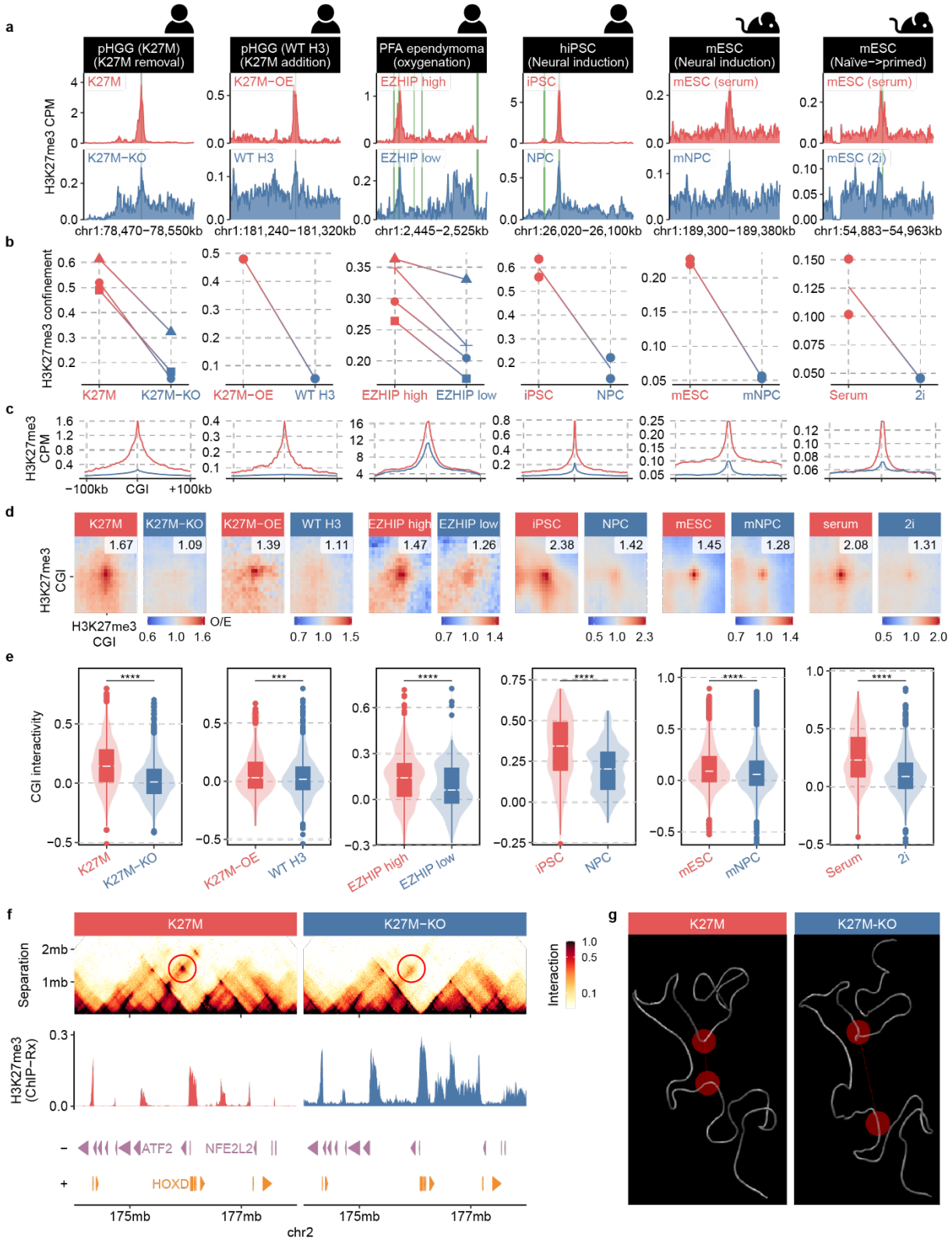
a
pHGG (K27M) (K27M removal)
pHGG (WT H3) (K27M addition)
PFA ependymoma (oxygenation)
hiPSC (Neural induction)
mESC (Neural induction)
mESC (Naïve->primed)
H3K27me3 CPM
K27M
K27M−KO
K27M−OE
WT H3
EZHIP high
EZHIP low
iPSC
NPC
mESC (serum)
mNPC
mESC (2i)
chr1:78,470−78,550kb
chr1:181,240−181,320kb
chr1:2,445−2,525kb
chr1:26,020−26,100kb
chr1:189,300−189,380kb
chr1:54,883−54,963kb
b
H3K27me3 confinement
Serum
2i
c
−100kb
CGI
+100kb
d
H3K27me3 CGI
O/E
serum
e
CGI interactivity
f
Separation
2mb
1mb
H3K27me3 (ChIP−Rx)
ATF2
NFE2L2
HOXD
175mb
177mb
chr2
g
Interaction

Figure 1. Restricted H3K27me3 occurs in brain tumor and developmental contexts and associates with stronger distal interactions between CpG islands

a. Distribution of H3K27me3 (coverage tracks in units of counts-per-million-alignments) in brain tumor and developmental contexts demonstrating distinction of confined versus diffuse profiles
b. Metric of H3K27me3 signal confinement (fragment cluster score at 10kb, see methods) in diverse contexts confirming genome-wide distinction of confined versus diffuse profiles
c. Metaplots showing H3K27me3 aggregate signals around the top 1000 most enriched CpG islands, normalized by total read depth
d. Average pairwise Hi-C interaction among the top 1000 most H3K27me3-enriched CpG islands, showing the stronger interactions in cells with confined H3K27me3 signal
e. Quantification of pairwise loop strength among the top 1000 most H3K27me3-enriched CpG islands, confirming the stronger interactions in H3K27me3-confined cells are statistically significant
f. An representative locus in pGBM cell line BT245 (K27M versus KO) demonstrating the association of H3K27me3 confinement with stronger long-range interaction
g. CSynth polymer simulation of same locus shown in (f), visualizing the impact of H3K27me3 confinement in bridging distal chromatin segments from otherwise disjoint domains

Figure 2

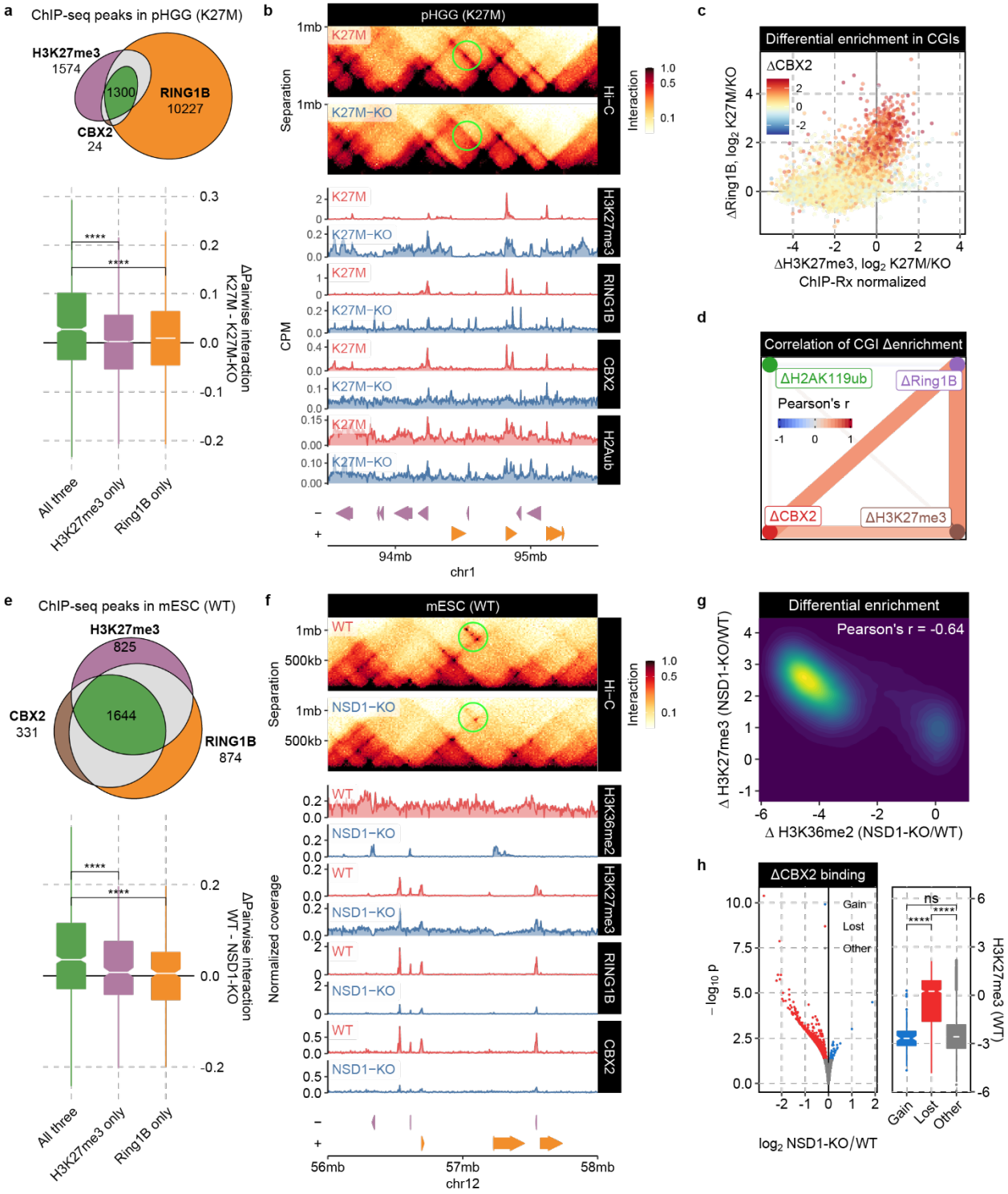
a
ChIP-seq peaks in pHGG (K27M)
H3K27me3
1574
1300
RING1B
10227
CBX2
24
ΔPairwise interaction
K27M - K27M-KO
All three
H3K27me3 only
Ring1B only
b
pHGG (K27M)
K27M
K27M-KO
Separation
Hi-C
Interaction
CPM
H3K27me3
RING1B
CBX2
H2Aub
94mb
95mb
chr1
c
Differential enrichment in CGIs
ΔCBX2
ΔRing1B, log2 K27M/KO
ΔH3K27me3, log2 K27M/KO
ChIP-Rx normalized
d
Correlation of CGI Δenrichment
ΔH2AK119ub
ΔRing1B
Pearson's r
ΔCBX2
ΔH3K27me3
e
ChIP-seq peaks in mESC (WT)
H3K27me3
825
CBX2
331
1644
RING1B
874
ΔPairwise interaction
WT - NSD1-KO
All three
H3K27me3 only
Ring1B only
f
mESC (WT)
WT
NSD1-KO
Separation
Hi-C
Interaction
Normalized coverage
H3K36me2
H3K27me3
RING1B
CBX2
56mb
57mb
58mb
chr12
g
Differential enrichment
Pearson's r = -0.64
Δ H3K27me3 (NSD1-KO/WT)
Δ H3K36me2 (NSD1-KO/WT)
h
ΔCBX2 binding
Gain
Lost
Other
−log10 p
log2 NSD1-KO/WT
ns
H3K27me3 (WT)

Figure 2. Confined H3K27me3 induces cPRC1 concentration leading to compaction of Polycomb bodies, in both brain tumor and developmental contexts

a. (top) Euler diagram of peak calls for H3K27me3 and PRC1 sub-units CBX2 & RING1B in K27M pGBM cell line BT245; (bottom) differential (K27M versus KO) pairwise HiC interaction for various peak overlap subsets, showing the sites marked by all three (H3K27me3, RING1B, CBX2) have the strongest differential interactions.
b. Representative locus of differential interaction between cPRC1 sites, along with ChIP-seq profiles of H3K27me3, RING1B, CBX2 and H2AK119ub; note that H2AK119aub profile remaining largely unchanged upon K27M-KO
c. Correlation of signal enrichment differences in CpG islands between K27M and K27M-KO, showing that CBX2 is most enriched in the regions with high enrichment of both H3K27me3 and RING1B, confirming strong association between H3K27me3 confinement with enhanced cPRC1 recruitment
d. Partial correlation network of differential enrichment of H3K27me3, RINGB1, CBX2 and H2AK119ub, with line width also signifying the magnitude of correlation coefficient. H2AK119ub is only weakly correlated the other three highly correlated markers, implicating cPRC1 rather than ncPRC1 determines the difference between K27M and KO.

Figure 3

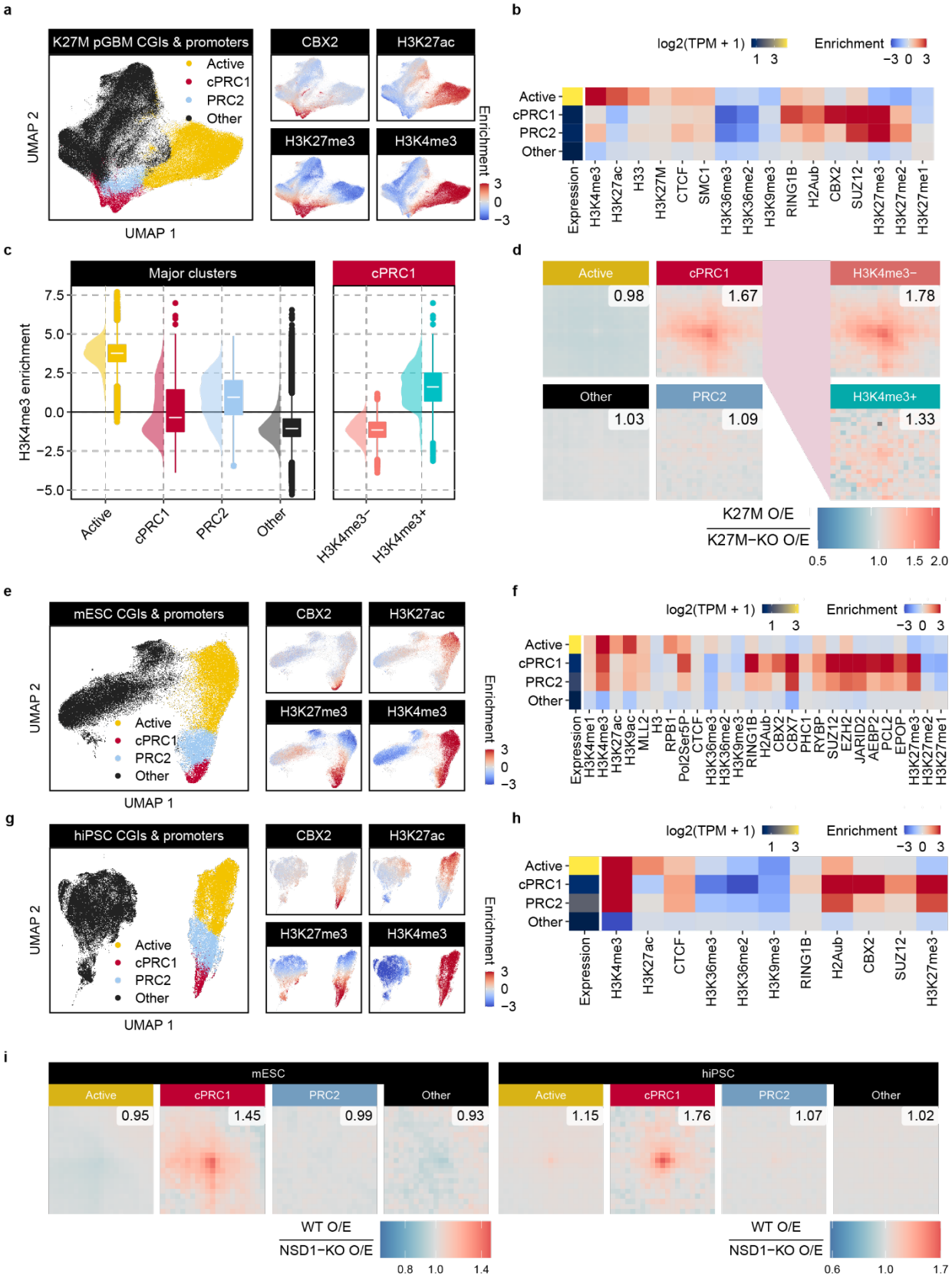
a
K27M pGBM CGIs & promoters
Active
cPRC1
PRC2
Other
UMAP 2
UMAP 1
CBX2
H3K27ac
H3K27me3
H3K4me3
Enrichment
3
0
−3
b
log2(TPM + 1)
1 3
Enrichment
−3 0 3
Active
cPRC1
PRC2
Other
Expression
H3K4me3
H3K27ac
H33
H3K27M
CTCF
SMC1
H3K36me3
H3K36me2
H3K9me3
RING1B
H2Aub
CBX2
SUZ12
H3K27me3
H3K27me2
H3K27me1
c
Major clusters
cPRC1
H3K4me3 enrichment
7.5
5.0
2.5
0.0
−2.5
−5.0
Active
cPRC1
PRC2
Other
H3K4me3−
H3K4me3+
d
Active
cPRC1
H3K4me3−
0.98
1.67
1.78
Other
PRC2
H3K4me3+
1.03
1.09
1.33
K27M O/E
K27M−KO O/E
0.5
1.0
1.5
2.0
e
mESC CGIs & promoters
Active
cPRC1
PRC2
Other
UMAP 2
UMAP 1
CBX2
H3K27ac
H3K27me3
H3K4me3
Enrichment
3
0
−3
f
log2(TPM + 1)
1 3
Enrichment
−3 0 3
Active
cPRC1
PRC2
Other
Expression
H3K4me1
H3K4me3
H3K27ac
H3K9ac
MLL2
H3
RPB1
Pol2Ser5P
CTCF
H3K36me3
H3K36me2
H3K9me3
RING1B
H2Aub
CBX2
CBX7
PHC1
RYBP
SUZ12
EZH2
JARID2
AEBP2
PCL2
EPOP
H3K27me3
H3K27me2
H3K27me1
g
hiPSC CGIs & promoters
Active
cPRC1
PRC2
Other
UMAP 2
UMAP 1
CBX2
H3K27ac
H3K27me3
H3K4me3
Enrichment
3
0
−3
h
log2(TPM + 1)
1 3
Enrichment
−3 0 3
Active
cPRC1
PRC2
Other
Expression
H3K4me3
H3K27ac
CTCF
H3K36me3
H3K36me2
H3K9me3
RING1B
H2Aub
CBX2
SUZ12
H3K27me3
i
mESC
Active
cPRC1
PRC2
Other
0.95
1.45
0.99
0.93
WT O/E
NSD1−KO O/E
0.8
1.0
1.4
hiPSC
Active
cPRC1
PRC2
Other
1.15
1.76
1.07
1.02
WT O/E
NSD1−KO O/E
0.6
1.0
1.7

Figure 3. Clustering high-dimensional profiles of chromatin features highlights a distinctive role of H3K4me3 in regulating compaction of polycomb bodies

a. UMAP embedding and HDBSCAN clustering of CpG island & promoter chromatin profiles (as listed in panel b) using data from three K27M pGBM cell lines, identify four different clusters
b. Average signals of transcription and chromatin features for CGIs & promoters in different classes, demonstrating unique chromatin states captured for the four clusters: Active (enriched for H3K4me3 and H3K27ac), cPRC1 (with both PRC1 and PRC2 marks), PRC2 (with SUZ12 and H3K27me3, lacking CBX2), and Other (no enrichment for all)
c. H3K4me3 enrichment distribution in the four clusters, with a bimodal distribution in the cPRC1 cluster, revealing the distinction between H3K4me3+ versus H3K4me3- sites
d. Differential pairwise interaction between regions within the four clusters, showing the association of H3K4me3- cPRC1 sites with K27M-specific looping in pGBM cell line BT245
e. UMAP embedding and HDBSCAN clustering of CpG island & promoter chromatin profiles (as listed in panel f) using data from various mESC lines, identify four different clusters
f. Average signals of transcription and chromatin features for CGIs & promoters in the four clusters, consisting with panel b, except H3K4me3 is also enriched in cPRC1 and PRC2 clusters
g. UMAP embedding and HDBSCAN clustering of CpG island & promoter chromatin profiles (as listed in panel h) using data from various hiPSC lines, identify four different clusters
h. Average signals of transcription and chromatin features for CGIs & promoters in the four clusters, similar to panel f, where H3K4me3 is enriched in Active, cPRC1 and PRC2 clusters
i. Differential pairwise interaction between regions within the four clusters, showing the strongest enrichment in the cPRC1 cluster. note that no further sub-classification is made for cPRC1 targets based on H3K4me3 as all of them are bivalent in mESCs/hiPSCs.

Figure 4

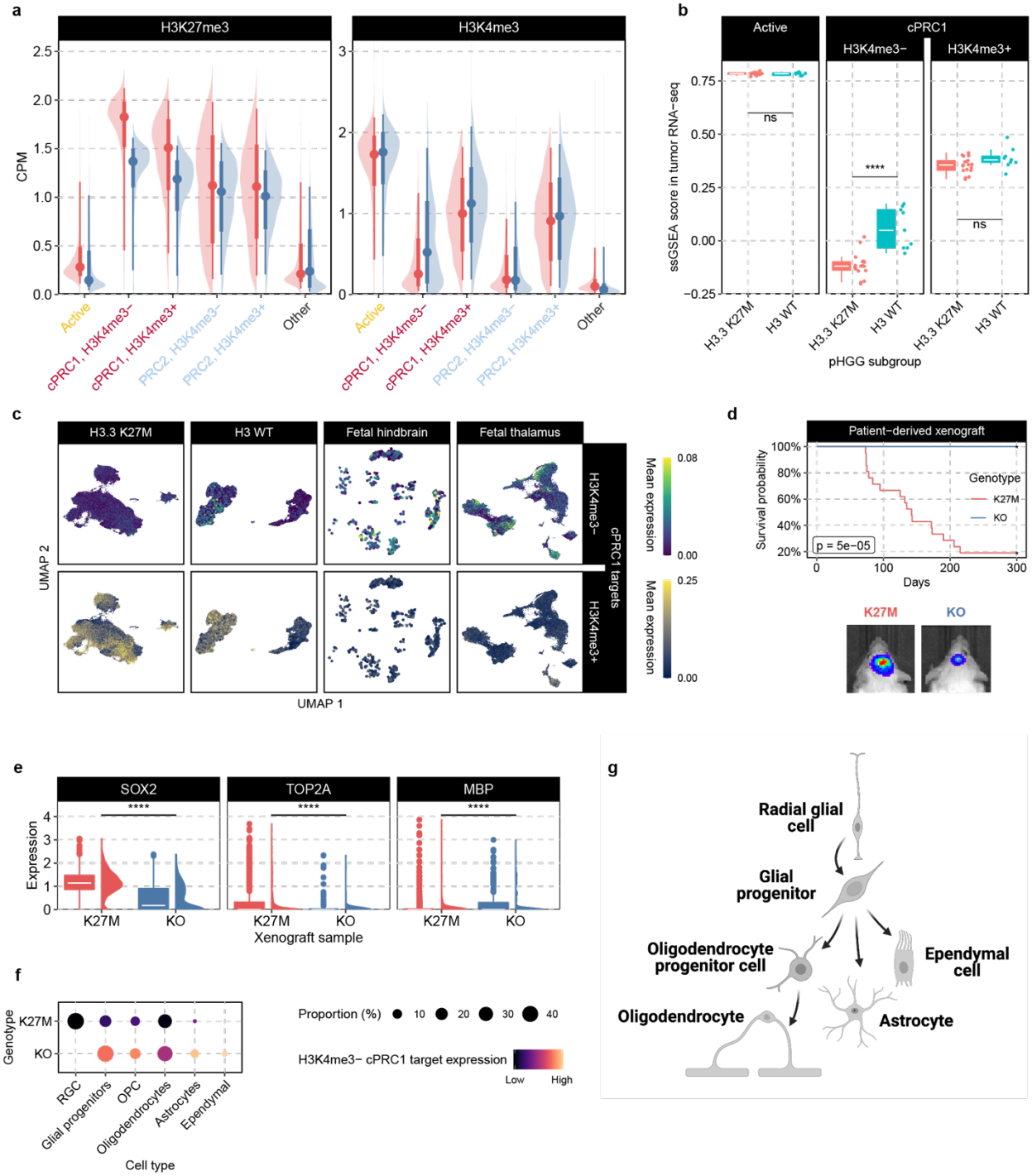
a
H3K27me3
H3K4me3
CPM
Active
cPRC1, H3K4me3−
cPRC1, H3K4me3+
PRC2, H3K4me3−
PRC2, H3K4me3+
Other
b
Active
cPRC1
H3K4me3−
H3K4me3+
ssGSEA score in tumor RNA−seq
ns
****
H3.3 K27M
H3 WT
pHGG subgroup
c
H3.3 K27M
H3 WT
Fetal hindbrain
Fetal thalamus
H3K4me3−
H3K4me3+
cPRC1 targets
UMAP 2
UMAP 1
Mean expression
d
Patient−derived xenograft
Survival probability
Genotype
K27M
KO
p = 5e−05
Days
e
SOX2
TOP2A
MBP
Expression
Xenograft sample
f
Genotype
RGC
Glial progenitors
OPC
Oligodendrocytes
Astrocytes
Ependymal
Cell type
Proportion (%)
H3K4me3− cPRC1 target expression
Low
High
g
Radial glial cell
Glial progenitor
Oligodendrocyte progenitor cell
Ependymal cell
Oligodendrocyte
Astrocyte

Figure 4. Compaction of Polycomb bodies is associated with the repression of target genes

a. Comparison of H3K27me3 and H3K4me3 signal between K27M pGBM cell line BT245 with its isogenic K27M-KO counterpart, revealing the gain of H3K4me3 especially in cPRC1 H3K4me3- sites
b. cPRC1 H3K4me3- targets identified in cell line models are consistently more repressed in bulk RNA-seq datasets of primary patient tumors, unlike bivalent cPR1 (i.e., H3K4me3+) targets
c. cPRC1 H3K4me3- targets are repressed in a homogenous manner across various cell types revealed by scRNA-seq in K27M pGBM, whereas select subpopulations appear to show elevated expression of those genes in WT pGBM and fetal brains, demonstrating the association between repression of cPRC1 H3K4me3- target genes and Polycomb bodies compaction
d. Patient-derived xenograft model recapitulates tumorigenic effect of K27M in contrast to KO. (Top) Kaplan-Meier survival analysis for xenograft mice, (bottom) *in vivo* imaging of tumor cells.
e. K27M cells in xenografts consistently show higher expression of stemness markers SOX2 and TOP2A and lower expression of differentiation marker MBP
f. Comparison of scRNA-seq from K27M and K27M-KO PDXs confirm upregulation of H3K4me3- cPRC1 targets is accompanied by an increase in the proportion of more differentiated cell types in K27M-KO
g. Developmental trajectory of neural cell types related to gliomagenesis

Figure 5

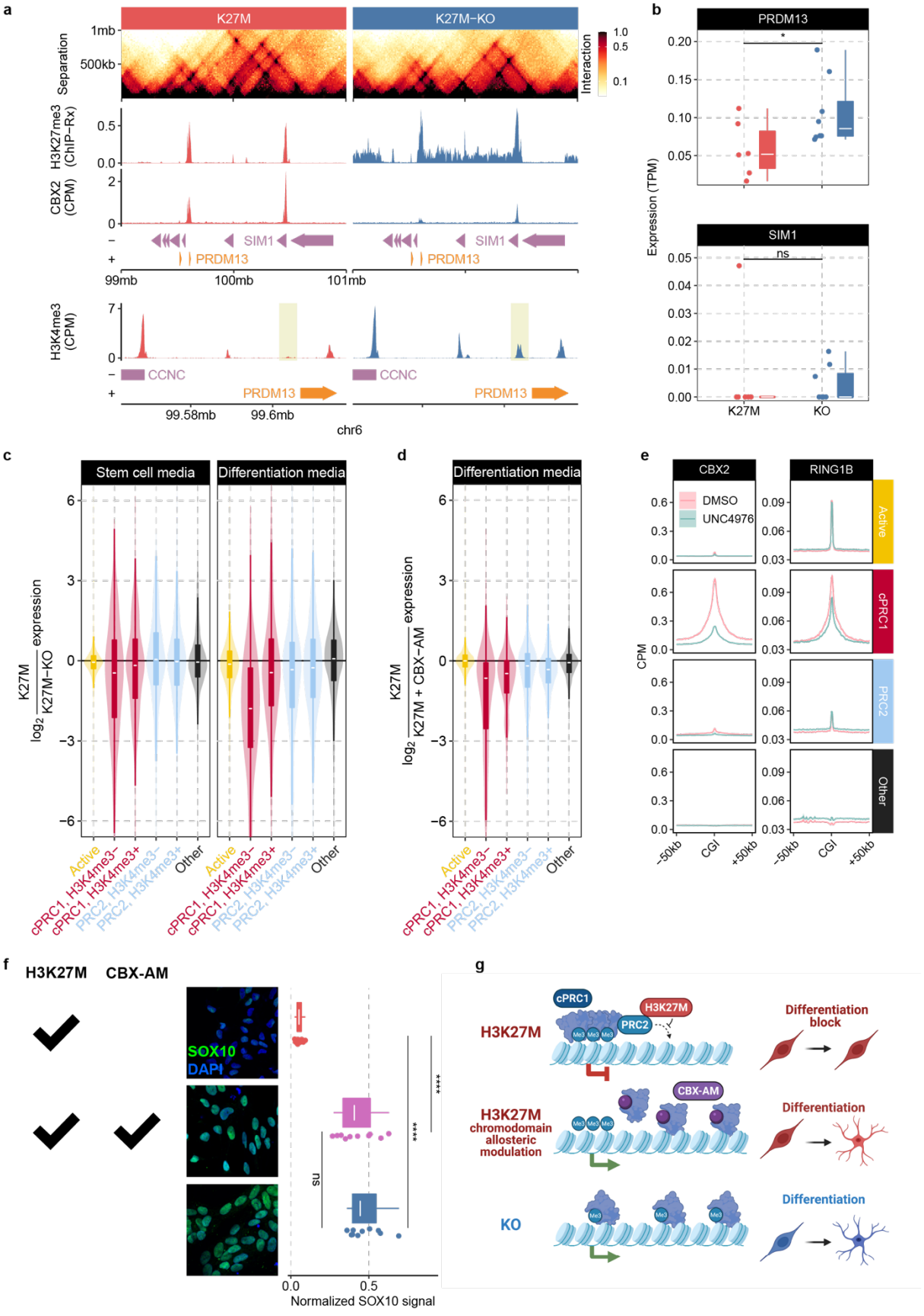
a
K27M
K27M−KO
Separation
1mb
500kb
Interaction
1.0
0.5
0.1
H3K27me3 (ChIP−Rx)
CBX2 (CPM)
SIM1
PRDM13
99mb
100mb
101mb
H3K4me3 (CPM)
CCNC
PRDM13
99.58mb
99.6mb
chr6
b
PRDM13
SIM1
Expression (TPM)
ns
K27M
KO
c
Stem cell media
Differentiation media
log2 K27M / K27M−KO expression
Active
cPRC1, H3K4me3−
cPRC1, H3K4me3+
PRC2, H3K4me3−
PRC2, H3K4me3+
Other
d
Differentiation media
log2 K27M / K27M + CBX−AM expression
e
CBX2
RING1B
DMSO
UNC4976
CPM
Active
cPRC1
PRC2
Other
−50kb
CGI
+50kb
f
H3K27M
CBX-AM
SOX10
DAPI
ns
****
Normalized SOX10 signal
g
cPRC1
H3K27M
PRC2
Me3
H3K27M
Differentiation block
CBX-AM
H3K27M chromodomain allosteric modulation
Differentiation
KO
Differentiation

Figure 5. Upregulation of cPRC1 target genes upon the removal of cPRC1-mediated chromatin compaction

a. Representative loci (around the genes PRDM13 and SIM1) of K27M-specific cPRC1-associated loop, bridging sites depleted of H3K4me3 in K27M but appears upon K27M-KO
b. Modest transcriptomic consequences arise in the two example genes after loop dissolution upon K27M-KO in stem cell media
c. Differential expression, specifically of cPRC1 targets, become heightened after differentiation compared to stem cell media
d. Similar transcriptional de-repression of cPRC1 targets is recapitulated via the application of a CBX allosteric modulator to K27M cells, demonstrating the link between cPRC1-mediated chromatin compaction and repression of cPRC1 targets
e. a
f. Up-regulation of differentiation markers observed in both K27M-KO and CBX-AM treated K27M cells in pGBM line BT245
g. Summary of CBX-AM treatment and K27M-KO's effect on the differentiation of K27M pGBM cells

Figure 6

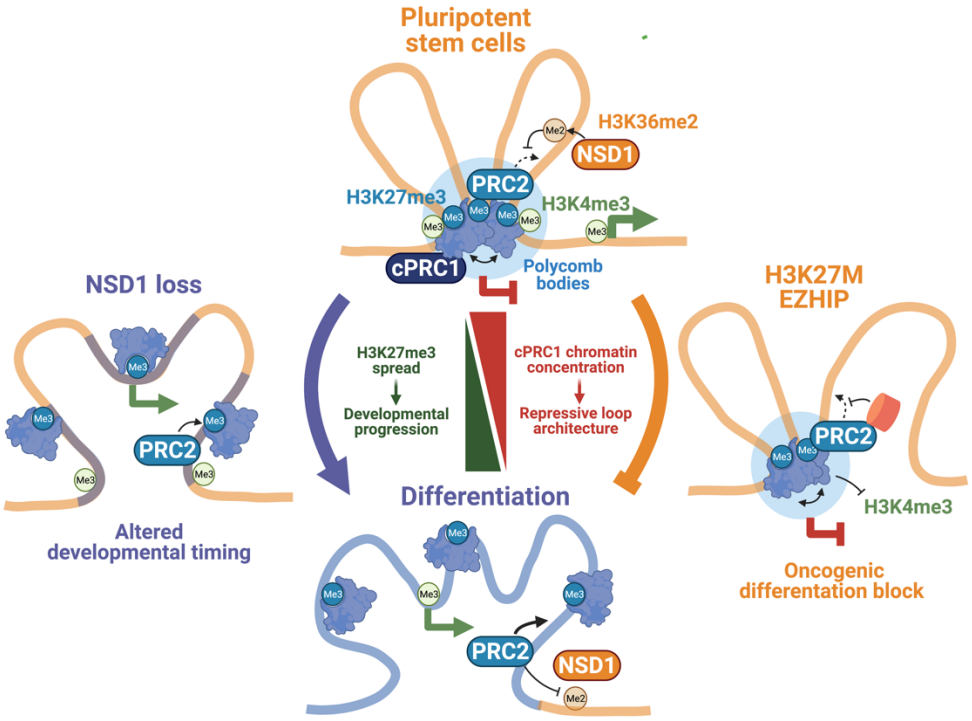

Figure 6. Model of the link between PRC2 spread and cPRC1 chromatin architecture causing altered developmental outcomes

Our understanding of the epigenome and its normal and abnormal regulation is going to increase at the present rapid rate. The fundamental knowledge emerging is going to provide ever increasing ramifications for translational science in areas such as cancer. New targeting strategies are going to allow us to build on already exciting indications that epigenetic therapy could provide a tremendous component for cancer therapy and for other diseases as well such as neurodegenerative disorders, diabetes, and so on.

Stephen B Baylin

Chapter 4

Discussion

Panorama of chromatin re-organization in health and disease

The preceding chapters outline molecular portraits of embryogenesis with an emphasis on the germline as well as of diseases associated with abnormal developmental progression. Ascertainment of the very same 3D epigenomic factors and processes as essential components of both healthy development and pediatric afflictions underscores universal regulatory mechanisms whose elucidation will carry far-reaching implications. Although strategies such as genome-wide CRISPR screens can provide tremendous value in narrowing down the scope of disease-relevant genes,[68] elucidation of the mechanistic cascade is no less important for moving towards the ultimate aim of uncovering therapeutically actionable insights. We've shown that a chromatin-centric perspective is especially apt for the integration of multi-omics datasets to unite upstream genetic alterations with downstream phenotypic outcomes as well as to pinpoint not only the crucial determinants of unimpeded and healthy differentiation themselves, but also the means through which they act; and this feat was only made possible by fully capitalizing on the complementary information revealed by orthogonal assays targeting various aspects of cellular activity such as different facets of the epigenome, nucleome, and transcriptome. Through detailed dissection of biolog-

ical contexts undergoing dramatic 3D epigenome remodelling, whether it be to the benefit or detriment of the system, we unveiled unexpected modes of genome regulation that bear significant relevance to understanding pathogenesis. Our systematic analysis of global 3D epigenomic features, both within and across omics layers, charts an illuminating path in navigating the sea of high-dimensional multi-omics datasets.

Filling in the gap of mammalian germline nucleome trajectory

Germ cells' unique role in facilitating the transmission of genetic information across generations places them squarely at the origin of totipotency. Nonetheless, previous efforts have placed greater emphasis on the completion of meiosis, fertilization, and early zygotic development due to a combination of technical factors as well as greater interest in the genesis of a entirely new life; as a result, while still an intensively investigated period, the mitotic development of germ cells spanning the blastocyst stage until germline stem cells have remained less understood (Fig. 4.1).[69] This particular stretch of germ cell development comprises a number critical cell fate decision known to involve sweeping epigenome remodelling, with perhaps the most drastic one being epigenetic reprogramming in primordial germ cells.

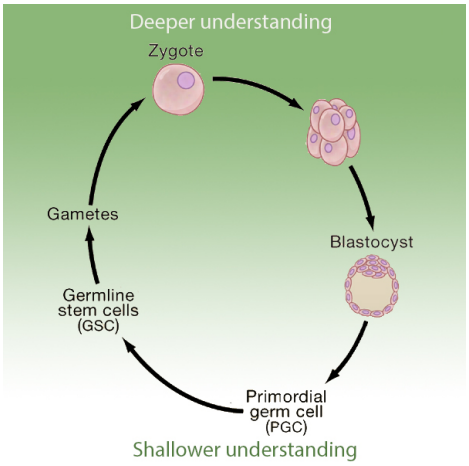

Figure 4.1: Cycle of gametogenesis. Adapted from Seydoux & Braun [69] with permission

Epigenetic reprogramming is known as one of the most unique remodelling developmental events, as the genome-wide de-methylation wipes the slate clean and potentiates the activation for essential germline expression programs via a combination of promoter de-methylation and removal of heterochromatic modifications such as H3K9me3 and H2AK119ub.[70] In this vulnerable stage of genome-wide hypomethylation, H3K27me3's expansion has been previously reported to provide a layer of restraint,[71] and our dataset indeed confirms this phenomenon as well as newly uncover a corresponding shrinkage

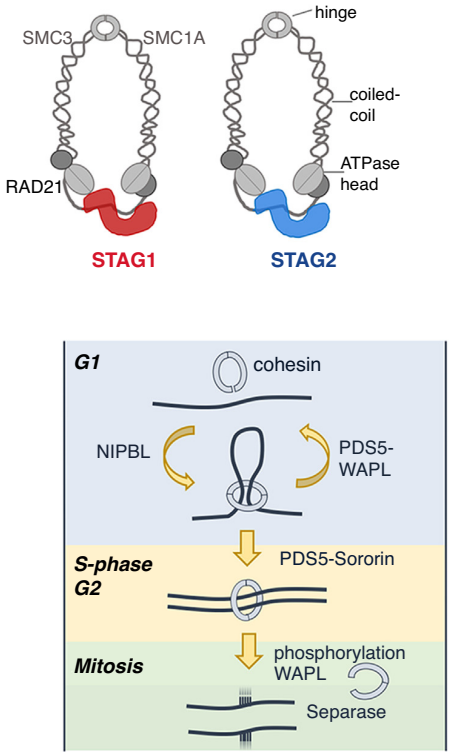

Figure 4.2: Functions of cohesin in 3D genome organization. Reproduced from Cuadrado & Losada [72] with permission

of H3K36me2 – once again highlighting the two chromatin marks' close coupling. Nevertheless, we discovered abundant enhancer signatures such as open chromatin and H3K4me1 pervade across the genome, bringing into question what other mechanisms exist to prevent these elements from driving spurious activation. Looking beyond histone modifications, we were able to identify elevated insulation as a novel hallmark of epigenetic reprogramming, emphasizing the importance of maintaining proper enhancer-promoter wiring for bridling a hypo-methylated genome. In contrast to the conventional view of de-DNA de-methylation promoting CTCF binding,[73] we saw that enhanced insulation in PGCs was not associated with differential CTCF patterns – but rather a shortening of cohesin/CTCF's residence time at boundary elements. As we did not detect strong associations between insulation change and differential signals for any of the myriad epigenetic modifications profiled, we consider this to implicate alternative mechanisms. Beyond epigenetic modifications, the loop extrusion machinery's chromatin association can be governed through diverse processes ranging from varying the subunit composition of cohesin (e.g., SA1- vs SA2-containing cohesin) to fluctuating levels of cohesin loading or unloading proteins including NIPBL and WAPL (Fig. 4.2).[72] Earlier reports have claimed that, though both SA1 and SA2 are associated with NIBPL-independent cohesin loading onto chromatin at R-loops, cohesin-SA1 preferentially contributes to greater insulation at TAD boundaries while cohesin-SA2 instead demonstrates greater association with PRC1-mediated compaction.[74] On the other hand, defects in cohesin loading via mutations NIBPL has been previously associated not only with a weakening of domain structures, but also directly implicated with developmental delay in Cornelia de Lange syndromes.[75] As we found the 3D genome organization of PGCLCs concurrently matches phenotypes observed for alterations in both cohesin-intrinsic and -extrinsic factors (e.g., broader compartments, shorter loops), further work is necessary to resolve the ambiguity. In particular, deter-

mining the most important mechanism at play in modulating physiological chromatin insulation will be essential to understanding germline nucleome dynamics at a deeper level as well as bear relevance to both developmental and chromatin biology at large – especially considering the broad purview of loop extrusion in gene regulation.

Re-methylation of the entire genome following the sweeping loss of DNA methylation during epigenetic reprogramming has led most to believe that the broader epigenome and nucleome may undergo a similar re-setting. Indeed, our observation of transient changes such as temporary increase of H3K27me3 and H3K4me1 as well as decrease of H3K36me2 specifically at the lowest point of DNA methylation, with a rapidly ensuing rebound, is consistent with this proposition. On the other hand, we noted that nucleome re-organization remarkably progresses in a monotonic manner, with decompaction continuing unaffected throughout epigenetic reprogramming, culminating in a highly euchromatized genome in spermatogonia. The remaining heterochromatic region persisting in the loosened spermatogonial genome was linked by us to the expansion of H3K9me3 into broad domains that engage in both local and distal aggregation, often corresponding to pericentromeric regions. The demonstrated association between H3K9me3 domain expansion with heightened heterochromatic aggregation thus provides a physiological context in which the genomic distribution of histone modifications is tightly coupled with higher-order chromatin organization,[24] adding to the growing body of evidence highlighting liquid-liquid phase separation and nuclear condensates as a pertinent regulatory modality.[29] Through FISH, we were additionally able to visualize that spermatogonial chromosomes show minimal attachment to the peripheral nuclear lamina, save for pericentromeric heterochromatin (PCH) that

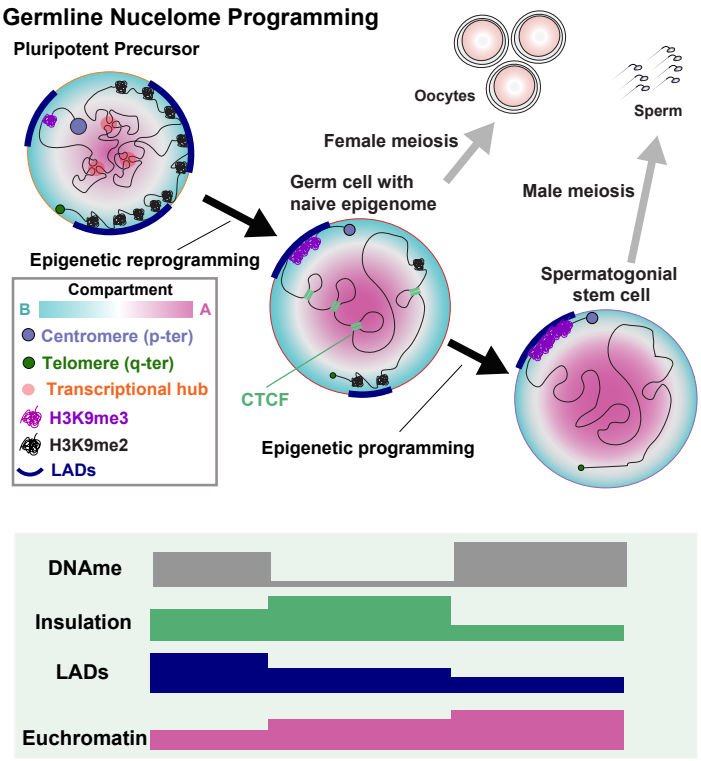

Figure 4.3: Germline nucleome dynamics.

migrates from the nuclear interior radially outwards. As the assembly of pericentromeres into dense chromocenters have been previously noted as a prominent feature of mouse spermatogenesis, with the structure even persisting after meiosis,[76] our finding thus pinpoints the origin of this process. The drastic radial repositioning of chromosome we witnessed also suggests a decoupling of periphery organization of germline progenitors with terminally differentiated germ cells, which is consistent with the knowledge that lamina associated domains are established in a wholly de novo manner post fertilization.[77] At smaller scales, we determined that the elevated insulation in PGCs is swiftly weakened in spermatogonia stem cells as CTCF became evicted from chromatin due to methylation on H3K9 and H3K36 as well as DNA in spermatogonia stem cells. We subsequently demonstrated that the lost of CTCF binding can promote both transcriptional up- and down-regulation, in line with prior accounts of acute CTCF depletion causing varied transcriptomic effects.[78] But importantly, we found a robust relationship between ectopic enhancer-promoter contacts facilitated by the loss of insulatory boundaries with up-regulation of genes central to meiotic pathways; and in germline stem cells with impaired spermatogenic potential, we saw an incomplete erasure of the very same boundaries. These descriptions thus significantly bolster the molecular portrait of male germ cell development in its entirety from multiple angles (Fig. 4.3)

Enabling studies of 3D epigenomic alterations in a dynamic physiological context

Many proteins serve specialized functions such as the recognition or transmission of particular agonists, but chromatin modifiers (e.g., writers of epigenetic modifications) and architectural proteins (e.g., cohesin, lamin) moulding the global 3D epigenome and therefore can have far-reaching effects, modulating multiple pathways and setting off elaborate cascades.[79] In addition to genetic and transcriptomic information, chromatin profiling has demonstrated that unique biological contexts, whether it be a specific cell type or a particular cancer subtype, could also be defined by salient 3D epigenetic signatures.[26] Given this link, there is a growing need for models that can faithfully reproduce these context-specific features, either at steady-state or even as as a dynamic process, in easily manipulated systems such as cell lines rather than laborious animal models or intricate organoid cultures. The *in vitro* model of murine gametogenesis here illustrates the utility of accurately recapitulating differentiation in a dish.[80] In particular, this system allows for large amounts of very specific cell types along germ cell differentiation to be generated in a reproducible manner, which critically enables the use of resource-intensive 3D epigenome

profiling techniques such as Hi-C in a straightforward manner and yield data with excellent signal-to-noise ratios. As the *in vitro* differentiation process was previously demonstrated to closely mirror the *in vivo* developmental trajectory and ultimately yield fully functional gametes, this model also facilitates the temporal assessment of 3D epigenome kinetics as well as direct evaluation of biological-relevant consequences by measuring spermatogenic potential. As the germline is known to undergo substantial 3D epigenome remodelling in a condensed period, it furnishes a rich setting to dissect chromatin dynamics; and the ongoing development of analogous *in vitro* systems in primates and other species also holding significant promise for future cross-species comparisons.[45]

During the acquisition of an androgenic DNA methylome after epigenetic reprogramming as PGCs differentiate into spermatogonia, select areas of the genome fail to become fully methylated, giving rise to broad partially methylated domains (PMDs). Using the *in vitro* system, we demonstrated that PMDs of spermatogonia stem cells can be directly traced back to their progenitor PGCs re-directing H3K9me3 into and H3K36me2 away from regions destined to eventually become PMDs. Therefore, this designates a physiological window for which the likes of super-resolution microscopy and live-cell imaging can be carried out to probe the mechanisms giving rise to hypo-methylated regions with high temporal resolution,[40,81] bearing relevance for both cancer and aging given the association of PMDs with mitotic history.[82] Our finding that PCH repositions from the nuclear interior towards the periphery along differentiation towards spermatogonia also provides an opportunity to determine the requisite co-factors involved in such large-scale chromosomal radial repositioning, for example, through a CRISPR screen. Seeing that PCH is known to yet again re-organizes into a singular chromocenter in the nuclear interior after meiosis, this signifies a highly dynamic period in development that can help clarify the consequences of improper radial repositioning of chromosomal territories. Subsequently, the implicated processes can be compared to other cases of similar inversion events such as rod photoreceptors with uniquely inverted chromatin organization.[83] The severely DNA hypo-methylated genome of PGCs, too, represents a chance to closely assess what contributes to proper maintenance of genome integrity in this vulnerable state. For instance, we've already identified enhanced chromatin insulation as an additional layer of restraint. Since aberrant DNA hypo- and hyper-methylation are ubiquitous features of carcinogenesis,[84] a deeper mechanistic understanding of the genome's intrinsic defense mechanisms in a naturally hypo-methylated state will aid the design of strategies to either steer malignant cells towards a healthier state

or push them over the edge. Altogether, the interplay between different modes and scales of 3D genome organization represents a direly under-explored angle for addressing pathological defects.

Balancing act of euchromatin versus heterochromatin

The vast collection of epigenome profiles across diverse cell types has established that the genome is segregated into discrete domains with chromatin states defined by distinct combinations of epigenetic modifications.[85] As many modifications undergo coordinated changes are can be thought of as redundant from an informational standpoint, several key markers have emerged as useful indicators for prominent high-level domain classes such as H3K36 methylation for euchromatin, H3K27 methylation for facultative heterochromatin, and H3K9 methylation for constitutive heterochromatin.[86] In particular, it's been demonstrated that changes in H3K27 methylation patterns can be both induced by the distribution of H3K36 methylation and through perturbations to PRC1/2 sub-units or co-factors and histone H3 itself (e.g., H3K27M or the H3K27M-mimic – EZHIP).[87] By systematically profiling a host of published as well as newly generated samples, we showed that H3K27me3 distributions can be generally categorized into focused versus diffuse modes of chromatin patterning across developmental and disease-relevant contexts. These include not only H3K27M and EZHIP, but also the loss of H3K36 methyltransferase NSD1 (removal of H3K36me2 leading to H3K27me3 spread), over-expression of H3K36 methyltransferase NSD2 (increase of H3K36me2 leading to H3K27me3 shrinkage), loss of H2AK119 deubiquitinase BAP1 (diffusion of H2AK119ub accompanied by H3K27me3 spread due to PRC2's H2AK119ub-reading activity), loss of linker histone H1 (chromatin decompaction hampering PRC2 spread), among other prominent disease-associated mutations in chromatin modifiers. Additionally, we noted that the confinement of H3K27me3 to CpG islands and promoters was more prevalent among progenitor cell types when compared to more differentiated stages, therefore linking confined H3K27me3 with an early cellular state still possessing considerable differentiation potential. Although previous reports have noted an association between focal H3K27me3 with heightened long-range interaction in mouse embryonic stem cells,[88] we systematically extended this finding to other lineages as well as several epigenetically dysregulated cancers (e.g., PFA ependymoma with EZHIP over-expression, glioblastoma carrying the H3K27M mutation, multiple myeloma with duplicated NSD2).

Pursuing this 3D epigenomic relationship further, we specifically identified the binding of a H3K27me3 reader, canonical PRC1 (cPRC1), to designate regions participating in elevated long-range interactions concomitant with H3K27me3 confinement. This close coupling between epigenetics and 3D genome organization falls in line with cPRC1's known capacity to facilitate liquid-liquid phase separation via mechanisms such as the associative properties of cPRC1 subunit CBX2's intrinsically disordered regions.[89]

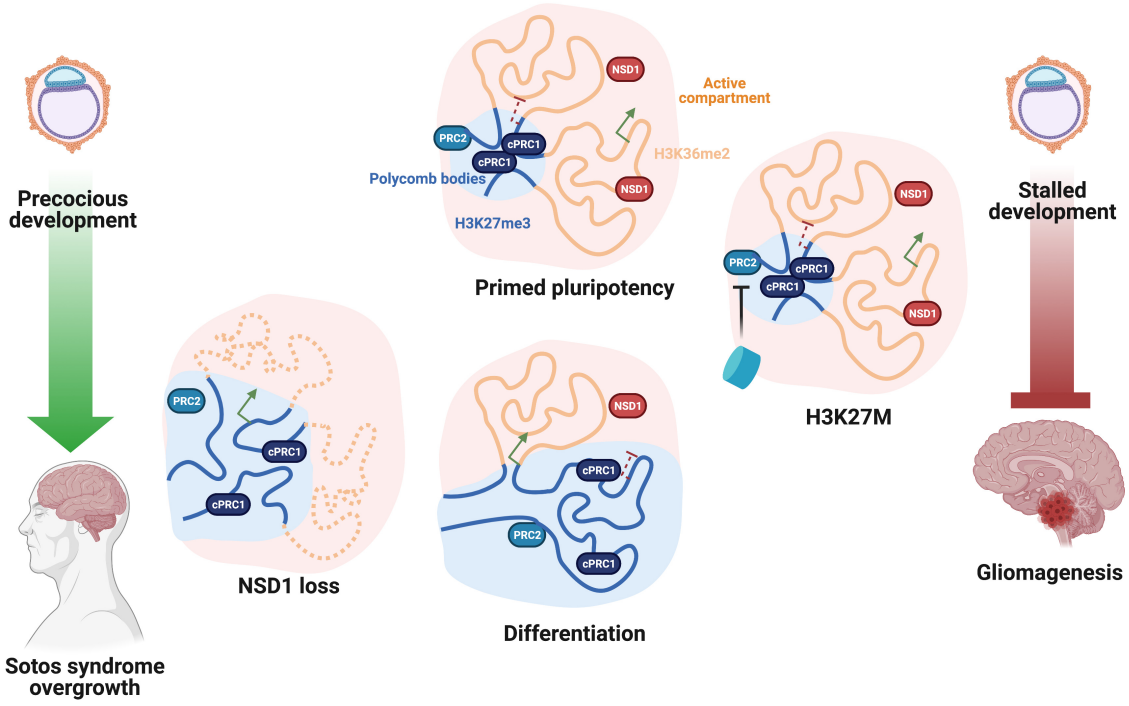

Figure 4.4: Polycomb-associated chromatin architecture.

Although the chromatin states of H3K27me3-enriched regions bound by cPRC1 are largely conserved across cell types and species, we found that cancer systems (H3K27M gliomas in particular) diverge from mammalian stem cells in terms of bivalency, with the former possessing both H3K4me3+ (bivalent) and H3K4me3- (non-bivalent) cPRC1 targets while only bivalent sites were present in the latter cases.[18] Yet the spreading of H3K27me3, and therefore dilution of cPRC1, led to greater differential interaction for non-bivalent promoters than bivalent ones in H3K27M GBMs, further implicating the balance between heterochromatic Polycomb and euchromatic trithorax systems beyond regulation of local chromatin environment to additionally governing higher-order chromatin organization.[90] In stem

cells, the obligate expansion of H3K27me3 from nucleation sites as a consequence of decrease in NSD1-mediated H3K36me2 nevertheless results in a loss of long-range interaction between cPRC1 targets and modest increase in gene expression. Considering the over-representation of developmental regulators among Polycomb targets,[65] counting the likes of Hox genes as well as numerous tumor suppressor and oncogenes, our results indicate that the Polycomb system modulates cellular plasticity by means of both proximal and distal processes alike, especially in healthy and malignant stem-like cells (Fig. 4.4).

Therapeutically transforming the 3D epigenome

In view of the firm connection between epigenomic defects and pathogenesis based on evidence such as driver mutations in chromatin modifier genes, therapeutic development targeting the epigenome have been advancing at full steam (Fig. 4.5).[91] Indeed, a slew of inhibitors for epigenetic regulators has received regulatory approval in recent years: azacitidine, an inhibitor of DNA methyltransferases, for the treatment of acute myeloid leukemia, panobinostat, an inhibitor of histone de-acetylases, for the treatment of multiple myeloma, tazemetostat, a histone methyltransferase inhibitor (targeting EZH2, a component of PRC2), for the treatment of follicular lymphoma.[8] While many compounds act through competitive inhibition and prevent binding of the physiological substrate to the affected enzyme in a global fashion, more recent advances in E3 ligase modulators that can enable the recognition of neosubstrates have expanded the druggable space of proteins beyond conventional targets such as enzymes to even transcription factors and other epigenetic players.[92] In parallel, CRISPR-based technologies are enabling precision epigenome edits through the fusion of chromatin modifiers to inactive Cas9 proteins, thereby allowing sequence-specific targeting.[93] To fully capitalize on the growing collection of molecular instruments for biomedical aims, the initial target selec-

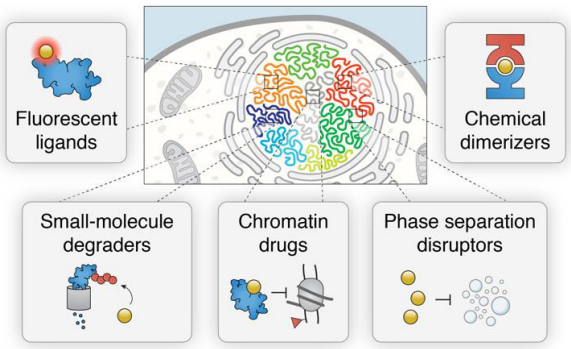

Figure 4.5: Chromatin-targeting drugs and probes. Reproduced from Cermakova & Hodges [91] with permission

tion stands as one of the most critical steps.

Through integration of multi-omics datasets traversing the epigenome, nucleome, and transcriptome, we were able to single out cPRC1-mediated aggregation of distal genomic regions as a key mechanism repressing developmental targets in H3K27M GBMs. As this specific subgroup of pediatric brain tumors has been associated with a stalled development phenotype based on single cell transcriptomic signatures,[58] the natural progression was to identify methods capable of alleviating this blockade through perturbing the hurdles in place. Our findings related to cPRC1 thus presented an excellent target in CBX2, as it is the key factor in both the recognition of H3K27me3 as well as contributing to the self-association of cPRC1 complexes to drive long-range interaction across long genomic separations. On this basis, we were able to quickly dial in a small-molecule treatment regime and observe clear impacts in terms of not only the de-repression of previously silent genes cPRC1 targets, but more important the up-regulation of key marker genes of differentiated cell types to a comparable level to cells with H3K27M fully removed via CRISPR-Cas9 knockout. This process thus highlights the immense potential of rational therapeutic design through first unravelling the epigenomic mechanisms contributing to tumor-intrinsic properties, consequently facilitating efficient translation of early discovery insights to downstream development.

Chapter 5

Conclusion

Genetics' leap to the forefront of biology since the turn of the millennium is in no small part thanks to monumental efforts encyclopedically cataloging sequence variation such as the Human Genome Project, the International HapMap Project, the 1000 Genomes Project, and more recently the UK Biobank. Nonetheless, perhaps more decisive in accentuating genetics in the public conscience has been everyday uses such as prenatal genetic screening and genetic ancestry testing, affording more personal insights. In other words, it's become evident that fundamental biological research must be carried out in lock-step with clinically oriented translational endeavours, as the former can serendipitously bear significant consequence for the latter. Being the immediate layer of organization above DNA strands, chromatin dynamics have emerged as the natural progression as the field looks beyond DNA. With this step up in scale comes along a dramatic escalation in complexity, demanding multi-faceted characterizations of genome regulation. At the same time, the reward for untangling such an intricate network of chromatin remodelling processes can be immense, since it would allow effective use of incredible biotechnological advances and expanding therapeutic arsenal.

As our understanding of germline developmental improves via the thorough investigation of current systems such as the vitro differentiation model of gametogenesis in mouse, this knowledge could be in turn used to propel the betterment of comparable setups in other species such as human. Simultaneously, the increasing capabilities of single cell technologies will enable analogous efforts for *in vivo* samples, additionally providing complementary insights into key aspects such as the cellular microenvironment during physiological development. Ultimately, the insights obtained from these systems will enable significant progress towards realizing the full potential of stem cell reprogramming, addressing fundamental needs in reproductive medicine. Nevertheless, the pursuit of these efforts must also heed bioethical concerns, as choreographing life itself must be approached sensitively and aim towards bringing equitable benefits

to all those in need.

The ballooning literature emphasizing the 3D epigenome's importance thus far has focused on select well-understand model systems such as embryonic stem cells, but as our discovery of distal cis-regulatory process such as cPRC1-associated looping as a pivotal disease mechanism highlight that these processes can have far-reaching impacts. Yet the clarification of these processes often proves non-trivial, as interplay can take place at multiple scales (e.g., individual genomic elements versus expansive domains), modalities (e.g., local chromatin compaction versus long-range spatial aggregation) and mechanisms (e.g., active loop extrusion competing with passive phase separation). Nevertheless, our work demonstrates that it is viable to methodically disentangle these interrelated phenomena through carefully overlaying multi-omics datasets on top of the wealth of existing knowledge, and paints a blueprint for future efforts of understanding different diseases from a chromatin perspective.

Looking beyond the genome, epigenome, and nucleome, there remain other under-explored aspects of the mysterious tiny pearls that are the cells constituting life. These new frontiers range from a quantitative comprehension of the proteome and associated post-translational modifications, clarifying the physiological function of extrachromosomal DNA, as well as understanding the contributions of RNA-DNA and RNA-protein interactions, just to name a few. It is thus imperative to steadily adopt novel vantages and continuously update the axioms of life, pushing us to near frontiers of biomedicine. To thus effectively leverage these massive datasets of growing complexity, ever more sophisticated computational methods for their integration have been and will continue to be indispensable. More importantly, the efforts of computational scientists must be seamlessly united with those of experimental biologists to ensure the smooth and timely march towards a future of personalized medicine for all.

Chapter 6

References

1. Costello, A. & Badran, A. H. Synthetic Biological Circuits within an Orthogonal Central Dogma. *Trends in Biotechnology* **39**, 59–71. doi:10.1016/j.tibtech.2020.05.013 (Jan. 2021).
2. McCarty, M. Discovering genes are made of DNA. *Nature* **421**, 406–406. doi:10.1038/nature01398 (Jan. 2003).
3. Antonarakis, S. E. History of the methodology of disease gene identification. *American Journal of Medical Genetics Part A* **185**, 3266–3275. doi:10.1002/ajmg.a.62400 (June 2021).
4. Antonarakis, S. E. & Beckmann, J. S. Mendelian disorders deserve more attention. *Nature Reviews Genetics* **7**, 277–282. doi:10.1038/nrg1826 (Mar. 2006).
5. Shteinberg, M., Haq, I. J., Polineni, D. & Davies, J. C. Cystic fibrosis. *The Lancet* **397**, 2195–2211. doi:10.1016/s0140-6736(20)32542-3 (June 2021).
6. Tam, V. *et al.* Benefits and limitations of genome-wide association studies. *Nature Reviews Genetics* **20**, 467–484. doi:10.1038/s41576-019-0127-1 (May 2019).
7. Greally, J. M. A user's guide to the ambiguous word 'epigenetics'. *Nature Reviews Molecular Cell Biology* **19**, 207–208. doi:10.1038/nrm.2017.135 (Jan. 2018).
8. Bates, S. E. Epigenetic Therapies for Cancer. *New England Journal of Medicine* **383** (ed Longo, D. L.) 650–663. doi:10.1056/nejmra1805035 (Aug. 2020).
9. Greenberg, M. V. C. & Bourc'his, D. The diverse roles of DNA methylation in mammalian development and disease. *Nature Reviews Molecular Cell Biology* **20**, 590–607. doi:10.1038/s41580-019-0159-6 (Aug. 2019).
10. Zhou, V. W., Goren, A. & Bernstein, B. E. Charting histone modifications and the functional organization of mammalian genomes. *Nature Reviews Genetics* **12**, 7–18. doi:10.1038/nrg2905 (Nov. 2010).
11. Klemm, S. L., Shipony, Z. & Greenleaf, W. J. Chromatin accessibility and the regulatory epigenome. *Nature Reviews Genetics* **20**, 207–220. doi:10.1038/s41576-018-0089-8 (Jan. 2019).
12. Atlasi, Y. & Stunnenberg, H. G. The interplay of epigenetic marks during stem cell differentiation and development. *Nature Reviews Genetics* **18**, 643–658. doi:10.1038/nrg.2017.57 (Aug. 2017).
13. Slack, J. M. W. Conrad Hal Waddington: the last Renaissance biologist? *Nature Reviews Genetics* **3**, 889–895. doi:10.1038/nrg933 (Nov. 2002).

14. Granados, K., Poelchen, J., Novak, D. & Utikal, J. Cellular Reprogramming—A Model for Melanoma Cellular Plasticity. *International Journal of Molecular Sciences* **21**, 8274. doi:10.3390/ijms21218274 (Nov. 2020).

15. Boix, C. A., James, B. T., Park, Y. P., Meuleman, W. & Kellis, M. Regulatory genomic circuitry of human disease loci by integrative epigenomics. *Nature* **590**, 300–307. doi:10.1038/s41586-020-03145-z (Feb. 2021).

16. Hoadley, K. A. *et al.* Cell-of-Origin Patterns Dominate the Molecular Classification of 10,000 Tumors from 33 Types of Cancer. *Cell* **173**, 291–304.e6. doi:10.1016/j.cell.2018.03.022 (Apr. 2018).

17. Shlyueva, D., Stampfel, G. & Stark, A. Transcriptional enhancers: from properties to genome-wide predictions. *Nature Reviews Genetics* **15**, 272–286. doi:10.1038/nrg3682 (Mar. 2014).

18. Blanco, E., González-Ramírez, M., Alcaine-Colet, A., Aranda, S. & Croce, L. D. The Bivalent Genome: Characterization, Structure, and Regulation. *Trends in Genetics* **36**, 118–131. doi:10.1016/j.tig.2019.11.004 (Feb. 2020).

19. Hnisz, D., Day, D. S. & Young, R. A. Insulated Neighborhoods: Structural and Functional Units of Mammalian Gene Control. *Cell* **167**, 1188–1200. doi:10.1016/j.cell.2016.10.024 (Nov. 2016).

20. Jones, P. A., Issa, J.-P. J. & Baylin, S. Targeting the cancer epigenome for therapy. *Nature Reviews Genetics* **17**, 630–641. doi:10.1038/nrg.2016.93 (Sept. 2016).

21. Jani, K. S. *et al.* Histone H3 tail binds a unique sensing pocket in EZH2 to activate the PRC2 methyltransferase. *Proceedings of the National Academy of Sciences* **116**, 8295–8300. doi:10.1073/pnas.1819029116 (Apr. 2019).

22. Sanborn, A. L. *et al.* Chromatin extrusion explains key features of loop and domain formation in wild-type and engineered genomes. *Proceedings of the National Academy of Sciences* **112**. doi:10.1073/pnas.1518552112 (Oct. 2015).

23. Zheng, H. & Xie, W. The role of 3D genome organization in development and cell differentiation. *Nature Reviews Molecular Cell Biology* **20**, 535–550. doi:10.1038/s41580-019-0132-4 (June 2019).

24. Wang, L. *et al.* Histone Modifications Regulate Chromatin Compartmentalization by Contributing to a Phase Separation Mechanism. *Molecular Cell* **76**, 646–659.e6. doi:10.1016/j.molcel.2019.08.019 (Nov. 2019).

25. Davidson, I. F. & Peters, J.-M. Genome folding through loop extrusion by SMC complexes. *Nature Reviews Molecular Cell Biology* **22**, 445–464. doi:10.1038/s41580-021-00349-7 (Mar. 2021).

26. Anania, C. & Lupiáñez, D. G. Order and disorder: abnormal 3D chromatin organization in human disease. *Briefings in Functional Genomics* **19**, 128–138. doi:10.1093/bfgp/elz028 (Feb. 2020).

27. Nuebler, J., Fudenberg, G., Imakaev, M., Abdennur, N. & Mirny, L. A. Chromatin organization by an interplay of loop extrusion and compartmental segregation. *Proceedings of the National Academy of Sciences* **115**. doi:10.1073/pnas.1717730115 (July 2018).

28. Rhodes, J. D. *et al.* Cohesin Disrupts Polycomb-Dependent Chromosome Interactions in Embryonic Stem Cells. *Cell Reports* **30**, 820–835.e10. doi:10.1016/j.celrep.2019.12.057 (Jan. 2020).

29. Sabari, B. R., Dall'Agnese, A. & Young, R. A. Biomolecular Condensates in the Nucleus. *Trends in Biochemical Sciences* **45**, 961–977. doi:10.1016/j.tibs.2020.06.007 (Nov. 2020).

30. Norton, H. K. & Phillips-Cremins, J. E. Crossed wires: 3D genome misfolding in human disease. *Journal of Cell Biology* **216**, 3441–3452. doi:10.1083/jcb.201611001 (Aug. 2017).

31. Yugi, K., Kubota, H., Hatano, A. & Kuroda, S. Trans-Omics: How To Reconstruct Biochemical Networks Across Multiple 'Omic' Layers. *Trends in Biotechnology* **34**, 276–290. doi:10.1016/j.tibtech.2015.12.013 (Apr. 2016).

32. Goodwin, S., McPherson, J. D. & McCombie, W. R. Coming of age: ten years of next-generation sequencing technologies. *Nature Reviews Genetics* **17**, 333–351. doi:10.1038/nrg.2016.49 (May 2016).

33. Sigal, Y. M., Zhou, R. & Zhuang, X. Visualizing and discovering cellular structures with super-resolution microscopy. *Science* **361**, 880–887. doi:10.1126/science.aau1044 (Aug. 2018).

34. Van Mierlo, G. & Vermeulen, M. Chromatin Proteomics to Study Epigenetics — Challenges and Opportunities. *Molecular & Cellular Proteomics* **20**, 100056. doi:10.1074/mcp.r120.002208 (2021).

35. Rivera, C. & Ren, B. Mapping Human Epigenomes. *Cell* **155**, 39–55. doi:10.1016/j.cell.2013.09.011 (Sept. 2013).

36. Lu, C., Coradin, M., Porter, E. G. & Garcia, B. A. Accelerating the Field of Epigenetic Histone Modification Through Mass Spectrometry–Based Approaches. *Molecular & Cellular Proteomics* **20**, 100006. doi:10.1074/mcp.r120.002257 (2021).

37. Illumina. *For All You Seq – DNA* https://www.illumina.com/content/dam/illumina-marketing/documents/applications/ngs-library-prep/for-all-you-seq-dna.pdf (2016).

38. Kempfer, R. & Pombo, A. Methods for mapping 3D chromosome architecture. *Nature Reviews Genetics* **21**, 207–226. doi:10.1038/s41576-019-0195-2 (Dec. 2019).

39. Fudenberg, G. & Imakaev, M. FISH-ing for captured contacts: towards reconciling FISH and 3C. *Nature Methods* **14**, 673–678. doi:10.1038/nmeth.4329 (June 2017).

40. Takei, Y. *et al.* Single-cell nuclear architecture across cell types in the mouse brain. *Science* **374**, 586–594. doi:10.1126/science.abj1966 (Oct. 2021).

41. Illumina. *For All You Seq – RNA* https://www.illumina.com/content/dam/illumina-marketing/documents/applications/ngs-library-prep/for-all-you-seq-rna.pdf (2016).

42. Stark, R., Grzelak, M. & Hadfield, J. RNA sequencing: the teenage years. *Nature Reviews Genetics* **20**, 631–656. doi:10.1038/s41576-019-0150-2 (July 2019).

43. Hirabayashi, S. *et al.* NET-CAGE characterizes the dynamics and topology of human transcribed cis-regulatory elements. *Nature Genetics* **51**, 1369–1379. doi:10.1038/s41588-019-0485-9 (Sept. 2019).

44. Sasaki, H. & Matsui, Y. Epigenetic events in mammalian germ-cell development: reprogramming and beyond. *Nature Reviews Genetics* **9**, 129–140. doi:10.1038/nrg2295 (Feb. 2008).

45. Saitou, M. Mammalian Germ Cell Development: From Mechanism to In Vitro Reconstitution. *Stem Cell Reports* **16**, 669–680. doi:10.1016/j.stemcr.2021.01.008 (Apr. 2021).

46. Xia, W. & Xie, W. Rebooting the Epigenomes during Mammalian Early Embryogenesis. *Stem Cell Reports* **15**, 1158–1175. doi:10.1016/j.stemcr.2020.09.005 (Dec. 2020).

47. Flyamer, I. M. *et al.* Single-nucleus Hi-C reveals unique chromatin reorganization at oocyte-to-zygote transition. *Nature* **544**, 110–114. doi:10.1038/nature21711 (Mar. 2017).

48. Chen, Z., Djekidel, M. N. & Zhang, Y. Distinct dynamics and functions of H2AK119ub1 and H3K27me3 in mouse preimplantation embryos. *Nature Genetics* **53**, 551–563. doi:10.1038/s41588-021-00821-2 (Apr. 2021).

49. Du, Z. *et al.* Polycomb Group Proteins Regulate Chromatin Architecture in Mouse Oocytes and Early Embryos. *Molecular Cell* **77**, 825–839.e7. doi:10.1016/j.molcel.2019.11.011 (Feb. 2020).

50. Feinberg, A. P., Koldobskiy, M. A. & Göndör, A. Epigenetic modulators, modifiers and mediators in cancer aetiology and progression. *Nature Reviews Genetics* **17**, 284–299. doi:10.1038/nrg.2016.13 (Mar. 2016).

51. ICGC/TCGA Pan-Cancer Analysis of Whole Genomes Consortium. Pan-cancer analysis of whole genomes. *Nature* **578**, 82–93. doi:10.1038/s41586-020-1969-6 (Feb. 2020).

52. Zhao, S., Allis, C. D. & Wang, G. G. The language of chromatin modification in human cancers. *Nature Reviews Cancer* **21**, 413–430. doi:10.1038/s41568-021-00357-x (May 2021).

53. Nacev, B. A. *et al.* The expanding landscape of 'oncohistone' mutations in human cancers. *Nature* **567**, 473–478. doi:10.1038/s41586-019-1038-1 (Mar. 2019).

54. Jain, S. U. *et al.* H3 K27M and EZHIP Impede H3K27-Methylation Spreading by Inhibiting Allosterically Stimulated PRC2. *Molecular Cell* **80**, 726–735.e7. doi:10.1016/j.molcel.2020.09.028 (Nov. 2020).

55. Pollack, I. F., Agnihotri, S. & Broniscer, A. Childhood brain tumors: current management, biological insights, and future directions. *Journal of Neurosurgery: Pediatrics* **23**, 261–273. doi:10.3171/2018.10.peds18377 (Mar. 2019).

56. Bayliss, J. *et al.* Lowered H3K27me3 and DNA hypomethylation define poorly prognostic pediatric posterior fossa ependymomas. *Science Translational Medicine* **8**. doi:10.1126/scitranslmed.aah6904 (Nov. 2016).

57. Harutyunyan, A. S. *et al.* H3K27M induces defective chromatin spread of PRC2-mediated repressive H3K27me2/me3 and is essential for glioma tumorigenesis. *Nature Communications* **10**. doi:10.1038/s41467-019-09140-x (Mar. 2019).

58. Jessa, S. *et al.* Stalled developmental programs at the root of pediatric brain tumors. *Nature Genetics* **51**, 1702–1713. doi:10.1038/s41588-019-0531-7 (Nov. 2019).

59. Soshnev, A., Josefowicz, S. & Allis, C. D. Greater Than the Sum of Parts: Complexity of the Dynamic Epigenome. *Molecular Cell* **62**, 681–694. doi:10.1016/j.molcel.2016.05.004 (June 2016).

60. Streubel, G. *et al.* The H3K36me2 Methyltransferase Nsd1 Demarcates PRC2-Mediated H3K27me2 and H3K27me3 Domains in Embryonic Stem Cells. *Molecular Cell* **70**, 371–379.e5. doi:10.1016/j.molcel.2018.02.027 (Apr. 2018).

61. Allshire, R. C. & Madhani, H. D. Ten principles of heterochromatin formation and function. *Nature Reviews Molecular Cell Biology* **19**, 229–244. doi:10.1038/nrm.2017.119 (Dec. 2017).

62. Farhangdoost, N. *et al.* Chromatin dysregulation associated with NSD1 mutation in head and neck squamous cell carcinoma. *Cell Reports* **34**, 108769. doi:10.1016/j.celrep.2021.108769 (Feb. 2021).

63. Lhoumaud, P. *et al.* NSD2 overexpression drives clustered chromatin and transcriptional changes in a subset of insulated domains. *Nature Communications* **10**. doi:10.1038/s41467-019-12811-4 (Oct. 2019).

64. Lu, C. *et al.* Histone H3K36 mutations promote sarcomagenesis through altered histone methylation landscape. *Science* **352**, 844–849. doi:10.1126/science.aac7272 (May 2016).

65. Blackledge, N. P. & Klose, R. J. The molecular principles of gene regulation by Polycomb repressive complexes. *Nature Reviews Molecular Cell Biology* **22**, 815–833. doi:10.1038/s41580-021-00398-y (Aug. 2021).

66. Maezawa, S. *et al.* SCML2 promotes heterochromatin organization in late spermatogenesis. *Journal of Cell Science*. doi:10.1242/jcs.217125 (Jan. 2018).

67. Ragazzini, R. *et al.* EZHIP constrains Polycomb Repressive Complex 2 activity in germ cells. *Nature Communications* 10. doi:10.1038/s41467-019-11800-x (Aug. 2019).

68. Bock, C. *et al.* High-content CRISPR screening. *Nature Reviews Methods Primers* 2. doi:10.1038/s43586-021-00093-4 (Feb. 2022).

69. Seydoux, G. & Braun, R. E. Pathway to Totipotency: Lessons from Germ Cells. *Cell* 127, 891–904. doi:10.1016/j.cell.2006.11.016 (Dec. 2006).

70. Mochizuki, K. *et al.* Repression of germline genes by PRC1.6 and SETDB1 in the early embryo precedes DNA methylation-mediated silencing. *Nature Communications* 12. doi:10.1038/s41467-021-27345-x (Dec. 2021).

71. Kurimoto, K. *et al.* Quantitative Dynamics of Chromatin Remodeling during Germ Cell Specification from Mouse Embryonic Stem Cells. *Cell Stem Cell* 16, 517–532. doi:10.1016/j.stem.2015.03.002 (May 2015).

72. Cuadrado, A. & Losada, A. Specialized functions of cohesins STAG1 and STAG2 in 3D genome architecture. *Current Opinion in Genetics & Development* 61, 9–16. doi:10.1016/j.gde.2020.02.024 (Apr. 2020).

73. Wiehle, L. *et al.* DNA (de)methylation in embryonic stem cells controls CTCF-dependent chromatin boundaries. *Genome Research* 29, 750–761. doi:10.1101/gr.239707.118 (Apr. 2019).

74. Cuadrado, A. *et al.* Specific Contributions of Cohesin-SA1 and Cohesin-SA2 to TADs and Polycomb Domains in Embryonic Stem Cells. *Cell Reports* 27, 3500–3510.e4. doi:10.1016/j.celrep.2019.05.078 (June 2019).

75. Garcia, P. *et al.* Disruption of NIPBL/Scc2 in Cornelia de Lange Syndrome provokes cohesin genome-wide redistribution with an impact in the transcriptome. *Nature Communications* 12. doi:10.1038/s41467-021-24808-z (July 2021).

76. Berrios, S. Nuclear Architecture of Mouse Spermatocytes: Chromosome Topology, Heterochromatin, and Nucleolus. *Cytogenetic and Genome Research* 151, 61–71. doi:10.1159/000460811 (2017).

77. Borsos, M. *et al.* Genome–lamina interactions are established de novo in the early mouse embryo. *Nature* 569, 729–733. doi:10.1038/s41586-019-1233-0 (May 2019).

78. Nora, E. P. *et al.* Targeted Degradation of CTCF Decouples Local Insulation of Chromosome Domains from Genomic Compartmentalization. *Cell* 169, 930–944.e22. doi:10.1016/j.cell.2017.05.004 (May 2017).

79. Chen, T. & Dent, S. Y. R. Chromatin modifiers and remodellers: regulators of cellular differentiation. *Nature Reviews Genetics* **15,** 93–106. doi:10.1038/nrg3607 (Dec. 2013).

80. Ishikura, Y. *et al.* In vitro reconstitution of the whole male germ-cell development from mouse pluripotent stem cells. *Cell Stem Cell* **28,** 2167–2179.e9. doi:10.1016/j.stem.2021.08.005 (Dec. 2021).

81. Eng, C.-H. L. *et al.* Transcriptome-scale super-resolved imaging in tissues by RNA seqFISH+. *Nature* **568,** 235–239. doi:10.1038/s41586-019-1049-y (Mar. 2019).

82. Decato, B. E. *et al.* Characterization of universal features of partially methylated domains across tissues and species. *Epigenetics & Chromatin* **13.** doi:10.1186/s13072-020-00363-7 (Oct. 2020).

83. Falk, M. *et al.* Heterochromatin drives compartmentalization of inverted and conventional nuclei. *Nature* **570,** 395–399. doi:10.1038/s41586-019-1275-3 (June 2019).

84. Ehrlich, M. DNA hypomethylation in cancer cells. *Epigenomics* **1,** 239–259. doi:10.2217/epi.09.33 (Dec. 2009).

85. Dixon, J., Gorkin, D. & Ren, B. Chromatin Domains: The Unit of Chromosome Organization. *Molecular Cell* **62,** 668–680. doi:10.1016/j.molcel.2016.05.018 (June 2016).

86. Hyun, K., Jeon, J., Park, K. & Kim, J. Writing, erasing and reading histone lysine methylations. *Experimental & Molecular Medicine* **49,** e324–e324. doi:10.1038/emm.2017.11 (Apr. 2017).

87. Phillips, R. E., Soshnev, A. A. & Allis, C. D. Epigenomic Reprogramming as a Driver of Malignant Glioma. *Cancer Cell* **38,** 647–660. doi:10.1016/j.ccell.2020.08.008 (Nov. 2020).

88. McLaughlin, K. *et al.* DNA Methylation Directs Polycomb-Dependent 3D Genome Reorganization in Naive Pluripotency. *Cell Reports* **29,** 1974–1985.e6. doi:10.1016/j.celrep.2019.10.031 (Nov. 2019).

89. Plys, A. J. *et al.* Phase separation of Polycomb-repressive complex 1 is governed by a charged disordered region of CBX2. *Genes & Development* **33,** 799–813. doi:10.1101/gad.326488.119 (June 2019).

90. Schuettengruber, B., Bourbon, H.-M., Croce, L. D. & Cavalli, G. Genome Regulation by Polycomb and Trithorax: 70 Years and Counting. *Cell* **171,** 34–57. doi:10.1016/j.cell.2017.08.002 (Sept. 2017).

91. Cermakova, K. & Hodges, H. Next-Generation Drugs and Probes for Chromatin Biology: From Targeted Protein Degradation to Phase Separation. *Molecules* **23,** 1958. doi:10.3390/molecules23081958 (Aug. 2018).

92. Chamberlain, P. P. & Hamann, L. G. Development of targeted protein degradation therapeutics. *Nature Chemical Biology* **15,** 937–944. doi:10.1038/s41589-019-0362-y (Sept. 2019).

93. Nakamura, M., Gao, Y., Dominguez, A. A. & Qi, L. S. CRISPR technologies for precise epigenome editing. *Nature Cell Biology* **23**, 11–22. doi:10.1038/s41556-020-00620-7 (Jan. 2021).

Appendix A

Supplementary information for chapter 2

The following pages contain additional supplementary figures for chapter 2: Nucleome programming for the foundation of totipotency in mammalian germline development.

Appendix figure S1

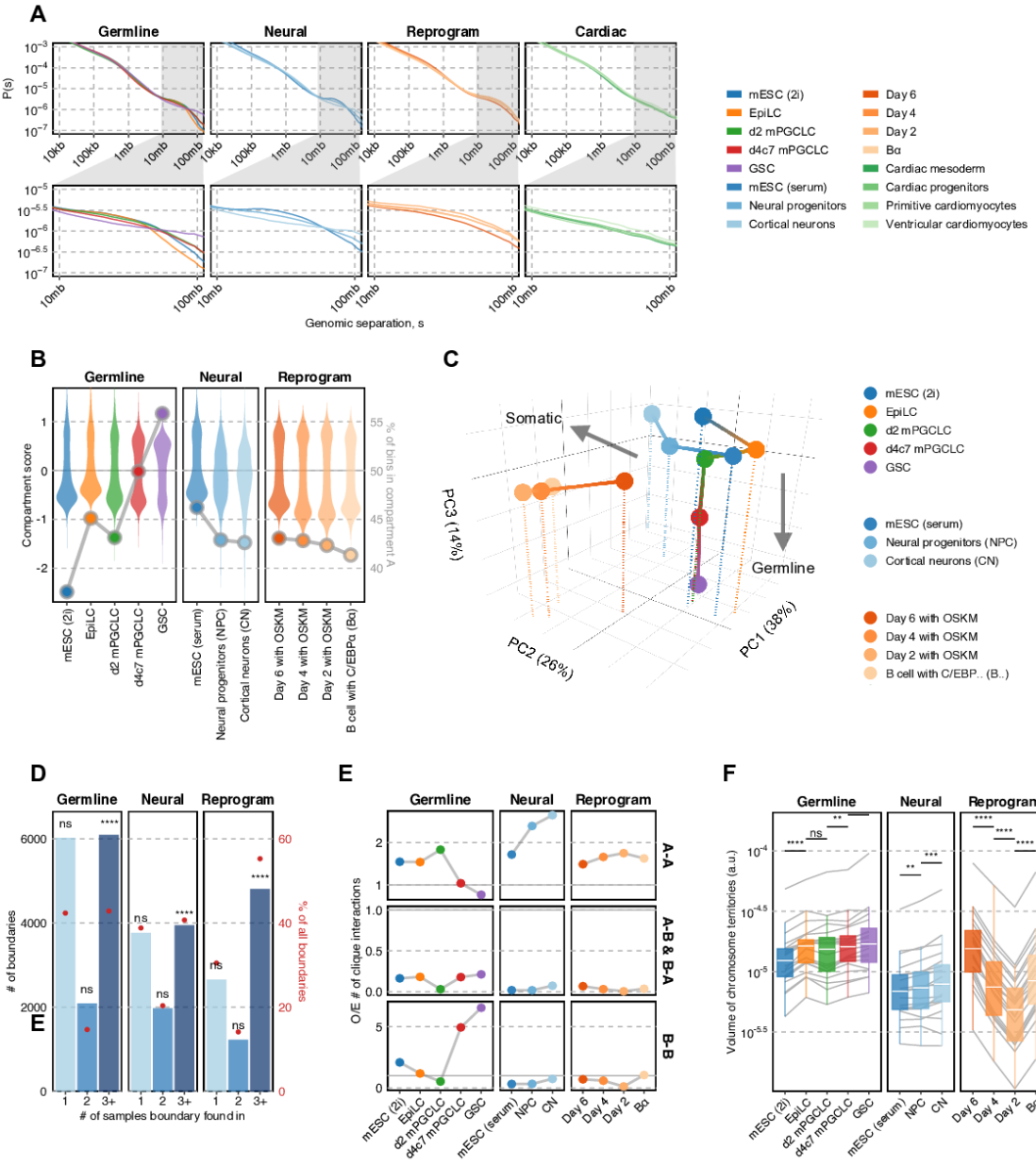

Appendix Figure S1. Hi-C analysis with other lineages.

(A) Contact probability decay across different inter-loci separation distances for different lineages (neural induction (Bonev et al, 2017); B cell reprogramming (Stadhouders et al, 2018)), demonstrating a gain of distal interactions along differentiation, especially at distances >50 Mb.

(B) Transitions in euchromatin-vs-heterochromatin bias during the course of different lineages at 100 kb resolution. (left axis: violin plots) Distribution of compartment scores; (right axis: dots) ratio of A:B compartment bins.

(C) PCA of compartment scores at 100 kb resolution comparing different lineages. Somatic differentiation is mostly reflected in PCs 1 & 2, while germ cell differentiation manifests in PC3.

(D) Degree of TAD boundary conservation in different lineages. Consistent across different lineages, more than 40% TAD boundaries are significantly conserved across differentiation. One-sided permutation tests were carried out by shuffling sample labels 100000 times, with p-values (left to right, top to bottom): 1, 1, 1e-5, 1, 1, 1e-5, 1, 1, 1e- 5.

(E) Enrichment of TAD-TAD interactions involved in max cliques (size $\geqslant 3$) during the development of different lineages.

(F) Convex hull volumes of CSynth-produced chromosome 3D models during the development of different lineages, after normalization to unit backbone length. n = 19. P- values are computed using Wilcoxon rank-sum tests. Wilcoxon signed-rank test p-values (left to right): 1.91e-6, 1.89e-1, 1.69e-3, 2.61e-4, 1.69e-3, 1.68e-4, 1.91e-6, 1.91e-6, 1.91e-6.

Appendix figure S2

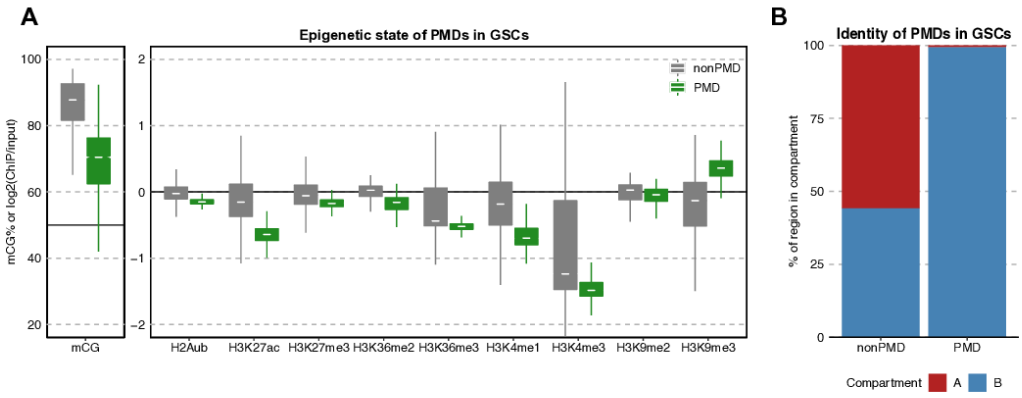

Appendix Figure S2. PMD analysis with epigenome and higher-order chromatin structure.

(A) %mCG and enrichment of various histone modifications in PMDs and non-PMDs.

(B) Proportion of A/B compartment in PMDs and non-PMDs.

Appendix figure S3

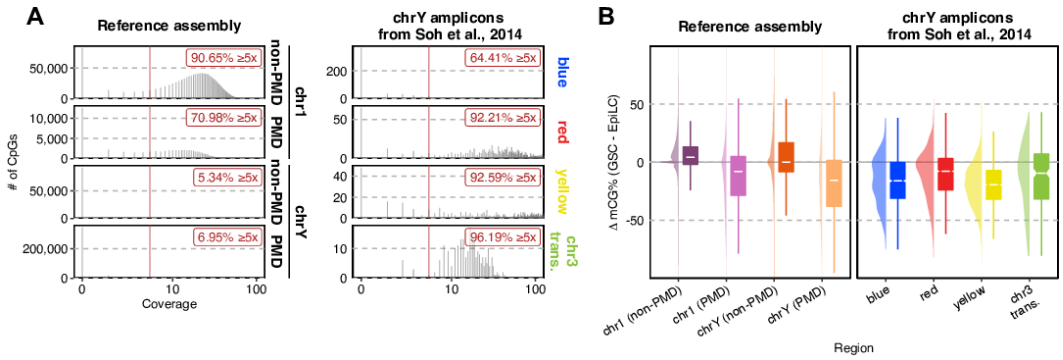

Appendix Figure S3. Methylome analysis on Y chromosome using alternative mapping method.
(A) Histogram of the PBAT coverage in different genomic regions using two alignment methods. (Left) In the conventional mapping approach of alignment against the reference genome, CpGs on chromosome Y exhibit significantly lower coverage than those on autosomes. (Right) Through direct mapping to the ampliconic sequences covering more than 80% of chromosome Y (Soh et al, 2014), most CpGs are now well-covered.
(B) Differential methylation within and outside GSCs' PMDs. Whereas GSCs are methylated at a level comparable to EpiLCs outside of PMDs, chromosome Y (most of which are PMDs) is found to be substantially hypomethylated using both conventional (left) and direct mapping (right).

Appendix figure S4

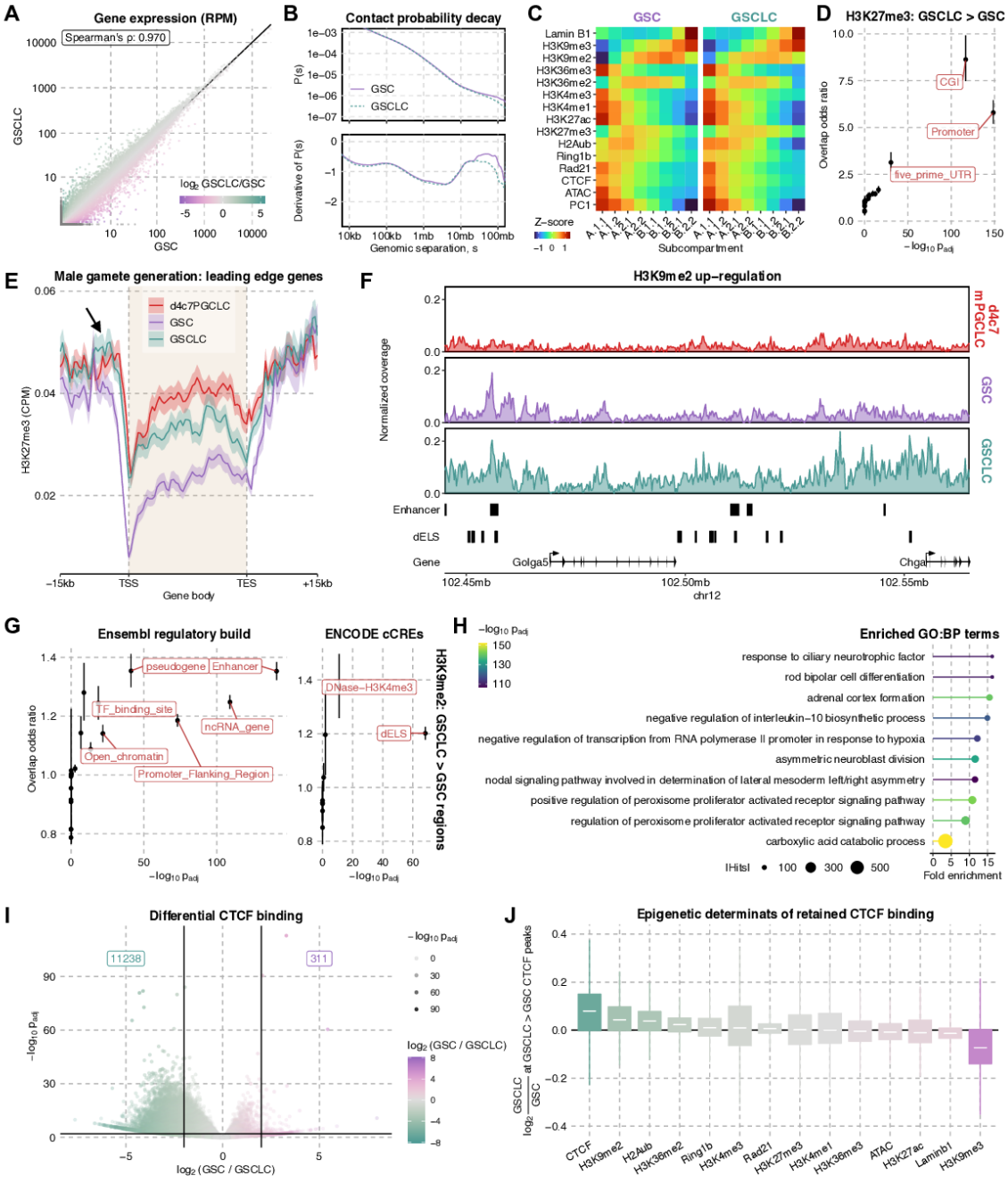

Appendix Figure S4. Nucleome differences between functional GSCs and spermatogenically-impaired GSCLCs.

(A) Scatter plot of gene expression values between GSCLCs and GSCs based on 3'-seq. (B) Contact probability decay across different inter-loci separation distances. In agreement with the observations from chromosome-wide contact maps, GSCLCs have reduced distal interaction frequencies as compared to GSCs.

(C) Enrichment patterns of epigenetic signals in an 8-state model yield comparable types of states between cell types.

(D) Regions with higher H3K27me3 in GSCLCs than GSCs predominantly correspond to CpG islands and promoters based on overlap enrichment analysis against the Ensembl Regulatory build. The point marks the mean while error bars indicate standard errors. (E) Metagene plots of H3K27me3 for leading edge genes of "male gamete generation" in d4c7 mPGCLCs, GSCs and GSCLCs. The thick line marks the mean while the upper and lower limits indicate standard errors.

(F) Example locus of GSCLC-specific enrichment of H3K9me2 marking intergenic cis- regulatory elements.

(G) Overlap enrichment analysis of regions with higher H3K9me2 in GSCLCs than GSCs against the Ensembl Regulatory build (left) and ENCODE cCREs (right). Elevated H3K9me2 mostly affects distal enhancer elements. The point marks the mean while error bars indicate standard errors.

(H) Pathway enrichment analysis of distal elements with enhancer-like signatures ("dELS") from the ENCODE cCRE database overlapping regions with higher H3K9me2 in GSCLCs than GSCs.

(I) Volcano plot of differential CTCF binding sites. Scatter plot of CTCF enrichment across all peaks in GSCs and GSCLCs, with 11238 peaks substantially higher levels of CTCF in GSCLCs than GSCs.

(J) Correlation between differential CTCF binding and enrichment of various epigenetic marks.

SUPPLEMENTARY REFERENCES

Bonev B, Mendelson Cohen N, Szabo Q, Fritsch L, Papadopoulos GL, Lubling Y, Xu X, Lv X, Hugnot J-P, Tanay A et al (2017) Multiscale 3D Genome Rewiring during Mouse Neural Development. Cell 171: 557-572.e524

Soh S, Y.Q., Alföldi J, Pyntikova T, Brown G, Laura, Graves T, Minx J, Patrick, Fulton S, Robert, Kremitzki C, Koutseva N, Mueller L, Jacob et al (2014) Sequencing the Mouse Y Chromosome Reveals Convergent Gene Acquisition and Amplification on Both Sex Chromosomes. Cell 159: 800-813

Stadhouders R, Vidal E, Serra F, Di Stefano B, Le Dily F, Quilez J, Gomez A, Collombet S, Berenguer C, Cuartero Y et al (2018) Transcription factors orchestrate dynamic interplay between genome topology and gene regulation during cell reprogramming. Nature Genetics 50: 238-249

Appendix B

Supplementary information for chapter 3

The following pages contain additional supplementary figures for chapter 3: **H3K27me3 spreading organizes canonical PRC1 chromatin architecture to regulate developmental transcriptional program.**

Figure S1

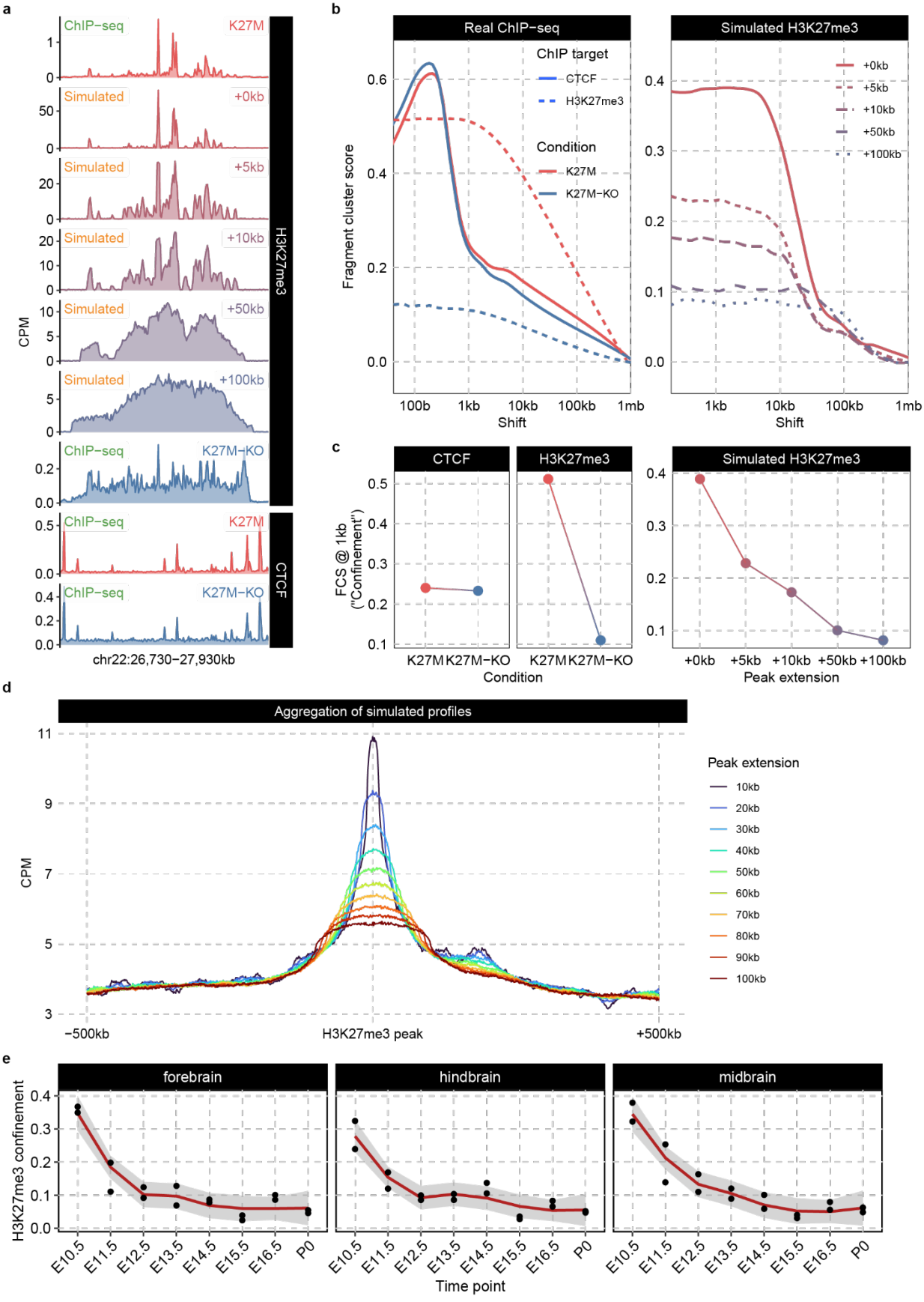
a
ChIP−seq
K27M
Simulated
+0kb
+5kb
+10kb
+50kb
+100kb
H3K27me3
CPM
ChIP−seq
K27M−KO
CTCF
chr22:26,730−27,930kb
b
Real ChIP−seq
ChIP target
CTCF
H3K27me3
Condition
K27M
K27M−KO
Fragment cluster score
100b
1kb
10kb
100kb
1mb
Shift
Simulated H3K27me3
+0kb
+5kb
+10kb
+50kb
+100kb
c
CTCF
H3K27me3
FCS @ 1kb ("Confinement")
K27M K27M−KO
Condition
Simulated H3K27me3
+0kb +5kb +10kb +50kb +100kb
Peak extension
d
Aggregation of simulated profiles
CPM
−500kb
H3K27me3 peak
+500kb
Peak extension
10kb
20kb
30kb
40kb
50kb
60kb
70kb
80kb
90kb
100kb
e
forebrain
hindbrain
midbrain
H3K27me3 confinement
E10.5
E11.5
E12.5
E13.5
E14.5
E15.5
E16.5
P0
Time point

Supplemental figure 1

a. Experimental and simulated ChIP-seq coverage tracks of H3K27me3 and CTCF around a representative locus, showing different levels of confinement for H3K27me3
b. Genome-wide fragment cluster score computed at various shift distances for experimental and simulated ChIP-seq datasets, demonstrating the distinction between confined versus diffuse profiles of H3K27me3; note that CTCF lacks change between K27M and KO
c. Fragment cluster score specifically at 1kb shift distance, a choice for measuring "confinement"
d. Aggregate plots for depth-normalized simulated H3K27me3 datasets with various specified peak widths, confirming the various levels of confinement in simulated H3K27me3 profiles
e. Confinement scores of H3K27me3 (fragment cluster score at 10kb, see methods) for in vivo samples from the developing mouse brain

Figure S2

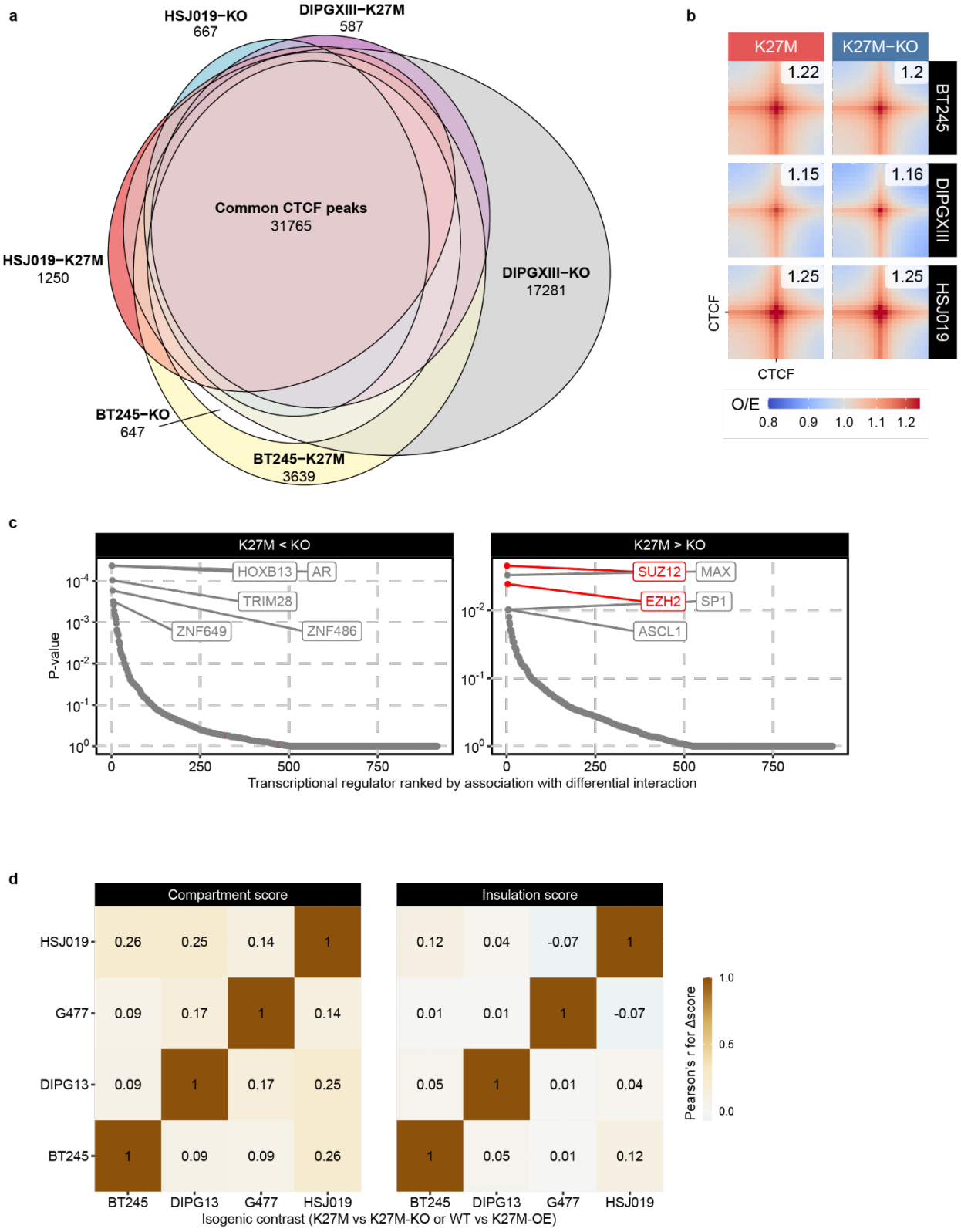
a
HSJ019−KO
667
DIPGXIII−K27M
587
Common CTCF peaks
31765
HSJ019−K27M
1250
DIPGXIII−KO
17281
BT245−KO
647
BT245−K27M
3639
b
K27M
K27M−KO
1.22
1.2
BT245
1.15
1.16
DIPGXIII
1.25
1.25
HSJ019
CTCF
CTCF
O/E
0.8 0.9 1.0 1.1 1.2
c
K27M < KO
K27M > KO
HOXB13
AR
TRIM28
ZNF649
ZNF486
SUZ12
MAX
EZH2
SP1
ASCL1
P-value
Transcriptional regulator ranked by association with differential interaction
d
Compartment score
Insulation score
HSJ019
G477
DIPG13
BT245
0.26 0.25 0.14 1
0.09 0.17 1 0.14
0.09 1 0.17 0.25
1 0.09 0.09 0.26
0.12 0.04 -0.07 1
0.01 0.01 1 -0.07
0.05 1 0.01 0.04
1 0.05 0.01 0.12
BT245 DIPG13 G477 HSJ019
BT245 DIPG13 G477 HSJ019
Isogenic contrast (K27M vs K27M-KO or WT vs K27M-OE)
Pearson's r for Δscore
1.0
0.5
0.0

Supplemental figure 2

a. Euler diagram of CTCF peak calls for isogenic comparisons of pGBMs with and without K27M, demonstrating substantial overlap
b. Piled-up pairwise Hi-C interaction of the union CTCF peak set with convergent motif orientations, showing a lack of differential CTCF interactions between K27M and KO
c. BART3D analysis investigating transcriptional regulators whose binding sites are enriched in regions with differential interactions between isogenic K27M and K27M-KO comparisons; note that polycomb-related factors are enriched in regions with K27M-specific interactions
d. Correlation of compartment/insulation score differences (K27M versus KO/WT) between isogenic comparisons; the weak correlation coefficients demonstrate lack of consistent changes in compartment/domain structures upon the removal or overexpression of K27M

Figure S3

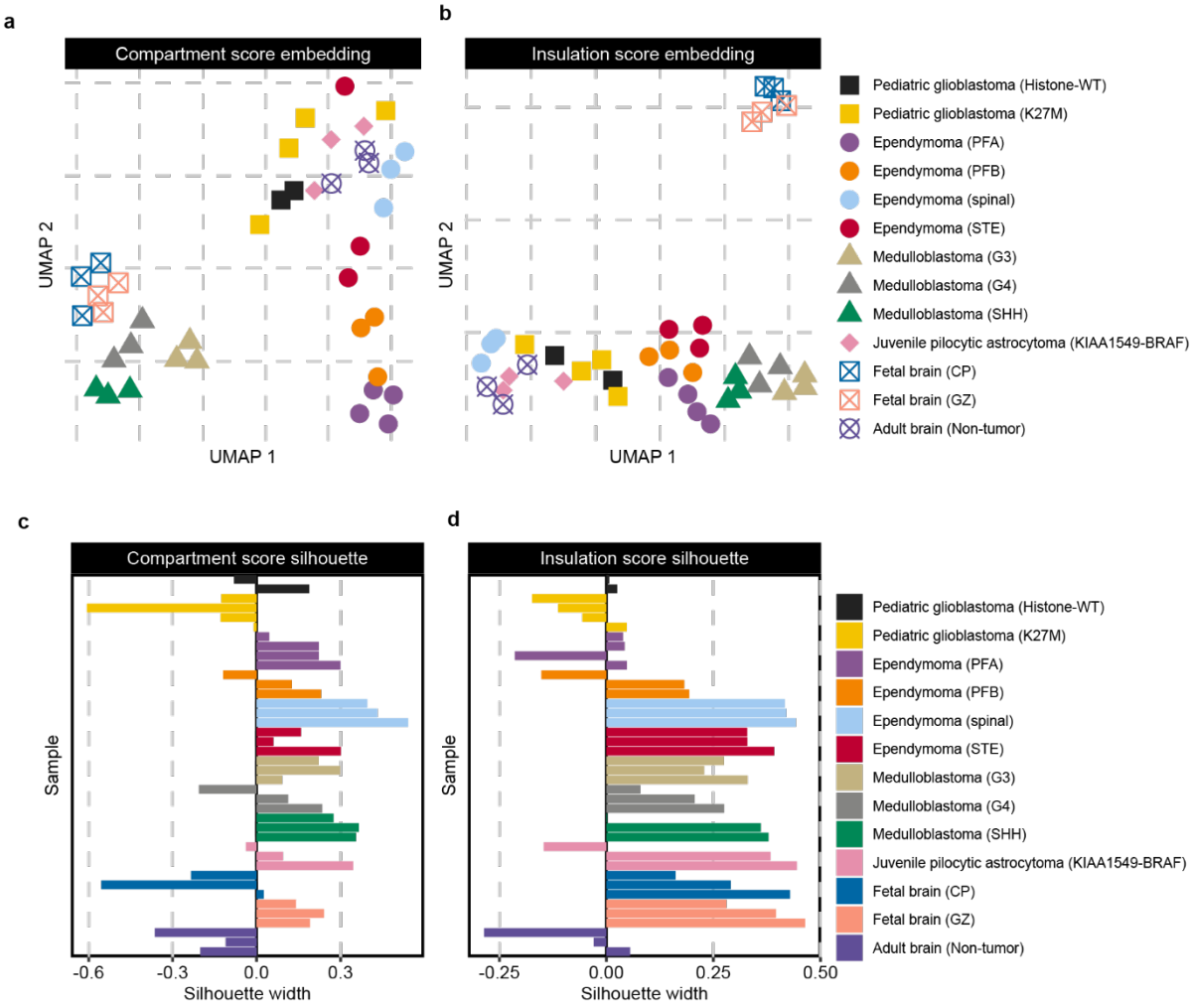
a
Compartment score embedding
UMAP 2
UMAP 1
b
Insulation score embedding
UMAP 2
UMAP 1
Pediatric glioblastoma (Histone-WT)
Pediatric glioblastoma (K27M)
Ependymoma (PFA)
Ependymoma (PFB)
Ependymoma (spinal)
Ependymoma (STE)
Medulloblastoma (G3)
Medulloblastoma (G4)
Medulloblastoma (SHH)
Juvenile pilocytic astrocytoma (KIAA1549-BRAF)
Fetal brain (CP)
Fetal brain (GZ)
Adult brain (Non-tumor)
c
Compartment score silhouette
Sample
-0.6
-0.3
0.0
0.3
Silhouette width
d
Insulation score silhouette
Sample
-0.25
0.00
0.25
0.50
Silhouette width
Pediatric glioblastoma (Histone-WT)
Pediatric glioblastoma (K27M)
Ependymoma (PFA)
Ependymoma (PFB)
Ependymoma (spinal)
Ependymoma (STE)
Medulloblastoma (G3)
Medulloblastoma (G4)
Medulloblastoma (SHH)
Juvenile pilocytic astrocytoma (KIAA1549-BRAF)
Fetal brain (CP)
Fetal brain (GZ)
Adult brain (Non-tumor)

Supplemental figure 3

a. UMAP embedding based on genome-wide correlation of compartment score tracks among diverse primary tissue, showing that K27M pGBMs samples do not cluster together
b. UMAP embedding based on genome-wide correlation of insulation score tracks, showing again K27M pGBMs do not form a clear cluster
c. Silhouette width based on genome-wide correlation of compartment score tracks, demonstrating lack of distinct compartment score signature for K27M pGBMs
d. Silhouette width based on genome-wide correlation of insulation score tracks, confirming the lack of insulation score signature for K27M pGBMs

Figure S4

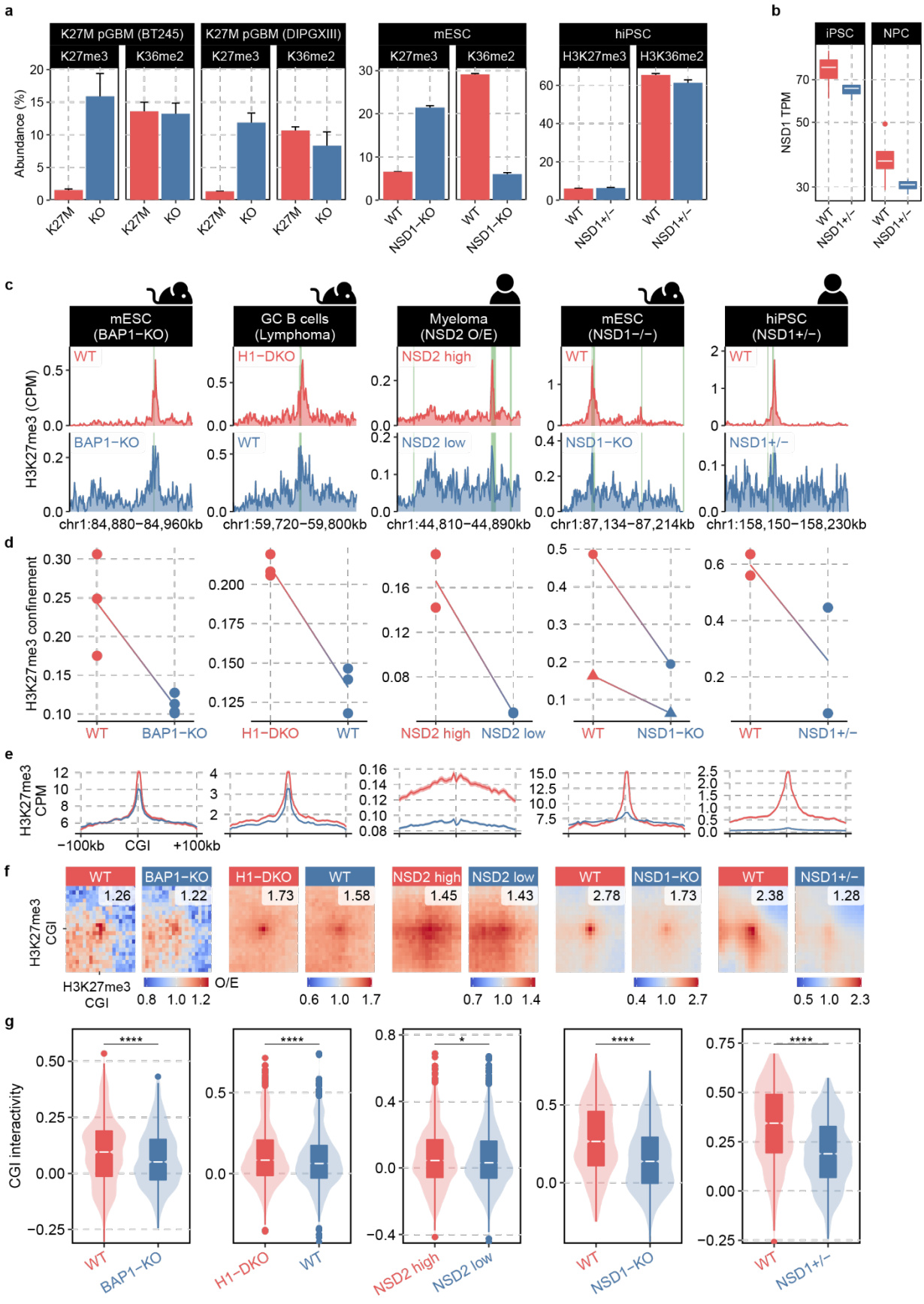
a
K27M pGBM (BT245)
K27M pGBM (DIPGXIII)
mESC
hiPSC
K27me3
K36me2
H3K27me3
H3K36me2
Abundance (%)
K27M
KO
WT
NSD1-KO
NSD1+/-
b
iPSC
NPC
NSD1 TPM
c
mESC (BAP1−KO)
GC B cells (Lymphoma)
Myeloma (NSD2 O/E)
mESC (NSD1−/−)
hiPSC (NSD1+/−)
H3K27me3 (CPM)
BAP1−KO
H1−DKO
NSD2 high
NSD2 low
NSD1−KO
NSD1+/−
chr1:84,880−84,960kb
chr1:59,720−59,800kb
chr1:44,810−44,890kb
chr1:87,134−87,214kb
chr1:158,150−158,230kb
d
H3K27me3 confinement
e
H3K27me3 CPM
−100kb
CGI
+100kb
f
H3K27me3 CGI
O/E
g
CGI interactivity

Supplemental figure 4

a. Global abundance of H3K27me3 and H3K36me2 measured by quantitative histone mass spectrometry, in pGBM and stem cell contexts, showing the H3K27me3 gain upon K27M-KO and H3K36me2 loss upon NSD1-KO leading to the change of the other mark.
b. Expression of NSD1 in NCRM1 hiPSCs and NPC, confirming the downregulation of NSD1 upon heterozygous NSD1 loss
c. H3K27me3 coverage tracks (in units of counts-per-million-alignments) around representative loci in various cancer and stem cell contexts demonstrating distinction of confined versus diffuse profiles
d. Metric of H3K27me3 signal confinement (fragment cluster score at 10kb, see methods), confirming genome-wide distinction between confined versus diffuse profiles
e. H3K27me3 aggregate plots around the top 1000 most enriched CpG islands, normalized by coverage
f. Average pairwise Hi-C interaction among the top 1000 most H3K27me3-enriched CpG islands, showing the stronger interaction in samples with confined H3K27me3
g. Quantification of pairwise loop strength among the top 1000 most H3K27me3-enriched CpG islands, confirming the stronger interactions in H3K27me3-confined samples are statistically significant

Figure S5

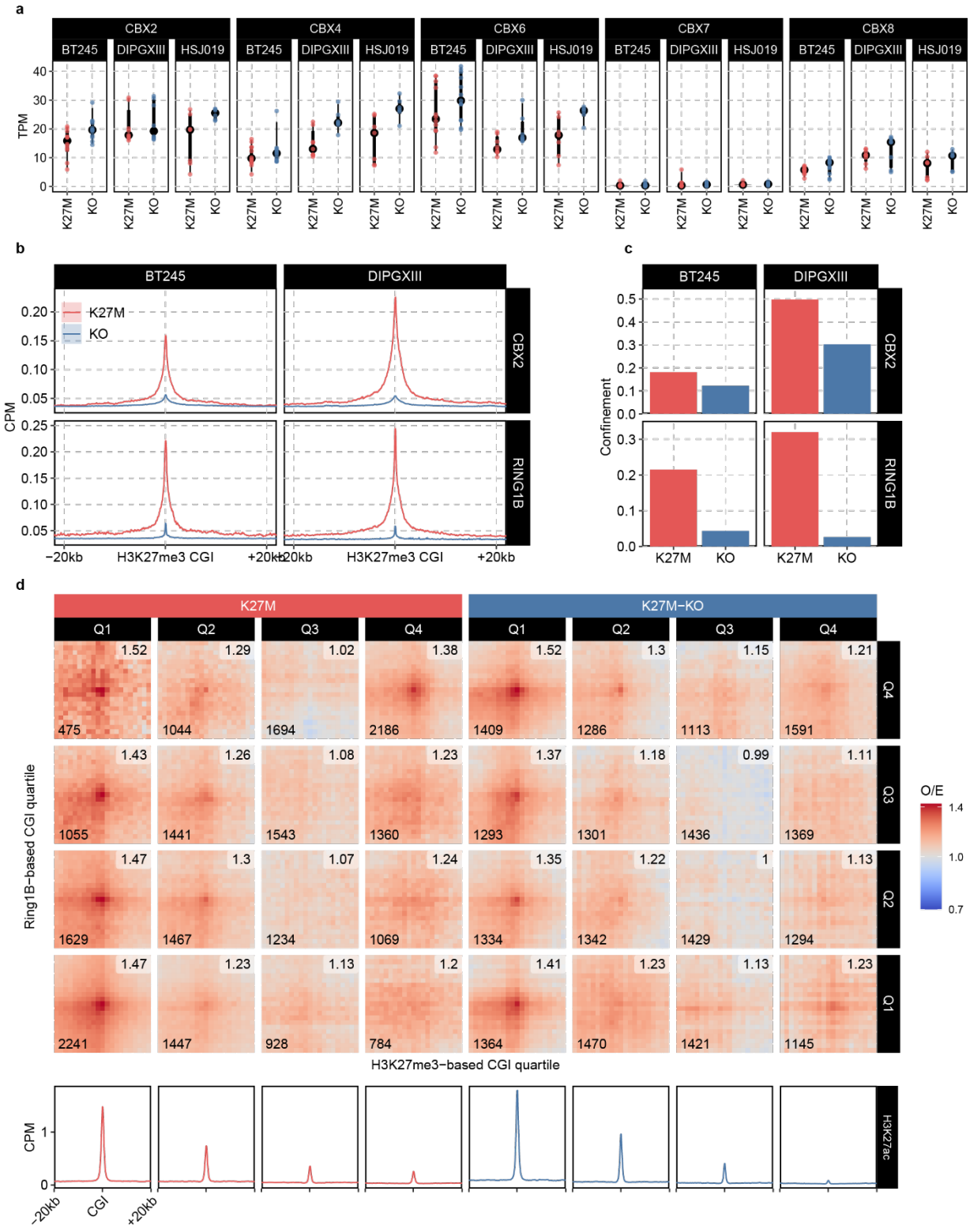
a
CBX2
CBX4
CBX6
CBX7
CBX8
BT245
DIPGXIII
HSJ019
TPM
K27M
KO
b
BT245
DIPGXIII
K27M
KO
CBX2
RING1B
CPM
−20kb
H3K27me3 CGI
+20kb
c
Confinement
d
K27M
K27M−KO
Q1
Q2
Q3
Q4
Ring1B−based CGI quartile
H3K27me3−based CGI quartile
O/E
H3K27ac
CGI

Supplemental figure 5

a. Expression of PRC1-subunit CBX proteins in pGBM K27M cell lines based on bulk RNA-seq
b. Metaplots showing RING1B/CBX2 aggregate signals around all CpG islands, normalized by total read depth
c. Metric of RING1B/CBX2 ChIP-seq signal confinement (fragment cluster score at 10kb, see methods) in diverse contexts confirming diffusion upon removal of K27M
d. Piled-up pairwise interaction of CpG islands divided based on their H3K27me3 and RING1B enrichment quartile in K27M pGBM cell line BT245, confirming the most differential K27M-specific enrichment of distal looping in the CGIs with both highest (i.e. Q4) H3K27me3 and RING1B. CGIs lacking H3K27me3 (Q1) and enriched for H3K27ac also engage in strong pairwise interactions, with or without RING1B binding.

Figure S6

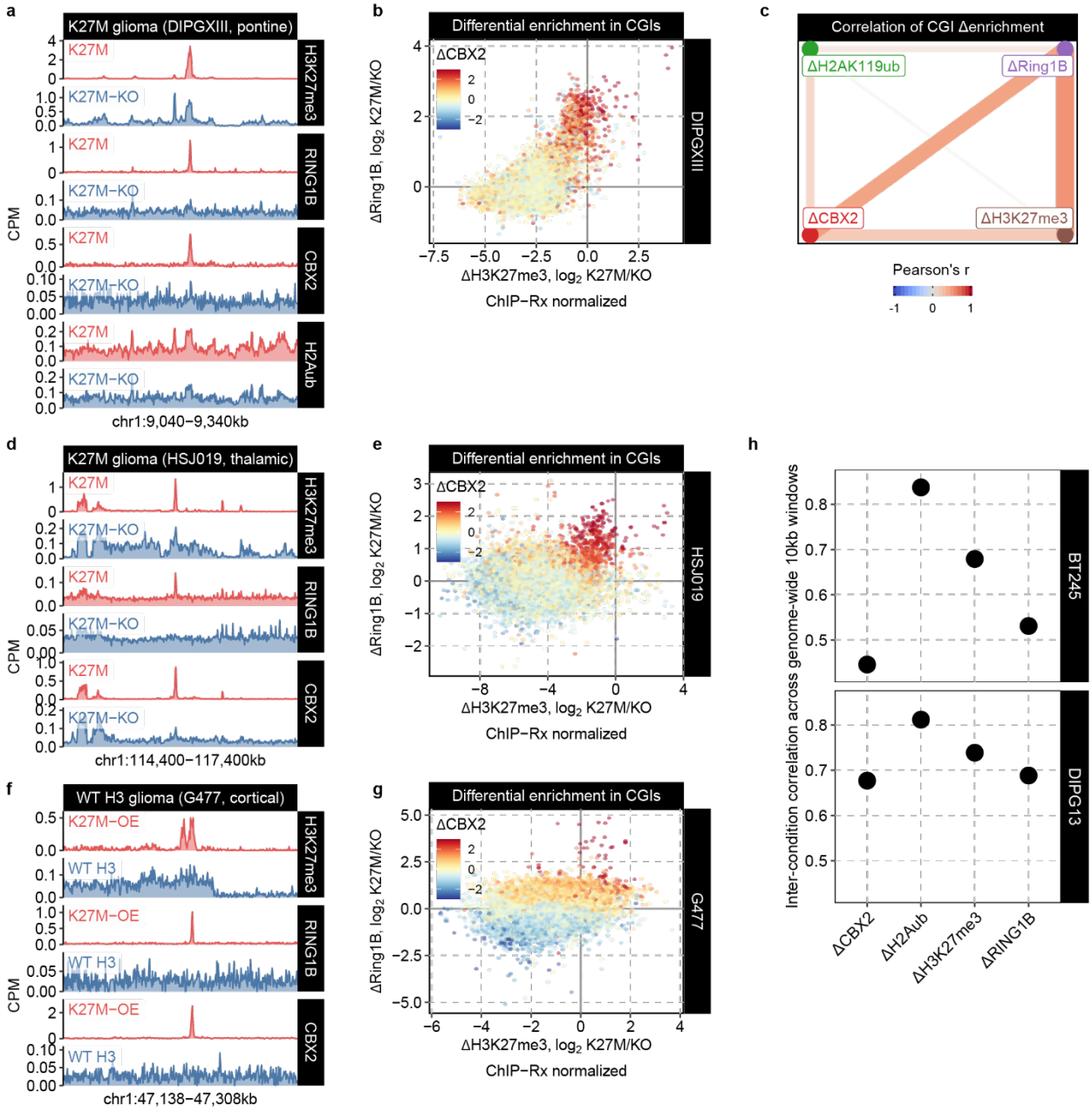
a
K27M glioma (DIPGXIII, pontine)
K27M
K27M−KO
H3K27me3
RING1B
CBX2
H2Aub
CPM
chr1:9,040−9,340kb
b
Differential enrichment in CGIs
ΔCBX2
DIPGXIII
ΔRing1B, log2 K27M/KO
ΔH3K27me3, log2 K27M/KO
ChIP−Rx normalized
c
Correlation of CGI Δenrichment
ΔH2AK119ub
ΔRing1B
ΔCBX2
ΔH3K27me3
Pearson's r
d
K27M glioma (HSJ019, thalamic)
chr1:114,400−117,400kb
e
HSJ019
f
WT H3 glioma (G477, cortical)
K27M−OE
WT H3
chr1:47,138−47,308kb
g
G477
h
Inter-condition correlation across genome-wide 10kb windows
BT245
DIPG13
ΔCBX2
ΔH2Aub
ΔH3K27me3
ΔRING1B

Supplemental figure 6

a. Representative locus of cPRC1 dilution following H3K27me3 spread, reproducible in another pGBM K27M cell line, DIPGXIII
b. As (a), except for an additional pGBM K27M cell line, HSJ019
c. Correlation of signal enrichment differences in CpG islands between K27M and K27M-KO, showing that CBX2 is most enriched in the regions with high enrichment of both H3K27me3 and RING1B, confirming strong association between H3K27me3 confinement with enhanced cPRC1 recruitment in another pGBM K27M cell line, DIPGXIII
d. Correlation network of differential enrichment of H3K27me3, RINGB1, CBX2 and H2AK119ub, showing the weak correlation between H2AK119ub and the rest three, implicating cPRC1 rather than ncPRC1 determines the difference between K27M and KO in another pGBM K27M cell line, DIPGXIII
e. As (c), except for an additional cell line, HSJ019
f. As (a), except for a pGBM WT H3 cell line, G477
g. As (c), except for a pGBM WT H3 cell line, G477
h. Global correlation of signal enrichment confirming H2AK119ub as being the least different between K27M and K27M-KO

Figure S7

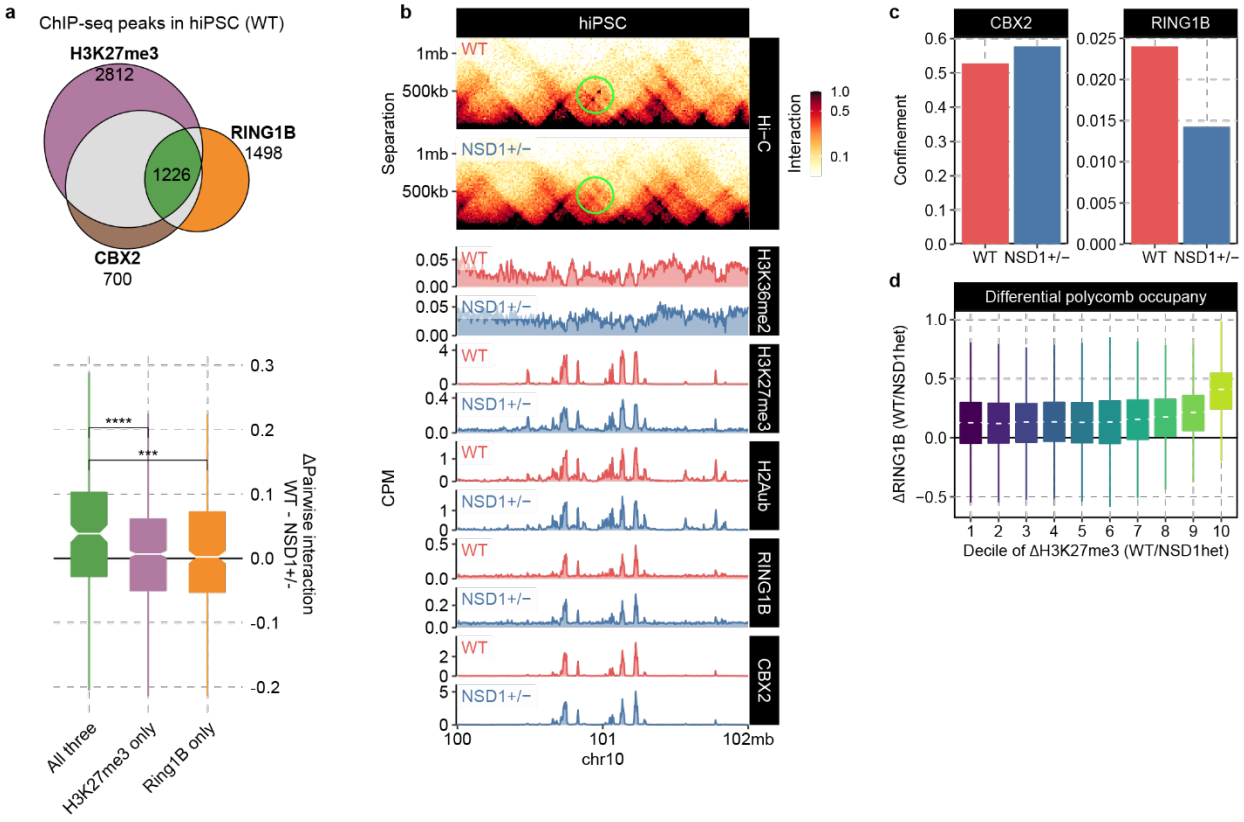
a
ChIP-seq peaks in hiPSC (WT)
H3K27me3
2812
RING1B
1498
1226
CBX2
700
ΔPairwise interaction
WT - NSD1+/-
0.3
0.2
0.1
0.0
-0.1
-0.2
****
***
All three
H3K27me3 only
Ring1B only
b
hiPSC
1mb
500kb
WT
NSD1+/-
Separation
Hi-C
Interaction
1.0
0.5
0.1
CPM
H3K36me2
H3K27me3
H2Aub
RING1B
CBX2
100
101
102mb
chr10
c
CBX2
RING1B
Confinement
WT
NSD1+/-
d
Differential polycomb occupany
ΔRING1B (WT/NSD1het)
Decile of ΔH3K27me3 (WT/NSD1het)

Supplemental figure 7

a. (top) Euler diagram of peak calls for H3K27me3 and PRC1 sub-units CBX2 & RING1B in WT hiPSCs cell line BT245; (bottom) differential (K27M versus KO) pairwise HiC interaction for various peak overlap subsets, showing the sites marked by all three (H3K27me3, RING1B, CBX2) have the strongest differential interactions.
b. Representative locus of differential interaction between cPRC1 sites, along with ChIP-seq profiles of H3K36me2, H3K27me3, RING1B, CBX2 and H2AK119ub in WT and NSD1+/- hiPSCs
c. Metric of PRC1 ChIP-seq signal confinement (fragment cluster score at 10kb, see methods), confirming dilution of RING1B upon heterozygous loss of NSD1
d. Differential RING1B binding in CpG islands stratified by differential H3K27me3 between WT and NSD1+/- hiPSCs. Coordinated depletion of RING1B and H3K27me3 is observed, especially for CGIs with the greatest loss of H3K27me3.

Figure S8

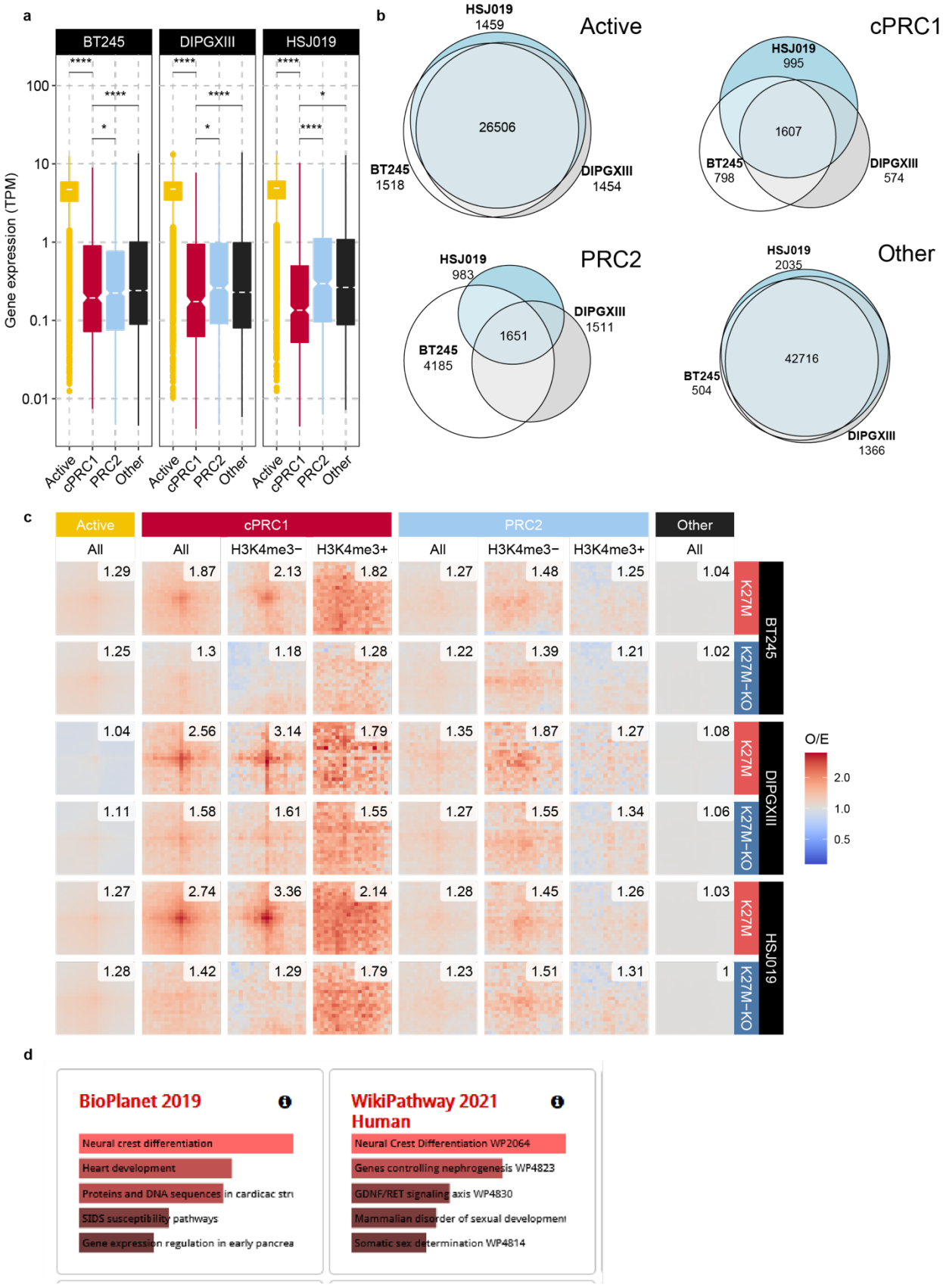
a
BT245
DIPGXIII
HSJ019
Gene expression (TPM)
Active
cPRC1
PRC2
Other
b
Active
HSJ019
1459
26506
BT245
1518
DIPGXIII
1454
cPRC1
HSJ019
995
1607
BT245
798
DIPGXIII
574
PRC2
HSJ019
983
1651
DIPGXIII
1511
BT245
4185
Other
HSJ019
2035
42716
BT245
504
DIPGXIII
1366
c
Active
cPRC1
PRC2
Other
All
H3K4me3−
H3K4me3+
1.29
1.87
2.13
1.82
1.27
1.48
1.25
1.04
1.25
1.3
1.18
1.28
1.22
1.39
1.21
1.02
1.04
2.56
3.14
1.79
1.35
1.87
1.27
1.08
1.11
1.58
1.61
1.55
1.27
1.55
1.34
1.06
1.27
2.74
3.36
2.14
1.28
1.45
1.26
1.03
1.28
1.42
1.29
1.79
1.23
1.51
1.31
1
K27M
K27M−KO
BT245
DIPGXIII
HSJ019
O/E
2.0
1.0
0.5
d
BioPlanet 2019
Neural crest differentiation
Heart development
Proteins and DNA sequences in cardiac str
SIDS susceptibility pathways
Gene expression regulation in early pancrea
WikiPathway 2021 Human
Neural Crest Differentiation WP2064
Genes controlling nephrogenesis WP4823
GDNF/RET signaling axis WP4830
Mammalian disorder of sexual development
Somatic sex determination WP4814

Supplemental figure 8

a. Expression of genes associated with the promoters from the four clusters, demonstrating the lowest transcription levels in the cPRC1 cluster
b. Euler diagram of sites from the four clusters showing concordance of "Active" and "Other" sites among the three K27M pGBM cell lines, and less for "cPRC1" and "PRC2" sites
c. Piled-up differential pairwise Hi-C interaction for regions within the four clusters in other K27M pGBM cell lines, recapitulating the specific association between cPRC1 regions and K27M-specific looping
d. Enrichr pathway over-representation analysis of consensus cPRC1 targets among three K27M pGBM cell lines, demonstrating the enrichment in development and neuron differentiation

Figure S9

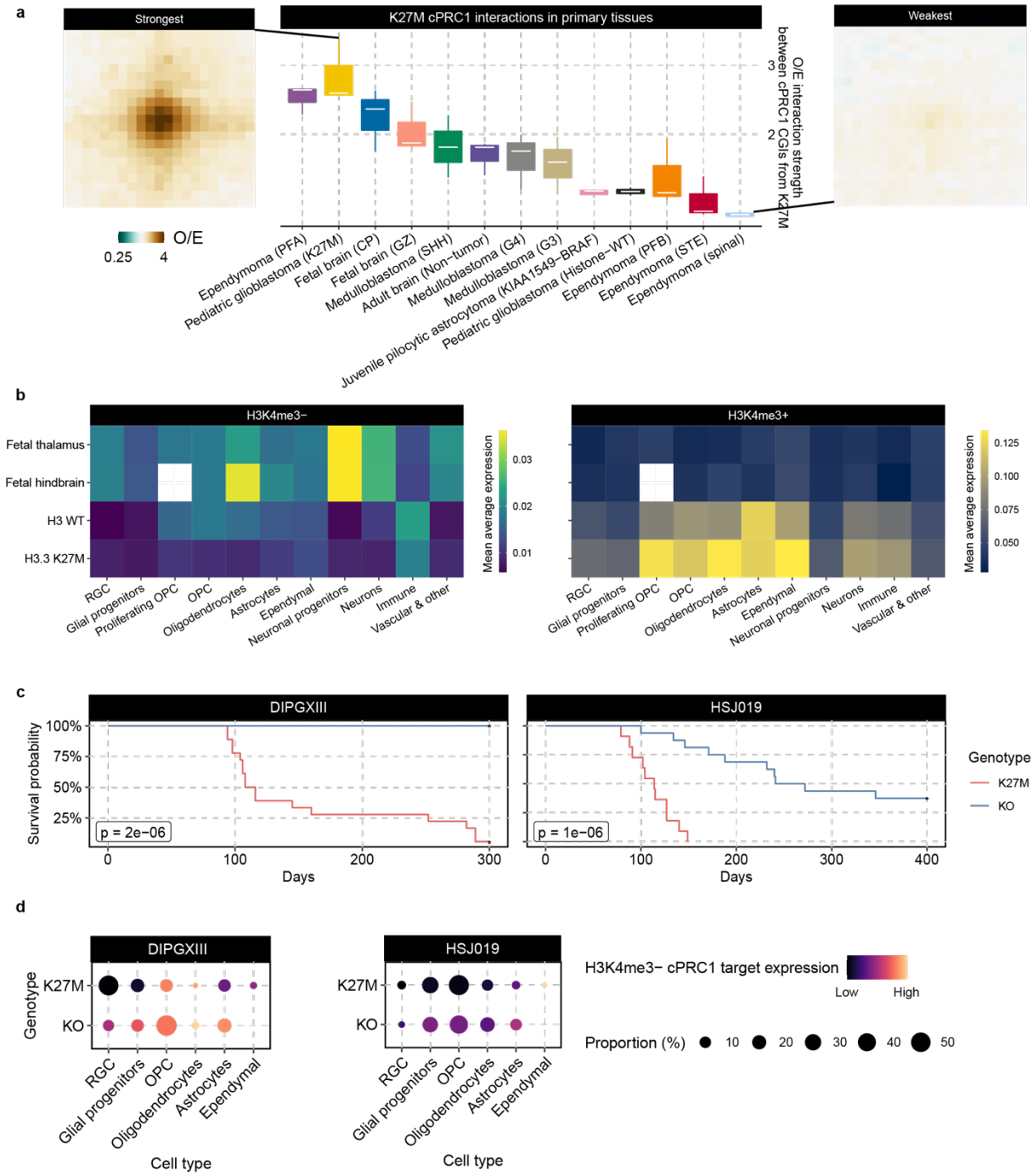
a
Strongest
K27M cPRC1 interactions in primary tissues
Weakest
O/E interaction strength between cPRC1 CGIs from K27M
O/E
0.25
4
Ependymoma (PFA)
Pediatric glioblastoma (K27M)
Fetal brain (CP)
Fetal brain (GZ)
Medulloblastoma (SHH)
Adult brain (Non−tumor)
Medulloblastoma (G4)
Medulloblastoma (G3)
Juvenile pilocytic astrocytoma (KIAA1549−BRAF)
Pediatric glioblastoma (Histone−WT)
Ependymoma (PFB)
Ependymoma (STE)
Ependymoma (spinal)
b
H3K4me3−
H3K4me3+
Fetal thalamus
Fetal hindbrain
H3 WT
H3.3 K27M
Mean average expression
RGC
Glial progenitors
Proliferating OPC
OPC
Oligodendrocytes
Astrocytes
Ependymal
Neuronal progenitors
Neurons
Immune
Vascular & other
c
DIPGXIII
HSJ019
Survival probability
100%
75%
50%
25%
p = 2e−06
p = 1e−06
Days
Genotype
K27M
KO
d
DIPGXIII
HSJ019
Genotype
K27M
KO
Cell type
H3K4me3− cPRC1 target expression
Low
High
Proportion (%)
10
20
30
40
50

Supplemental figure 9

a. Pairwise HiC interactions among regions consistently labelled as H3K4me3- cPRC1 targets among three K27M pGBM cell lines, in Hi-C maps of primary tissue – revealing strongest interaction in K27M pGBMs and PFA EPNs, followed by the fetal brain
b. Mean expression of cPRC1 target genes per cell, averaged over all cells with the same cell type label, from scRNA-seq of primary tissue. H3.3K27M uniquely demonstrates repression of H3K4me3- cPRC1 targets
c. Kaplan-Meier survival analysis for xenograft mice using two other pGBM K27M cell lines
d. Comparison of scRNA-seq from K27M and K27M-KO PDXs confirm increased H3K4me3-cPRC1 target gene expression is accompanied by an increase in the proportion of more differentiated cell types

Figure S10

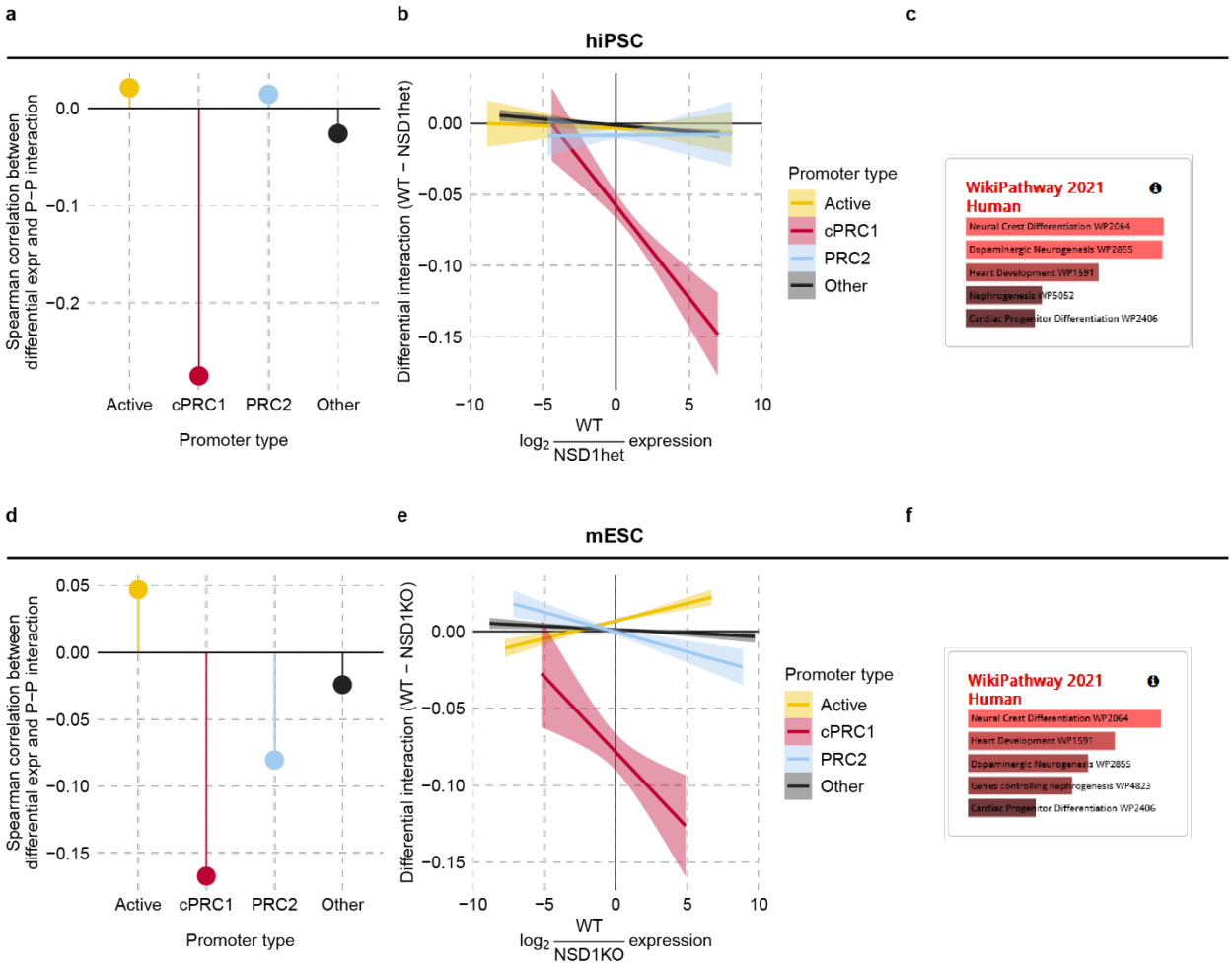
a
b
c
hiPSC
Spearman correlation between differential expr and P–P interaction
0.0
−0.1
−0.2
Active
cPRC1
PRC2
Other
Promoter type
Differential interaction (WT – NSD1het)
0.00
−0.05
−0.10
−0.15
−10
−5
0
5
10
log2 WT / NSD1het expression
Promoter type
Active
cPRC1
PRC2
Other
WikiPathway 2021 Human
Neural Crest Differentiation WP2064
Dopaminergic Neurogenesis WP2855
Heart Development WP1591
Nephrogenesis WP5052
Cardiac Progenitor Differentiation WP2406
d
e
f
mESC
Spearman correlation between differential expr and P–P interaction
0.05
0.00
−0.05
−0.10
−0.15
Active
cPRC1
PRC2
Other
Promoter type
Differential interaction (WT – NSD1KO)
0.00
−0.05
−0.10
−0.15
−10
−5
0
5
10
log2 WT / NSD1KO expression
Promoter type
Active
cPRC1
PRC2
Other
WikiPathway 2021 Human
Neural Crest Differentiation WP2064
Heart Development WP1591
Dopaminergic Neurogenesis WP2855
Genes controlling nephrogenesis WP4823
Cardiac Progenitor Differentiation WP2406

Supplemental figure 10

a. Correlation between differential expression and differences in mean intra-class pairwise interaction score between WT and NSD1+/- hiPSCs. Strong anti-correlation between expression and looping changes was found uniquely for cPRC1 target genes
b. Trends in the relationship between differential expression and looping between WT and NSD1+/- hiPSCs, with strong negative slope solely observed for cPRC1 target genes
c. Enrichr pathway over-representation analysis of cPRC1 targets in mESCs, demonstrating the enrichment in brain development
d. Correlation between differential expression and differences in mean intra-class pairwise interaction score between WT and NSD1-KO mESCs. Strong anti-correlation between expression and looping changes was found uniquely for cPRC1 target genes
e. Trends in the relationship between differential expression and looping between WT and NSD1-KO mESCs, with strong negative slope solely observed for cPRC1 target genes
f. Enrichr pathway over-representation analysis of cPRC1 targets in mESCs, demonstrating the enrichment in brain development

Figure S11

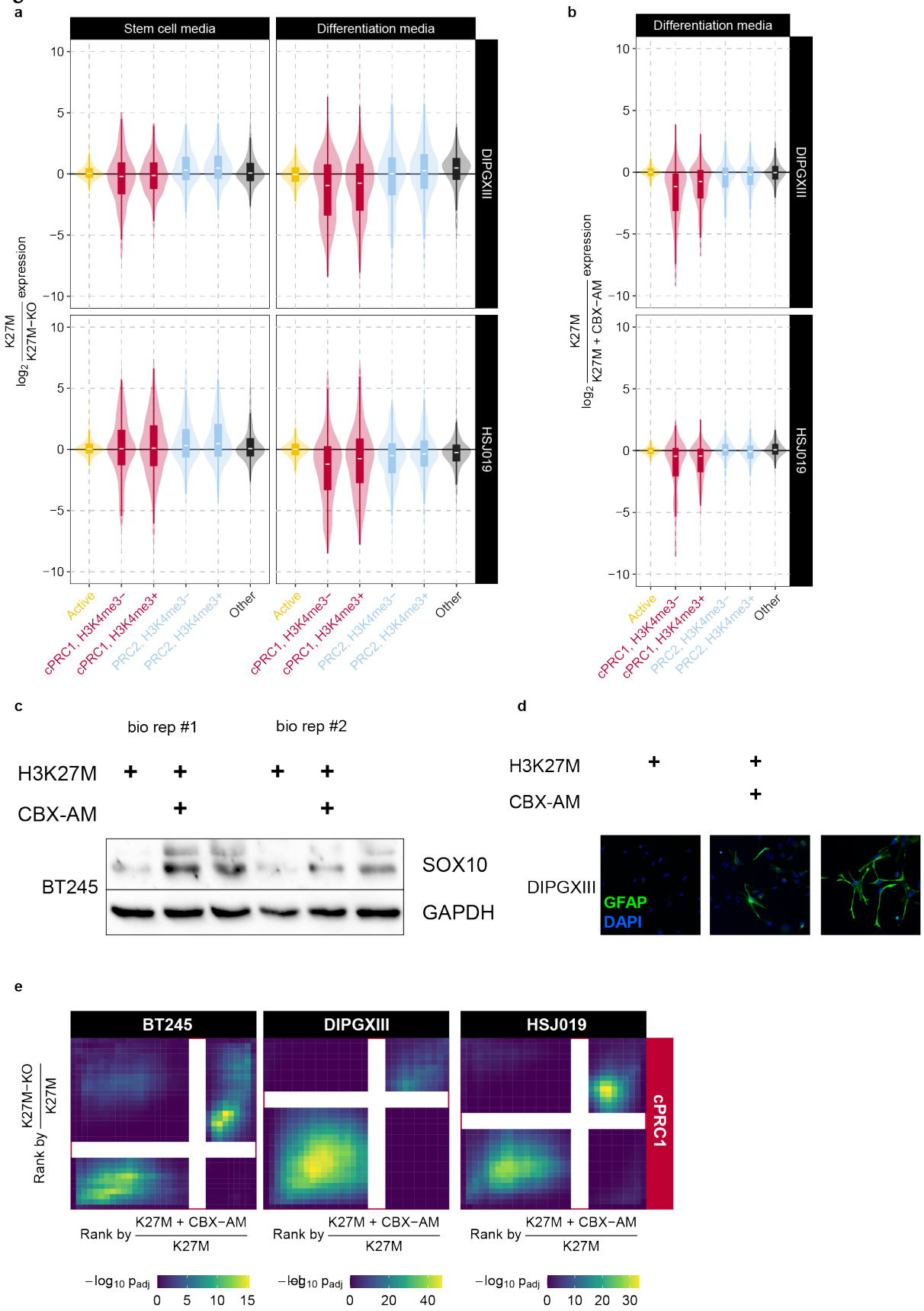
a
Stem cell media
Differentiation media
DIPGXIII
HSJ019
log2 K27M / K27M−KO expression
Active
cPRC1, H3K4me3−
cPRC1, H3K4me3+
PRC2, H3K4me3−
PRC2, H3K4me3+
Other
b
Differentiation media
log2 K27M / K27M + CBX−AM expression
c
bio rep #1
bio rep #2
H3K27M
CBX-AM
BT245
SOX10
GAPDH
d
H3K27M
CBX-AM
DIPGXIII
GFAP
DAPI
e
BT245
DIPGXIII
HSJ019
cPRC1
Rank by K27M−KO / K27M
Rank by K27M + CBX−AM / K27M
−log10 padj
0 5 10 15
0 20 40
0 10 20 30

Supplemental figure 11

a. Differential expression, specifically of cPRC1 targets, become heightened after differentiation, recapitulated in additional K27M pGBM cell lines DIPGXIII and HSJ019
b. Up-regulation of differentiation markers observed for both K27M-KO and CBX-AM treated K27M cells, in additional K27M pGBM cell lines DIPGXIII and HSJ019
c. Up-regulation of differentiation markers observed in both K27M-KO and CBX-AM treated K27M cells in pGBM line BT245
d. Up-regulation of differentiation markers observed in both K27M-KO and CBX-AM treated K27M cells in pGBM line DIPGXIII
e. Rank-rank hypergeometric overlap of differential expression for cPRC1 target genes between parental K27M pGBM cells versus K27M-KO or CBX-AM treated cells. Expressional changes induced by CBX-AM and K27M-KO were found to be significantly correlated across three different cell lines.

Appendix C

Copyright permissions

Copyright permissions have been obtained for all figures adapted from previous publications.

Select figures are licensed under the Creative Commons Attribution 4.0 International License or the Creative Commons Attribution-NonCommercial-NoDerivatives 4.0 International License. To view a copy of these licenses, please visit the linked webpages or send a letter to Creative Commons, PO Box 1866, Mountain View, CA 94042, USA.

Additional permissions have been obtained from Springer Nature, Oxford University Press, and Elsevier with the following license numbers:

- 5282171050176
- 5282171015352
- 5282170979067
- 5282170759703
- 5282170661528
- 5282170617699
- 5282170580839
- 5282170547432
- 5282170513172
- 5282170466735
- 5282170421049
- 5282170376648

- 52821605669 33
- 52821605294 65
- 52821604837 52
- 52821604246 58
- 52821603451 19
- 52821602556 34
- 52821601222 52
- 52821600139 43
- 52821412327 40

Full license agreements are available upon request.